Weathering and climate linkage at seasonal to kilo-year timescales: Evidence from water and sediment chemistry

A Thesis
Submitted in Partial Fulfillment of the Requirements for the Degree of
Doctor of Philosophy

by
Anupam Samanta
20163453

Indian Institute of Science Education and Research
Pune 411008 India

February 2022

To

All My Well Wishers

भारतीय विज्ञान शिक्षा एवं अनुसंधान संस्थान पुणे
INDIAN INSTITUTE OF SCIENCE EDUCATION AND RESEARCH PUNE
डॉ. होमी भाभा मार्ग, पुणे 411008, महाराष्ट्र, भारत I Dr. Homi Bhabha Road, Pune 411008, Maharashtra, India
T +91 20 2590 8001 W www.iiserpune.ac.in

IISER PUNE

Certificate

Certified that the work incorporated in the thesis entitled "**Weathering and climate linkage at seasonal to kilo-year timescales: Evidence from water and sediment chemistry**" submitted by **Mr. Anupam Samanta** was carried out by the candidate, under my supervision. The work presented here or any part of it has not been included in any other thesis submitted previously for the award of any degree or diploma from any other university or institution.

Tripathy
22/2/22

Date: 22nd February 2022
Place: Pune

Dr. Gyana Ranjan Tripathy
(Supervisor)

मानव संसाधन विकास मंत्रालय, भारत सरकार का स्वायत्त संस्थान
An Autonomous Institution of the Ministry of Human Resource Development, Government of India

भारतीय विज्ञान शिक्षा एवं अनुसंधान संस्थान पुणे
INDIAN INSTITUTE OF SCIENCE EDUCATION AND RESEARCH PUNE
डॉ. होमी भाभा मार्ग, पुणे 411008, महाराष्ट्र, भारत | Dr. Homi Bhabha Road, Pune 411008, Maharashtra, India
T +91 20 2590 8001 W www.iiserpune.ac.in
IISER PUNE

Declaration

I declare that this written submission represents my idea in my own words, and where others' ideas have been included, I have adequately cited and referenced the original sources. I also declare that I have adhered to all principles of academic honesty and integrity and have not misrepresented or fabricated, or falsified any idea/data/fact/source in my submission. I understand that violation of the above will be cause for disciplinary action by the Institute and can also evoke penal action from the sources which have thus not been properly cited or from whom proper permission has not been taken needed.

Anupam Samanta

Date: 22nd February 2022
Place: Pune

Anupam Samanta
ID: 20163453

Acknowledgement

Ph.D. is a long, dynamic journey with lots of uncertainties. It is one of the most challenging periods of life. Although research and scientific discovery are the priority, Ph.D. also shapes our outlook towards life. I will fully utilize this opportunity to express my sincere gratitude to all those associated with my Ph.D. life.

I am grateful to my advisor, Dr. Gyana Ranjan Tripathy, for his constant support, guidance, and tolerating my whimsical mind over the last five years. He taught me to use geochemical data as a tool efficiently to solve various scientific problems. Constant discussion with him always steered the course of my Ph.D. journey. I appreciate his meticulous stance in teaching me even the slightest details of chemical processing of samples, analyses, and interpretation of data. He has been excellent in understanding the academic freedom of a student, which is crucial in maintaining the work-life balance during the Ph.D. tenure.

I am thankful to Dr. Naveen Gandhi, a long-term collaborator of our research group from the Indian Institute of Tropical Meteorology (IITM) Pune, for giving me IITM laboratory access for speleothem research. I would like to thank Dr. B. Nagender Nath from the National Institute of Oceanography (NIO) Goa, who actively collaborated and provided marine sediment cores for my Ph.D. project. I am indebted to all my research collaborators, Dr. Rajani Panchang Dhumal, Dr. Ravi Bhushan, Dr. Santosh K. Rai, Dr. S. K. Parcha, Dr. Shreyas Managave, Dr. Vineet Goswami, Mr. M. G. Yadava, Dr. B. N. Goswami, Dr. Sudha Rajamani, Dr. Ritima Das, Dr. Ankush Shrivastava, Mr. A. Phanindra Reddy, Mr. Satyabrata Das, Ms. Nisha Bharti, Mr. Manesh Prakash Joshi, for their support, scientific discussion, and laboratory access during my doctoral research.

I am grateful to my research advisory committee (RAC) members, Prof. Vikrant Jain and Dr. Neena J Mani, for their insightful thoughts on my Ph.D. project. I am thankful to Prof. Shyam Sundar Rai, Dr. Argha Banerjee, Dr. Utsav Mannu, whose suggestions constantly improved my scientific knowledge.

My parents and other family members have always been a constant support in all aspects of my life, including my Ph.D. journey. A word of thank you would be too small for them. Subhronil Mondal, Jyotirmoy Paul, Mahesh Halder have always been my closest friends.

Their views on my research helped me in developing new interdisciplinary ideas. I thank Anirban Mondal, Abhijit Bhattacharya, Raja Boragapu, Nilesh Sandbhor, Saurabh Choubey for staying with me in my difficult times and not-so-difficult times. I am grateful to my friends Abhinav Prakash Gahlot, Sudeb Ghosh, Sattwick Halder, Anweshi Dewan, and many more for their friendship. I also feel lucky to have lovely juniors like Sabyasachi Mandal, Joyjit Sen, Aswin Pradeep.

No research is possible without the support of my labmates Danish, Jimmy, Rakesh, Achyuth, present and ex-members of our GRASP Lab, and other colleagues from the ECS department. This time I take the opportunity to express my sincere gratitude for their support. I acknowledge Mr. Vikrant Bartakke, Mr. Parveen Nasa, and other staff members of IISER Pune for providing administrative and technical support. I thank Mr. Sunil Kumar Pathak and Mr. Ebin Varghese from Metrohm, Mr. Priyesh Patil, Mr. Piyush Deokar, Mr. Vikrant Parnaik, and Mr. Mahesh Jawahire from Thermo Fisher Scientific and other service engineers for their constant support for running our instrument facilities smoothly and making my Ph.D. life much more straightforward. Moreover, support from Mr. Sandeep Chavan and other housekeeping personnel are duly acknowledged.

I am thankful to University Grants Commission (UGC) for funding my Ph.D. research. I would also like to thank IISER Pune for providing extended fellowship, Scivic Engineering Pvt Ltd., and Innoplexus Consulting Services Pvt Ltd. for one-time financial support beyond five years of UGC fellowship. I also thank the Department of Science and Technology, India, for the financial support to Dr. Gyana Ranjan Tripathy and Dr. Neena J Mani under the National Mission on Strategic Knowledge for Climate Change (NMSKCC) for this Ph.D. project. Above all, I sincerely acknowledge all those taxpayers Indian citizens for their contributions to scientific research and development.

Abstract

Continental erosion plays a dominant role in global biogeochemical and climatic cycles. Intensity of this land-surface (erosion) process is disproportionally higher in the tropics, mainly due to its conducive climate (rainfall and temperature). The main objective of this thesis work is to investigate the interaction between erosion and climate over multiple timescales, ranging from seasonal to kilo-years. Towards this, geochemical and isotopic analyses of paleo-archives (sedimentary records from the Arabian Sea and upper Indus (Zanskar) River basin, and speleothem) and weekly variation of river water chemistry (Brahmaputra River) have been carried out. The chronology of the speleothem (~9200 - 3950 yrs BP), collected from the Gupteswar Cave (Odisha, India), was established using U-Th isotopic systematic, whereas the age ranges for the Zanskar sediment section (~22400 - 1450 yrs BP) and two Arabian Sea cores (SSK40/GC06 (~3560 yrs BP - recent); SSK40/GC10 (~7150 - 800 yrs BP)) were constrained using radiocarbon ages.

Seasonality in chemical erosion pattern of the Brahmaputra River basin: Time-series analyses of the Brahmaputra River (Guwahati, India) water chemistry show seasonal changes. The degree of seasonality for the elemental abundances and their ratios, however, is less pronounced at Guwahati when compared to those with other Himalayan (Ganga and Salween) rivers. The monthly averaged Ca/Si ratios for the Brahmaputra show minimal (~6 %) variation compared to that (~17 %) observed for the Ganga outflow, points to the minimal role of runoff in regulating the erosion pattern of this river. Inverse model calculations estimated the silicate-derived fraction of cations and Sr for monsoon and non-monsoon seasons, respectively, are statistically indifferent. Observations from this study suggest that the erosion intensity in the Brahmaputra basin is not limited by runoff/water-rock interaction time and is more regulated by rapid mechanical erosion at around eastern syntaxis.

Reconstruction of Holocene variability of the erosion patterns using marine records: Geochemical investigation of two sediment cores raised from the Arabian Sea (SSK40/GC06 and SSK40/GC10) was carried out to assess the climatic control on erosion patterns during the Holocene period. The high-resolution geochemical study of these cores shows insignificant temporal change in immobile elemental (Al, Ti, and rare earth elements (REEs)) concentrations and REE patterns, indicating no major change in sedimentary sources. However, trends of

multiple weathering indices point to fluctuating chemical erosion patterns during the Meghalayan stage (4200 yr BP to present). The recent intensification of chemical erosion from 1600 yr BP to the present is not synchronous with any major change in the southwest (SW) monsoon during this period. However, this erosion change is consistent with the rise in C4 vegetation, possibly due to sustained agricultural practices in the SW-dominated regions. Human-induced increase in C4 vegetation with shallow root systems may promote efficient sediment transport and hence, intense erosion of young soils with faster dissolution kinetics. Further, down-core variations in the Al-normalized ratios (Ba/Al, TOC/Al, and S/Al) and enrichment factors of redox-sensitive elements (U and Mo) of the SSK40/GC10 core were useful in identifying a shift in oceanic (bottom water) redox state from oxic to anoxic bottom water condition since ~ 4.2 kyr BP. The timing of this change is synchronous to the earlier reported drought phase at the beginning of the Meghalayan stage, underscoring climatic control on the bottom water redox state. Major outcomes from past erosion reconstruction showed modern-day chemical erosion rates are anthropogenically influenced and may not serve as representative riverine value for long-term chemical (e.g., ^{87}Sr/^{86}Sr, ^{187}Os/^{188}Os) budgets.

Reconstruction of past erosion patterns using terrestrial records: Chemical and Sr-Nd isotopic investigation of river section sediments from the upper Indus (Zanskar) basin was used to reconstruct the Himalayan erosion pattern during the last glacial-interglacial cycle. The temporal trends of the Sr-Nd isotopic compositions show a sudden shift in sediment provenance at around the Bølling-Allerød climate event. The temporal trends of selected chemical weathering indices (K/Al, CIA) also show an increased chemical erosion rate during this warmer climatic phase. This change in the Himalayan erosion can be linked to glacial retreat and continuous exposure of fresh minerals during this warm and humid phase (Bølling-Allerød climate event), establishing a strong coupling between erosion and climate.

Reconstruction of past rainfall using speleothem δ^{18}O record: High-resolution oxygen isotopic data (δ^{18}O) of the speleothem from the core monsoon zone were used to reconstruct the natural variability of the Indian summer monsoon (ISM) during the mid-Holocene period. These data reveal the impact of the Indian Ocean on short-term extreme climate events over the ISM regime. On the contrary, the North Atlantic (NA) climatic changes control the long-term trends of ISM variability. The δ^{18}O data identify a super-drought event spanning ~200 years, at around 6.5 kyr BP, synchronous to the negative Indian Ocean Dipole state. This study also shows that the broad declining nature of ISM during the middle to late Holocene is linked to south-ward migration of the Inter-tropical convergence zone and/or change in NA climate.

Contents

List of Tables

List of Figures

Chapter 1

Introduction

1.1 Introduction

Continental erosion plays a key role in regulating marine biogeochemical cycles by supplying bio-essential major and trace elements to the ocean ecosystem. These low-temperature surficial processes also contribute to the consumption of atmospheric CO_2, shaping Earth's surface and sediment production. Intensity of these processes is regulated by several natural factors, including tectonics, climate, basin slope, lithology, and vegetation. On million-year timescales, tectonics play an important role in regulating the erosion rates, mainly by increasing elevation and exposing larger land areas (Chamberlin, 1899; Raymo and Ruddiman, 1992). For instance, the silicate erosion rates have been found to increase significantly since the uplift of the Himalaya and Tibetan plateau, which resulted in a global cooling phase via steady consumption of atmospheric CO_2 (Raymo and Ruddiman, 1992). However, studies on contemporary and past (kilo-year) timescales have documented stronger control of climate on erosion rates (Clift et al., 2008; Cai et al., 2019; Hein et al., 2017; Lupker et al., 2013; Miriyala et al., 2017; Rahaman et al., 2009; Wan et al., 2017). Global compilation of denudation rates of river basins shows that the physical and chemical erosion rates are strongly correlated (Dixon and von Blanckenburg, 2012; Larsen et al., 2010, 2014; Larsen and Montgomery, 2012; Singh et al., 2005; von Blanckenburg, 2005). This correlation reflects an increase in chemical erosion due to continuous exposure of fresh minerals through physical erosion in the basin (Blum and Erel, 1995). The chemical erosion rates in river basins, after decoupling the physical erosion dependency, are found to be regulated by climatic (temperature and rainfall patterns) factors (von Blanckenburg, 2005). The erosion intensity of rivers flowing through the "weathering-limited" regions shows a strong dependency on climatic parameters (e.g., temperature and runoff), whereas the chemical erosion for the "transport-limited" basins involves completely weathered products (West et al., 2005; West, 2012). The erosion rates of transport-limited (than weathering-limited) basins, therefore, show lesser dependency on climatic factors. Further, a large number of earlier studies have also documented that the erosion rates are controlled by several non-climatic factors, such as vegetation, lithology, and hill slope angles (Bluth and Kump, 1994; Mandal et al., 2015; Singh et al., 2005; White et al., 1999). These diverging views on controlling factors on the intensity of erosion limit the precise prediction of continental fluxes to nearby seas in response to climatic changes.

The rivers flowing through the tropics are characterized by higher temperature and rainfall, and hence, their erosion patterns can provide useful clues about erosion-climate interactions. The water discharge of rivers from India is strongly influenced by the Indian summer monsoon (ISM) and exhibits large seasonality in the runoff. The water fluxes of these rivers vary by an order of magnitude within 1-year duration, with higher (~70-80 %) discharge being observed during the summer monsoon (JJAS) seasons. In response to seasonal runoff changes, the concentrations of dissolved constituents of these rivers also show significant seasonal variation. These seasonal concentration-discharge (C-Q) variations are mainly linked to the dilution factor and/or weathering intensity of the basin (Godsey et al., 2009). This C-Q relation, in general, follows a power law ($C = k \times Q^{-b}$; k and b are constants), and it is found to be distinctly different for different elements (Godsey et al., 2009). For a chemostatic element (i.e., $b = 0$), the concentration does not change significantly with runoff. The chemostatic behaviour of a solute mainly depicts a longer fluid residence time in a basin than the amount of time required to achieve chemical equilibrium (Maher, 2011). In contrast, a non-chemostatic behaviour can arise from multiple factors, which include variable solute mixing, primary mineral abundance, weathering reactions at the surface and sub-surface regions, water permeability, fluid transit time, and catchment slope angles (Godsey et al., 2009; Ibarra et al., 2016; Jenckes et al., 2022; Maher, 2011; Torres et al., 2015). The C-Q relationship of a basin, therefore, is mostly regulated by the weathering reaction and fluid flow in a catchment. These relationships are also crucial in estimating the discharge-weighted weathering rates for river basins. The available chemical weathering rates for river basins are mostly estimated based on a snapshot and/or limited seasonal changes (Gaillardet et al., 1999; Moon et al., 2014). Model calculations showed that the weathering rate estimations with limited samples are associated with large uncertainty (30-40 %), and a precise rate calculation should include a reasonable number ($n > 40$) of seasonal data (Moon et al., 2014). Recognizing this, a part of this thesis investigates the weekly variation in water chemistry of the Brahmaputra River system to assess the runoff-erosion coupling at a seasonal scale and to estimate the annual (chemical) silicate erosion rates of this Himalayan river basin. Prior to this, a large number of time-series studies have already been conducted for the Ganga River system (Bickle et al., 2005, 2018; Boral et al., 2021; Chakrapani and Saini, 2009; Tipper et al., 2006; Tripathy et al., 2010). However, there exist limited studies on other major Himalayan rivers, such as Brahmaputra (Rai and Singh, 2007; Singh et al., 2005) and Irrawaddy-Salween (Chapman et al., 2015) rivers. These studies document higher intensities of chemical erosion in the Himalayan rivers during the monsoon season than during the lean flow stages, underscoring the important role of runoff on erosion. Krishnaswami et al. (1999), based on limited seasonal chemical and $^{87}Sr/^{86}Sr$ data from the Ganga headwaters, have suggested an increased solute supply from the silicate weathering during lean (than peak) flow stages. High water-rock interaction time during lean flow stages is expected to promote the dissolution of resistant silicate minerals (Tripathy et al., 2010). Further, Tipper et al. (2006) have also invoked the role of solute supply from groundwater during the lean flow periods to explain the observed time-series water chemistry and Sr isotopes of a mono-lithological first-order stream from the Ganga River system. The seasonal changes in the chemical erosion in the Ganga basin may also be driven by (i) differential solute supply from tributaries in response to their spatio-temporal rainfall (runoff) pattern (Bickle et al., 2018) and/or (ii) ion-exchange processes (Boral et al., 2021). Additionally, episodes of flash-flooding events at regional scales have also been found to influence the water chemistry of large river systems (Rai and Singh, 2007).

Terrestrial and marine sediments preserve signatures of past continental erosion processes. Terrestrial sediments are mostly detrital in nature and hence, can provide a precise and high-resolution record of past erosion patterns. Chemical composition of the silicate fraction of these sediments is independent of any contributions from biogenic/authigenic sources, and hence, has often been used to trace the temporal changes in the sediment provenances. Similarly, the chemistry of marine sediments is also regulated by multiple inputs, such as detrital, biogenic, and authigenic supplies. The silicate fraction of these sediments, therefore, can also be used efficiently to reconstruct continental erosional variations. Also, the variation in sediment compositions, particularly the abundances of redox-sensitive elements, can serve as reliable proxies for past changes in oceanic redox states. The abundance and distribution of biogenic elements ($CaCO_3$ and TOC) and redox-sensitive elements (S, Mo, U, V, Cr and enrichment factors of Mo and U) in sediments serve as reliable indicators of the past bottom water redox conditions. Redox-sensitive elements form stable oxyanion complexes in oxygenated water conditions and get reduced to particle-reactive phases by forming organometallic complexes in anoxic/sulfidic conditions (Tribovillard et al., 2006). Hence, enrichment of these elements in sedimentary records can provide a measure of the redox state of the overlying water column during sediment deposition. In contrast, the enrichment of biointermediate elements, such as barium, in sediments reflect degree of particulate $BaSO_4$ scavenging from water column via barite super-saturation through large barium and sulfate release through decomposition of organic matters, and hence, can be used to constrain the past productivity patterns (Dehairs et al., 2000). This study, therefore, used sediment chemistry of marine and continental records to infer both past erosion patterns and oceanic redox state.

The oceanic sediments are largely comprised of riverine supply of sediments, with sub-ordinate particulate contributions from authigenic and biogenic pathways. Global river systems deliver about 19 billion tons of sediments annually to the oceans (Milliman and Farnsworth, 2011). This riverine sediment flux corresponds to an average global sediment production rate of ~200 tons/km^2/yr, disproportionally lower than that reported for the tropical river basins (~3648 tons/km^2/yr (for the northern hemisphere); Syvitski et al., 2003). The high sediment production and hence, erosion intensity in the tropics have often been linked to the conducive climate (warm temperature and high rainfall) in the basins, which underscores a strong climate-erosion linkage (Clift et al., 2008; Hein et al., 2017; Limmer et al., 2012; Lupker et al., 2013; Peketi et al., 2020; Tripathy et al., 2014; Wan et al., 2017). Understanding this climatic sensitivity of continental erosion is central to predicting the response of land-surface processes (water and soil resources) and oceanic biogeochemical cycle (Knight and Harrison, 2012). Available studies show a variable degree of climatic sensitivity of the erosion process for different river catchments. These studies show intense chemical and physical erosion rates during warm and humid periods compared to cold and drier phases. In contrast, studies based on lead and beryllium isotopes of marine sedimentary archives have challenged this erosion and climate linkage at a millennial timescale and show stable (area-normalized) weathering fluxes, despite significant changes in temperature and rainfall during the Quaternary (Foster and Vance, 2005; von Blanckenburg et al., 2015) and Neogene (Caves Rugenstein et al., 2019; Willenbring and von Blanckenburg, 2010) periods. Although the exact cause for these diverging results is not known, it is plausible that the indirect effect of climate on watershed vegetation patterns may also regulate the erosion intensity.

The climatic changes have also been found to influence the relative contribution of sediment provenances in river basins. For instance, Sr-Nd isotopic study of floodplain sediments from the Ganga (Rahaman et al., 2009) and Indus (Clift et al., 2008) river basins have shown significant provenance changes in response to variation in monsoon strength during the last few kilo-years. Consistent with these findings, Tripathy et al. (2011) have also shown a relative decline in sediment supply from the Himalayas compared to the peninsular Indian rivers to the Bay of Bengal during the last glacial maxima, mainly due to the weakening of the southwest monsoon. In contrast to these studies, geochemical studies of the Arabian Sea (Goswami et al., 2012) and the Bay of Bengal (Galy et al., 2008; Lupker et al., 2013) sedimentary records show insignificant provenance variation during the Holocene. In addition to physical erosion, a few temporal studies on the chemical erosion pattern of this region have also been carried out to assess their climatic interaction. Recent studies by Miriyala et al. (2017) and Sebastian et al. (2019) have shown intense chemical erosion in the Irrawaddy basin and Indo-Burman ranges due to the intensification of the monsoon. Additionally, Limmer et al. (2012) have shown that the locus of erosion in a given basin (upper versus lower reaches) may also vary during different phases. However, von Blanckenburg et al. (2015) have decoupled climate and land-surface processes and have shown an insignificant change in the area-normalized weathering fluxes in response to climate change during the Quaternary period. Further, a few recent studies have also documented an increase in chemical erosion rates during the late Holocene period due to the impact of various non-climatic parameters such as human-induced land use and vegetation pattern (Bayon et al., 2012; Huang et al., 2018; Ponton et al., 2012; Rawat et al., 2021; Wan et al., 2015). Precise understanding of the anthropogenic forces on chemical erosion patterns is hampered by limited high-resolution data on erosion intensity variations during the last few kilo-years with significant human activities. This thesis attempts to assess the impact of anthropogenic influences on the chemical erosion pattern during the late Holocene period using the high resolution major and trace elemental geochemistry of a radiocarbon-dated sediment core from the eastern Arabian Sea.

Efforts have also been made during this thesis work to reconstruct the natural variability of the Indian summer monsoon during the mid-Holocene period using oxygen isotopic records of cave calcite. Existing studies based on stable isotopic signatures of speleothem (Kathayat et al., 2017) and lake records from northern India (Dixit et al., 2014a) have documented a strong relation between ISM variability and human civilization. Further, earlier studies have also documented decadal to millennial-scale variability of the ISM using various marine and terrestrial archives, which include foraminiferal records from the Arabian Sea (Gupta et al., 2003, 2005; Staubwasser et al., 2003), speleothem (Berkelhammer et al., 2012; Fleitmann et al., 2003; Kathayat et al., 2017) and lake records (Dixit et al., 2014a; Prasad et al., 2014). The ISM variability over a centennial-to-millennial timescale, primarily reported from the marine sedimentary records, is mainly regulated by external solar forcing and ocean-atmospheric interactions (Bond et al., 2001; Naidu and Malmgren, 1995; Staubwasser et al., 2003; Stuiver and Braziunas, 1993; Thamban et al., 2007). The North Atlantic (NA) climatic condition also influences the ISM on a millennial timescale. Earlier studies have also reported the influence of freshwater influx, due to glacial lake outbursts, to the North Atlantic (NA) and the subsequent changes in thermohaline circulations on the ISM variability (Chiang et al., 2008; Dong and Sutton, 2002; Kleiven et al., 2008; Liu et al., 2013). Gupta et al. (2003, 2005) have investigated the oxygen isotopic records of foraminifera and species assemblages of an Arabian Sea sediment core to establish the impact of solar insolation and the interaction between the ocean and atmosphere systems on the Indian monsoon during the Holocene. In contrast, the ISM strength on a decadal timescale is mostly regulated by different modes of the Pacific Ocean, such as El Niño-Southern Oscillation (ENSO) and Pacific Decadal Oscillation (PDO). However, Goswami et al. (2015) have suggested that the Atlantic Multidecadal Oscillation (AMO) and sea surface temperature induced Indian Ocean Dipole (IOD) events also regulate the ISM at a multi-decadal scale. Prasad et al. (2014), based on a lake record investigation, have showed prolonged dry phases at the beginning of the Holocene period and at the onset of late-Holocene (4.6 to 3.9 kyr BP). These dry phases were synchronous to the regional warming associated with the Indo-pacific Warm Pool, which underscores the importance of Indian Ocean sea surface temperature in regulating the ISM variability through atmospheric teleconnections (Anandh and Vissa, 2020; Dutt et al., 2015; Goswami and Xavier, 2005; Goswami et al., 2006; Krishnan and Sugi, 2003; Li et al., 2017; Lechleitner et al., 2017; Myers et al., 2015; Sinha et al., 2005).

The oxygen isotopic composition ($\delta^{18}O$) of speleothem serve as a reliable tool to reconstruct the past ISM variation. The speleothem $\delta^{18}O$ is largely regulated by several factors such as wind circulation pattern, moisture sources, temperature, and rainfall amount. Among these, the large variability observed in the $\delta^{18}O$ values for the tropical speleothem points to the dominance of the monsoonal rainfall amount in regulating the isotopic signatures. The $\delta^{18}O$ values show minimal changes (-0.23 ‰ /°C) with respect to temperature changes, whereas the amount effect at a global scale shows -1.5 ‰ of $\delta^{18}O$ changes per 100 mm of rainfall variation (Ayalon et al., 1998; Bar-Matthews et al., 1996, 1997, 2003; Cruz et al., 2005; Dansgaard, 1964; Dorale et al., 1992; Fricke and O'Neil, 1999; Gascoyne, 1992; Genty et al., 2014; Lauritzen and Lundberg, 1999; Yadava and Ramesh, 2005; Yurtsever and Gat, 1981). Available studies on speleothem $\delta^{18}O$ values show a large temporal variation, which confirms the significant change in the ISM intensity during the Holocene period (Band et al., 2018;

Berkelhammer et al., 2010, 2012; Gautam et al., 2019; Kathayat et al., 2017; Lone et al., 2014; Raza et al., 2017; Sinha et al., 2005, 2007, 2011; Sinha et al., 2018; Yadava and Ramesh, 2006). A compilation study by Kaushal et al. (2018) on available Indian speleothem records has documented the influence of solar insolation, climatic conditions of the North Atlantic, and the sea surface temperature of the Pacific Ocean on the ISM variability. About 1 ‰ change in speleothem $\delta^{18}O$ is found to reflect rainfall changes corresponding to ~27 W/m^2 of solar insolation variation (Battisti et al., 2014; Kaushal et al., 2018; LeGrande and Schmidt, 2009). Further, Reddy et al. (2021) have also established the influence of solar and oceanic forcing on the ISM variability during the Late-Holocene period. Reconstruction of monsoon intensity based on western Himalayan speleothem records (Timta Cave) has documented enhanced precipitation coupled with North Atlantic climatic conditions during the Bølling-Allerød warm phase (Sinha et al., 2005). The oxygen isotopic record of speleothem from the Dandak Cave, central India, spanning over Medieval Warm Period and Little Ice Age, reveals an underestimation of monsoon rainfall variability from the available short instrumental records of the ISM by about 30 % (Sinha et al., 2007). A speleothem $\delta^{18}O$ record from north-eastern India (Mawmluh Cave) has documented an abrupt shift in the Indian monsoon pattern ~4000 years ago (Berkelhammer et al., 2012). This abrupt shift in the monsoon pattern is synchronous to the global drought event at the beginning of the Meghalayan stage. Most of these available speleothem studies are from the peripheral region of the ISM domain, with limited high-resolution data on the ISM variability during the mid-Holocene period. Recognizing this, high-resolution oxygen isotopic signatures of a speleothem sample collected from the core monsoon have been investigated as a part of this thesis work to reconstruct the ISM variability during the mid-Holocene period. These data were also used to constrain the driving mechanisms for the natural variability of the ISM during the mid-Holocene.

1.2 Objectives of this thesis

This thesis work mainly focuses on erosion-climate interaction at seasonal and millennial timescales. The following major objectives have been identified for this study.

- To investigate the temporal variation in river water chemistry of the Brahmaputra River at weekly intervals to assess the impact of climatic parameters (runoff) on the Himalayan erosion pattern at a seasonal timescale.

- To investigate chemical and isotopic signatures of marine (Arabian Sea) sediments to evaluate the climate and erosion coupling (at a millennial timescale) during the Holocene period.
- To investigate geochemical and Sr-Nd isotopic data of a terrestrial sedimentary section from the upper Indus (Zanskar River) basin to trace the Himalayan erosion pattern during the last glacial-interglacial cycle.
- To reconstruct the natural variability of the Indian summer monsoon during the mid-Holocene period using a well-dated speleothem from the core monsoon zone.

1.3 Structure of the thesis

The ***chapter 1*** of this thesis introduces the continental erosion process and its importance in the chemical and climatic cycles. Additionally, available information on past Indian summer monsoon variability using sedimentary archives and speleothem $\delta^{18}O$ data are highlighted. It also presents a review of available literature information on erosion, climate (ISM variability), and their interaction to identify available research gaps and objectives of the study.

The ***chapter 2*** provides thorough details about the samples, their geohydrological information, and depth-age relation. The analytical methods adopted during this study for the chemical and isotopic measurements of the samples are also presented in this chapter.

The ***chapter 3*** focuses on the climatic sensitivity of chemical erosion at the seasonal scale. It presents time-series major ions and Sr concentrations data (at weekly intervals) for the Brahmaputra River water. These data and their inverse modelling are used to apportion the solute sources and seasonality in the chemical erosion intensity of this large Himalayan river system.

The ***chapter 4*** deals with the geochemical and isotopic compositions of two sediment cores from the eastern Arabian Sea. It describes the Holocene variability in the chemical erosion pattern and marine redox state.

The ***chapter 5*** presents chemical and Sr-Nd isotopic study of a river sediment section from the upper Indus (Zanskar) basin. The data were used to reconstruct the Himalayan erosion pattern during the last glacial-interglacial period and to assess the climatic sensitivity of erosion in this mountainous region.

The ***chapter 6*** presents oxygen isotopic data of a U-Th dated speleothem from the core monsoon region (Gupteswar Cave, Odisha). These isotopic data were used to reconstruct the ISM variability during the middle Holocene period, which in turn provide clues for control of Indian Ocean on monsoon variations.

The ***chapter 7*** summarizes the major outcomes of this thesis on erosion and climate interaction. It also provides the future scope of research on this low-temperature aquatic process and its controlling factors.

Chapter 2

Material and Methods

The primary objective of this thesis work is to understand the erosion and climate interaction at different timescales, ranging from seasonal to kilo-year timescales. Additionally, the rainfall patterns were also reconstructed to understand the climatic changes during the mid to late Holocene period. Towards this, time-series river water samples and various paleoclimatic archives (e.g., marine and terrestrial sedimentary records and speleothem) were collected and used for isotopic and geochemical analyses during this study. The marine archives used in this study are two sediment cores raised from the eastern Arabian Sea, whereas the terrestrial record is a river section from the upper Indus (Zanskar) basin. This chapter focuses on geological and climatological details of the samples and their locations. Further, it also provides methodological details adopted during this thesis work for the isotopic and geochemical analyses.

2.1 Material

2.1.1 Time-series sampling of river water

Time-series sampling of river water from the Brahmaputra River was carried out to assess the seasonal changes in the chemical erosion pattern in response to runoff variation. The surface water samples from the Brahmaputra mainstream at Guwahati, India (26.145 °N; 91.736 °E; Fig. 2.1) were collected weekly to biweekly intervals for one year (Oct., 2016-Oct., 2017). The study site, Guwahati, is situated in the lower reaches of the river basin, and it accounts for about 90 % of both the water flux and drainage area of the river.

The Brahmaputra River originates from Mount Kailash in south-central Tibet at an elevation of 5300 m (Jain et al., 2007). The drainage area of the river is about 580,000 km^2. The river travels through a total length is 2880 km, out of which it flows through about 1500 km in the highly-elevated Tibetan plateau region with a steeper slope (1.63 m/km) and then makes almost a U-turn near the eastern syntaxis to enter India (Goswami, 1985; Sarma, 2005). It subsequently merges with the Ganga River before falling into the Bay of Bengal (Fig. 2.1).

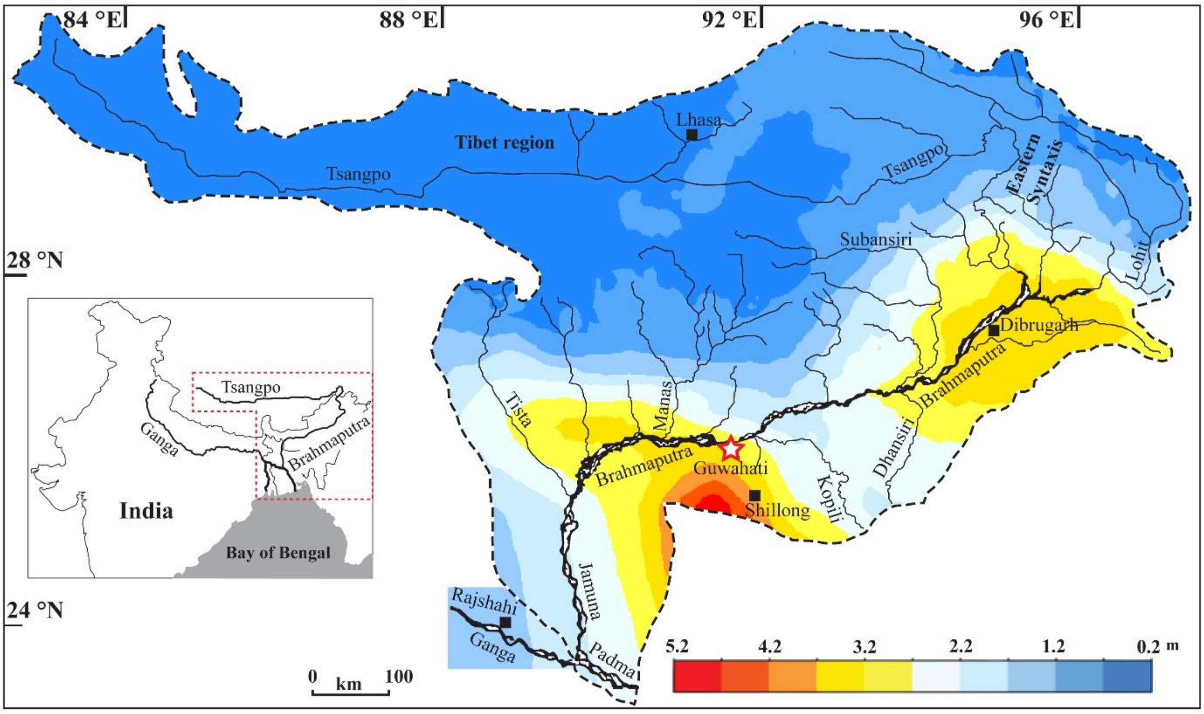

Figure 2.1. *Drainage basin map of the Brahmaputra River system. In this study, time-series water sampling at Guwahati (marked as star) was carried out on weekly basis for one year (2016-17). The spatial distribution of cumulative rainfall in the basin during the sampling period is also shown (Data source: https://trmm.gsfc.nasa.gov/).*

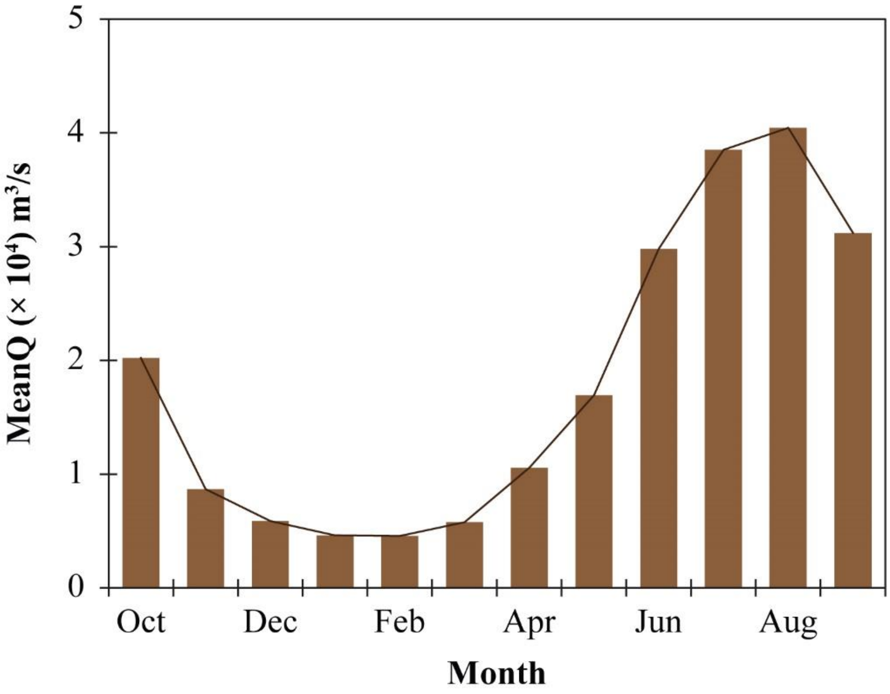

Figure 2.2. *Average monthly water discharge data of the Brahmaputra River (average of 23 years (1956-1979) data) near the sampling site (Data source: http://www.grdc.sr.unh.edu/).*

The major tributaries of the river are the Lhasa He (Zangbo), Lohit, Dibang, Subansiri, Manas, and Tista (Singh et al., 2005). The water flux of the river near the present study site (Guwahati) is 5.71 × 10^{14} L/yr (Global Runoff Data Centre, discharge metadata set (*http://www.grdc.sr.unh.edu*) at Pandu) (Fig. 2.2). The major source of water to the stream is the southwest monsoon (June-September), which contributes 60-85 % of the annual flux. Additionally, this basin also receives significant rainfall (20-35 %) during the pre-monsoon (March-May) period (Jain et al., 2007; Sarma, 2005) due to north-westerly thunderstorms. The perennial river also receives an appreciable amount of snowmelt and base flow supplies during the pre-monsoon period (Immerzeel et al., 2010; Kaser et al., 2010). The climate of the basin shows significant spatial variation. The northern part of the basin in the Tibetan region falls in the cold and arid region, whereas the southern part is warm and humid. The annual precipitation in the southern part (2300 mm; Jain et al., 2007) is about double the basinal average (1071 mm; Immerzeel et al., 2010).

The river Brahmaputra flows through a diverse geological terrain, which has been discussed in detail in previous literature (Hren et al., 2007; Rai and Singh, 2007; Singh et al., 2005, 2006). Briefly, the river mainly drains through the Tibet, Transhimalayan Indo-Tsangpo Suture Zone (ITSZ), Mishmi Hills, the litho units of Higher and Lesser Himalaya, Siwaliks, and Quaternary alluvium (Singh et al., 2005). The Tibetan plateau is mainly dominated by turbidites, gabbroic to granodioritic batholiths, and ophiolite sequences. The Mishmi Hills are composed of calc-alkaline, diorite-tonalite-granodiorite complexes, and tholeiitic metavolcanics (Kumar, 1997). The Higher Himalayan region comprises granites, gneisses, schists, and marbles, whereas the Lesser Himalaya comprises quartzites, dolostones, shales, granites, gneisses, and schists. The Siwaliks sequences are mainly composed of reworked sediments from the Higher and Lesser Himalayas.

2.1.2 Marine sedimentary records

Marine sedimentary records can serve as reliable archives of the continental erosion patterns. Two sediment cores from the eastern Arabian Sea have been investigated in this thesis work to understand the Holocene variability of erosion in the Indian sub-continent. These marine gravity cores (SSK40/GC06 and SSK40/GC10) were raised during the 40th expedition of RV Sindhu Sankalp in 2012 under the GEOSINKS project and was archived at the CSIR-National Institute of Oceanography (NIO), Goa. Details of the sampling locations and water depth of these cores are included in Table 2.1. Briefly, these cores are mainly from the shallow

Table 2.1: *Details of the marine sediment cores raised from the eastern Arabian Sea.*

Core ID	Latitude °N	Longitude °E	Water depth m	Core length cm	Avg. sedimentation rate mm/yr
SSK40/GC06	20°59.98317	69°43.32958	54.54	265	0.75
SSK40/GC10	17°59.89123	72°22.45161	51.65	275	0.41

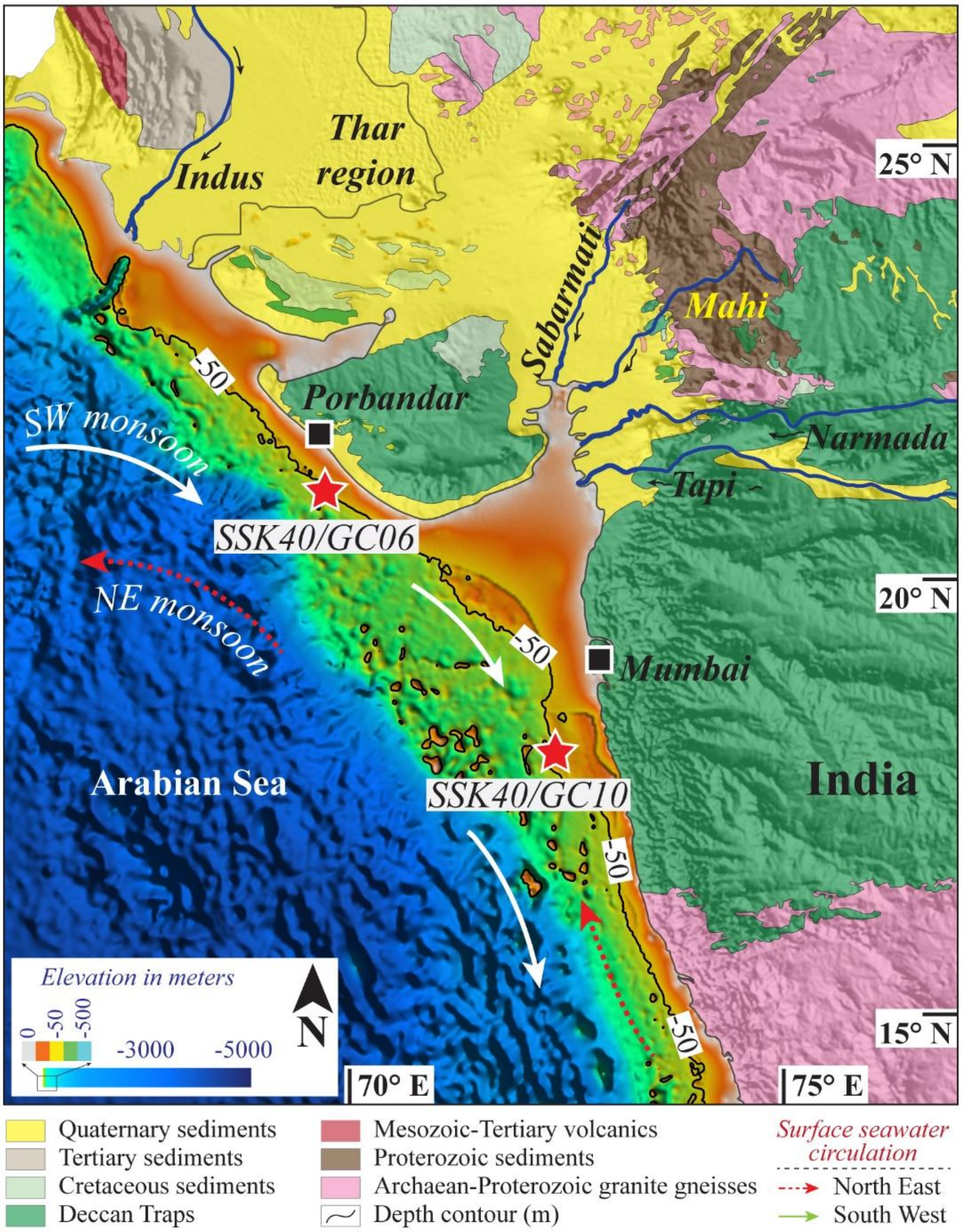

Figure 2.3. *Location map of the marine sediment cores from the eastern Arabian Sea. Geology of the surrounding region and surface water circulation pattern are also shown.*

marine setting with a water depth of ~50 m (Fig. 2.3). These sediment cores were sub-sampled at a resolution of 1 cm and stored in sealed plastic bags at NIO. These samples were subsequently brought to IISER Pune for geochemical and isotopic analyses. The sediment samples from these cores are mostly silty and calcareous in nature.

In the present day, the eastern Arabian Sea receives sediments primarily through the riverine sources from the Himalayan region by the Indus River system (annually ~400 million tons; Milliman et al., 1984) and also from the Deccan Traps and the Indian Peninsular region through the major river system like Narmada, Tapi, Mahi, Sabarmati as well as through several small west-flowing streams originated from the Western Ghats (~100 million tons/yr; Alagarsamy and Zhang, 2005; Chandramohan and Balchnad, 2007). Additionally, the region also receives sediments through aeolian sources from the surrounding deserts, i.e., Thar and Arabian and African Peninsula (~100 million tons/yr). Additionally, the core sites are also expected to receive significant biogenic supplies, mainly due to high oceanic productivity in this part of the Arabian Sea (Calvert et al., 1995; Kessarkar et al., 2018; Qasim, 1977).

Table 2.2: *Radiocarbon ages of (A, B) foraminifera samples from the eastern Arabian Sea sedimentary cores and (C) organic carbon of the river section (Padum, India) from the Zanskar basin.*

	Core ID	**Depth**	**Radiocarbon age**	**Calibrated age**	**Median age**
		cm	years	yr BP	yr BP
Marine Sediments*	SSK40/GC06	20-21	739 ± 109	0-305	207
		83-84	1500 ± 69	765-967	876
		130-131	1555 ± 69	826-1044	938
		190-191	2292 ± 72	1587-1824	1710
		250-251	3495 ± 74	3054-3316	3171
	SSK40/GC10	11-12	2616 ± 21	1811-2032	1921
		37-38	4713 ± 69	4602-4849	4556
		89-90	6603 ± 81	6787-7059	6700
		128-129	6999 ± 79	7247-7429	7141
Terrestrial Sediments	PDM18	5-10	2368 ± 52	2339-2488	2418
		56-61	10311 ± 84	11937-12451	12135
		112-117	12373 ± 48	14244-14803	14448
		142-147	15165 ± 153	18288-18639	18481
		168-173	17881 ± 63	21483-21917	21744

Reservoir age correction: $\Delta R = 166 \pm 65$ (Southon et al., 2002); BP: Before present (1950 AD)

The depth-age relation of the marine sediment cores has been constrained using the ^{14}C analysis of foraminifera samples of mixed species from different depths. Foraminifera samples were separated by processing about 20-30 grams of (bulk wet) sediments. The radiocarbon (^{14}C) measurements were conducted using the Accelerator Mass Spectrometry (AMS) facility of Physical Research Laboratory, India. The measured radiocarbon ages of the forams were corrected for the reservoir age for a ΔR value of 166 ± 65 (Southon et al., 2002) and calibrated to calendar age using Calib 7.1 (8.2 for SSK40/GC10 core) (Reimer et al., 2013; Stuiver et al., 2021) model (Table 2.2). The ^{14}C data of the SSK40/GC06 core sediments show that the core archives a continuous sedimentary record of the last ~3560 yr with an average sedimentation rate of 0.75 mm/yr (n = 53). The radiocarbon ages show that the SSK40/GC10 sediments were deposited between ~7.2 kyr BP and ~0.8 kyr BP. The sedimentation rate varies between 0.1 and 0.88 mm/yr (mean: 0.41 mm/yr) (Fig. 2.4). The SSK40/GC10 core was investigated to

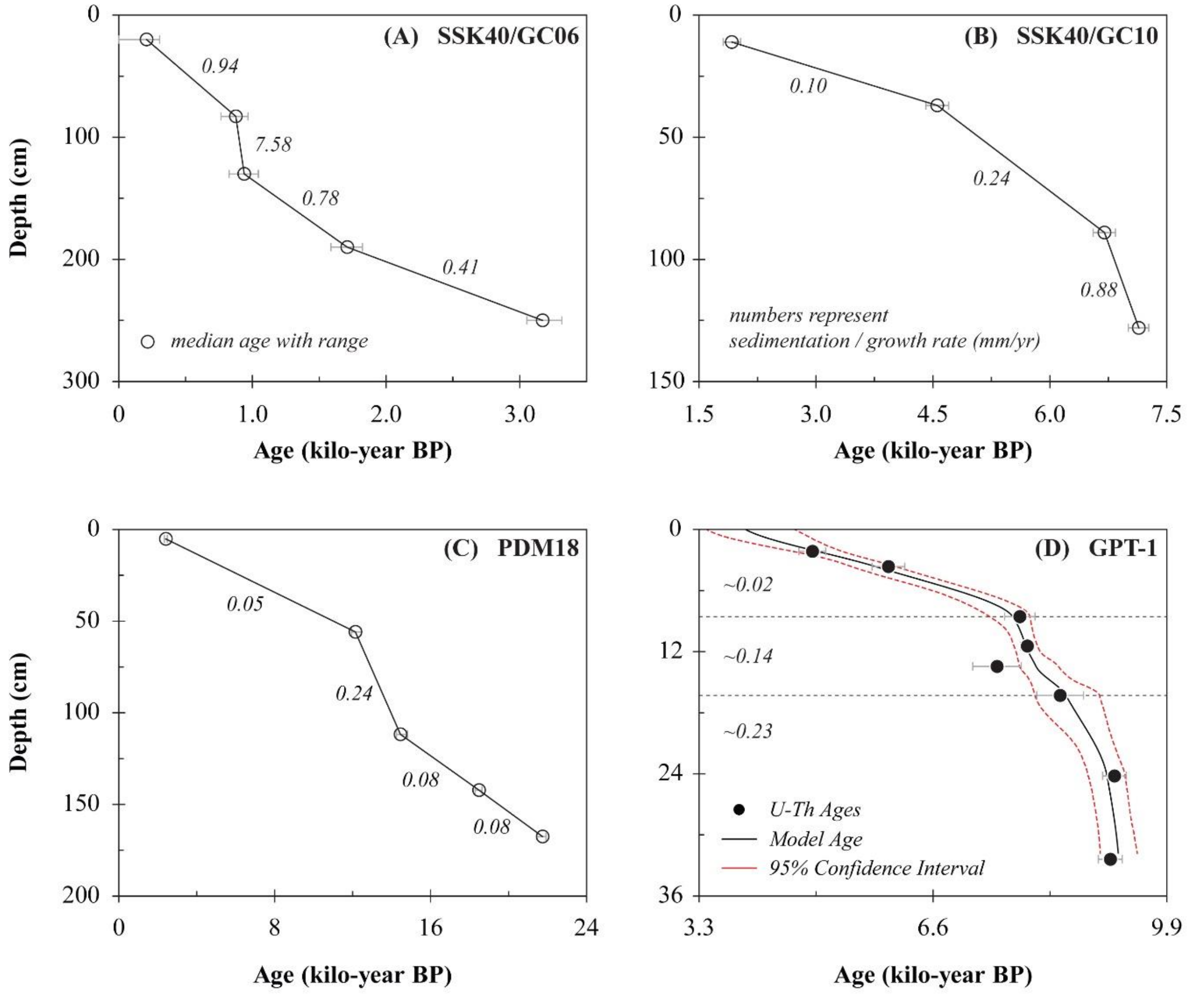

Figure 2.4. *Radiocarbon chronology of (A-B) foraminifera samples from the eastern Arabian Sea sediment cores; (C) bulk organic carbon samples from river section sediments from the Zanskar River basin. (D) U-Th chronology of GPT-1 speleothem from the Gupteswar Cave.*

reconstruct erosional changes across the Meghalayan stage boundary (~4.2 kyr BP), which is marked by a global drought phase (Arz et al., 2006; Berkelhammer et al., 2012; Cullen et al., 2000; Marshall et al., 2011). With this strategy, high resolution major and trace elemental analyses of the top portion (~1.5 m) of this core were carried out.

2.1.3 Terrestrial archives

2.1.3.1 River section sediments from the upper Indus (Zanskar) River basin

Terrestrial sedimentary records are good archives for reconstructing past erosion patterns, mainly due to their limited sources and relatively higher deposition rates. In this study, we have collected a river section (33° 28.669´ N, 76° 53.532´ E) from the upper Zanskar River basin in the Himalaya to assess the erosion variability during the last glacial-interglacial cycle. This river section (length ~ 1.8 m) was collected from the bank of the Tsarap tributary at Padum and immediately before its confluence with Tstod to form the Zanskar River (Fig. 2.5). The major tributaries of the Zanskar are Tsarap, Stod, Kurna, Markha, and Oma. Originating from Pensi La, the Stod converges with the Tsarap to form the Zanskar near Padum and subsequently which joins the Indus mainstream at Nimu. The Zanskar River is one of the major tributaries of the Indus River in its upper reaches. It is situated in the northwestern part of the Himalayan mountain range, which is also one of the central pathways for routing water and sediments from the western Himalayas to the Arabian Sea (Clift et al., 2001). The modern drainage basin of the Zanskar River occupies around 14,939 km^2 of the highly-elevated terrain on the southern part of the Tibetan Plateau (Fig. 2.5; Jonell et al., 2017). The Zanskar River catchment is often called the cold desert because of its cold and arid climatology. The average air temperature shows significant variation between winter, ranging from -14 °C to -2.8 °C, and summer (10.2 °C to 24.7 °C) seasons (Taylor and Mitchell, 2000). The mean annual precipitation shows significant spatial variation; the upper catchment region receives around 200 to 400 mm, whereas the lower catchment receives a relatively lower amount of precipitation (~150 mm/year; Bookhagen et al., 2009; Lee et al., 2014). Weather station data from the Sutlej River basin and the hydrological modelling data show that the upper Indus River receives 30 % to 50 % of annual precipitation through winter snowfall. About 66 % of the annual discharge of the streams is produced by the snow and glacier melts (Bookhagen and Burbank, 2010; Burbank et al., 2012). This region receives precipitation via the Indian summer monsoon during the summer seasons (June to August) and snowfall during winter seasons due to the western disturbances (Bookhagen et al., 2005; Owen and Benn, 2005). The Higher Himalayan

Crystalline zone in the south is primarily dominated by the Indian summer monsoon (ISM), whereas the westerlies mainly influence the Ladakh batholith in the northern part of the region. The chronology of the river section was established using radiocarbon dating of organic matter. These radiocarbon ages of the Zanskar River section confirm their deposition during ~ 22.4 to 1.4 kyr BP (Table 2.2; Fig. 2.4), with no major depositional hiatus.

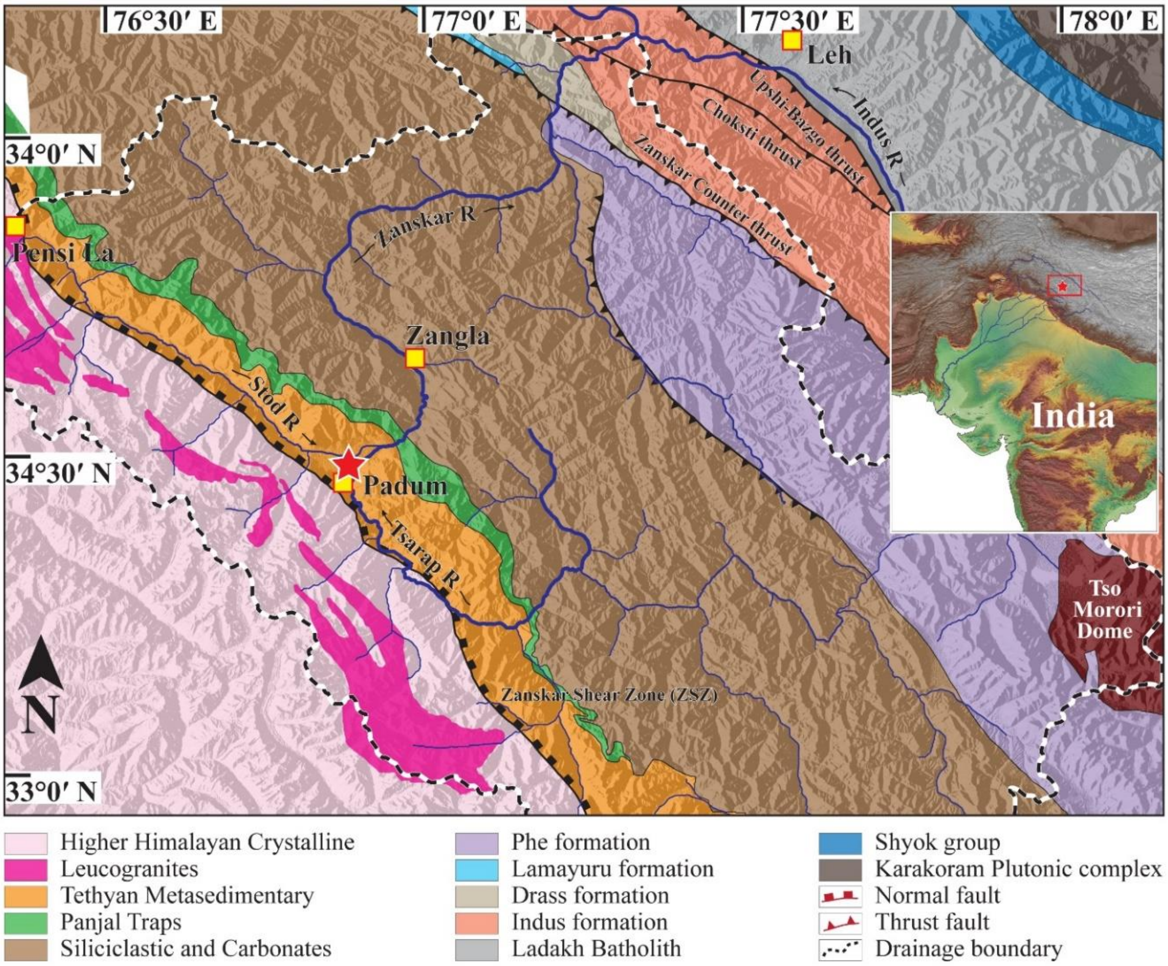

Figure 2.5. *Geological map of the Zanskar River basin in the western Himalaya. The star symbol stands for sampling site for the PDM18 river section (modified after Chahal et al., 2019).*

2.1.3.1.1 Geological settings of the Zanskar River basin

The major litho-tectonic groups exposed in the Zanskar catchment are Higher Himalayan Crystalline (HHC), the Tethyan Sedimentary Sequence (TSS), and the Indo-Tsangpo Suture Zone (ITSZ; Fig. 2.5). The Zanskar Shear Zone (ZSZ), ~150 km long synorogenic extensional structure, is the major tectonic boundary that separates the HHC and

TSS. This northward dipping shear zone (ZSZ) is part of the ~2000 km-long South Tibetan Detachment System (STDS) (Burchfiel and Royden, 1985; Burchfiel et al., 1992; Dèzes et al., 1999; Herren, 1987). The HHC is mainly comprised of para and ortho-gneisses of Proterozoic to early-Paleozoic time and late-Paleozoic granitic, leucogranites, metapelites, and migmatites in this region. The metamorphic grade of these HHC rocks varies from amphibolite to lower-granulite facies (Dèzes et al., 1999; DeCelles et al., 2004; Gehrels et al., 2003; Henderson et al., 2010; Herren, 1987; Honegger, 1982; Horton and Leech, 2013; Noble and Searle, 1995; Pognante and Lombardo, 1989; Pognante et al., 1990; Schlup et al., 2003, 2011; Searle, 1986; Searle et al., 1992; Walker et al., 2001). The massive granitic injections, induced by the partial melting, were associated with the rapid exhumation of the Greater Himalaya between the Main Central Thrust and the Zanskar Shear Zone (Leloup et al., 2010; Robyr et al., 2006). Similar intrusions are also observed in the lower Tethyan Himalayan series (Dèzes et al., 1999; Noble and Searle, 1995; Robyr et al., 2006). The Tethyan Sedimentary Sequence is situated in the north of the HHC, essentially the pre-collisional sedimentary sequence on the northern margin of Greater India. The TSS is primarily comprised of the low-grade meta-sedimentary rocks, sandstones, limestones, dolostones, and shales, with the typical passive margin depositional signature (Gaetani et al., 1983, 1986; Garzanti et al., 1986; Green et al., 2008). Further, the Tso Morari Crystalline complex of the Ordovician of age, which occur in between TSS and ITSZ (parallel to the ZSZ), has metamorphic grade up to lower amphibolite facies (Dèzes et al., 1999; Fuchs, 1987; Gaetani et al., 1986; Steck et al., 1993; Thakur, 1981). In the north, ITSZ representing India and Eurasia collisional boundary is comprised of thrusted ophiolite sequences and the Indus Molasse sandstones (Clift et al., 2002; Henderson et al., 2010; Pedersen et al., 2001; Searle et al., 1990; Yin and Harrison, 2000). The ITSZ also contains the sediments of deep-marine condition, the Lamayuru Complex, mainly the black shales with pyritisation, thrusted forearc sediments, volcano-clastic sediments, mostly sandstone (Henderson et al., 2010; Searle, 1986; Searle et al., 1990; Sinclair and Jaffey, 2001; Thakur, 1981).

2.1.3.2 Cave calcite deposit

A 33-cm long stalagmite sample (GPT-1) was collected from the Gupteswar Cave, Odisha, in the eastern part of India (18° 45´ N, 82° 10´ E; Elevation ~ 457 m). The cave location falls in the core-monsoon zone of the Indian summer monsoon domain and receives a large amount of rainfall due to the tropical convergence (Rajeevan et al., 2010). The Gupteswar Cave region receives annual precipitation of ~1500 mm, out of which about 75 to 80 % of the rainfall occurs during the southwest monsoon (JJAS) season (Fig. 2.6). The mean air temperature for this region is 25.5 °C. The surrounding rock types around the cave are limestones, purple shale, and quartzite (Yadava and Ramesh, 2005). Presently the cave region is mainly covered with dense C3-type vegetation cover. This speleothem record was used to reconstruct the past rainfall pattern during the mid to late Holocene period. The chronology of the speleothem has been established based on eight U-Th isotopic data using the MC-ICP MS facility at the University of Queensland (Hellstrom, 2006) (Table 2.3). The interpolation of ages between depths was done using the COPRA 2.3.1 model, which involves a Monte-Carlo simulation approach (Breitenbach et al., 2012). These ages confirm that the growth of the GPT-1 occurs between 3954 and 9213 yr BP with no major depositional hiatus. The growth rate of this sample shows significant temporal variation, with about ten times lower rate (0.02 mm/yr) in the top part of the speleothem than that (0.14-0.23 mm/yr) of the bottom part (Fig. 2.4D). The time-resolution of the δ^{18}O data generated in this study varies between 1 and 113 yrs, with an average of 5 yrs.

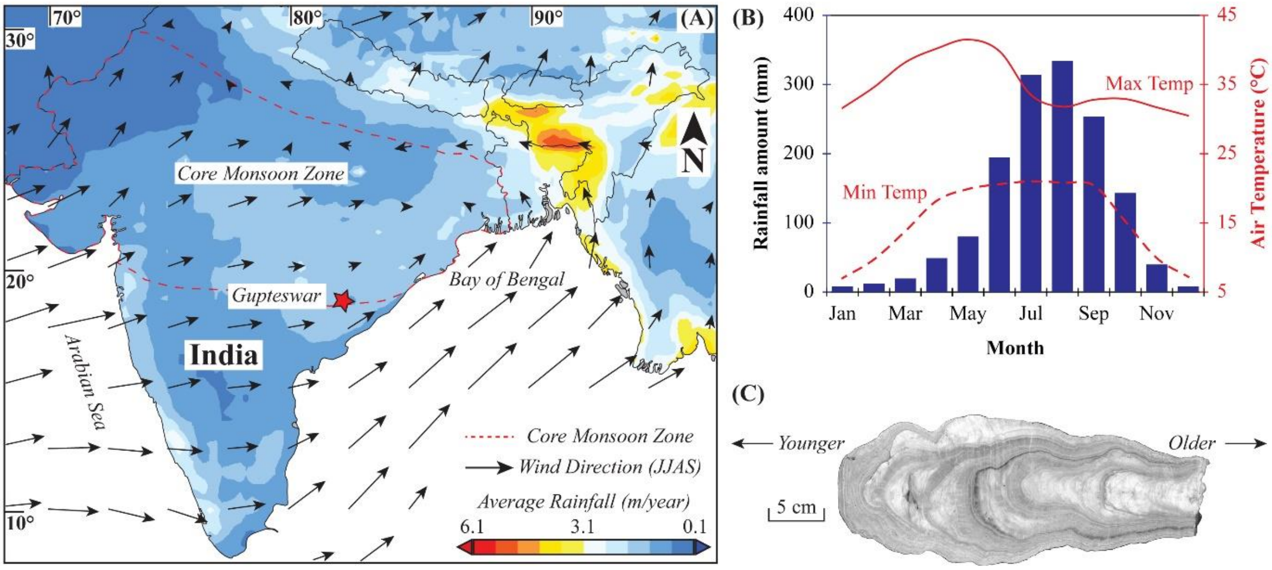

Figure 2.6. *(A) Location map of the speleothem (GPT-1) from the Gupteswar Cave, India. Colours in the map depict 20-year (2000-2019) average annual rainfall pattern (Data source: https://giovanni.gsfc.nasa.gov/giovanni) and the arrows show wind direction during the southwest monsoon period (NCEP Reanalysis data). (B) Monthly rainfall distribution for the cave site and the temperature, minimum (solid line) and maximum (dashed line), variation for a nearby meteorological station IMD Jagdalpur (Climatological Table 1981-2010). (C) Scanned picture of the GPT-1 speleothem.*

Table 2.3: *U-Th isotopic data of the speleothem (GPT-1) from the Gupteswar Cave, India.*

Depth	**^{238}U**	**^{232}Th**	**^{230}Th/ ^{232}Th**	**^{230}Th/^{238}U**	**^{234}U/ ^{238}U**	**^{230}Th Age (yr)**	**^{230}Th Age (yr)**	**^{234}U/ ^{238}U$_{\text{Initial}}$**	**^{230}Th Age (yr BP)**
mm	ppb	ppb				Uncorrected	Corrected	Corrected	Corrected
21.5	222.70	23.99	2.38 ± 0.01	0.0844 ± 0.0003	1.5127 ± 0.0005	6247 ± 19	4965 ± 190	1.5293 ± 0.0016	4897 ± 190
36.5	50.14	6.97	2.36 ± 0.01	0.1083 ± 0.0005	1.6049 ± 0.0009	7597 ± 34	6039 ± 230	1.6297 ± 0.0024	5971 ± 230
85.5	40.88	5.38	3.07 ± 0.01	0.1333 ± 0.0006	1.6153 ± 0.001	9353 ± 41	7892 ± 215	1.6431 ± 0.0024	7824 ± 215
114.5	108.30	5.99	6.77 ± 0.02	0.1234 ± 0.0004	1.6198 ± 0.0007	8608 ± 30	7998 ± 93	1.6398 ± 0.0011	7930 ± 93
134.5	39.19	8.36	2.04 ± 0.01	0.1431 ± 0.0007	1.64 ± 0.0009	9914 ± 51	7572 ± 343	1.6776 ± 0.0039	7504 ± 343
163	53.90	11.20	2.26 ± 0.01	0.1548 ± 0.0006	1.6433 ± 0.0007	10735 ± 42	8460 ± 330	1.6822 ± 0.0037	8392 ± 330
242	50.29	5.28	4.4 ± 0.02	0.1522 ± 0.0007	1.6728 ± 0.0009	10351 ± 50	9229 ± 167	1.7028 ± 0.0021	9161 ± 167
324	51.66	5.42	4.31 ± 0.02	0.1488 ± 0.0006	1.6422 ± 0.0007	10312 ± 43	9170 ± 168	1.6706 ± 0.0019	9102 ± 168

** All errors are in 1σ position. Yr BP = years before present (1950 AD).*

Chronological calculations were made following Hellstrom (2006) and using an initial ^{230}Th/^{232}Th = 0.5 ± 0.15.

Table 2.4: *Replicate Sr-Nd isotopic analyses of the PDM18 sediments.*

Sample ID	**^{87}Sr/^{86}Sr**		**^{143}Nd/^{144}Nd**		**ε_{Nd}**	
	(I)	(II)	(I)	(II)	(I)	(II)
PDM18/34-36	0.72764 ± 0.000004	0.72762 ± 0.000004	0.511765 ± 0.000006	0.511765 ± 0.000004	-17.0	-17.0
PDM18/52-54	0.74720 ± 0.000005	0.74775 ± 0.000005	0.511708 ± 0.000008	0.511717 ± 0.000006	-18.1	-18.0
PDM18/60-62	0.74666 ± 0.000007	0.74690 ± 0.000006	0.511725 ± 0.000006	0.511720 ± 0.000004	-17.8	-17.9

2.2 Analytical methodology

Chemical and isotopic analyses of several types of samples (e.g., water, sediments, and speleothem) have been carried out during this thesis work. These analyses involve measurement of multiple proxies after careful chemical processing and data quality checks. Figure 2.7 depicts the workflow of the geochemical and isotopic measurements conducted during this study. The analytical methodologies adopted during these measurements are detailed below.

2.2.1 Isotopic analyses

2.2.1.1 Sr-Nd isotopes of sediments

The Sr and Nd isotopic ratios were measured in the silicate fraction of the terrestrial sediment samples. These measurements were carried out using established protocols (Singh et al., 2008; Tripathy et al., 2011). Briefly, about 5 grams of oven-dried and powdered samples were decarbonated by treating with 0.6 N HCl at 80 °C for ~30 min in an ultrasonic bath. The residue sediment was centrifuged, washed with deionized water, and dried. This residue represents the silicate fraction of the sediment. About 200 mg of silicate fraction of sediments were completely digested with (ultra-pure) HF-HNO_3-HCl acids in a microwave digestion system. The pure Sr and Nd fractions from the solution were extracted using the conventional chromatography approach. The isotopes of these pure Sr and Nd fractions were measured using the multi-collector ICP MS (MC ICP-MS; Neptune Plus, Thermo Scientific) at Wadia Institute of Himalayan Geology, Dehradun. The measured $^{87}Sr/^{86}Sr$ and $^{143}Nd/^{144}Nd$ ratios were corrected for instrumental mass fractionation by normalizing measured $^{87}Sr/^{86}Sr$ and $^{143}Nd/^{144}Nd$ with respect to their natural values, viz. 0.1194 and 0.7219, respectively. Several samples were also measured in replicates (Table 2.4) along with the international reference standards (NBS987 for Sr and JNdi-1 for Nd) to constrain the precision and accuracy of the measurements. The measured $^{87}Sr/^{86}Sr$ for the NBS987 is found to be 0.710279 ± 0.000008 (1σ, n = 5), consistent with its reported value. The $^{143}Nd/^{144}Nd$ of JNdi standard is measured to be 0.512090 ± 0.0000057 (1σ, n = 5) matches well with its reported value. The procedural blank of Sr (~1400 pg) and Nd (400 pg) were also measured during the analysis and found to be several orders of magnitude lower than the total amount of Sr and Nd processed from the samples. The Nd isotopic data were reported in the ε units, which is defined as follows:

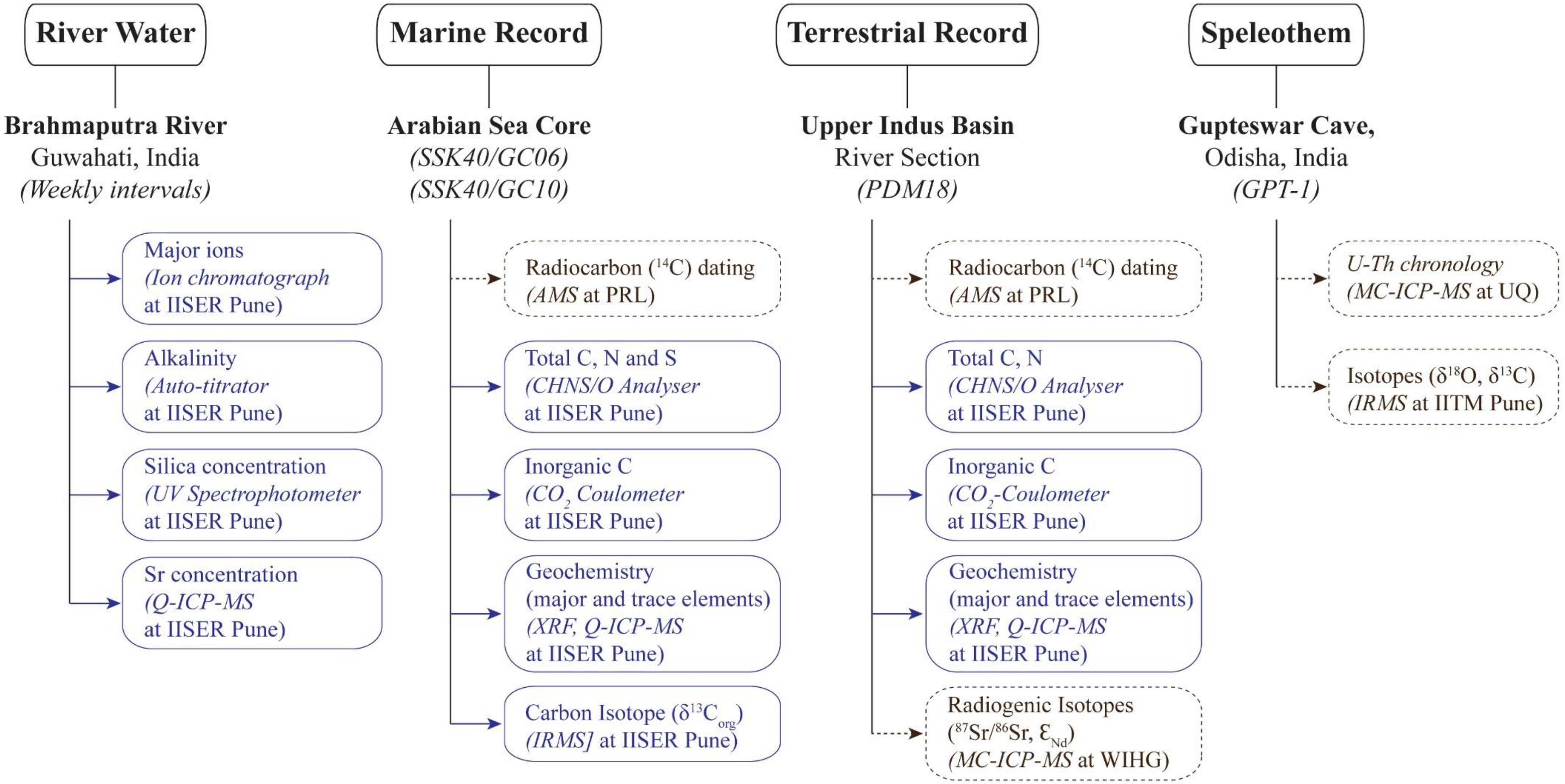

Figure 2.7. *Flow diagram of the analytical methods adopted during this thesis work.*

$$\varepsilon_{Nd} = \left[\frac{(^{143}Nd/^{144}Nd)_{sample}}{(^{143}Nd/^{144}Nd)_{CHUR}} - 1\right] \times 10^4$$

where the measured Nd isotopic ratio of the sample, ^{143}Nd/^{144}Nd, is normalized with respect to present-day Nd isotopic ratio of the Chondritic Uniform Reservoir (CHUR), $^{143}\text{Nd}/^{144}\text{Nd}_{\text{CHUR}}$ = 0.512638; Jacobsen and Wasserburg, 1980).

2.2.1.2 Carbon isotopes of sediments

The sedimentary $\delta^{13}C_{org}$ values were also measured in the decarbonated (0.6 N HCl leached sediment) fraction of the sediments from the Arabian Sea. Towards this, about 10 to 20 mg of decarbonated sediments were combusted at about 1050 °C using an elemental analyzer (EA) to liberate the CO_2 gas. The isotopic signals of the CO_2 gas were measured using the isotope ratio mass spectrometer (IRMS; Elementar ISO Link) facility at IISER Pune. The carbon isotopic data were reported in δ-notation $\left(\delta^{13}\text{C} = \frac{\left(^{13}\text{C}/^{12}C\right)_{\text{sample}}}{\left(^{13}\text{C}/^{12}\text{C}\right)_{\text{V-PDB}}} - 1 \times 1000\right)$. The isotopic compositions of reference material were constantly monitored to establish the accuracy of the measurements. Further, several samples were also measured in replicates to monitor the external reproducibility of the analysis (Table 2.5). The average precision of $\delta^{13}C_{org}$ analysis is always better than ± 0.15 ‰.

Table 2.5: *Replicate analyses of carbon isotopic composition for the samples.*

Sample ID	**$\delta^{13}C_{org}$ (‰)**	
	(i)	(ii)
GC06/1-2	-19.9	-20.4
GC06/9-10	-19.4	-19.9
GC06/43-44	-19.3	-19.3
GC06/54-55	-19.5	-19.6
GC06/57-58	-19.2	-19.2
GC06/61-62	-19.5	-19.6
GC06/70-71	-19.2	-19.4
GC06/174-175	-20.0	-20.0
GC06/178-179	-19.7	-19.8
GC06/205-206	-19.8	-19.7
GC06/255-256	-20.3	-20.3

2.2.1.3 Oxygen and carbon isotopes of speleothem

Oxygen and carbon isotopic analyses of the speleothem were carried out following Sinha et al. (2018). These isotopic analyses were conducted for 1013 samples along the growth axis of the cave calcite. These measurements were carried out using an Isotope Ratio Mass Spectrometer (IRMS) (Delta-V Plus, Thermo Scientific) with a gas-bench set up at the Indian Institute of Tropical Meteorology, Pune. For this, the speleothem sample was sub-sampled using a micro-driller at 100 µm intervals. Further, ~100 to 150 µg sample was taken in a glass vial for isotopic measurement. This glass vial was flushed with helium gas to remove all the atmospheric CO_2. The calcite sample in the vial was subsequently treated with ~0.1 ml of 100 % phosphoric acid at 80 °C to form CO_2 gas. The isotopic signals of CO_2 gas were measured, which were subsequently corrected for isobaric interferences to compute the carbon and oxygen isotopic values. International (NBS18 and NBS19) and laboratory (Makrana marble from PRL) standards were regularly measured to constrain the precision and accuracy of the measurements. The average precision of oxygen isotopic analysis is about 0.1 ‰, whereas that of the carbon isotopic measurements is ~1 ‰. The oxygen isotopic data are reported in standard δ-notation (in ‰ units) $\left(\delta^{18}O = \frac{\left({}^{18}O/{}^{16}O\right)_{\text{sample}}}{\left({}^{18}O/{}^{16}O\right)_{\text{V-PDB}}} - 1 \times 1000\right)$ where V-PDB stands for Vienna Pee Dee Belemnite.

2.2.2 Elemental analysis

2.2.2.1 Geochemical analysis of water samples

As mentioned earlier, the water samples from the Brahmaputra River were collected at weekly to biweekly intervals for one year. These samples were collected from an over-bridge to ensure their collection from the midstream. The collected water samples were stored in pre-cleaned high-density polyethylene (HDPE) bottles after rinsing a few times with the ambient water. After completion of sampling, all the forty samples were brought together to IISER Pune for their chemical analyses. The water samples were filtered through 0.2 µm nylon filters and stored in pre-cleaned polypropylene (PP) bottles. Chemical analyses of these samples were carried out using conventional approaches (Tripathy et al., 2010). The alkalinity of the samples was measured using an auto-titrator (Metrohm Titrino Plus 877). Dissolved silica concentrations were measured by the conventional molybdenum-blue method using a spectrophotometer (Evolution 300, Thermo Scientific). Concentrations of cations (Ca^{+2}, Mg^{+2},

Na^+, and K^+) and anions (Cl^-, SO_4^{-2}, and NO_3^-) were measured using ion chromatography (Metrohm Compact IC Plus 882) instrument. Accuracy of the analyses was monitored by measuring standards of known concentrations and for external reproducibility (precision), replicate analyses of a few samples were carried out. The accuracy and precision of these analyses were found to be 4 % and 2 %, respectively. The normalized inorganic change balance (NICB = $100 \times [(TZ^+ - TZ^-)/((TZ^+ + TZ^-)/2)]$; where TZ^+ and TZ^- stand for total cations and anions in equivalent units) for all the samples were computed; the average NICB was ± 4 % (n = 40), ensuring good data quality and/or measurement of all major dissolved constituents present in the river.

Table 2.6: *Analyses of dissolved Sr concentration of the NIST-1640a reference material.*

Sample ID	**Measured Conc.** μg/L
NIST-1640a/1	121
NIST-1640a/2	127
NIST-1640a/3	121
NIST-1640a/4	118
NIST-1640a/5	120
NIST-1640a/6	120
Average	121
STDEV	3
Reported value	126.03 ± 0.91

The dissolved Sr concentration of the filtered samples was measured using the Quadrupole ICP-MS (iCAP Q, Thermo Scientific) instrument. These water samples were diluted and acidified to a 2 % HNO_3 medium to match the concentration level and matrix of the standards. The intensity of ^{88}Sr of the samples was quantified using a standard calibration approach. All the samples were analysed in replicates for the Sr analyses, and these analyses constrained the external reproducibility (4 %; n = 40) of the measurement. The accuracy of Sr measurement was monitored by analysing an international natural water reference material (NIST-1640a); the measured (121 ± 3 μg/L (1σ; n = 6)) and reported (126.0 ± 0.9 μg/L) Sr concentrations of the NIST-1640a standard constrains the accuracy for the measurement to be 4 % (Table 2.6).

2.2.2.2 Geochemical analysis of sediment samples

Geochemical analyses of sediment samples, both in bulk and silicate fraction, were carried out following the analytical methodology of Tripathy et al. (2014). Briefly, about 30 g of the sediments were dried at 60 °C in a hot-air oven and powdered to ~100 µm size using an agate mortar and pestle. Further, the powdered sediment samples were washed with deionized water several times to remove the sea-salt content from these samples. Prior analyses, a small aliquot of the sample was dried at 60 °C and kept in a desiccator for cooling. A known amount (~100 mg) of these water-washed, and dried samples were digested completely using HF-HNO_3-HCl acids in a microwave digestion (Anton Paar) system at IISER Pune. Typically, the samples were diluted to 50,000 times for major elemental analyses and 5,000 times for trace elemental measurements. The major (Na, K, Ca, Mg, Al, Fe, Ti, and Mn) and trace (V, Cr, Co, Ni, Cu, Zn, Rb, Sr, Mo, Ba, Th, U, and rare-earth elements) elemental concentrations of the digested solutions, in 0.3 N HNO_3 medium, were measured using a Quadrupole Inductively Coupled Plasma Mass Spectrometer (iCAP Q, Thermo Scientific) following a standard calibration approach. Two certified geological reference materials (USGS BCR-2 and BHVO-2) have been processed and analysed to constrain the data accuracy during the ICP-MS measurement. The average accuracy for these analyses is found to be better than 5 %.

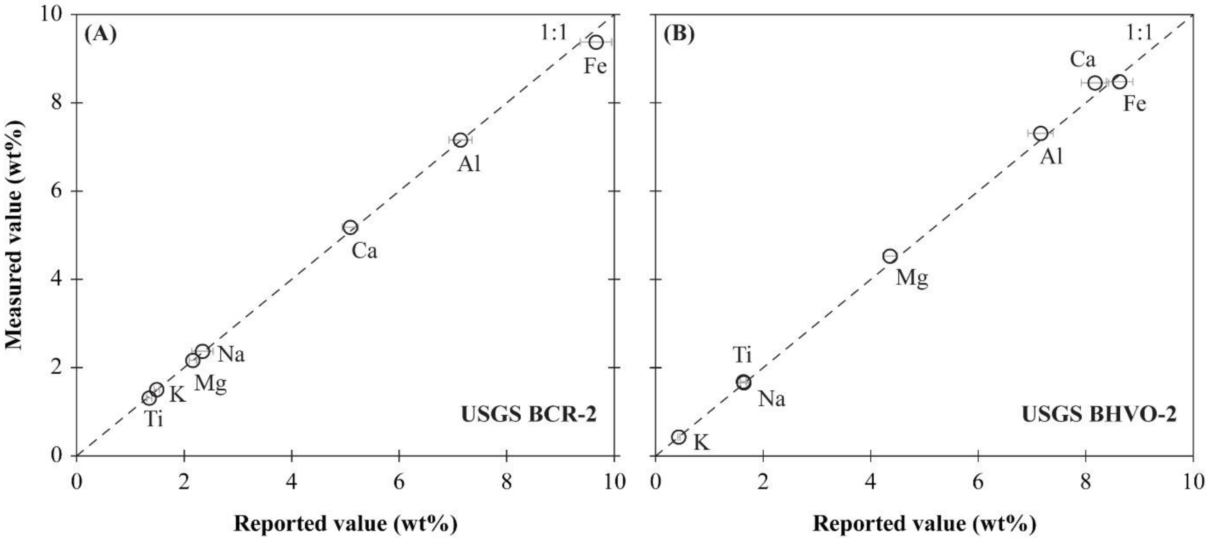

Figure 2.8. *Comparison between reported and measured elemental concentrations of the certified reference materials: (A) USGS BCR-2 and (B) USGS BHVO-2. The dotted straight line reflects the 1:1 line.*

Table 2.7: *Comparison of measured and reported values of the certified reference material, USGS BCR-2, and BHVO-2 using ICP-MS. Major elements (Na-Ti) are in wt%. Trace elements (V-Lu) are in µg/g.*

	BCR-2				**BHVO-2**			
Element	**Recommended**		**Measured**		**Recommended**		**Measured**	
	Mean	STDEV	Mean	STDEV	Mean	STDEV	Mean	STDEV
Na	2.34	0.08	2.37	0.20	1.64	0.06	1.66	0.12
K	1.49	0.04	1.51	0.05	0.43	0.01	0.43	0.02
Ca	5.09	0.08	5.18	0.15	8.17	0.12	8.45	0.25
Mg	2.16	0.03	2.17	0.07	4.36	0.07	4.53	0.13
Al	7.14	0.10	7.16	0.21	7.16	0.08	7.31	0.24
Fe	9.66	0.15	9.38	0.29	8.63	0.14	8.48	0.25
Ti	1.35	0.03	1.31	0.05	1.63	0.2	1.68	0.06
V	416	14	422	13	317	11	324	7
Cr	18	2	19	1	280	19	286	14
Mn	1520	60	1534	40	1290	40	1329	27
Co	37	3	37	1	45	3	46	1
Ni	12.6	0.3	12.5	1.4	119	7	120	5
Cu	19	2	19	1	127	7	119	3
Zn	127	9	128	6	103	6	100	5
Rb	48	2	49	1	9.8	1.0	8	0.2
Sr	346	14	350	8	389	23	414	9
Mo	248	17	251	12	4.07	0.16	4	0.2
Ba	683	28	709	19	130	13	129	8
Th	6.2	0.7	6.2	0.2	1.2	0.3	1.4	0.1
U	1.69	0.19	1.69	0.03	0.4	0.035	0.4	0.010
La	25	1	25.6	0.5	15	1	15.1	0.3
Ce	53	2	54.2	1.3	38	2	37.8	0.7
Pr	6.8	0.3	7.0	0.2	5.3	0.028	5.4	0.095
Nd	28	2	29	0.6	25.0	1.8	24.3	0.4
Sm	6.7	0.3	6.8	0.2	6.2	0.4	6.3	0.1
Eu	2.0	0.1	2.0	0.0	2.0	0.012	2.1	0.053
Gd	6.8	0.3	7.0	0.2	6.3	0.2	6.3	0.1
Tb	1.07	0.04	1.09	0.03	0.9	0.006	1.0	0.022
Dy	6.42	0.055	6.5	0.136	5.3	0.028	5.4	0.076
Ho	1.33	0.06	1.35	0.03	1.0	0.04	1.0	0.0
Er	3.67	0.038	3.7	0.080	2.5	0.014	2.5	0.074
Tm	0.54	0.006	0.55	0.013	0.3	0.0031	0.3	0.0062
Yb	3.5	0.2	3.6	0.1	2.0	0.2	2.0	0.1
Lu	0.51	0.02	0.52	0.02	0.28	0.01	0.28	0.01

The measured and reported data for these standards are compared in Table 2.7. Figure 2.8 clearly depicts the good match between the measured and reported values for the standards and hence, ensures good data quality. Further, the measured concentrations for all elements fall within the range of reported concentrations for these reference material. Several samples were also processed and analysed in replicates to constrain the external reproducibility (precision) of the measurements. The average precision of these analyses is 4 % (Table 2.8). The procedural blank for these analyses is found to be several orders lower in magnitude than the sample signal, and hence, no blank corrections were made.

Unlike the bulk samples, the silicate fractions of sediments were analysed for their major oxide contents using an X-ray fluorescence (XRF) instrument at IISER Pune (S8 Tiger, Bruker) and trace elements using the Q-ICPMS instrument. For the XRF analyses, a known amount of decarbonated sediment sample (cf. section 2.2.1.1) was ashed at 650 °C for 4 hours to find the loss of ignition (LOI) of the sample. The LOI was determined from the difference between initial and ashed sample weight (Table A2.1, Annexure Table). The ashed sediment was fused by maintaining a fixed sample-to-flux ratio for both the samples and the standards. We have used a mixture of Lithium tetraborate (66 %) and Lithium metaborate (34 %) as a flux. About 0.55 g of the sediment/standard sample and ~ 9.35 g of the flux was fused in a platinum crucible at 1100 °C to prepare a glass bead. These beads were bombarded with a primary x-ray which releases electron from innermost shell, which was re-filled by an electron from the nearby outer shells by releasing energy as a secondary x-ray. The intensity of this fluorescent x-ray of characteristic wavelength were quantified to compute the oxide concentrations. We have used a wide range of standards of geological materials (feldspar, clay, dolomite, gypsum, limestone, bauxite, etc.) available in the GEO-QUANT package to establish the relationship between fluorescent x-ray intensity and concentration. The major oxide concentrations for the samples were measured using this standard calibration line. The accuracy of the XRF analysis was monitored by measuring the oxide content of two certified reference materials (USGS BCR-2 and BHVO-2).

The inorganic, organic carbon, nitrogen, and sulfur contents of the sediments were measured using the CHNS and CO_2-Coulometer instruments at IISER Pune (Tripathy et al., 2014). Total carbon, nitrogen, and sulfur concentrations of the water-washed samples were measured using a CHNS analyser (Flash Smart, Thermo Scientific). For this, about 15-20 mg of water-washed samples were combusted at ~1065 °C, and the liberated gases were quantified

Table 2.8: *Replicate analyses of major and trace elements of the sediment samples.*

Sample ID		Na	K	Ca	Mg	Al	Fe	Ti	V	Cr	Mn	Co	Ni	Cu	Zn	Rb	Sr	Mo	Ba	Th	U
		wt. %							μg/g												
GC06/9-10	(I)	0.98	1.44	4.20	2.23	7.31	6.71	0.87	152	147	689	30	73	83	75	82	217	13.1	156	8.2	2.9
	(II)	0.78	1.40	4.22	2.15	7.12	6.54	0.86	153	148	691	29	72	89	87	82	220	12.8	155	8.0	2.9
GC06/33-34	(I)	0.97	1.50	4.80	2.31	7.35	6.77	0.87	148	144	677	29	73	79	83	84	248	14.4	165	8.1	2.8
	(II)	0.72	1.40	4.64	2.16	6.94	6.35	0.81	148	143	647	29	70	81	90	82	240	13.4	164	8.0	2.8
GC06/150-151	(I)	0.72	1.56	4.30	2.29	7.33	6.59	0.83	147	137	649	28	70	84	79	84	226	12.6	160	8.0	3.1
	(II)	0.72	1.56	4.31	2.28	7.40	6.59	0.81	147	140	663	29	73	86	91	88	234	14.8	166	8.1	3.1
GC06/215-216	(I)	0.77	1.34	5.26	2.09	6.34	5.74	0.79	135	138	598	27	64	70	76	76	300	16.1	155	8.9	3.0
	(II)	0.81	1.41	5.48	2.16	6.57	5.87	0.81	131	137	574	26	64	73	135	74	296	14.9	166	7.7	2.9
GC06/239-240	(I)	0.99	1.50	5.98	2.34	7.10	6.39	0.88	146	142	661	28	66	73	115	77	325	14.4	163	7.8	2.9
	(II)	0.96	1.44	5.72	2.26	6.86	6.23	0.86	141	137	652	27	66	71	83	75	317	15.5	161	7.9	2.8
	(III)	0.83	1.38	5.80	2.15	6.51	6.03	0.87	142	141	656	27	65	77	138	75	323	16.5	173	8.1	2.9
GC06/54-55/S	(I)	0.85	1.44	0.86	1.06	7.69	6.19	1.03	158	191	387	14	76	64	47	95	85	5.3	219	10.2	1.4
	(II)	0.86	1.47	0.88	1.07	7.75	6.27	1.07	160	179	388	14	73	63	53	96	87	5.1	222	10.3	1.5
GC06/103-104/S	(I)	0.87	1.41	0.90	0.97	7.27	5.70	1.06	153	199	379	12	83	56	42	88	90	5.8	230	10.3	1.5
	(II)	0.86	1.40	0.90	0.96	7.28	5.70	1.04	155	182	375	12	73	56	50	87	90	5.1	245	10.0	1.5
GC06/159-160/S	(I)	0.80	1.45	0.83	0.96	7.49	5.78	1.03	146	163	348	12	66	58	48	95	80	4.3	220	10.2	1.5
	(II)	0.80	1.44	0.73	0.95	7.53	5.78	1.04	145	186	349	12	76	58	43	95	79	4.9	207	10.1	1.4
GC06/165-166/S	(I)	0.94	1.47	1.01	0.98	7.39	5.70	1.04	156	182	381	13	74	58	44	91	99	4.8	232	9.9	1.4
	(II)	0.95	1.47	1.00	0.99	7.37	5.71	1.05	152	181	382	12	72	56	46	91	100	4.7	256	9.9	1.5

Table 2.8 *(continued)*

Sample ID		Na	K	Ca	Mg	Al	Fe	Ti	V	Cr	Mn	Co	Ni	Cu	Zn	Rb	Sr	Mo	Ba	Th	U
		wt. %							µg/g												
GC06/170-171/S	(I)	0.79	1.46	0.72	0.97	7.59	5.73	1.02	145	174	346	12	69	56	44	96	81	4.6	225	9.9	1.4
	(II)	0.80	1.43	0.72	0.97	7.46	5.72	1.02	145	165	342	12	66	56	42	95	80	4.4	204	10.1	1.3
GC06/220-221/S	(I)	0.95	1.44	0.98	0.93	7.21	5.48	1.05	148	190	370	12	75	53	40	88	101	4.9	228	10.2	1.6
	(II)	0.92	1.41	0.96	0.90	7.01	5.40	1.03	143	177	363	11	69	53	36	86	97	4.7	213	10.0	1.5
GC06/244-245/S	(I)	1.03	1.43	1.13	0.99	7.29	5.84	1.09	155	178	401	13	70	54	43	84	109	4.8	227	9.6	1.5
	(II)	1.01	1.41	1.12	0.98	7.19	5.84	1.08	155	195	399	13	79	54	46	84	106	5.2	244	9.7	1.5
GC10/30-31	(I)	0.62	1.09	18.70	1.89	4.71	4.24	0.45	93	123	718	20	53	13	77	59	3329	0.67	66	5.1	3.2
	(II)	0.59	1.10	18.99	1.92	4.79	4.18	0.46	91	120	709	19	51	13	78	58	3266	0.61	56	5.0	3.1
GC10/45-46	(I)	0.55	1.14	20.10	2.00	5.03	4.42	0.48	90	113	691	20	51	28	76	55	3188	0.35	63	5.4	3.3
	(II)	0.55	1.15	20.08	2.03	5.05	4.44	0.49	91	112	698	19	56	28	71	55	3150	0.45	56	4.9	3.3
GC10/111-112	(I)	0.51	1.10	19.96	1.97	4.93	4.40	0.48	88	110	687	18	50	28	75	53	3161	0.40	51	5.0	2.9
	(II)	0.53	1.13	20.10	2.00	5.08	4.41	0.49	90	112	697	19	51	30	69	56	3194	0.41	49	4.9	3.1
PDM18/22-24	(I)	0.54	0.84	25.43	1.55	2.84	1.79	0.21	28	138	402	5.6	64	15	28	47	524	2.8	163	9.0	2.2
	(II)	0.54	0.85	25.72	1.55	2.84	1.78	0.21	30	138	388	6.3	63	15	30	47	539	2.8	143	8.3	2.2
PDM18/32-34	(I)	0.62	1.22	18.87	1.85	3.97	2.36	0.30	46	141	402	9.3	65	19	40	64	446	2.7	210	14.3	3.0
	(II)	0.65	1.23	19.01	1.90	4.05	2.39	0.29	46	139	410	9.4	63	19	45	66	462	2.6	229	15.4	3.2
PDM18/36-38	(I)	0.64	1.41	18.78	1.88	4.74	2.63	0.29	56	50	330	8.6	13	19	47	80	483	0.6	247	14.0	2.7
	(II)	0.63	1.36	18.76	1.87	4.60	2.56	0.29	54	52	328	8.6	14	18	50	77	486	0.7	243	14.3	2.8
PDM18/44-46	(I)	0.63	1.14	21.35	1.82	3.67	2.13	0.24	42	141	352	7.4	64	16	30	63	462	2.8	222	9.2	2.1
	(II)	0.63	1.11	21.28	1.81	3.59	2.08	0.24	42	129	335	7.1	58	17	48	60	464	2.5	215	9.4	2.2

Table 2.8 *(continued)*

Sample ID		La	Ce	Pr	Nd	Sm	Eu	Gd	Tb	Dy	Ho	Er	Tm	Yb	Lu
		µg/g													
GC06/9-10	(I)	24.3	51.7	6.2	24.1	5.6	1.4	5.4	0.8	4.9	0.94	2.7	0.40	2.4	0.36
	(II)	24.3	51.4	6.2	24.1	5.3	1.4	5.5	0.9	4.9	1.00	2.8	0.38	2.6	0.34
GC06/33-34	(I)	23.7	51.0	6.1	23.6	5.1	1.4	5.5	0.8	4.6	0.95	2.5	0.39	2.4	0.35
	(II)	23.5	50.9	6.0	23.2	5.2	1.4	5.2	0.8	4.5	0.93	2.5	0.37	2.3	0.32
GC06/150-151	(I)	23.2	49.9	5.9	23.4	5.1	1.3	5.0	0.8	4.6	0.92	2.5	0.36	2.3	0.32
	(II)	24.2	51.2	6.1	23.6	5.1	1.4	5.3	0.8	4.6	0.91	2.5	0.38	2.4	0.34
GC06/215-216	(I)	22.6	47.3	5.6	22.2	5.0	1.3	5.1	0.8	4.2	0.89	2.2	0.35	2.2	0.31
	(II)	22.2	46.9	5.6	22.0	4.9	1.3	5.0	0.7	4.4	0.87	2.3	0.34	2.2	0.32
GC06/239-240	(I)	23.0	49.6	5.7	22.8	5.2	1.4	5.3	0.8	4.5	0.89	2.4	0.37	2.5	0.34
	(II)	22.9	48.5	5.8	22.4	5.3	1.4	5.4	0.8	4.5	0.87	2.5	0.35	2.3	0.31
	(III)	24.8	51.5	6.2	24.0	5.7	1.4	5.2	0.8	4.7	0.95	2.5	0.40	2.5	0.35
GC06/54-55/S	(I)	15.4	29.6	3.2	11.3	2.2	0.6	1.8	0.3	1.9	0.41	1.2	0.20	1.3	0.20
	(II)	15.5	30.0	3.3	11.2	2.3	0.6	1.9	0.3	2.0	0.42	1.3	0.20	1.4	0.21
GC06/103-104/S	(I)	15.8	30.7	3.4	11.7	2.3	0.6	1.9	0.3	2.0	0.41	1.2	0.19	1.3	0.19
	(II)	16.0	30.9	3.5	12.0	2.2	0.6	1.8	0.3	2.0	0.41	1.2	0.18	1.3	0.21
GC06/159-160/S	(I)	15.4	29.5	3.3	11.3	2.0	0.6	1.8	0.3	1.8	0.41	1.2	0.18	1.3	0.21
	(II)	15.4	29.5	3.3	11.1	2.0	0.5	1.8	0.3	1.8	0.40	1.2	0.18	1.4	0.20
GC06/165-166/S	(I)	16.2	31.6	3.5	12.2	2.3	0.6	1.9	0.3	1.9	0.40	1.2	0.20	1.3	0.21
	(II)	16.5	32.0	3.5	12.5	2.3	0.6	2.0	0.3	1.9	0.41	1.3	0.20	1.4	0.20
GC06/170-171/S	(I)	15.3	29.6	3.2	11.5	2.0	0.5	1.6	0.3	1.7	0.38	1.1	0.18	1.3	0.19
	(II)	15.4	29.6	3.1	11.3	2.1	0.6	1.7	0.3	1.8	0.38	1.2	0.18	1.3	0.18
GC06/220-221/S	(I)	16.2	31.4	3.6	12.5	2.3	0.7	2.0	0.3	2.1	0.41	1.3	0.20	1.4	0.21
	(II)	16.0	31.4	3.5	12.0	2.1	0.6	1.9	0.3	1.9	0.41	1.2	0.18	1.2	0.18
GC06/244-245/S	(I)	15.9	31.3	3.6	12.3	2.4	0.6	1.9	0.3	1.9	0.41	1.2	0.20	1.4	0.21
	(II)	16.1	31.1	3.5	12.0	2.4	0.7	2.1	0.3	2.0	0.42	1.3	0.20	1.3	0.21
PDM18/22-24	(I)	23.9	47.9	5.6	20.2	4.1	0.70	3.5	0.52	2.9	0.59	1.6	0.24	1.6	0.23
	(II)	23.0	44.7	5.2	19.4	3.8	0.68	3.5	0.52	3.0	0.67	1.7	0.27	1.8	0.26
PDM18/32-34	(I)	36.2	71.3	8.3	29.9	5.8	0.96	4.8	0.68	3.9	0.80	2.0	0.30	2.0	0.31
	(II)	39.2	77.8	9.0	32.3	6.2	0.94	5.4	0.73	4.0	0.76	2.1	0.31	2.1	0.32
PDM18/36-38	(I)	35.4	69.5	8.0	29.0	5.7	1.01	5.1	0.71	4.0	0.80	2.2	0.33	2.1	0.31
	(II)	36.3	71.6	8.2	29.9	5.6	0.97	4.9	0.74	4.2	0.84	2.3	0.32	2.2	0.32
PDM18/44-46	(I)	25.5	50.0	5.8	20.8	4.3	0.74	3.5	0.49	2.7	0.54	1.5	0.23	1.4	0.21
	(II)	24.7	48.5	5.5	20.5	4.1	0.76	3.5	0.51	2.9	0.56	1.6	0.24	1.6	0.22

Table 2.9: *Replicate analyses of total carbon and total nitrogen, analyses of the sediment samples.*

Sample ID	Total Carbon		Total Nitrogen	
	wt. %			
	(I)	(II)	(I)	(II)
GC06/1-2	2.17	2.18	0.114	0.117
GC06/5-6	2.16	2.15	0.113	0.113
GC06/25-26	2.51	2.49	0.135	0.135
GC10/57-58	2.30	2.29	0.109	0.110
GC10/61-62	2.31	2.15	0.107	0.103
GC06/66-67	2.34	2.32	0.113	0.113
GC06/117-118	2.24	2.24	0.096	0.094
GC06/139-140	2.26	2.26	0.099	0.100
GC06/154-155	2.11	2.14	0.089	0.093
GC06/165-166	2.32	2.27	0.087	0.089
GC06/174-175	2.33	2.34	0.093	0.093
GC06/178-179	2.43	2.46	0.090	0.095
GC06/186-187	2.34	2.36	0.089	0.089
GC06/195-196	2.45	2.45	0.088	0.086
GC06/205-206	2.46	2.48	0.085	0.086
PDM18/12-14	7.30	7.24	0.018	0.017
PDM18/16-18	7.75	7.63	0.023	0.024
PDM18/18-20	7.25	7.32	0.018	0.017
PDM18/34-36	6.13	6.12	0.028	0.026
PDM18/46-48	6.38	6.42	0.014	0.014
GC10/3-4	7.86	7.91	na	na
GC10/29-30	5.71	5.68	na	na
GC10/30-31	5.69	5.66	na	na
GC10/39-40	5.64	5.61	na	na
GC10/56-57	5.62	5.64	na	na
GC10/70-71	5.67	5.68	na	na
GC10/85-86	5.64	5.60	na	na
GC10/104-105	5.70	5.67	na	na
GC10/123-124	5.74	5.72	na	na
GC10/129-130	5.79	5.69	na	na

na: not analyzed

Table 2.10: *Reproducibility of the sulfur analyses of the sediment samples.*

Sample ID	**Sulfur**	
	wt. %	
	(I)	(II)
GC10/0-1	0.14	0.15
GC10/13-14	0.30	0.31
GC10/93-94	0.29	0.28
GC10/113-114	0.50	0.53

Table 2.11: *Reproducibility of the sedimentary inorganic carbon measurements.*

Sample ID	**$CaCO_3$**	
	wt. %	
	(I)	(II)
GC06/66-67	10.7	10.4
GC06/132-133	10.4	10.2
GC06/165-166	11.7	11.2
GC06/261-262	15.6	15.4
GC06/108-109	10.3	10.4
GC10/3-4	61.7	58.2
GC10/6-7	64.5	65.8
GC10/10-11	68.0	71.2
GC10/17-18	47.6	52.2
GC10/31-32	45.6	46.2
GC10/33-34	44.9	46.4
GC10/35-36	45.8	44.9
GC10/113-114	43.8	42.5
PDM18/28-30	68.1	67.5
PDM18/48-50	55.4	56.2
PDM18/50-52	39.4	39.6
PDM18/52-54	37.5	38.6
PDM18/54-56	39.8	39.5

using the standard calibration approach to measure the C, N, and S concentrations. One soil reference material (USGS SGR-1) was used to constrain the accuracy of the measurement. The average accuracy for the C and N analyses is better than 2 % (Table 2.9), whereas that for the sulfur analysis was found to be ~4 % (Table 2.10). The organic carbon content was computed by subtracting the inorganic carbon content from the total carbon content. The inorganic carbon content was measured using a CO_2 coulometer. Towards this, about 10 to 15 mg powder samples were treated with phosphoric acid at 80 °C in a closed vial, and the liberated CO_2 was quantified to measure the carbonate concentrations of the samples using the CO_2-Coulometer (UIC Inc) instrument. Several replicate samples were measured to constrain the precision of the analysis. The average precision for the carbonate analysis was better than 3 % (Table 2.11).

Chapter 3

Seasonal Variation in Chemical Erosion Pattern: Evidence from Time-series Analyses of the Brahmaputra River Water Chemistry

3.1 Introduction

Chemical weathering of rocks is mostly an acid-base reaction, where minerals present in the rock serve as the base and the naturally-occurring acids serve as the proton donor. The frequently found acids in nature are carbonic, sulfidic and organic acids. Carbonic-acid mediated weathering of silicate minerals and their subsequent conversion into carbonates in oceans act as a major sink for atmospheric CO_2 over geological timescales. Although several controlling factors (temperature, physical erosion, basin relief, lithology, etc.) have been recognized, surface runoff plays a dominant role in regulating the intensity of this land-surface process in river basins (Dalai et al., 2002; Gaillardet et al., 1999; Riebe et al., 2004; Singh et al., 2005; Torres et al., 2015; West et al., 2005; White and Blum, 1995). A large number of studies on major ion chemistry of rivers have shown relatively higher chemical erosion rates during peak flow seasons and preferentially higher solute contribution from weathering of resistant minerals (such as silicates compared to carbonates) during lean flow stages of the streams (e.g., Ganga (Bickle et al., 2018; Krishnaswami et al., 1999; Tipper et al., 2006; Tripathy et al., 2010); Brahmaputra (Rai and Singh, 2007); Salween (Chapman et al., 2015); Godavari (Jha et al., 2009); Mekong (Noh et al., 2009)). These changes in weathering rates and patterns are mainly due to seasonal variations in water-rock interaction time, changes in solute supply from different lithological units, and/or high input from deep groundwater (Galy and France-Lanord, 1999; Rai and Singh, 2007; Tipper et al., 2006). On the contrary, existing evidence also shows the insignificant change in elemental concentrations in response to water discharge of several watersheds from the US (United States of America) with diverse catchment lithology (Godsey et al., 2009; Ibarra et al., 2016). This chemostatic behaviour in these basins hints at the occurrence of a buffering mechanism against solute dilution, and the mechanism may be linked to longer fluid residence time compared to the time required to reach chemical equilibrium in these basins (Maher, 2011). These divergent observations on the climate and weathering relationship warrant more time-series studies of rivers with large seasonality in their discharges (Moon et al., 2014).

The rivers influenced by the Indian summer monsoon are often characterized by large (an order of magnitude) seasonal changes in their water fluxes. This thesis work investigates time-series major ions, silica, and Sr concentration data for the Brahmaputra River (at Guwahati, India) at weekly to biweekly intervals to constrain its solute sources and their relative contributions during different flow stages. The average monthly water discharge of the river varies by about 10 times (from 4577 to 40439 m^3/s), with about 60-85 % of flux is supplied during the monsoon season alone (Jain et al., 2007). This large river system predominantly flows through the Himalayan and Tibetian regions and supplies ~ 1.8 % of the global water flux from only 0.4 % of the global continental area (Das et al., 2016; Singh, 2007). Prior to this, few earlier studies have also reported seasonal variations of the water chemistry for the Himalayan rivers, such as the Ganga (Bickle et al., 2005, 2018; Chakrapani and Saini, 2009; Tipper et al., 2006; Tripathy et al., 2010), Brahmaputra (Rai and Singh, 2007; Singh et al., 2005), Irrawaddy and Salween (Chapman et al., 2015). These studies based on time-series trends of elemental and Sr isotopic ratios have shown relatively higher contributions from silicate weathering during their lean flow stages (Tipper et al., 2006; Rai and Singh, 2007). Owing to seasonality in mineral weathering, the annual elemental fluxes of these Himalayan rivers were found to be significantly different when estimated based on time-series and single/limited season data (Tripathy et al., 2010). Therefore, more time-series analyses of these river systems were urged for their precise flux estimation. Outcomes from this study show an increasing trend in chemical weathering rates during the monsoon. However, the relative solute supply from different mineral weathering shows minimal seasonality in the Brahmaputra mainstream.

3.2 Results

Time-series surface water chemistry data, dissolved major ions, silica, and Sr concentrations of the Brahmaputra mainstream at Guwahati (26.145 °N; 91.736 °E) are listed in Table 3.1. These samples, as mentioned earlier (cf. Chapter 2), were collected at weekly to biweekly interval for a duration of one year. In absence of real-time data, earlier reported average seasonal water discharge data (GRDC site, Pandu) for a nearby site have been used (*http://www.grdc.sr.unh.edu*). Water chemistry at this location is expected to be a balance between supply of solutes from chemical weathering of rocks and other sources, and removal of solutes through various aquatic processes (e.g. calcite precipitation (Jacobson et al., 2002) and/or biological uptake (Fontorbe et al., 2003)) in the upper reaches. The chemical compositions of these samples, therefore, should represent the chemical erosion (and, not weathering) pattern of the basin.

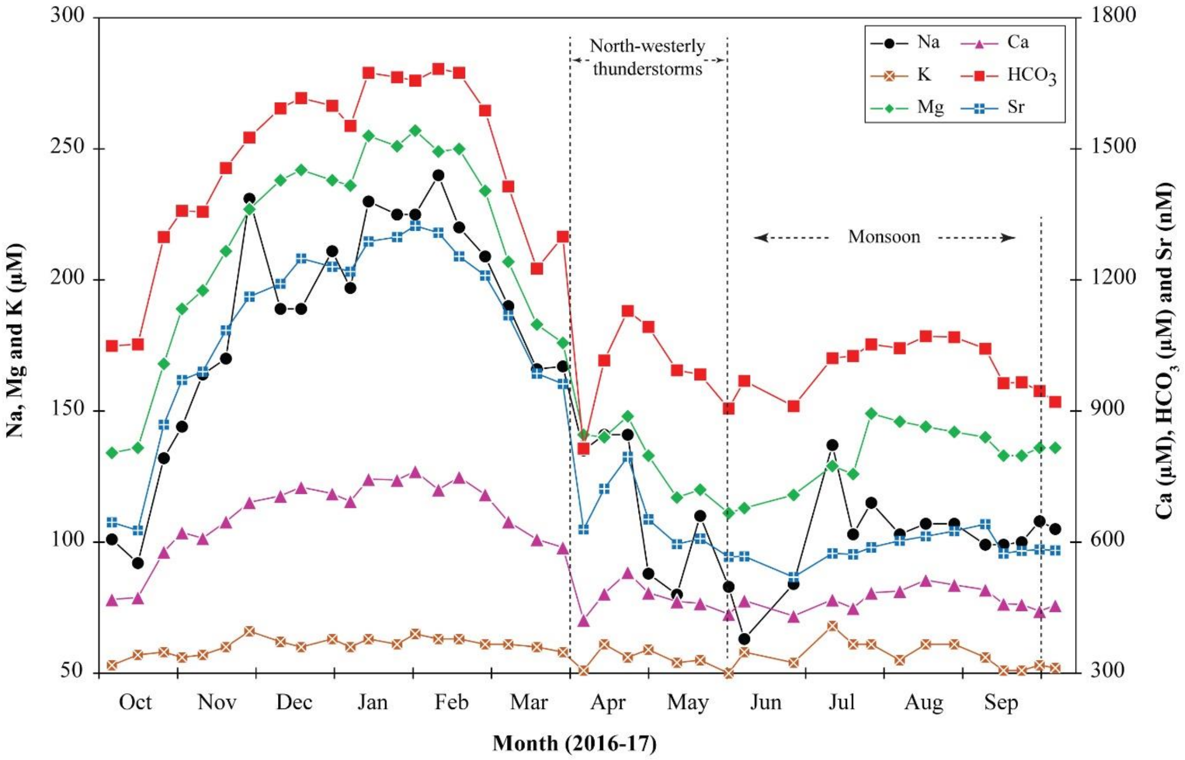

Figure 3.1. *Time-series variation of elemental concentrations (Na, Mg, Ca, Sr, HCO_3 and SiO_2) of the Brahmaputra River at Guwahati during the sampling period (2016-17). Higher elemental concentrations were observed for lean flow periods compared to those during the peak flow stages. This river basin, in addition to monsoon, also receives appreciable rainfall during April and May due to north-westerly thunderstorms.*

The time-series water chemistry data of the Brahmaputra show significant temporal variation during the sampling period (Fig. 3.1). The total dissolved solids (TDS) in these samples vary significantly between 96 and 180 mg/L, with a discharge-weighted average value of 115 mg/L. This average TDS content is about 20 % higher than that reported as the global average for rivers (94 mg/L; Meybeck, 2003). The Brahmaputra mainstream water chemistry was plotted in a Piper diagram which is characterized mostly as Ca-Mg-HCO_3 type, pointing to the dominance of carbonate (and/or Ca-Mg (alumina) silicates) weathering in the basin (Fig.

3.2). On average, Ca and Mg (in µEq units) dominate the total cation (TZ^+) content of the samples and account for 68 % and 20 % of the TZ^+ respectively. The concentration of Ca varies significantly between 422 and 762 µM (mean: 564 ± 115 µM), whereas Mg varies from 111 to 257 µM (mean: 173 ± 50 µM). These data compare well with that reported earlier for the Brahmaputra at Guwahati (Singh et al., 2005; Table 3.2)). The average Na (145 ± 52 µM) of this river (Table 3.1) is lower compared to that reported for global rivers (Na ~ 240 µM; Meybeck, 2003). Alkalinity dominates the anion content of the river and accounts for ~77 % of their total anion (TZ^-). The dissolved sulfate content of the river varies from 96 to 234 µM, where the lower values belong to the monsoon samples. Average nitrate content in these samples (11 ± 7 µmol/L; Table 3.1) is found comparable to that reported for rain in the Bangaldesh (~8.6 µmol/L; Galy and France-Lanord, 1999), pointing to minimal impact of anthropogenic sources to this large river system. Further, no significant relation between K and NO_3 concentrations rules out any solute through agricultural sources. The average silica (154 ± 30 µM) content of the river is similar to that of the global average values (145 µM; Meybeck, 2003), possibly hinting at a similar intensity of silicate weathering in this basin compared to that reported for the global rivers.

Chemical compositions of the Brahmaputra River water at Guwahati showed seasonal variations and the relative standard deviation in the elemental concentrations for Na (36 %), K (8 %), Ca (20 %), Mg (29 %), HCO_3 (23 %), Cl (44 %), SO_4 (27 %), NO_3 (61 %) and Si (20 %) are found to be different. These elemental changes of the Brahmaputra are comparable with that observed for the Ganga, although the discharge variations in the case of the Ganga (about 25 times; from 1751 to 43030 m^3/s) are higher compared to the Brahmaputra (about 10 times; from 4577 to 40439 m^3/s) (*http://www.grdc.sr.unh.edu*). These monthly discharges correspond to a runoff change from 0.02 to 0.17 m/yr for the Brahmaputra and 0.01 to 0.24 m/yr for the Ganga outflow. Abundances of most of the elements show significant seasonal variation with relatively lower values during peak flow stages compared to lean flow periods (Fig. 3.1). The decrease in concentrations of the Brahmaputra River was observed since the April month as the basin also receives appreciable rainfall during these pre-monsoon months due to north-westerly thunderstorms (Fig. 2.2; cf. Chapter 2; section 2.1.1). The observed elemental variations in Figure 3.1 can be attributed either to the dilution effect and/or seasonality in source contributions to the dissolved load of the river. The seasonal change in elemental concentrations is significantly lower (about 1.5 times) compared to that of the water discharge, which varies by about 10 times and hence, cannot be attributed to the dilution effect alone.

Table 3.1: *Time series dissolved major ions, silica, and Sr concentrations data for the Brahmaputra mainstream at Guwahati, India.*

Sample ID	Date	Na	K	Ca	Mg	Cl	SO$_4$	HCO$_3$	NO$_3$	SiO$_2$	Sr	TDS	TZ$^-$	TZ$^+$	NICB*
		µM									nM	mg/L	µEq		%
BMP16/01	5/Oct/16	101	53	469	134	30	124	1049	8	137	645	110	1335	1360	2
BMP16/02	15/Oct/16	92	57	473	136	30	109	1053	6	112	627	107	1307	1367	4
BMP16/03	25/Oct/16	132	58	578	168	37	149	1298	6	162	869	135	1639	1682	3
BMP16/04	1/Nov/16	144	56	622	189	37	173	1358	5	173	971	144	1746	1822	4
BMP16/05	9/Nov/16	164	57	609	196	46	169	1356	11	185	990	145	1751	1831	4
BMP16/06	18/Nov/16	170	60	647	211	46	187	1456	5	185	1085	155	1881	1946	3
BMP16/07	27/Nov/16	231	66	691	227	86	197	1526	21	185	1162	166	2027	2133	5
BMP16/08	9/Dec/16	189	62	706	238	51	198	1593	8	192	1191	169	2048	2139	4
BMP16/09	17/Dec/16	189	60	726	242	46	202	1616	6	195	1249	171	2072	2185	5
BMP16/10	29/Dec/16	211	63	711	238	61	213	1599	11	195	1230	172	2097	2172	4
BMP16/11	5/Jan/17	197	60	693	236	53	210	1553	10	192	1219	167	2036	2115	4
BMP16/12	12/Jan/17	230	63	744	255	60	226	1674	6	196	1288	180	2192	2291	4
BMP16/13	23/Jan/17	225	61	742	251	55	230	1664	3	193	1298	178	2182	2272	4
BMP16/14	30/Jan/17	225	65	762	257	99	222	1656	12	195	1324	180	2211	2328	5
BMP16/15	8/Feb/17	240	63	720	249	71	234	1683	3	192	1308	180	2225	2241	1
BMP16/16	16/Feb/17	220	63	749	250	69	223	1674	6	190	1254	179	2195	2281	4
BMP16/17	26/Feb/17	209	61	709	234	63	221	1588	7	182	1210	171	2100	2156	3
BMP16/18	7/Mar/17	190	61	647	207	62	196	1414	17	173	1119	154	1885	1959	4
BMP16/19	18/Mar/17	166	60	606	183	59	197	1226	24	160	986	140	1703	1804	6
BMP16/20	28/Mar/17	167	58	588	176	46	181	1299	13	160	962	140	1720	1753	2

Table 3.1 (*continued*)

Sample ID	**Date**	**Na**	**K**	**Ca**	**Mg**	**Cl**	**SO_4**	**HCO_3**	**NO_3**	**SiO_2**	**Sr**	**TDS**	**TZ^-**	**TZ^+**	**NICB***
		µM									nM	mg/L	µEq		%
BMP16/21	5/Apr/17	135	51	422	141	45	199	814	24	128	629	103	1281	1312	2
BMP16/22	13/Apr/17	141	61	482	140	50	141	1016	17	143	722	113	1365	1446	6
BMP16/23	22/Apr/17	141	56	531	148	39	147	1129	13	142	795	122	1475	1555	5
BMP16/24	30/Apr/17	88	59	484	133	33	103	1093	18	109	652	110	1350	1381	2
BMP16/25	11/May/17	80	54	464	117	24	102	993	13	116	595	102	1234	1296	5
BMP16/26	20/May/17	110	55	460	120	42	127	984	7	131	608	106	1287	1325	3
BMP16/27	31/May/17	83	50	435	111	27	104	906	11	109	566	96	1152	1225	6
BMP16/28	6/Jun/17	63	58	466	113	25	96	969	17	98	567	99	1203	1279	6
BMP16/29	25/Jun/17	84	54	431	118	20	114	911	1	121	520	97	1160	1236	6
BMP16/30	10/Jul/17	137	68	468	129	55	110	1021	34	145	574	111	1330	1399	5
BMP16/31	18/Jul/17	103	61	449	126	29	111	1026	13	148	572	108	1290	1314	2
BMP16/32	25/Jul/17	115	61	484	149	29	131	1053	9	150	588	113	1353	1442	6
BMP16/33	5/Aug/17	103	55	488	146	24	124	1044	9	133	603	111	1325	1426	7
BMP16/34	15/Aug/17	107	61	513	144	27	134	1071	6	140	613	115	1372	1482	8
BMP16/35	26/Aug/17	107	61	502	142	27	135	1069	10	140	625	114	1376	1456	6
BMP16/36	7/Sep/17	99	56	491	140	21	153	1043	8	125	641	113	1378	1417	3
BMP16/37	14/Sep/17	99	51	459	133	21	131	964	10	128	574	104	1257	1334	6
BMP16/38	21/Sep/17	100	51	457	133	21	131	966	6	130	580	104	1255	1331	6
BMP16/39	28/Sep/17	108	53	442	136	24	141	946	8	137	583	104	1260	1317	4
BMP16/40	4/Oct/17	105	52	455	136	23	155	921	14	136	581	105	1268	1339	5

**Normalized inorganic charge balance (NICB) = $100*[(TZ^+ - TZ^-)/((TZ^+ + TZ^-)/2)]$*

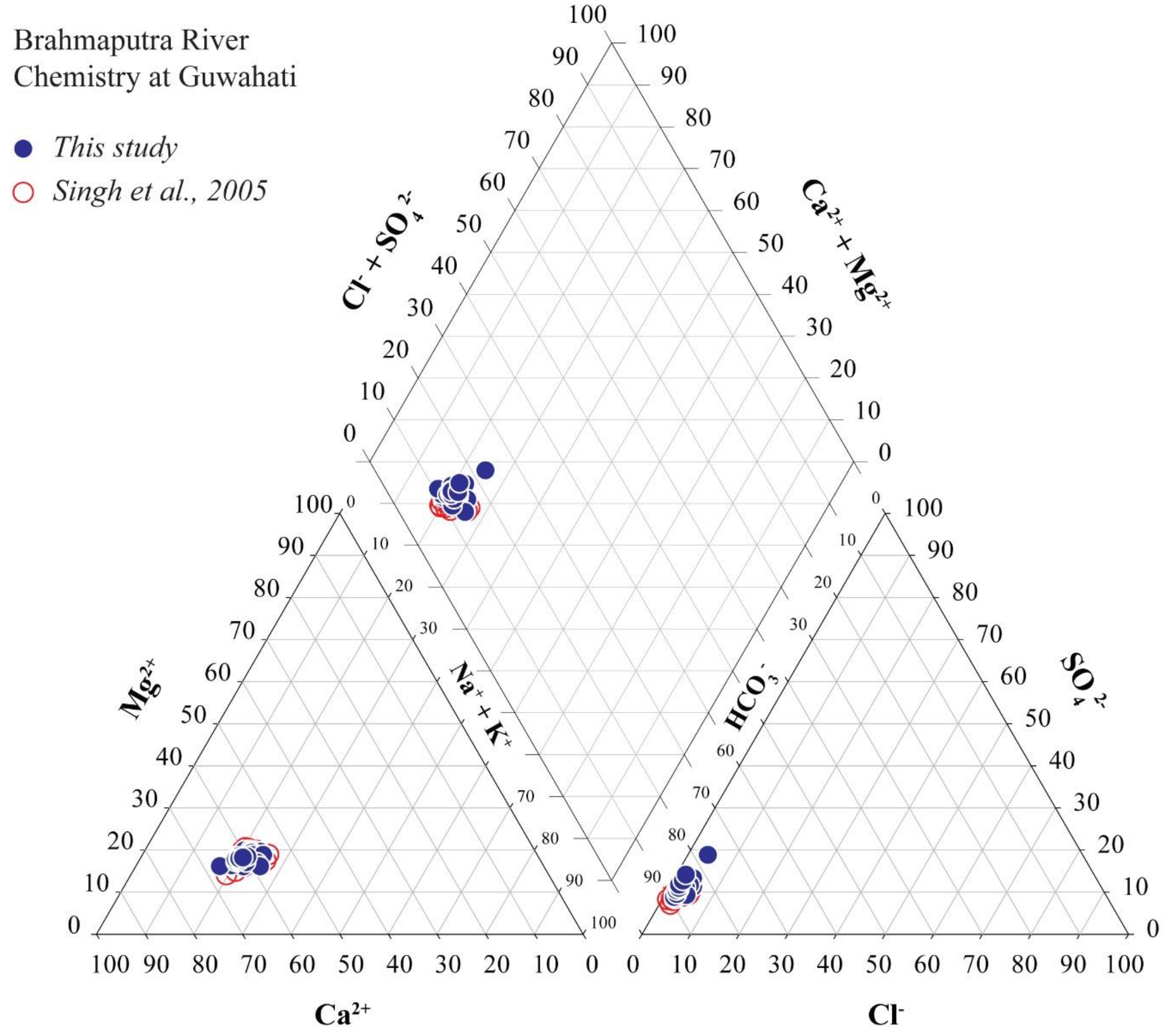

Figure 3.2. *Piper diagram for the Brahmaputra River water chemistry dataset. Data distribution shows dominance of carbonate weathering in this river basin. For data comparison earlier reported water chemistry data (red circle) are also included (Singh et al., 200).*

The Sr concentrations of the Brahmaputra samples vary between 520 and 1324 nM, with an average value of 854 ± 290 nM. The mean Sr concentration compares well with that reported earlier at Guwahati (970 ± 261 nM; Rai and Singh, 2007) but is lower compared to the global riverine Sr concentration (1220 nM; Peucker-Ehrenbrink et al., 2010). Like other cations, concentrations of Sr at Guwahati also show significant seasonal variation with about 1.5 times lower values during the monsoon compared to the non-monsoon samples (Fig. 3.1). Dissolved Sr shows a strong correlation with Ca ($r^2 = 0.98$; n = 40) and Mg ($r^2 = 0.97$; n = 40, pointing to their similar sources. The Ca-Sr regression line yields a Ca/Sr ratio of 0.39, which is intermediate to that reported for carbonates (~5.0; Krishnaswami et al., 1999) and silicates (~0.29; Singh et al., 2006) from this basin. The supply of Ca and Sr from gypsum dissolution can also be a potential solute source to the Brahmaputra basin. This proposition is consistent with the significant correlation observed for Ca ($r = 0.89$; $n = 40$; $p < 0.01$) and Sr ($r = 0.92$; $n = 40$; $p < 0.01$) with the SO_4 concentrations at Guwahati.

Table 3.2: *Decadal variation in the (discharge-weighted) water chemistry data for the Brahmaputra River at Guwahati, India. The major ion and Sr compositions have remained the same for the last ~50 years.*

Year of collection	No. of samples	Na	K	Ca	Mg	Cl	SO_4	HCO_3	SiO_2	Sr	TDS	Ref.
2016-2017	40 (12 months)	115	58	501	145	33	135	1080	139	676	115	(1)
1999-2000	17* (09 months)	118	63	517	145	34	122	1209	163	810	126	(2, 3)
1982	02 (Apr, Dec.)^	121	52	457	177	33	124	1126	162	876	118	(4, 5)
1979	01 (July)	159	79	425	119	107	100	-	123	-	-	(6)
1971-1972	6 (06 months)	138	86	405	174	114		1159	173	-	112	(7)

All concentration data are reported in µM units, except for the TDS (in mg/L);
**After excluding one outlier sample; ^Average of the two data is presented;*
(1) Present study; (2) Singh et al., 2005; (3) Rai and Singh, 2007; (4) Sarin et al., 1989;
(5) Krishnaswami et al., 1992; (6) Hu et al., 1982; (7) Handa, 1972.

3.3 Discussion

3.3.1 Decadal variation

Prior to this work, few studies have reported dissolved major ions and Sr elemental data for seasonal (Handa, 1972; Rai and Singh, 2007; Singh et al., 2005) and/or single (Hu et al., 1982; Krishnaswami et al., 1992; Sarin et al., 1989) samples from the Brahmaputra River at Guwahati. These literature and present data together span a period of 46 years (Table 3.2). Comparison of these datasets can provide information on decadal variation in the water chemistry of the Brahmaputra and the role of man-made activities in regulating these changes, if any. The average concentrations of most of the elements show remarkable similarity for the last five decades (Table 3.2), indicating an insignificant influence of anthropogenic activities on major ion chemistry of the Brahmaputra River in recent years. The observed decadal variation for most of the constituents (Na, Ca, Mg, HCO_3, SiO_2, Sr, and TDS) is within ± 20 %

(Table 3.2). The decadal spread for SO_4 content, after excluding one datum with ~4 times lower concentration, is also found to be minimal (12 %). The major difference is observed for the Cl content; the pre-1980 Cl data (111 ± 5 µM) is found to be ~80 µM higher than that reported for post-1980 samples (33 ± 1 µM). This decrease in Cl concentration does not commensurate with the decadal Na trend. Although the exact cause for this difference is unknown, the dissolved Cl concentrations for the last 35 years were found to be very consistent and show a data spread of only ± 0.3 %.

In addition to decadal variation, this study also compared the monthly data analysed for samples collected at Guwahati during 1999-2000 (Singh et al., 2005) and 2016-17 (This study). The chemical composition of one sample from June 1999 was strongly affected by a flash flood event (Rai and Singh, 2007) and hence, was not considered here for constraining the general decadal trend. Figure 3.3 depicts that most of the elemental concentrations have remained constant (within ± 20 %) at a monthly timescale for the last 20 years. However, the chloride and sodium concentrations in some of the samples were found to have larger deviations (Fig.

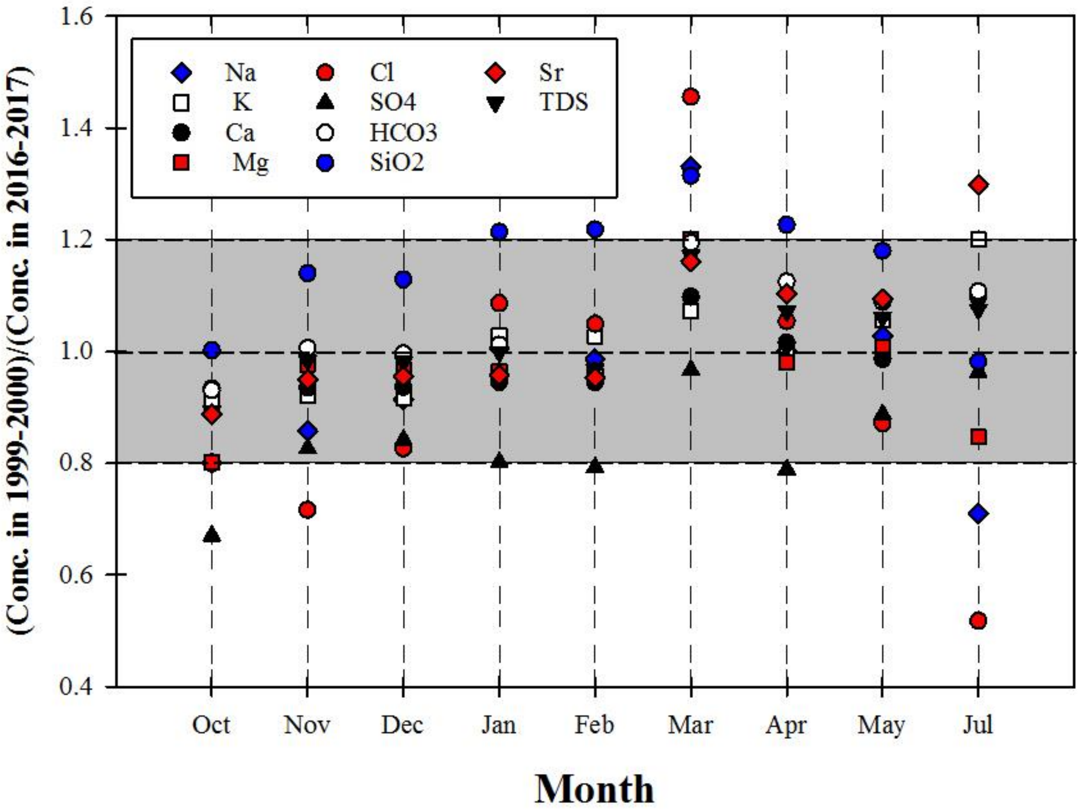

Figure 3.3. *Data comparison of monthly-averaged Brahmaputra River chemistry at Guwahati during 2016-17 (This study) and those reported earlier for 1999-2000 (Singh et al., 2005). No significant change in major ion compositions was observed during last ~20 years.*

3.3). In general, the major ions chemistry at Guwahati has mostly remained invariant at both monthly (Fig. 3.3) and annual (Table 3.2) timescales for the last ~50 years. This consistency in datasets points to minimal anthropogenic impact on the major ion chemistry of the river and also ensures that the present outcomes on annual chemical fluxes and weathering rates are good representative estimates for the basin.

3.3.2 Seasonality in water chemistry

Co-variation between water discharge (Q) and solute concentrations (C) provides clues about hydrological control on the runoff chemistry (Clow and Mast, 2010; Godsey et al., 2009). These two parameters in river basins often follow an empirical power law: $C = a \times Q^b$, where a and b are constant values. The b value nearly equals to -1 for efficient dilution of an element with water, whereas this value is closer to 0 for a chemostatic element, whose concentration remains near-constant irrespective of change in Q value (Godsey et al., 2009). In large river systems, the *b*-values show large spatial variations with chemostatic ($b \sim 0$) behaviour in their upper reaches and dominancy of dilution ($b \sim -1$) effect towards the lowland regions (Bouchez et al., 2017; Torres et al., 2015). Figure 3.4A depicts the correlation between monthly average C and Q data in a log-log plot for the Brahmaputra. The real-time discharge data for this sampling period was not available, and hence, the long-term average of water discharge data from a nearby location (at Pandu; GRDC dataset) has been used for this study. The *b* values for Na (-0.38), Ca (-0.21), Mg (-0.29), HCO_3 (-0.22), SiO_2 (-0.18) and Sr (-0.37) at Guwahati are statistically significant ($p < 0.01$) and vary between 0 and -1. These *b* values were compared with those reported for selected Himalayan-Tibetan Plateau (HTP) rivers (Ganga, Irrawaddy, Salween, Yangtze, and Pearl) and the global average for rivers (Table 3.3). The silica concentration behaves chemostatic in the Brahmaputra basin and also for HTP and global rivers. The b values for most of the elements at Guwahati (Table 3.3) are found to be more negative compared to those for the HTP and global rivers, pointing to their dilutional behaviour. In contrast to these elements, the K ($b \sim -0.04$) and NO_3 ($b \sim 0.08$) for the Brahmaputra are found chemostatic in nature. Although the exact cause for this behaviour is unclear, the dilution effect of K and NO_3 may have buffered through their possible increase in concentration due to the leaching of organic soil horizons during the monsoon period (Walling and Webb, 1986). The chemostatic behaviour of K in this basin may also be linked to longer fluid residence time in a basin than the amount of time required to achieve chemical equilibrium and/or seasonal influence of ion-exchange on K in this basin. More data on other alkali metals (eg. Rb) and

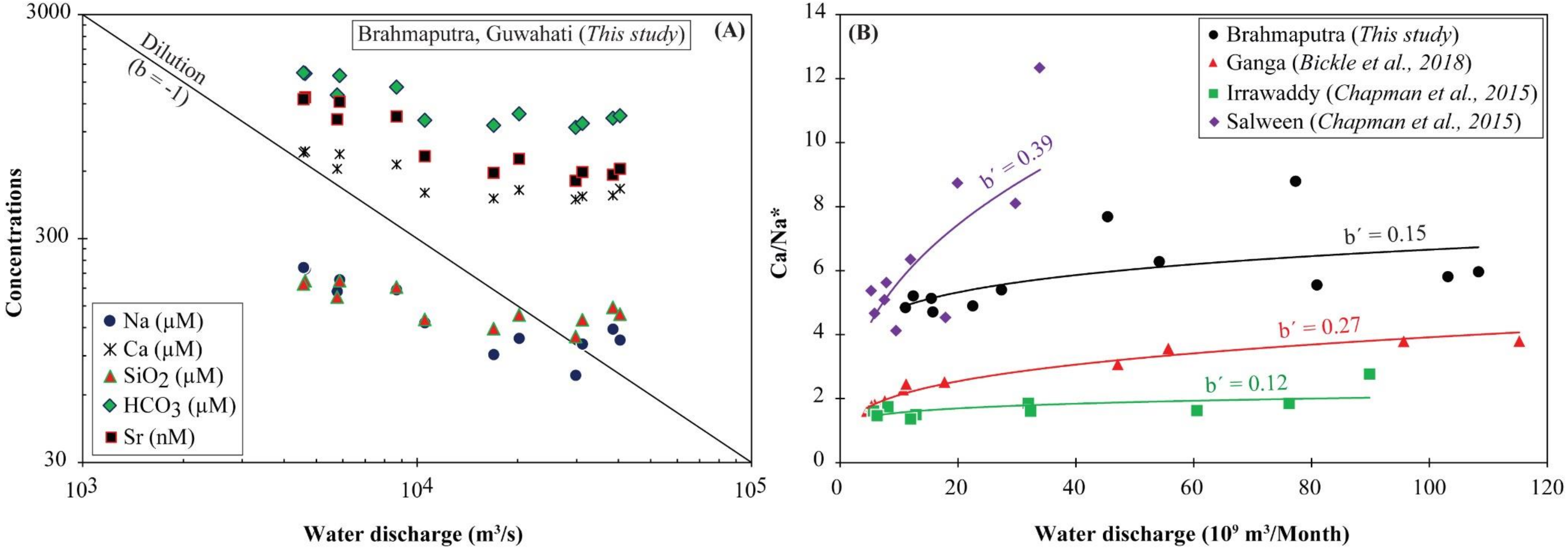

Figure 3.4. *(A) Co-variation between average monthly concentrations of major ions and water discharge data (in log-log scale) for the Brahmaputra River. The straight line represents the theoretical concentration-discharge trend for dilution effect (b = -1) only. In absence of real-time discharge data, average monthly water fluxes reported for a near-by GRDC site (Pandu) were used. (B) Variation of monthly-averaged Ca/Na* ratios with water discharge (Q) of the Brahmaputra River. For comparison, similar data reported earlier for other Himalayan rivers (Ganga (Bickle et al., 2018), Irrawaddy and Salween (Chapman et al., 2015)) are also plotted. Relatively lower Ca/Na* ratios, which are indicative of higher input from silicates than carbonates, are observed during non-monsoon periods. The coefficient (b'-values) from the power-law regression fit, Ca/Na* = $Q^{b'}$ for these trends are also shown.*

their seasonal trends can provide better clues about this propositions on seasonality of K concentrations.

We have also investigated the monthly variation of Ca/Na* (where Na* = Na-Cl, which should reflect the rain-corrected Na concentration) with respect to the water discharge (Fig. 3.4B) to understand seasonality in chemical weathering, if any, for the Brahmaputra. The characteristic Ca/Na* ratio for carbonates (50 ± 20; Millot et al., 2003) and silicates (1.3 ± 0.7; Singh et al., 2005) from this basin are distinctly different, and hence, this ratio can provide clues on relative solute contributions from weathering of silicates and carbonates. The Ca/Na* ratio for the Brahmaputra River varies between 4.3 and 12.3, intermediate to that of their possible source rocks. Despite its higher water flux, the seasonality in Ca/Na* for the Brahmaputra River is relatively less pronounced (b' ~0.1) compared to other Himalayan rivers, viz. Ganga (Bickle et al., 2018), Irrawaddy and Salween (Chapman et al., 2015) at their outflows (Fig. 3.4B). Figure 3.4B also shows seasonality in the Ca/Na* ratios with relatively lower during the lean flow periods than that during the peak flow stages. Variation in the Ca/Na* in any river basin may result from (i) different relative solute contribution from weathering of its possible sources and/or (ii) significant loss of dissolved Ca due to calcite supersaturation. The exact role of these processes on the dissolved Ca/Na* variations is discussed in the following section.

Table 3.3: *Comparison of b-values of concentration (C) discharge (Q) relationship ($C = Q^b$) for different Himalayan and Tibetan rivers at their outflow.*

River	Ca	Mg	Na	HCO_3	Si	Data source
Brahmaputra	-0.21	-0.29	-0.38	-0.22	-0.18	Present study
Ganga	-0.10	-0.25	-0.36	-0.18	-0.02	Bickle et al., 2018
Irrawaddy	-0.16	-0.26	-0.26	-0.22	-0.10	Chapman et al., 2015
Salween	-0.06	-0.32	-0.39	-0.16	-0.02	Chapman et al., 2015
Changjiang	-0.12	-0.23	-	-0.12	-	Chen et al., 2002
Pearl	-0.33	-0.23	-	-0.22	-	Zhang et al., 2007
Global	-0.13	-0.18	-0.24	-0.12	-0.06	Moon et al., 2014

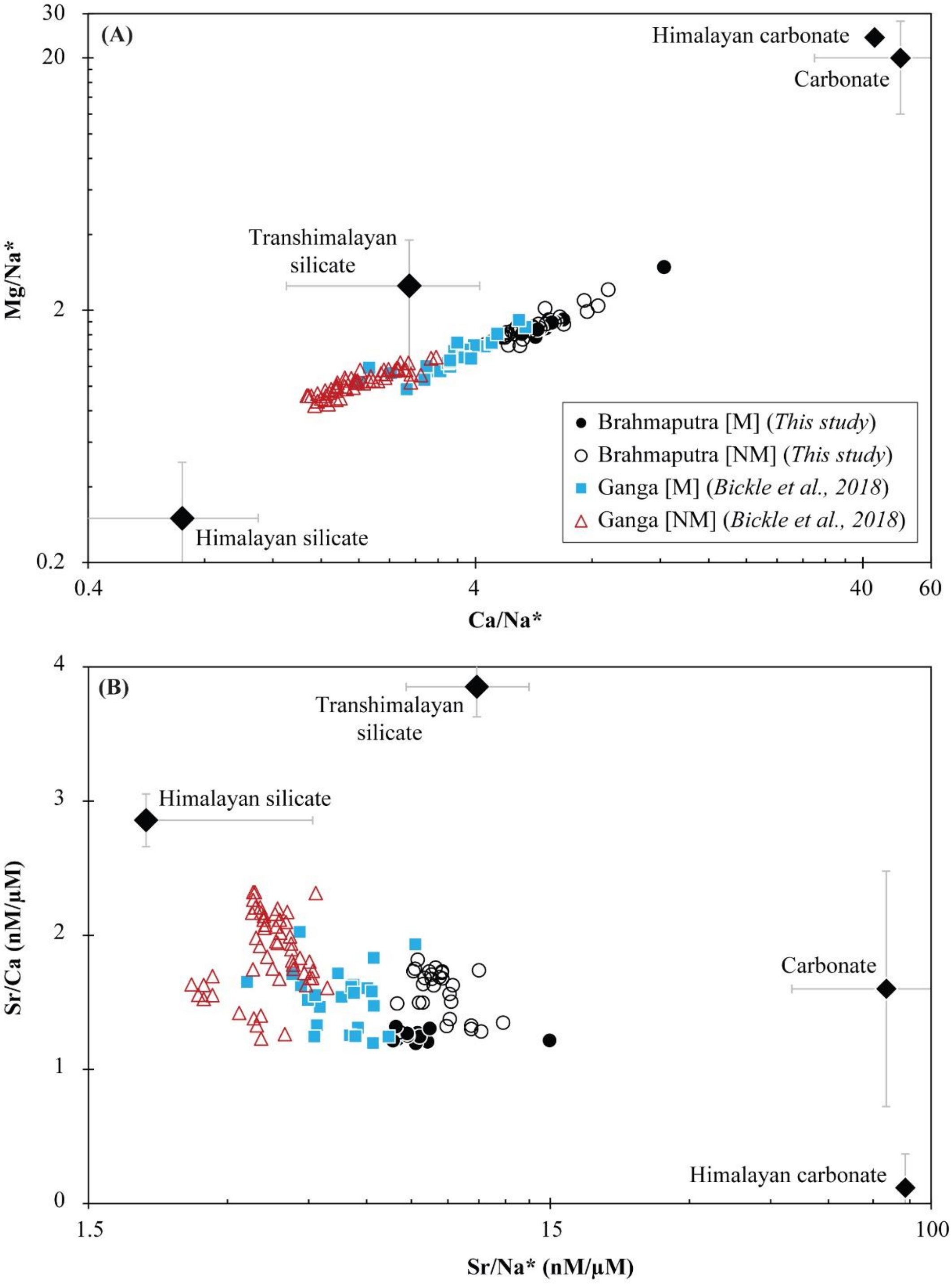

Figure 3.5. *Data comparison of monthly-averaged Brahmaputra River chemistry at Guwahati during 2016-17 (This study) and those reported earlier for 1999-2000 (Rai and Singh; 2007). No significant change in major ion compositions was observed during last ~20 years.*

A mixing diagram between Ca/Na* and Mg/Na* of the Brahmaputra samples has been plotted (Fig. 3.5A) in order to better constrain the sources and their seasonal contribution. The major sources of riverine solutes for the Brahmaputra River are carbonates and silicates from the Himalaya and Trans-Himalaya; their average compositions are also included in Fig. 3.5A. All the data from this study fall well within the mixing zone of these possible sources. These data, however, do not show any systematic seasonal change in relative contributions from their sources. A similar mixing trend was also observed between Sr/Ca and Sr/Na* ratios (Fig. 3.5B) with no appreciable seasonality. In addition to silicate and carbonate contributions, the data distribution in the Sr/Ca and Sr/Na* plot requires an additional source with relatively lower values. We, based on significant Ca-SO_4 and Sr-SO_4 correlations (cf. section 3.2), hypothesize gypsum dissolution as one of these additional sources which can supply an appreciable amount of Ca and Sr to the streams. We recognize here that these correlations with dissolved sulfates can also be attributed to oxidative weathering of sulfides in the basin (Galy and France-Lanord, 1999). However, this proposition could not be evaluated in this study due to the lack of suitable proxy data (such as pH, $\delta^{13}C$, and $\delta^{34}S$) for this process. It is worth mentioning here that the Sr concentrations of the Gypsum from the Himalayas (1027 µg/g; Singh et al., 1998) were reported to be significantly higher than that of the continental crust (320 µg/g; Rudnick and Gao, 2003). An appreciable amount of solute supply through evaporite dissolution to the Himalayan rivers has also been invoked by Krishnaswami et al. (1999) to explain the missing source for the Ca/Sr-$^{87}Sr/^{86}Sr$ covariance for the Ganga headwaters. A hint for possible solute supply from gypsum to the Brahmaputra also comes from the Sr/Ca-Ca plot (Fig. 3.6), which shows higher Sr/Ca ratios for samples with high Ca content. A general increase in Ca in river waters should decrease the Sr/Ca ratios, which is clearly not the case for the Brahmaputra. The lowering of the Sr/Ca ratio can arise due to (i) supply of Sr and Ca from a source with relatively lower Sr/Ca ratios than other major sources and/or (ii) removal of Ca due to calcite supersaturation. A significant linear correlation between Ca and Sr concentrations (Fig. 3.6) indicates their similar sources and also rules out any preferential loss of Ca during calcite precipitation. The calcite lattice preferentially favours more incorporation of Ca (than Sr) into the lattice, and hence, the Ca removal via supersaturation should perturb the linear Ca-Sr trend, which is clearly not the case for the Brahmaputra (Fig. 3.6). Efforts were also made to compute the calcite supersaturation indices (CSI) to assess the removal of Ca, if any, from the Brahmaputra River system. The pH and temperature data for the present samples were not available, and hence, the CSI could not be calculated for the present dataset. We, however, used earlier reported data for Brahmaputra samples at its outflow (at Chilmari) during two different seasons (Galy and France-Lanord, 1999). The CSI values for these samples are found to be under-saturated (-0.66) during monsoon and supersaturated (0.41) during the non-monsoon period. Although the non-monsoon samples show positive CSI values, this is not a sufficient condition to establish the removal of Ca from the river as calcite precipitation in a basin depends complicatedly on CO_2 release during water flow and the presence of nucleation to initiate the precipitation (Szramek and Walter, 2004). There exists a lack of evidence to support calcite precipitation in the Brahmaputra basin, and hence, we are unsure of Ca loss from this river water. The exact extent of Ca removal through calcite precipitation can be best assessed through stable Ca isotopic study of the water samples.

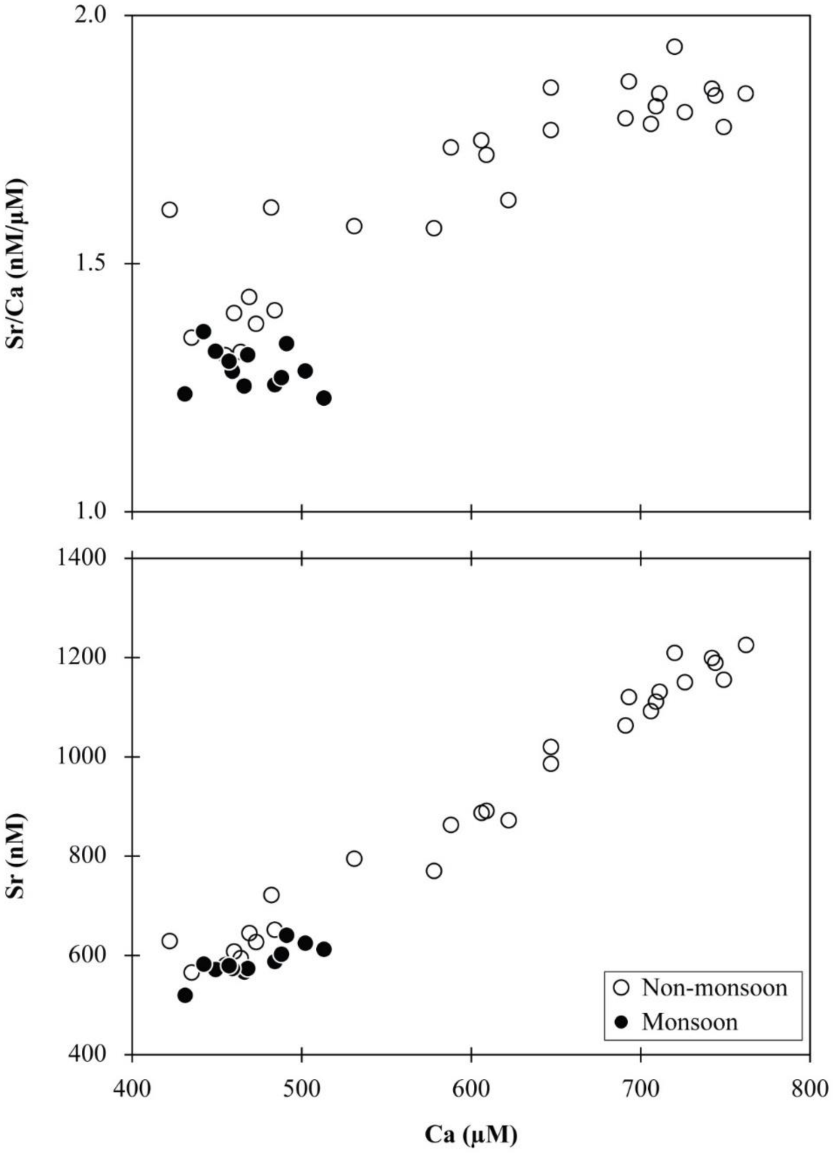

Figure 3.6. *Correlation plots between (A) Ca and Sr/Ca, and (B) Ca and Sr for the Brahmaputra River. A strong linear trend between Ca and Sr points to their similar sources and also, minimal removal of Ca through calcite precipitation.*

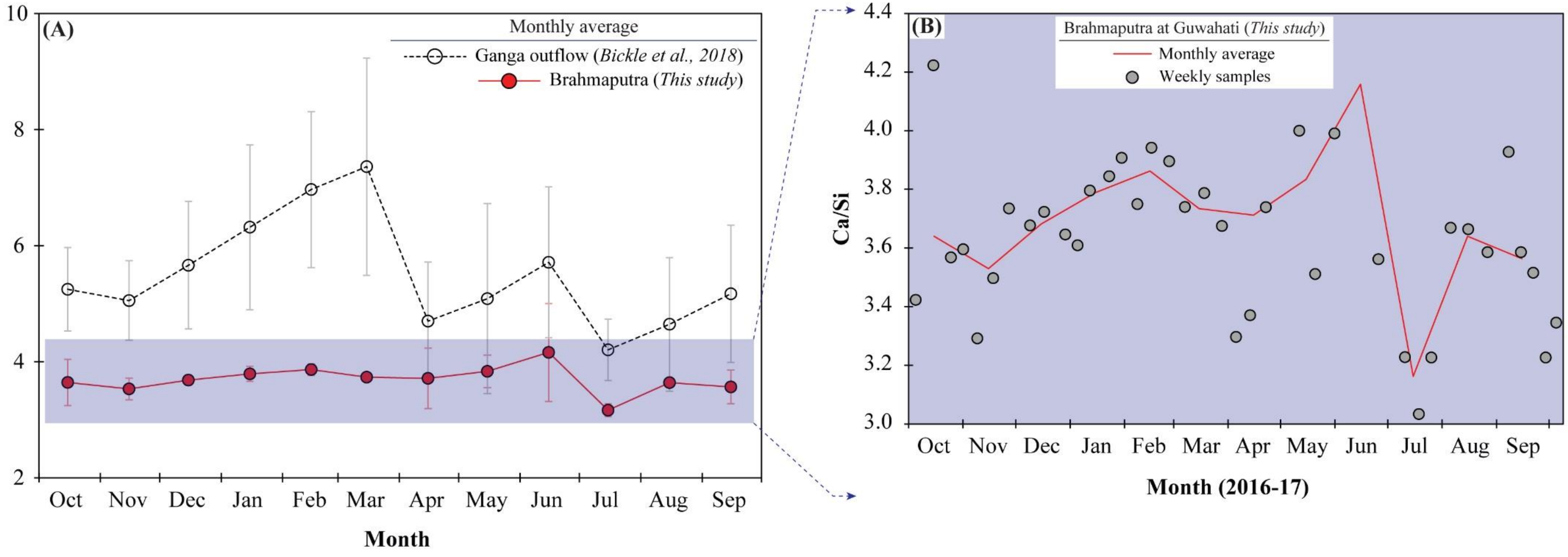

Figure 3.7. *(A) Comparison of average monthly variations in Ca/Si ratios for the Brahmaputra (This study) and Ganga (at Farakka; Bickle et al., 2018) rivers. The average Ca/Si ratio for the Brahmaputra is about two times lower than that at the Ganga outflow. (B) The magnified seasonal Ca/Si trend for the Brahmaputra at Guwahati is shown. Despite of minimal temporal variability (~6 %), the Ca/Si ratio at Guwahati also shows seasonality similar to that of the Ganga.*

The temporal changes in the riverine Ca/Si ratio may also reflect the seasonality in the preferential weathering of minerals (Fig. 3.7). The riverine Ca is derived mostly from weathering of both silicates and carbonates, whereas the dissolved silica is supplied through silicate dissolution. These ratios, therefore, are likely to reflect the relative contribution from silicates and carbonates to the river system. The Ca/Si ratios, and their seasonal trends for both Brahmaputra (This study) and the Ganga (Bickle et al., 2018) rivers are compared in Figure 3.7A. The month-averaged Ca/Si ratios of the Brahmaputra (3.7 ± 0.2) are about two times lower than that of the Ganga (6 ± 1), indicating relatively higher contributions from silicate weathering at Guwahati. Further, the monthly-averaged Ca/Si ratios for the Brahmaputra show minimal variations (~6 %) compared to that of the Ganga outflow (~17%). The minimal Ca/Si variations are intriguing, considering the higher annual runoff for the Brahmaputra (0.9 m/yr; Islam et al., 1999) than that of the Ganga (0.4 m/yr; Rai et al., 2010). The Ca/Si ratios at Guwahati during the monsoon (3.6 ± 0.4) and non-monsoon (3.7 ± 0.1) seasons are indifferent. The monthly-averaged Ca/Si ratios for the Ganga outflow show marginally lower ratios during the monsoon (4.9 ± 0.7) than the non-monsoon (5.8 ± 1.0) samples (Fig. 3.7). The relatively lower ratios for the Ganga during monsoon seasons can be complicatedly controlled by (i) relatively higher weathering of carbonates (than silicates) during peak flow periods (Bickle et al., 2018; Tipper et al., 2006; Tripathy et al., 2010) and/or (ii) non-conservative behaviour of silica in the Ganga floodplains (Fontorbe et al., 2013).

3.3.2.1 Na/K Variations and possible causes*

The Na*/K ratios of the Brahmaputra River showed significant seasonal variations with relatively higher values during the lean flow compared to peak flow stages (Fig. 3.8). Available chemical data for both upper (for Trisuli; Galy and France-Lanord, 1999) and lower (Ganga outflow at Farakka; Bickle et al., 2018) reaches of the Ganga river also show similar seasonal trends. In addition to this trend, earlier reported time-series data for the Brahmaputra at Guwahati (Rai and Singh, 2007) also confirm strong co-variation between Na*/K and $^{87}Sr/^{86}Sr$ ratios (Fig. 3.9A) with higher $^{87}Sr/^{86}Sr$ values being observed for samples with higher Na*/K ratios. The seasonal trend in Na*/K is mostly driven by variability in Na concentrations (~300 % variations) than that of the K (~35 % variation). However, the buffer mechanism that regulates the chemostatic nature of K may also contribute to the overall Na*/K trends. The possible causes for Na*/K variation are (i) relative seasonal change in weathering of Na-rich (Albite, Augite) versus K-rich (Muscovite, K-feldspar) minerals (Garzanti et al., 2011), (ii)

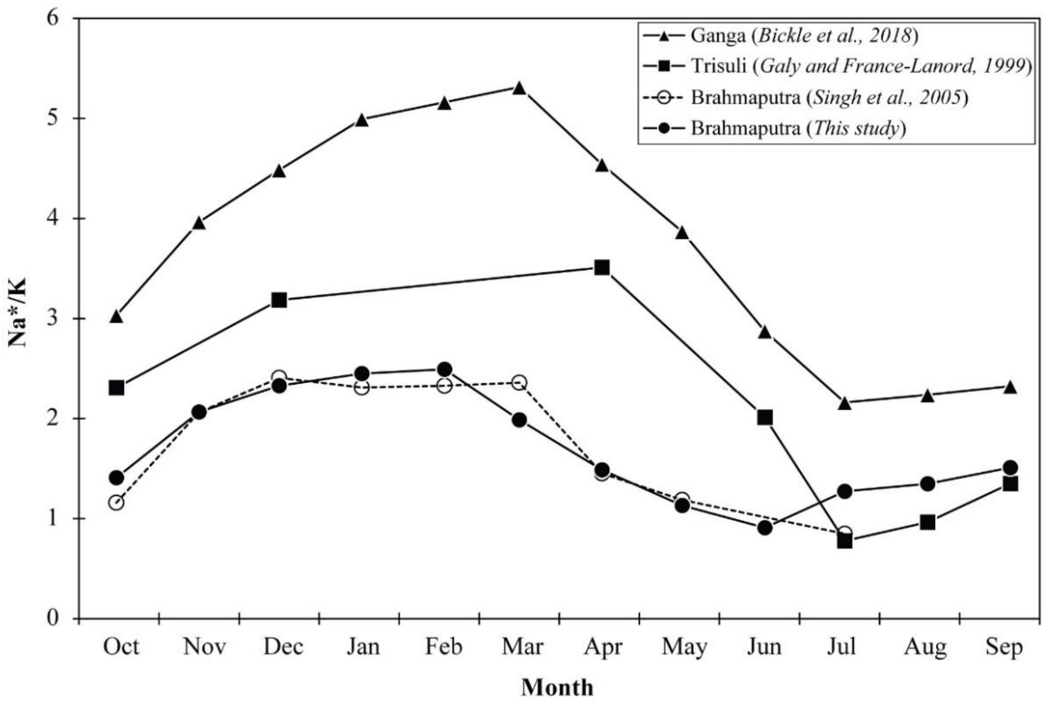

Figure 3.8. *Seasonality in Na*/K ratio for the Brahmaputra (Singh et al., 2005; This study) and Ganga (both at outflow (Bickle et al., 2018) and upper reaches (Galy and France-Lanord, 1999)) rivers. Systematic higher ratios are observed during the non-monsoon period, hinting at additional supply of Na from hot spring and/or non-chloride Na-salts.*

removal/addition of these elements during cation-exchange processes (Cerling et al., 1989), and/or (iii) supply of non-chloride Na from saline/alkaline soils and/or hot springs (Hren et al., 2009). As mentioned, one possible explanation for the seasonal Na*/K trend could be the relatively higher weathering of Na-rich minerals during lean flow phases. The weathering kinetics of Na-rich minerals (e.g., Albite) is relatively faster than those of K-rich (e.g., Muscovites) minerals (Lasaga, 1984; Lasaga et al., 1994). This proposition, however, is not consistent with the Na*/K-^{87}Sr/^{86}Sr trend (Fig. 3.9A) and also the expected weathering patterns due to higher water-rock interaction time during lean flow stages. The ^{87}Sr/^{86}Sr ratios of K-rich minerals, owing to their higher Rb concentrations, are expected to be highly radiogenic, and hence, preferential weathering of these minerals should lead to a higher ^{87}Sr/^{86}Sr and lower Na*/K ratios - which is in clear contrast to the observed pattern (Fig. 3.9A). Further, the higher water-rock interaction time during lean flow stages should promote relatively intense weathering of resistant K-rich minerals than the Na-silicates, which is not consistent with the observed higher Na*/K ratios during the non-monsoon period. This discussion confirms the minimal impact of preferential silicate dissolution on the Na*/K seasonality. Further, earlier studies have shown that riverine sodium can also come from cation-exchange processes, and

Cerling et al. (1989) have invoked the possible supply of about 34 % of Na in global rivers through this process. These processes are often found to be prominent in basins with significant abundances of smectite clays (Cerling et al., 1989). Available studies on the clay mineralogy of the Brahmaputra sediments confirm the minimal abundance of this clay type (Sarin et al., 1989) and hence, rule out this possibility as the cause for observed Na*/K trends.

We, therefore, hypothesize that the higher Na*/K ratio may have resulted from the supply from sodium carbonates and other non-silicate sources during the lean flow stages. This proposition draws support from the Na*/K-Na*/HCO_3 plot (Fig. 3.9B), which hints at a decrease in Na*/HCO_3 ratios and, therefore, an increase in HCO_3 concentration for lean flow months (Oct-Mar) with higher Na*/K ratios. This observation confirms a relatively higher supply from Na-HCO_3 source to the Brahmaputra during these months. Earlier studies have also reported the supply of these constituents from saline/alkaline soils to the surface runoff of Ganga river basins (Bickle et al., 2018; Rai et al., 2010). Although similar Na-salts (e.g., Borax, saline soils; Hren et al., 2007) have been reported for Brahmaputra basins, higher $^{87}Sr/^{86}Sr$ ratios for samples with enriched Na*/K values hints at appreciable solute supply from hot springs, which are highly radiogenic in Sr (~0.77 ± 0.02; Evans et al., 2001) compared to saline/alkaline soils (expected to have Sr isotopic value similar to river water; Rengarajan et al., 2009). The Sr isotopic data for the present samples were not available, and hence, we assessed the $^{87}Sr/^{86}Sr$ and Na*/HCO_3 co-variation for the Brahmaputra River using the earlier reported dataset (Rai and Singh, 2007). This co-variation showed a linear trend showing higher $^{87}Sr/^{86}Sr$ ratios for samples with higher Na*/HCO_3 ratios. The seasonality of Na*/K in the Brahmaputra basin seems to be driven mostly by appreciable solute supply from the hot spring to the river system. The lower Na*/K ratios and hence, the lesser influence of hot springs during monsoon is attributable to dilution of this input during peak flow stages. The seasonal impact of hot springs on the Na*/K ratio of Himalayan rivers is also evident from the time-series data reported for the Trisuli river from the upper reaches of the Ganga basin (Galy and France-Lanord, 1999; Evans et al., 2004). Compilation of these datasets shows a significant relationship between Na*/K and Ge/Si (Fig. 3.9C) for this river system from the upper reaches of the Ganga system. Ge/Si ratios being a reliable proxy for hot spring flux (Evans and Derry, 2002; Evans et al., 2004), this correlation confirms the influence of hot springs in regulating the seasonal changes in Na*/K for these Himalayan streams. We, however, could not evaluate similar co-variation between Na*/K and Ge/Si ratios for the Brahmaputra River due to the lack of dissolved Ge data.

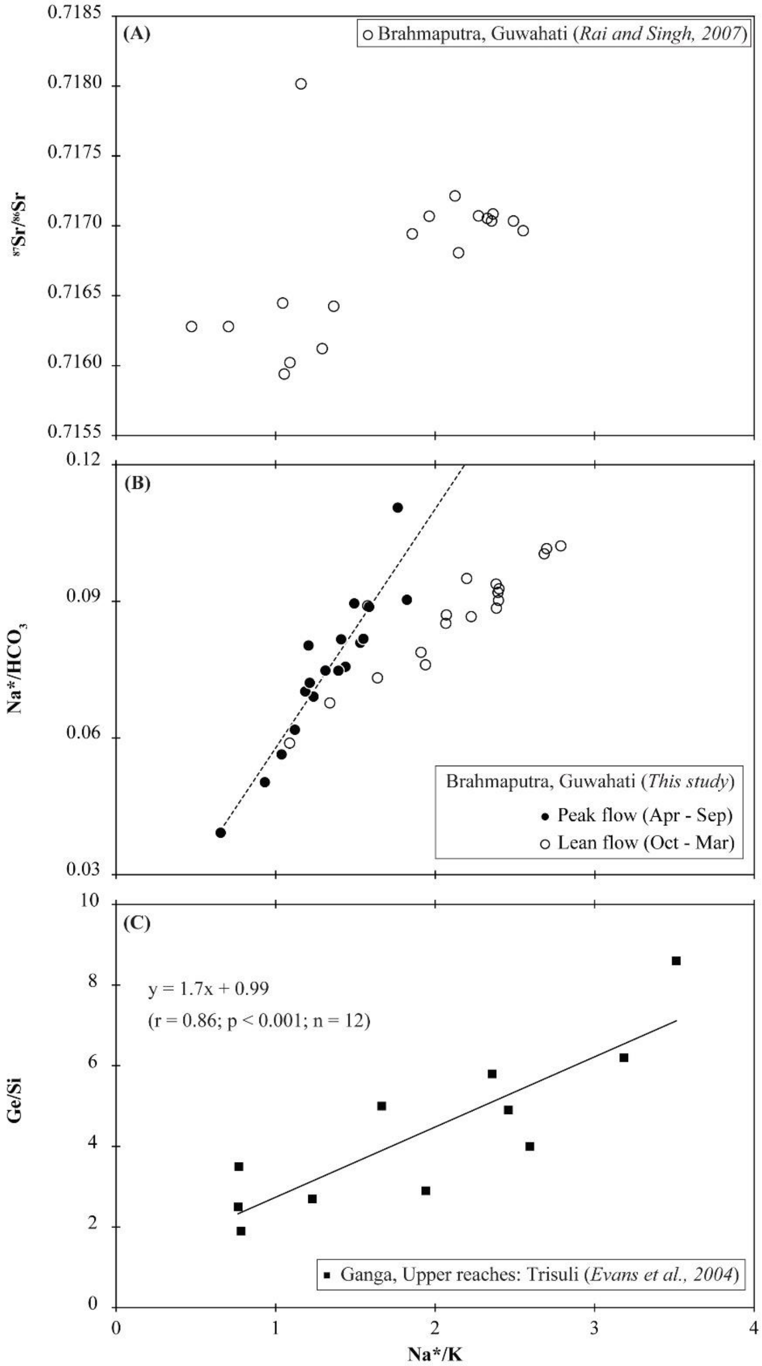

Figure 3.9. *(A) Earlier reported Na*/K and* $^{87}Sr/^{86}Sr$ *data for Guwahati (Rai and Singh, 2007) confirms relatively more radiogenic Sr isotopic composition for the lean flow samples. The Sr isotopic compositions for hot spring are reported to be higher than the alkaline soils. (B) Co-variation between Na*/K and Na*/*HCO_3 *at Guwahati (Present study) indicates that the lean-flow samples are characterized with relatively higher Na*/K and lower Na*/*HCO_3 *(hence, higher* HCO_3 *values). Deviation from the linear fit for the peak-flow samples hint at relatively higher supply from Na-*HCO_3 *type sources. (C) With a similar seasonal Na*/K trend, the samples from upper reaches of the Ganga (Trisuli) show strong co-variation between Na*/K and Ge/Si (an indices for hot spring supply; Evans et al., 2004). Data on Ge/Si ratio was not available for the Brahmaputra River to assess similar co-variations.*

3.3.3 Source-apportionment modelling

Earlier studies have successfully employed both forward (Galy and France-Lanord, 1999; Krishnaswami et al., 1999) and inversion (Gaillardet et al., 1999; Négrel et al., 1993; Tripathy and Singh, 2010) methods involving chemical mass balance equations to apportion relative contributions form possible sources of riverine solutes. The forward approach mainly employs an element mostly derived from silicate sources (e.g., Na, K, Si, or Mg) and average cationic ratios released during silicate weathering to estimate the silicate-derived cations (Krishnaswami and Singh, 1998). Riverine Na has been frequently used for this purpose, and its employment in forwarding modeling relies on the assumptions that (i) all the non-silicate sources of dissolved Na to the river are NaCl type, and (ii) the release of cationic ratios during silicate weathering is congruent in nature. The use of Na* as a silicate proxy, however, gets complicated for the basins with its supply also through non-silicate sources (Das et al., 2005; Rai et al., 2010; Rengarajan et al., 2009). In an earlier discussion based on Na*/K variation, we have demonstrated an appreciable supply of dissolved sodium to the Brahmaputra from sodium-salts (Hren et al., 2009) and/or hot springs (Craw et al., 2005) and hence, employment of Na* as a proxy for silicate weathering in this basin is challenging. Hren et al. (2009) have successfully used Si as a proxy for silicate weathering to compute the silicate weathering rate in the upper reaches of the Brahmaputra. This approach draws support from Singh et al. (2005), where the authors have demonstrated the dominancy of plagioclase conversion into kaolinites which releases a Si/Na ratio of ~2.0 to the river. We adopted this approach (Hren et al., 2009) for the present dataset to evaluate the reliability of this approach in constraining temporal changes in the relative contribution of cations from silicate dissolution. The estimated silicate-derived cation (Cat_S) values using this approach vary from 28 % to 40 %, with higher values during the monsoon samples. Interestingly, this seasonal pattern of silicate weathering is in clear contrast with earlier studies that showed relatively lower weathering of silicates during the monsoon period (Chapman et al., 2015; Krishnaswami et al., 1999; Tipper et al., 2006; Tripathy et al., 2010). Using the same forward method, a similar trend was also observed for an earlier reported dataset for Guwahati (Rai and Singh, 2007), which is in contrast with a robust proxy ($^{87}Sr/^{86}Sr$) for chemical weathering. This discrepancy hints at the non-conservative behaviour of dissolved Si and hence, may not be the suitable index for silicate weathering estimation at a seasonal scale. Non-conservative behaviour of silica in this basin may arise due to (i) seasonal change in plagioclase conversion intensity to kaolinites, (ii) the release ratio of Si/Na for basin-wide weathering reactions may not be ~2.0 and/or (iii) loss/gain of dissolved silica during various hydrological processes. Although our data do not suffice to establish this non-conservativeness of silica, some of these suggested weathering processes and their seasonality may also explain the near-chemostatic behaviour observed for silica for the Brahmaputra basin (Fig. 3.4A). It is worth mentioning here that our proposition on the non-conservative behaviour of Si is consistent with an earlier observation of silica removal from the Ganga floodplains by the secondary mineral formation and/or biological silica production (Fontorbe et al., 2013). The above discussion, therefore, raises concern in employing Si or Na* as reliable silicate indices for the Brahmaputra basin in its lower reaches.

3.3.3.1 Inverse modelling

An inverse method has been adopted in this study to estimate relative contributions from major solute sources to the Brahmaputra River at Guwahati (Gaillardet et al., 1999; Millot et al., 2003; Moon et al., 2007; Negrel et al., 1993; Wu et al., 2005). The computational code developed by Tripathy and Singh (2010) for inverse modelling has been used here. Details on the mathematical framework and optimization algorithm of this method have been provided in Tripathy and Das (2014). Briefly, the model finds the best fit for a set of mass balance equations (Eq. 3.1-3.2) relating Na-normalized ratios of elements, X (= Cl, Ca, Mg, Sr and HCO_3) of river water and its possible sources.

$$\left(\frac{\mathrm{X}}{\mathrm{Na}}\right)_{\mathrm{riv}} = \sum_{\mathrm{i}=1}^{4} \left(\frac{\mathrm{X}}{\mathrm{Na}}\right)_{\mathrm{i}} \times f_i \qquad (3.1)$$

$$1 = \sum_{\mathrm{i}=1}^{4} f_i \qquad (3.2)$$

where *i* represents the four major solute sources, viz. rain, silicate, carbonate, and hot springs, the subscript *riv* stands for river water composition. The f_i stands for a fraction of Na supplied from the source, *i*. The equations (3.1-3.2) can be rewritten in matrix form as *d = g(p)*, where *d* and *p* stand for matrices of data and model parameters. The measured data are expected to follow Gaussian distribution, whereas the model parameters are assumed to follow log-normal distribution (Gaillardet et al., 1999). The inverse model follows an iterative approach to find the best fit for the model parameters, which satisfies Eq. (3.1-3.2) with the least residual (Tarantola, 2005). The iteration loop starts from a set of *a-priori* data for model parameters and optimizes using a quasi-Newton optimization algorithm to find the *a-posteriori* model parameters and associated uncertainties. The *a-posteriori* results from the inversion model have been included in Table 3.4.

Average chemical compositions for these sources are constrained from available literature information (Evans et al., 2001; Galy and France-Lanord, 1999; Millot et al., 2002; Singh et al., 2005, 2006) and are listed in Table 3.4. The rainwater chemistry is largely influenced by seawater aerosols and hence, mostly NaCl type (Berner and Berner, 2012). The source contribution estimated for "rain" in this model, therefore, is inclusive of all sources with similar compositions, such as halites and saline soils. In addition to rain and silicates, dissolved Na can also come from its carbonate/bicarbonate and sulfate sources (hot springs and alkaline soil). The model estimation for "hot springs" quantifies contribution from these salts. Moon et al. (2007), owing to similar elemental ratios for carbonates and gypsum, have used an average composition in their inverse modelling to find the combined contribution from these sources to the Red River in Vietnam. A similar approach for these Ca-rich sources has also been adopted in this study. Further, the present source-apportionment model assumes that all dissolved K is of silicate origin (Galy and France-Lanord, 1999).

Table 3.4: *A-priori values for the model parameters used in the inverse model. For comparison, the a-posteriori ratios obtained from the model are also listed.*

	Cl/Na	**Ca/Na**	**Mg/Na**	**Sr/Na (×10^3)**	**HCO_3/Na**	**Ref.**
A-priori Information						
Rain	0.74 ± 0.1	2.2 ± 0.11	0.6 ± 0.1	2.1 ± 0.5	6.8 ± 0.5	(1)
Silicates	0	1.3 ± 0.7	1.0 ± 0.5	4.5 ± 2.3	4 ± 2	(2, 3)
Carbonates*	0	50 ± 20	20 ± 8	80 ± 30	100 ± 40	(4)
Hot-springs^	1.2 ± 0.3	4.4 ± 0.8	0.02 ± 0.01	1.2 ± 0.13	10 ± 4	(5)
A-posteriori Information						
Rain	0.8 ± 0.1	2.2 ± 0.11	0.64 ± 0.10	8 ± 1	6.4 ± 0.5	(6)
Silicates	0	0.7 ± 0.3	0.8 ± 0.1	2.7 ± 0.6	1.6 ± 0.6	
Carbonates*	0	19 ± 2	5.0 ± 0.5	20 ± 2	41 ± 4	
Hotsprings^	1.1 ± 0.1	4.3 ± 0.7	0.02 ± 0.01	1.1 ± 0.1	7 ± 2	

**Including gypsum contribution; ^Including saline-alkaline soil contribution;*
(1) Galy and France Lanord, 1999; (2, 3) Singh et al., 2005, 2006; (4) Millot et al., 2002;
(5) Evans et al., 2001; (6) This study.

Results from the inversion method on the amount of cations supplied from rain (11 ± 4 %), silicates (27 ± 4 %), carbonates (53 ± 7 %), and hot springs (10 ± 4 %) during the sampling period are listed in Table 3.5. The rain-derived cations (in %) is higher for non-monsoon (13 ± 3 %) than that of the monsoon (6 ± 1 %) samples. Consistent with this, the Sr supply through rain is also found to be higher during the non-monsoon seasons. The relatively lower cation supply from rain during monsoon is attributable to the intense supply of solutes via weathering in this period. Relative contributions from the hot springs to the dissolved solute load of the Brahmaputra are significantly lower and do not show any significant temporal change (Table 3.5). It is worth to mention although the relative contribution of rain and hot spring are statistically similar, however during the winter months, the contribution from hot springs is much lower than the rain. Although the exact reason is not very clear, lower supply from hot springs could be linked to the frozen ground conditions in the upper reaches of the Brahmaputra basin during the winter months. Additionally, some part of the basin also receives rainfall through western disturbances during the winter months, which further can increase rain contribution. Although we notice a proportionally higher carbonate contribution to the dissolved cations and Sr during the monsoon (56 ± 7 % (Cat_{carb}); 57 ± 6 % (Sr_{carb})) when compared to non-monsoon (51 ± 7 % (Cat_{carb}); 43 ± 8 % (Sr_{carb})) seasons, these estimates are statistically indifferent (Fig. 3.10). The broad seasonal trend of higher carbonate contribution during the monsoon season is consistent with earlier reported observations for the Himalayan rivers (Bickle et al., 2018; Rai and Singh, 2007; Tripathy et al., 2010). This observation has often been linked with faster dissolution kinetics of carbonates and lower water-rock interaction time during monsoon, which resists dissolution of resistant silicate minerals (Krishnaswami et al., 1999; Tipper et al., 2006).

The estimated Cat_s for Guwahati varies between 15 and 33 %, which are systematically lower than that reported earlier for this location using a forward method (35-52 %; Rai and Singh, 2007). This difference can be attributed to the over-estimation of Cat_s in the latter case due to the supply of non-chloride Na from hot springs / alkaline salt deposits. The amount of silicate-derived cations (Cat_s) at Guwahati varies between 102 and 406 µM, with a discharge-weighted value of 212 µM. The temporal trend of Cat_s (Fig. 3.10A) shows no distinct difference between the monsoon (26 ± 4 % (Jun-Sept)) and post-monsoon (27 ± 3 % (Oct-Feb)) samples; however, the Cat_s for the month of May (22 ± 2 %) is found systematically lower. The decline in Cat_s during the month of May could be an impact of glacial inflow during this summer month on the weathering pattern. Water chemistry during May showed a decrease in TDS and all other chemical constituents (Table 3.1), pointing to a possible rise in water discharge compared to previous months. This additional increase in water discharge is possibly from the glacial flux, which is expected to weather freshly-exposed surfaces and minerals with faster dissolution kinetics. The observed Cat_s trend is also consistent with that observed for the Sr_s (Fig. 3.10B).

Table 3.5: *Results from inverse modelling on relative contributions of dissolved cations and Sr concentrations from various possible sources.*

Sample ID	Relative supply of cation from (%)				Relative supply of Sr from (%)			
	Rain	Silicates	Carbonates	Hot-spring	Rain	Silicates	Carbonates	Hot-spring
BMP16/01	9 ± 2	24 ± 2	59 ± 6	10 ± 3	23 ± 7	22 ± 5	54 ± 8	2 ± 1
BMP16/02	9 ± 2	21 ± 2	61 ± 7	10 ± 3	23 ± 7	18 ± 4	58 ± 9	2 ± 1
BMP16/03	11 ± 2	24 ± 2	59 ± 6	8 ± 2	25 ± 7	22 ± 5	49 ± 7	2 ± 1
BMP16/04	11 ± 2	25 ± 2	59 ± 6	6 ± 2	25 ± 6	22 ± 5	48 ± 7	1 ± 1
BMP16/05	13 ± 2	28 ± 3	53 ± 6	8 ± 3	28 ± 7	25 ± 5	43 ± 6	2 ± 1
BMP16/06	13 ± 2	27 ± 3	55 ± 6	7 ± 2	28 ± 7	24 ± 5	43 ± 6	1 ± 1
BMP16/07	17 ± 2	30 ± 3	38 ± 5	15 ± 4	37 ± 9	29 ± 6	31 ± 5	3 ± 1
BMP16/08	13 ± 2	27 ± 3	55 ± 6	7 ± 2	28 ± 7	24 ± 5	43 ± 6	1 ± 1
BMP16/09	13 ± 2	27 ± 3	57 ± 6	5 ± 2	26 ± 6	23 ± 5	44 ± 7	1 ± 1
BMP16/10	15 ± 2	29 ± 3	49 ± 6	8 ± 3	32 ± 7	26 ± 6	38 ± 6	2 ± 1
BMP16/11	14 ± 2	28 ± 3	52 ± 6	6 ± 2	30 ± 7	25 ± 5	40 ± 6	1 ± 1
BMP16/12	14 ± 2	31 ± 3	49 ± 6	8 ± 3	29 ± 7	29 ± 6	38 ± 6	2 ± 1
BMP16/13	13 ± 2	31 ± 3	50 ± 6	7 ± 3	28 ± 7	29 ± 6	39 ± 6	1 ± 1
BMP16/14	21 ± 2	24 ± 3	42 ± 5	12 ± 3	44 ± 9	21 ± 5	33 ± 5	2 ± 1
BMP16/15	16 ± 2	32 ± 3	44 ± 5	10 ± 3	34 ± 8	29 ± 6	34 ± 5	2 ± 1
BMP16/16	15 ± 2	28 ± 3	48 ± 5	10 ± 3	33 ± 8	26 ± 6	38 ± 6	2 ± 1
BMP16/17	15 ± 2	29 ± 3	48 ± 5	9 ± 3	32 ± 7	26 ± 6	38 ± 6	2 ± 1
BMP16/18	17 ± 2	28 ± 3	47 ± 5	9 ± 3	35 ± 8	24 ± 5	36 ± 6	2 ± 1
BMP16/19	16 ± 2	26 ± 3	45 ± 5	10 ± 3	36 ± 8	23 ± 5	37 ± 6	2 ± 1
BMP16/20	13 ± 2	30 ± 3	49 ± 6	9 ± 3	28 ± 7	27 ± 6	40 ± 6	2 ± 1

Table 3.5: (*continue*)

Sample ID	**Relative supply of cation from (%)**				**Relative supply of Sr from (%)**			
	Rain	**Silicates**	**Carbonates**	**Hot-spring**	**Rain**	**Silicates**	**Carbonates**	**Hot-spring**
BMP16/21	12 ± 2	33 ± 3	37 ± 5	16 ± 3	30 ± 8	34 ± 7	34 ± 6	4 ± 1
BMP16/22	13 ± 2	30 ± 3	41 ± 5	16 ± 3	31 ± 8	28 ± 6	37 ± 6	4 ± 1
BMP16/23	11 ± 2	29 ± 3	49 ± 6	11 ± 3	25 ± 7	28 ± 6	43 ± 7	2 ± 1
BMP16/24	10 ± 2	19 ± 1	63 ± 7	10 ± 3	26 ± 7	14 ± 3	57 ± 9	2 ± 1
BMP16/25	8 ± 1	20 ± 2	64 ± 7	8 ± 2	20 ± 6	16 ± 4	60 ± 9	2 ± 1
BMP16/26	10 ± 2	25 ± 2	49 ± 5	17 ± 3	26 ± 7	23 ± 5	47 ± 7	4 ± 1
BMP16/27	9 ± 2	21 ± 2	59 ± 6	10 ± 3	23 ± 7	18 ± 4	55 ± 8	2 ± 1
BMP16/28	8 ± 2	15 ± 1	68 ± 7	8 ± 2	22 ± 7	9 ± 2	65 ± 10	2 ± 1
BMP16/29	5 ± 1	25 ± 2	60 ± 6	9 ± 2	15 ± 6	24 ± 5	62 ± 9	2 ± 1
BMP16/30	7 ± 2	30 ± 3	38 ± 5	25 ± 4	22 ± 8	34 ± 7	41 ± 7	7 ± 1
BMP16/31	6 ± 1	27 ± 2	55 ± 6	12 ± 3	18 ± 6	27 ± 6	55 ± 8	3 ± 1
BMP16/32	5 ± 1	28 ± 3	53 ± 6	12 ± 3	15 ± 6	31 ± 7	57 ± 8	4 ± 1
BMP16/33	5 ± 1	25 ± 2	58 ± 6	9 ± 2	15 ± 6	27 ± 6	60 ± 9	2 ± 1
BMP16/34	5 ± 1	25 ± 2	56 ± 6	10 ± 2	15 ± 6	27 ± 6	60 ± 9	3 ± 1
BMP16/35	6 ± 1	26 ± 2	57 ± 6	10 ± 2	16 ± 6	26 ± 6	58 ± 9	3 ± 1
BMP16/36	6 ± 1	25 ± 2	61 ± 6	7 ± 2	16 ± 6	24 ± 5	59 ± 9	2 ± 1
BMP16/37	5 ± 1	27 ± 2	58 ± 6	8 ± 2	15 ± 6	28 ± 6	58 ± 9	2 ± 1
BMP16/38	5 ± 1	27 ± 3	58 ± 6	8 ± 2	15 ± 6	28 ± 6	58 ± 8	2 ± 1
BMP16/39	6 ± 1	29 ± 3	54 ± 6	9 ± 2	16 ± 6	31 ± 7	53 ± 8	3 ± 1
BMP16/40	6 ± 1	28 ± 3	54 ± 6	9 ± 2	16 ± 6	30 ± 6	55 ± 8	2 ± 1

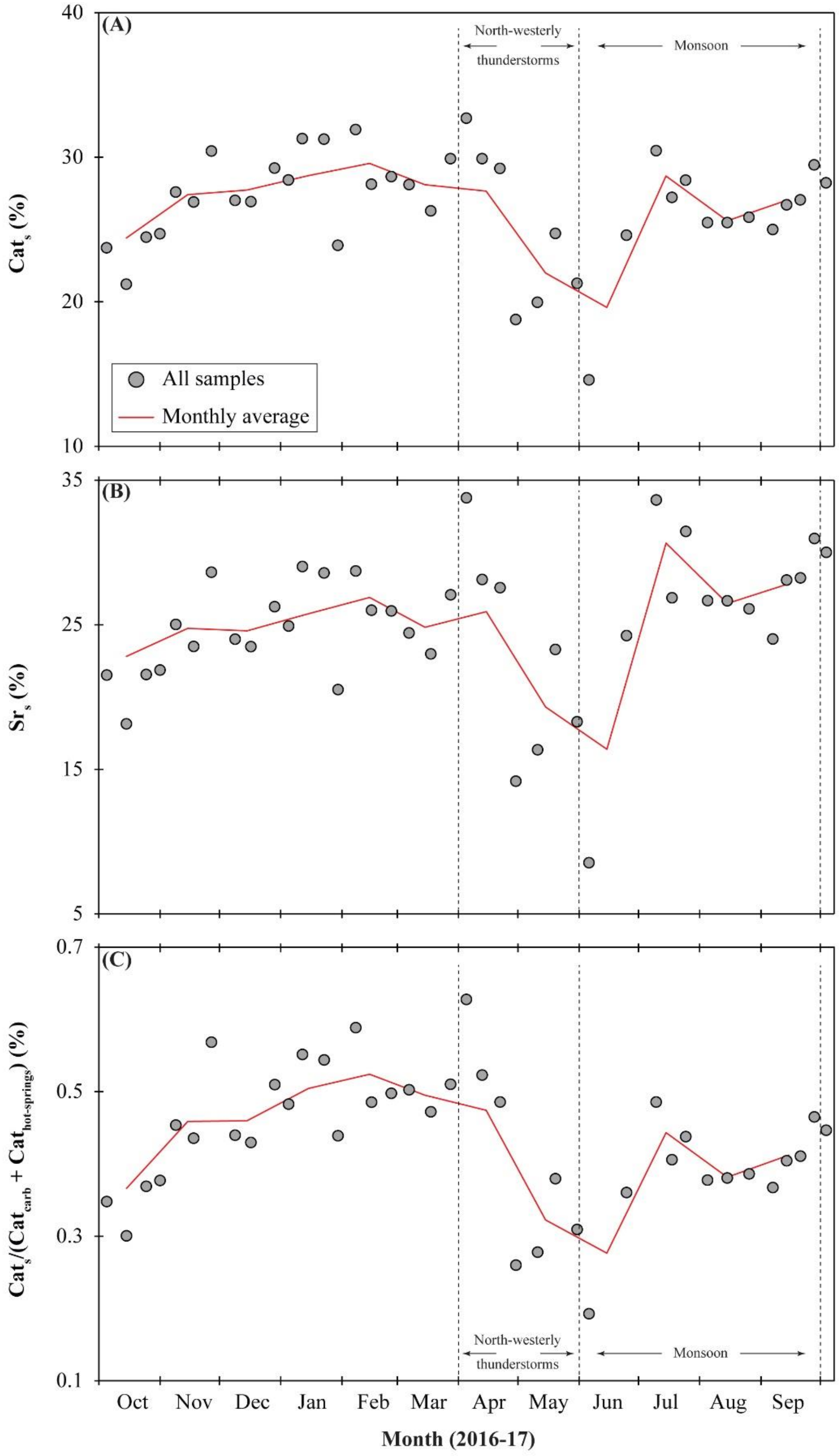

Figure 3.10. *Time-series variations of estimated (A) Cat$_s$, (B) Sr$_s$, and (C) Cat$_s$/(Cat$_{carb}$ + Cat$_{hot\ springs}$) for the Brahmaputra River at Guwahati. The seasonal averages of these parameters are found to be statistically the same. Systematically lower values are observed only for the month of May, attributable to the influence of glacial influx and related chemical weathering.*

However, the trends in Cat_s and Sr_s do not show any major change in the silicate weathering intensity during the monsoon and non-monsoon seasons. For a more critical evaluation, we have also investigated the $Cat_s/(Cat_{carb} + Cat_{hot\ springs})$ to assess seasonal change in relative contributions from silicates with that from weathering of other rock types. Although this ratio showed no statistical difference, its average for monsoon (0.4 ± 0.1) samples was systematically lower than the non-monsoon (0.5 ± 0.1) samples (Fig. 3.10C; Table 3.5). These mean values show relatively lower silicate weathering than weathering of other basinal rocks during the monsoon samples. These broad trends are consistent with that reported earlier for Himalayan rivers (Bickle et al., 2005, 2018; Chakrapani and Saini, 2009; Chapman et al., 2015; Rai and Singh, 2007; Singh et al., 2005; Tipper et al., 2006; Tripathy et al., 2010). However, in contrast to other Himalayan rivers, the temporal changes in source contribution from different minerals in the Brahmaputra are not statistically different, and hence, the climate (runoff)-weathering linkage in this basin seems less pronounced.

3.3.4 Controls on silicate erosion pattern

The flux-weighted average silicate erosion rate (SER; equation 3.3) for the Brahmaputra at Guwahati was 3.6×10^5 mol/km^2/yr. This weathering rate corresponds to 5.8 mm/kyr, considering an average density of silicate minerals as 2.6 gm/cc. SER for the Brahmaputra River basin is about 3 times higher than that reported as the global average for rivers (~2.0 mm/kyr; Gaillardet et al. 1999). Figure 3.11 compares the SER estimated during this thesis work for the Brahmaputra with that reported earlier for the upper Brahmaputra, Ganga, and the Indus basins (Gaillardet et al., 1999; Galy and France-Lanord, 1999; Rai et al., 2010; Singh et al., 2005).

$$\mathrm{SER} = \frac{Q}{A} \times (Na_S + K_S + Ca_S + Mg_S + SiO_2) \qquad (3.3)$$

where Q is the annual discharge, A is the river basin area, Na_s, K_s, Ca_s, and Mg_s are the silicate derived cations. The SER at Guwahati is observed to be about 10 times higher than that estimated earlier for the Tsangpo in the Tibet region. This distinctly lower weathering rate in the Tibetan part of the Brahmaputra (Fig. 3.11) is mainly due to the cold and dry climate, which does not favour the chemical weathering of minerals. Further, limited topographic variation with lower water-rock interaction time may also explain the lower erosion rate of the Tibetan region. This SER estimate for the Tibetan region is also lower compared to that for upper reaches of the Ganga (~5-11 mm/kyr; Dalai et al., 2002; Galy and France-Lanord, 1999). The higher SER for the upper Ganga can be attributed to conductive climate (temperature, rainfall), lithology, and higher physical erosion intensity in the Himalayas (than the Tibetan region) (Dalai et al., 2002). The average air temperature for the upper Ganga is higher by about 10 °C when compared to the Tibetan region (Fig. 3.11), which may also promote higher SER in the upper reaches of the Ganga (Dalai et al., 2002). The major controlling factors for SER in these Himalayan rivers have been often suggested to be climatic (runoff or temperature) and/or physical erosion. The observed minimal impact of short-term climate (runoff) on the seasonality of silicate weathering (Cat_s) at Guwahati points to the dominant role of physical erosion in regulating weathering of the Brahmaputra basin. Consistent with this proposition, the weathering fluxes of the Brahmaputra River at its outflow are disproportionally regulated by the ongoing rapid weathering near the eastern syntaxis. This localized area, corresponding to ~8 % area of the total drainage basin, supplies about ~40-45 % of sediment and ~20 % of dissolved load at the outflow (Singh and France-Lanord, 2002; Hren et al., 2007). Higher intensity of weathering at this spot can be due to higher runoff (~3 m/yr; Singh and France-Lanord, 2002) or higher physical weathering due to suddent change in basin slope (4.3 to 16.8 m/km; cf. Chapter 2; section 2.1.1). This runoff of the eastern syntaxis sub-basin (~ 3 m/yr) is significantly higher than the basinal runoff of the Brahmaputra (0.9 m/yr) and other Himalayan rivers (e.g., Ganga (0.4 m/yr); Irrawaddy (1.0 m/yr) and Salween (0.8 m/yr)). The seasonal trends of Cat_s and Ca/Si ratios at Guwahati point to the minimal role of surface runoff in regulating the SER. We, therefore, hypothesize that the steeper slope at and around the syntaxis promotes rapid mechanical weathering, which in turn intensifies the chemical weathering through the exposure of fresh minerals. This proposition on mechanical erosion supported SER is consistent with the earlier observed strong linkage between chemical and physical weathering for the Brahmaputra basin (Singh et al., 2005). In contrast, earlier studies have invoked the important role of mineral kinetics and climatic parameters in regulating weathering in fast-eroding terrains (Hilley et al., 2010; West et al., 2005). The exact cause for this difference can be best assessed with time-series water chemistry analyses of these streams, combined with proxy data (e.g., total suspended load and their chemical compositions) for corresponding physical weathering patterns.

3.4 Conclusion

Temporal variations in water chemistry of the Brahmaputra River (at Guwahati, India) have been investigated for a period of one year to infer seasonality in relative solute supply

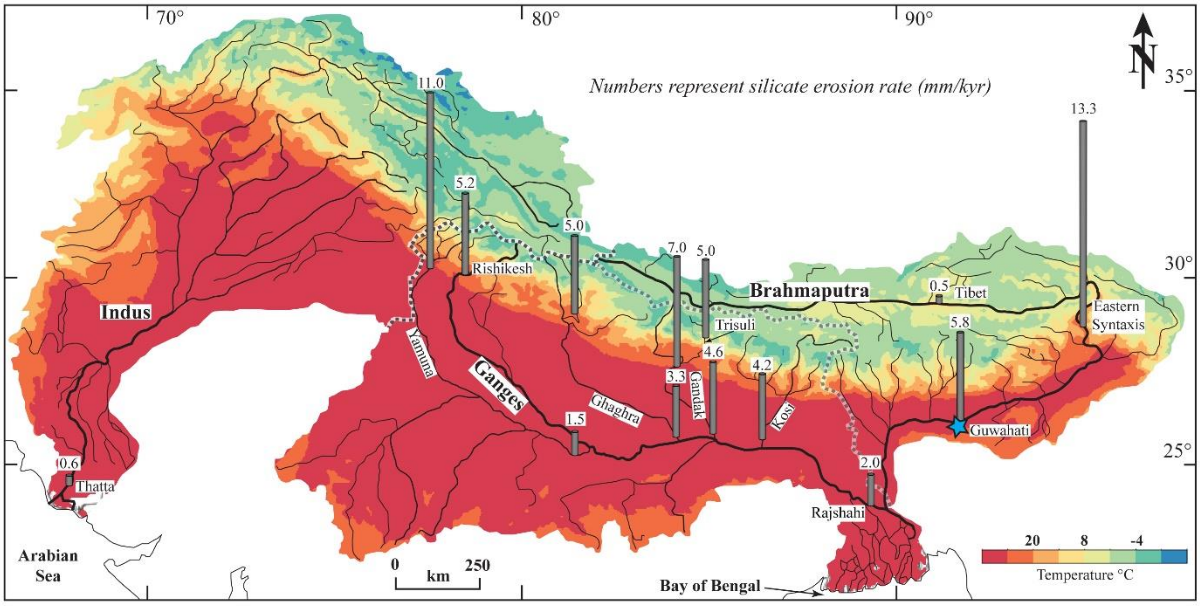

Figure 3.11. *Comparison of silicate erosion rates (SER; in mm/kyr) estimated for Brahmaputra at Guwahati with those reported earlier for the Himalayan (Brahmaputra (Singh et al., 2005), Ganga (Dalai et al., 2002; Galy and France-Lanord, 1999; Rai et al., 2010) and Indus (Gaillardet et al., 1999)) rivers. The spatial variation in SER for the Brahmaputra basin indicates that the erosion rate at Guwahati is largely regulated by intense chemical erosion at and around the eastern syntaxis compared to that in the Tibet region. For reference, spatial distribution of surface air temperature for the Himalayan basin during the present sampling period (Data source: https://giovanni.gsfc.nasa.gov/) is also provided.*

from different sources and its controlling factors. We have also used earlier reported time-series data for other Himalayan (e.g., Ganga, Salween, and Irrawaddy) rivers for comparison. Available major ion datasets from this and earlier studies for Guwahati show no major change in the water chemistry during the last ~50 years. Although the elemental abundances and their ratios for the Brahmaputra mainstream show seasonal changes, their degree of seasonality is less-pronounced at Guwahati when compared to those for other (Ganga and Salween) rivers. The monthly-averaged Ca/Si ratios for the Brahmaputra show minimal (~6 %) variation compared to that (~17 %) observed for the Ganga outflow. Relatively lower Ca/Si variability for the Brahmaputra, despite its (0.9 m/yr) higher runoff compared to the Ganga (0.4 m/yr), points to the minimal role of runoff in regulating the weathering pattern of this river. In contrast to these ratios, Na*/K ratios at Guwahati showed strong seasonality with higher values during lean flow stages. Comparison of Na*/K ratios with other chemical indices from this (HCO_3/Na*) and previous studies (^{87}Sr/^{86}Sr and Ge/Si) indicated relatively higher solute supplies from the hot springs to the Brahmaputra during lean flow periods. Inverse model calculations estimated Cat_s (26 ± 4 % and 27 ± 3 %) and Sr_s (26 ± 6 % and 24 ± 4 %) for monsoon and non-monsoon seasons, respectively, are statistically indifferent. However, the ratios of $Cat_s/(Cat_{carb} + Cat_{hot\ springs})$ show systematically higher ratios during the non-monsoon period, hinting at earlier observations of relative higher silicate contribution (compared to other rock dissolution) during lean flow stages. Observations from this study suggest that the weathering in the Brahmaputra basin is not limited by runoff/water-rock interaction time and is more regulated by rapid weathering at around eastern syntaxis with relatively steeper slopes and intense mechanical erosion than the upper reaches of the basin.

Chapter 4

Holocene Variability of the Erosion Pattern: Evidence from Marine Records

4.1 Introduction

Weathering of continental landmasses and subsequent transfer of the weathered materials to the ocean basins play a key role in controlling marine biogeochemistry. It also serves as a major sink for atmospheric CO_2 over the geological timescale and hence regulates the global climate cycle (Berner, 1995; Dupre et al., 2003; Raymo and Ruddiman, 1992; Walker et al., 1981). Several geological and climatic factors essentially control these low-temperature Earth-surface processes, which include lithology, tectonics, basin slope, runoff, temperature, and vegetation cover. Earlier studies have reported a strong relationship between climate and erosion rates, mainly when the climatic condition is relatively warm and humid (Hein et al., 2017; Lupker et al., 2013; Mirilaya et al., 2017; Wan et al., 2017). The Himalayan region, one of the most extensive geomorphic features on the Earth's surface, although contributes ~6-12 % of total sediments to the global ocean, diverging opinions exist on climate sensitivity of the erosion in the Himalayas (Clift et al., 2008; Galy and France-Lanord, 2001; Galy et al., 2008; Milliman and Meade, 1983; Rahaman et al., 2009; Tripathy et al., 2011, 2014). It has been documented that the climate in this region has varied significantly in the past (Fleitmann et al., 2003; Gupta et al., 2003; Herzschuh, 2006; Kathayat et al., 2017; Sarkar et al., 1990; Tiwari et al., 2005). Therefore, it is also expected to have variation in the erosion patterns in response to the change in climatic conditions. Several past studies have reported variable erosion rates in the past in response to climatic changes (Acharya and Chakrabarti, 2019; Clift et al., 2008; Rahaman et al., 2009; Tripathy et al., 2011, 2014). On the contrary, there is also evidence that suggests that the climate and erosional response are decoupled for the Himalayan river system (Burbank et al., 2003). Based on Sr-Nd isotopic composition, Kessarkar et al. (2003) and Goswami et al. (2012) showed that there is no major change in provenance for the eastern Arabian Sea sediments. Galy et al. (2008) have also reported similar observations for the Bay of Bengal sediments since the Last Glacial Maxima (LGM). The exact reason for this contrary response of climatic on erosion is not known.

In this chapter, efforts were made to reconstruct the tropical (chemical) erosion pattern during the Late Holocene period using geochemical (major and trace element) and isotopic ($\delta^{13}C_{org}$) signatures of two marine sediment cores (SSK40/GC10 and SSK40/GC06) collected from the eastern Arabian Sea. Additionally, the ocean redox state was also evaluated to understand the depositional conditions of these sedimentary records. The outcome of this study shows an insignificant change in erosion patterns during 7.2 to 2.6 kyr BP. However, after ~2.6 kyr BP, chemical erosion intensifies, whereas, during the last ~1600 years, this intensification is probably linked with the human-induced land-use patterns and agricultural activities. Variations in ocean redox state indices show a fluctuating bottom water condition. A shift from oxic to anoxic bottom water condition was observed since ~4.2 kyr BP. The results based on these two cores are presented below.

4.2 Sediment chemistry of the SSK40/GC10 core

The details and chronological information about the SSK40/GC10 sediment core from the eastern Arabian Sea are included in an earlier chapter (cf. Chapter 2, section 2.1.2). Briefly, this piston core was raised from a water depth of 50 m and radiocarbon ages of foraminifera samples constrain the chronology of this (~7150 - 800 yrs BP) core. The geochemical compositions of the SSK40/GC10 core sediments are provided in Table 4.1. The average organic carbon (TOC) concentration of the SSK40/GC10 sediments is 0.8 ± 0.4 wt% (n = 50), whereas the mean total nitrogen (TN) is 0.08 ± 0.03 wt%. The atomic TOC/TN ratios for these samples vary between 0.2 and 37.2. The average TOC/TN ratio is found (12 ± 5; after excluding two outliers) intermediate to that expected for marine (~6.6; Redfield, 1958) and terrestrial (≥ 20; Meyers, 1994) organic matter. The average S concentration in these samples is 3224 ± 1224 µg/g (n = 42), which is significantly higher than that reported for the upper continental crust (~610 µg/g; Rudnick and Gao, 2003). The carbonate concentrations of the SSK40/GC10 sediments vary between 23.7 and 74.3 wt% (mean 47 ± 8 wt%), which is comparable to or marginally lower than that reported for sediments from the eastern Arabian Sea (Acharya et al., 2015; Bhushan et al., 2001; Kessarkar et al., 2018; Kurian et al., 2013). Sediment dilution by these carbonate contents lead to lower concentrations of most of the major and trace elements in these (bulk) sediments, when compared to that observed for nearby river sediments and Thar dust (Table 4.2).

Concentrations of the major elements (Na (0.49-1.01 wt%), Mg (1.14-2.11 wt%), Al (2.37-5.08 wt%), K (0.49-1.18 wt%), Ca (17.69-30.79 wt%), Ti (0.26-0.50 wt%), and

Table 4.1: *Geochemical composition (bulk) of SSK40/GC10 core sediments.*

Sample ID	Age	Na	Mg	Al	K	Ca	Ti	Fe	V	Cr	Mn	Co	Ni	Cu	Zn	Rb	Sr	Mo	Ba	Th	U
	Yr BP				wt. %										µg/g						
GC10/0-1	806	0.51	1.52	3.54	0.63	20.9	0.34	3.28	52	108	312	12	41	23	50	36	1488	0.35	101	4.1	2.8
GC10/1-2	908	0.53	1.46	3.38	0.65	21.9	0.32	3.17	47	113	294	11	41	21	69	35	1445	0.34	99	3.7	2.8
GC10/3-4	1110	0.49	1.48	3.34	0.66	25.0	0.32	3.12	49	120	327	11	44	9	120	35	1615	0.73	81	3.3	2.8
GC10/6-7	1414	0.53	1.33	2.98	0.57	25.9	0.31	2.87	42	96	306	11	34	23	55	32	1749	0.54	33	3.3	2.5
GC10/8-9	1617	0.99	1.76	4.28	0.90	19.1	0.46	4.09	71	117	482	17	54	37	60	47	2086	0.98	66	3.9	3.5
GC10/10-11	1820	0.56	1.20	2.60	0.53	27.6	0.26	2.47	41	80	314	10	31	7	55	29	2119	0.51	11	3.1	2.5
GC10/12-13	2022	0.69	1.14	2.37	0.49	30.8	0.27	2.54	33	67	259	9	32	32	27	25	2182	0.46	35	2.4	2.2
GC10/13-14	2124	0.50	1.52	3.66	0.81	21.5	0.35	3.38	68	96	529	15	42	22	54	43	2699	0.74	36	3.7	3.0
GC10/15-16	2326	0.59	1.59	3.74	0.84	21.8	0.37	3.42	66	99	540	15	42	26	58	45	2711	0.49	36	3.8	2.9
GC10/17-18	2529	0.57	1.71	4.16	0.93	20.4	0.40	3.84	79	108	619	18	47	10	67	51	2938	0.58	59	4.4	3.2
GC10/20-21	2833	0.55	1.83	4.60	1.04	19.0	0.44	3.90	90	119	697	19	53	26	83	57	3182	0.43	77	5.2	3.5
GC10/23-24	3137	0.61	1.77	4.50	1.02	18.5	0.46	3.88	91	114	700	19	51	11	64	56	3202	0.57	70	4.7	3.3
GC10/26-27	3441	0.52	1.79	4.53	1.03	17.7	0.44	4.00	92	111	692	19	51	26	58	58	3238	0.45	53	5.0	3.2
GC10/27-28	3543	1.01	1.91	4.90	1.11	18.1	0.50	4.56	94	166	699	20	62	39	44	57	2957	0.84	91	4.6	3.1
GC10/28-29	3644	0.97	1.91	4.78	1.11	18.4	0.49	4.44	93	149	680	20	60	42	48	58	3039	0.67	75	4.7	3.1
GC10/29-30	3745	0.51	1.90	4.76	1.07	18.5	0.45	4.15	92	125	734	20	56	14	119	59	3297	0.73	80	5.2	3.2
GC10/30-31	3847	0.62	1.89	4.71	1.09	18.7	0.45	4.24	93	123	718	20	53	13	77	59	3329	0.67	66	5.1	3.2
GC10/31-32	3948	0.84	1.86	4.66	1.07	18.3	0.47	4.25	86	103	688	19	57	37	56	53	3049	0.41	103	4.4	2.9
GC10/32-33	4049	0.93	1.89	4.73	1.08	18.2	0.48	4.38	91	106	679	19	57	38	41	56	3026	0.50	65	4.6	3.0
GC10/33-34	4151	0.59	1.85	4.57	1.04	18.3	0.45	4.05	88	111	705	19	53	29	61	56	3243	0.42	68	4.9	3.1
GC10/35-36	4353	0.92	1.92	4.71	1.10	18.7	0.48	4.40	88	140	691	19	59	39	43	54	3019	0.52	70	4.6	3.0
GC10/36-37	4455	0.56	1.85	4.64	1.05	18.0	0.45	4.09	87	113	687	18	49	27	64	55	3046	0.31	57	4.9	2.9
GC10/39-40	4638	0.64	1.99	4.96	1.16	19.3	0.46	4.33	93	134	761	20	58	13	147	58	3266	1.06	91	4.8	3.2

Table 4.1 *(continued)*

Sample ID	Age	Na	Mg	Al	K	Ca	Ti	Fe	V	Cr	Mn	Co	Ni	Cu	Zn	Rb	Sr	Mo	Ba	Th	U
	Yr BP	wt. %							µg/g												
GC10/42-43	4762	0.58	1.89	4.56	1.04	18.4	0.45	3.94	87	115	662	19	50	27	66	55	3117	0.36	70	5.1	3.1
GC10/45-46	4886	0.55	2.00	5.03	1.14	20.1	0.48	4.42	90	113	691	20	51	28	76	55	3188	0.35	63	5.4	3.3
GC10/48-49	5010	0.87	1.98	4.82	1.13	18.4	0.48	4.48	92	106	705	21	60	38	43	57	3079	0.59	76	4.7	3.2
GC10/52-53	5174	0.57	1.98	4.77	1.10	19.4	0.46	4.23	87	115	708	19	50	25	75	53	3199	0.42	68	4.8	3.1
GC10/56-57	5339	0.64	2.08	5.08	1.15	19.6	0.47	4.29	93	120	710	20	52	13	64	59	3210	0.50	63	4.9	3.1
GC10/59-60	5463	0.59	1.94	4.79	1.09	19.3	0.46	4.21	86	111	690	18	49	26	56	53	3122	0.39	53	5.0	3.0
GC10/63-64	5628	0.68	1.95	4.89	1.12	19.2	0.46	4.21	89	110	711	19	53	12	65	57	3296	0.49	57	4.8	3.0
GC10/66-67	5752	0.55	1.97	4.82	1.12	19.5	0.47	4.16	90	123	755	19	54	26	69	58	3238	0.35	64	5.0	2.9
GC10/70-71	5917	0.59	2.03	5.00	1.15	19.5	0.48	4.49	93	126	774	21	56	13	148	58	3174	0.66	93	4.9	3.0
GC10/73-74	6040	0.59	1.99	4.89	1.14	18.9	0.45	4.36	86	127	662	19	59	25	344	56	3064	0.46	60	5.9	3.2
GC10/77-78	6205	0.64	1.92	4.77	1.11	18.2	0.44	4.22	85	110	685	19	50	12	84	56	3110	0.54	55	4.4	3.1
GC10/81-82	6370	0.57	1.95	4.76	1.09	18.5	0.47	4.16	90	119	712	18	49	26	78	54	3103	0.33	56	5.4	3.1
GC10/85-86	6535	0.63	1.93	4.80	1.08	18.4	0.47	4.11	88	115	677	18	49	12	71	54	3043	0.50	53	4.7	2.9
GC10/88-89	6659	0.61	1.94	4.79	1.07	18.7	0.46	4.13	90	114	722	19	50	28	60	53	3195	0.26	49	5.0	3.0
GC10/90-91	6711	0.57	1.98	4.76	1.09	19.5	0.47	4.21	88	113	696	19	49	25	53	55	3240	0.37	50	4.9	3.1
GC10/93-94	6745	0.65	2.09	5.07	1.16	19.4	0.48	4.37	92	119	731	20	51	12	62	58	3242	0.41	54	5.1	3.2
GC10/96-97	6779	0.55	2.04	4.97	1.13	18.6	0.46	4.47	91	119	694	20	50	24	68	55	3145	0.44	55	5.0	3.0
GC10/100-101	6824	0.61	1.94	4.80	1.08	19.0	0.47	4.20	85	113	700	18	48	26	56	52	3059	0.45	44	4.9	2.8
GC10/104-105	6870	0.58	2.09	4.98	1.15	19.5	0.48	4.51	93	132	737	20	55	13	148	57	3242	0.80	90	4.9	3.1
GC10/108-109	6915	0.56	2.04	4.85	1.11	18.9	0.47	4.46	91	115	707	20	54	25	57	58	3283	0.51	53	5.0	3.2
GC10/111-112	6949	0.51	1.97	4.93	1.10	20.0	0.48	4.40	88	110	687	18	50	28	75	53	3161	0.40	51	5.0	2.9
GC10/113-114	6971	0.61	2.11	5.02	1.18	19.5	0.48	4.72	93	117	729	21	54	12	74	57	3324	0.63	58	4.7	3.0

Table 4.1 *(continued)*

Sample ID	Age	Na	Mg	Al	K	Ca	Ti	Fe	V	Cr	Mn	Co	Ni	Cu	Zn	Rb	Sr	Mo	Ba	Th	U
	Yr BP	wt. %							µg/g												
GC10/117-118	7017	0.55	1.99	4.86	1.10	19.2	0.47	4.25	88	112	685	19	50	25	78	57	3148	0.37	53	5.2	2.9
GC10/120-121	7051	0.54	1.91	4.64	1.05	18.9	0.46	4.03	84	108	684	18	48	24	57	52	3123	0.35	54	4.8	2.9
GC10/123-124	7084	0.65	2.06	4.97	1.17	19.5	0.48	4.33	91	120	708	20	51	13	71	56	3334	1.76	62	4.9	3.0
GC10/126-127	7118	0.56	1.99	4.72	1.06	19.9	0.48	4.28	88	114	711	19	50	23	52	55	3340	0.41	44	4.9	3.0
GC10/129-130	7152	0.68	2.00	4.88	1.15	20.2	0.49	4.21	90	134	730	19	55	13	161	55	3276	0.83	98	4.4	2.9

Table 4.1 *(continued)*

Sample ID	Age	$CaCO_3$	TOC	TN	S	TOC/N
	Yr BP	wt. %				Atomic
GC10/0-1	806	56.3	1.01	0.12	0.14	9.5
GC10/1-2	908	59.8	0.89	0.12	0.13	8.5
GC10/3-4	1110	61.7	0.88	0.12	0.10	8.8
GC10/6-7	1414	64.5	0.68	0.10	0.16	8.1
GC10/8-9	1617	52.3	0.51	0.10	na	6.2
GC10/10-11	1820	71.2	0.40	0.08	0.07	5.6
GC10/12-13	2022	74.3	0.80	0.07	na	13.6
GC10/13-14	2124	55.7	0.52	0.07	0.30	8.8
GC10/15-16	2326	54.3	0.81	0.07	0.15	13.8
GC10/17-18	2529	47.6	0.88	0.08	0.18	13.0
GC10/20-21	2833	45.9	0.72	0.07	0.23	12.7
GC10/23-24	3137	43.9	0.77	0.06	0.25	14.1
GC10/26-27	3441	47.8	0.31	0.07	0.40	5.4

Table 4.1 *(continued)*

Sample ID	Age	$CaCO_3$	TOC	TN	S	TOC/N
	Yr BP	wt. %				Atomic
GC10/27-28	3543	42.8	0.91	0.07	na	16.0
GC10/28-29	3644	42.2	1.12	0.06	na	20.9
GC10/29-30	3745	42.2	0.94	0.06	0.30	18.4
GC10/30-31	3847	23.7	3.01	0.09	0.44	37.2
GC10/31-32	3948	45.6	0.76	0.06	na	14.1
GC10/32-33	4049	40.2	1.30	0.06	na	23.3
GC10/33-34	4151	44.9	0.67	0.07	0.43	11.8
GC10/35-36	4353	45.8	0.74	0.07	na	13.3
GC10/36-37	4455	41.9	0.91	0.06	0.42	17.0
GC10/39-40	4638	45.4	0.50	0.06	0.31	9.0
GC10/42-43	4762	45.8	0.58	0.07	0.28	10.3
GC10/45-46	4886	43.0	0.94	0.07	0.48	15.9
GC10/48-49	5010	44.0	0.92	0.07	na	15.7
GC10/52-53	5174	45.4	0.70	0.06	0.41	12.6
GC10/56-57	5339	49.5	0.02	0.14	0.47	0.2
GC10/59-60	5463	43.8	0.86	0.06	0.49	16.5
GC10/63-64	5628	45.2	0.64	0.07	0.44	10.5
GC10/66-67	5752	45.4	0.64	0.06	0.37	11.7
GC10/70-71	5917	39.3	1.23	0.06	0.32	23.1
GC10/73-74	6040	45.7	0.46	0.06	0.34	8.2
GC10/77-78	6205	44.3	0.66	0.07	0.32	11.4
GC10/81-82	6370	42.9	0.90	0.06	0.39	16.8
GC10/85-86	6535	46.5	0.38	0.08	0.50	5.3
GC10/88-89	6659	44.5	0.68	0.07	0.28	12.2
GC10/90-91	6711	45.3	0.90	0.06	0.20	17.1
GC10/93-94	6745	43.2	0.82	0.07	0.29	13.1
GC10/96-97	6779	43.6	0.70	0.06	0.35	12.7
GC10/100-101	6824	43.3	0.83	0.07	0.40	14.4
GC10/104-105	6870	44.8	0.62	0.21	0.32	3.5
GC10/108-109	6915	49.0	0.21	0.07	0.45	3.7
GC10/111-112	6949	45.4	0.62	0.07	0.45	10.8
GC10/113-114	6971	43.8	0.78	0.07	0.50	13.5
GC10/117-118	7017	42.9	0.95	0.07	0.34	16.4
GC10/120-121	7051	47.0	0.66	0.06	0.40	12.2
GC10/123-124	7084	46.5	0.48	0.07	0.43	8.4
GC10/126-127	7118	44.4	0.86	0.06	0.15	15.4
GC10/129-130	7152	43.9	0.81	0.10	0.16	9.7

na: not analyzed

Table 4.2: *Major and trace elemental data for the SSK40/GC10 core and their possible major sources (the Deccan Traps and the Thar Desert). Results from factor analysis of these data are also summarized here.*

Elements	**SSK40/GC10**		**Deccan Traps**[a]	**Thar Desert**[b]		**Factor - 1**	**Factor - 2**	**Factor - 3**	**Factor - 4**
	Mean ± 1σ	**Range**							
					Eigen Value	7.4	5.0	1.9	1.2
					% of variance	37.9	25.6	9.8	6.1
					Possible sources[#]	Detritus	Authigenic (Anoxic) removal	Authigenic (Sulfidic) removal	Authigenic (Oxic) removal
Na	0.63 ± 0.13	0.49 - 1.01	1.53 ± 0.45	1.76 ± 0.24		0.52	0.60	0.49	0.16
Mg	1.86 ± 0.22	1.14 - 2.11	3.45 ± 0.61	1.38 ± 0.55		0.90	0.19	-0.12	-0.16
Al	4.53 ± 0.64	2.37 - 5.08	7.47 ± 0.39	5.71 ± 1.14		0.92	-0.24	-0.10	-0.11
K	1.02 ± 0.18	0.49 - 1.18	0.45 ± 0.41	1.64 ± 0.26		0.64	-0.71	0.03	0.12
Ca	19.86 ± 2.49	17.69 - 30.79	7.16 ± 1.21	3.63 ± 0.37		-0.14	-0.23	-0.09	0.19
Ti	0.44 ± 0.06	0.26 - 0.5	1.28 ± 0.35	0.32 ± 0.07		0.91	0.06	0.25	-0.06
Fe	4.05 ± 0.5	2.47 - 4.72	9.91 ± 0.96	2.35 ± 1.2		0.91	0.25	0.14	-0.05
TOC	0.78 ± 0.4	0.02 - 3.01	-	-		-0.56	0.66	0.20	0.10
$CaCO_3$	47 ± 8	23.7 - 74.3	3.01 ± 4.71[c]	-		-	-	-	-
TN	0.08 ± 0.03	0.06 - 0.21	-	-		0.36	0.66	-0.35	-0.06
TOC/TN	13 ± 6	0.2 - 37.2	-	-		-	-	-	-
S	3224 ± 1224	726 - 5040	98 ± 130[d]	-		0.19	-0.59	0.29	-0.15
V	83 ± 16	33 - 94	321 ± 35	92 ± 11[e]		0.40	-0.87	0.08	0.14
Cr	115 ± 15	67 - 166	182 ± 52[c]	80 ± 5[e]		0.54	0.61	-0.24	0.16
Mn	644 ± 138	259 - 774	1451 ± 222	412 ± 145		-	-	-	-
Co	18 ± 3	9 - 21	57 ± 43	17 ± 3		0.67	-0.63	0.13	0.21
Ni	50 ± 7	31 - 62	69 ± 20	59 ± 6		0.79	0.41	0.10	0.19

Cu	23 ± 9	7 - 42	260 ± 84[c]	17 ± 5	0.26	0.40	0.71	-0.30
Zn	77 ± 48	27 - 344	176 ± 51[c]	35 ± 12	0.20	0.08	-0.73	0.12
Rb	52 ± 8	25 - 59	15 ± 19	65 ± 12	0.69	-0.61	-0.02	0.05
Sr	2960 ± 499	1445 - 3340	214 ± 59	297 ± 81	-	-	-	-
Mo	0.5 ± 0.2	0.3 - 1.8	-	-	0.44	0.34	-0.10	0.68
Ba	63 ± 19	11 - 103	164 ± 129	284 ± 31	-	-	-	-
Th	5 ± 1	2.4 - 5.9	2.2 ± 1.3	8.5 ± 5.1[f]	0.56	-0.01	-0.44	-0.59
U	3 ± 0.2	2.2 - 3.5	0.52 ± 0.26	1.3 ± 1.4[f]	0.58	0.67	-0.08	-0.12

Units of S and Trace element concentrations are in µg/g, whereas major elements are in wt%. TOC/TN ratio is the atomic ratio

[#]Factor analysis was carried out after carbonate-correction

a: Mahoney et al., 2000; b: Roy et al., 2006; c: Das and Krishnaswami, 2007; d: Crocket and Paul, 2004;

e: Kumar et al., 2020; f: Chatterjee and Ray, 2017

Fe (2.47-4.72 wt%)) of bulk sediment show significant depth variations (Table 4.1). The average concentrations for major and trace elements, except for Ca and Sr, are about two times lower than that reported for their possible sources (Table 4.2). A similar observation has also been reported earlier for a nearby sedimentary core in the eastern Arabian Sea, where core sediments contain >70 % of biogenic matter ($CaCO_3$ and TOC; Kessarkar et al., 2018). In contrast, Ca (~3-4 times) and Sr (~10 times) concentrations for the SSK40/GC10 sediments are significantly higher than those reported for its possible sources (Table 4.2). The enrichment of Ca and Sr is attributable to the high affinity of alkaline metals for carbonate minerals (Morse and Mackenzie, 1990). Figure 4.1 depicts the correlation of Al concentrations with selected major and trace elements. Most of the elements (Ti, Fe, K, V, Co, and Ni) show a significant correlation ($r > 0.8$) with Al, indicating the dominancy of detrital sources to the core site. Further, the slopes of the linear regression lines of these elements are found to be intermediate to the corresponding Al-normalized ratios for sediments derived from the Deccan Traps and alluvium deposits (Fig. 4.1).

A few parameters (CIA*, carbonate-corrected concentrations, and enrichment factors of Mo and U) have been used in the subsequent sections for data interpretation, which has been defined here. The modified Chemical Index of Alteration (CIA*) of the sediments was calculated using the following equation (Nesbitt and Young, 1982; Singh et al., 2008):

$$CIA^* = 100 \times \frac{Al_2O_3}{(Al_2O_3 + Na_2O + K_2O)} \qquad (4.1)$$

All the oxide phases are in molar units. The carbonate-corrected (X*) composition for a given element, *X*, was computed (Tripathy et al., 2014) following the equation 4.2. This equation assumes that the carbonate does not contribute the element X and hence, cannot be used for elements which are found in abundance in carbonates.

$$X^* = X \times \left[\frac{100}{100 - CaCO_3}\right] \qquad (4.2)$$

The enrichment factors of Mo (EF_{Mo}) and U (EF_U) have been computed using the following equations:

$$EF_{Mo} = \frac{\left(\frac{Mo}{Al}\right)_{sample}}{\left(\frac{Mo}{Al}\right)_{UCC}} \qquad (4.3)$$

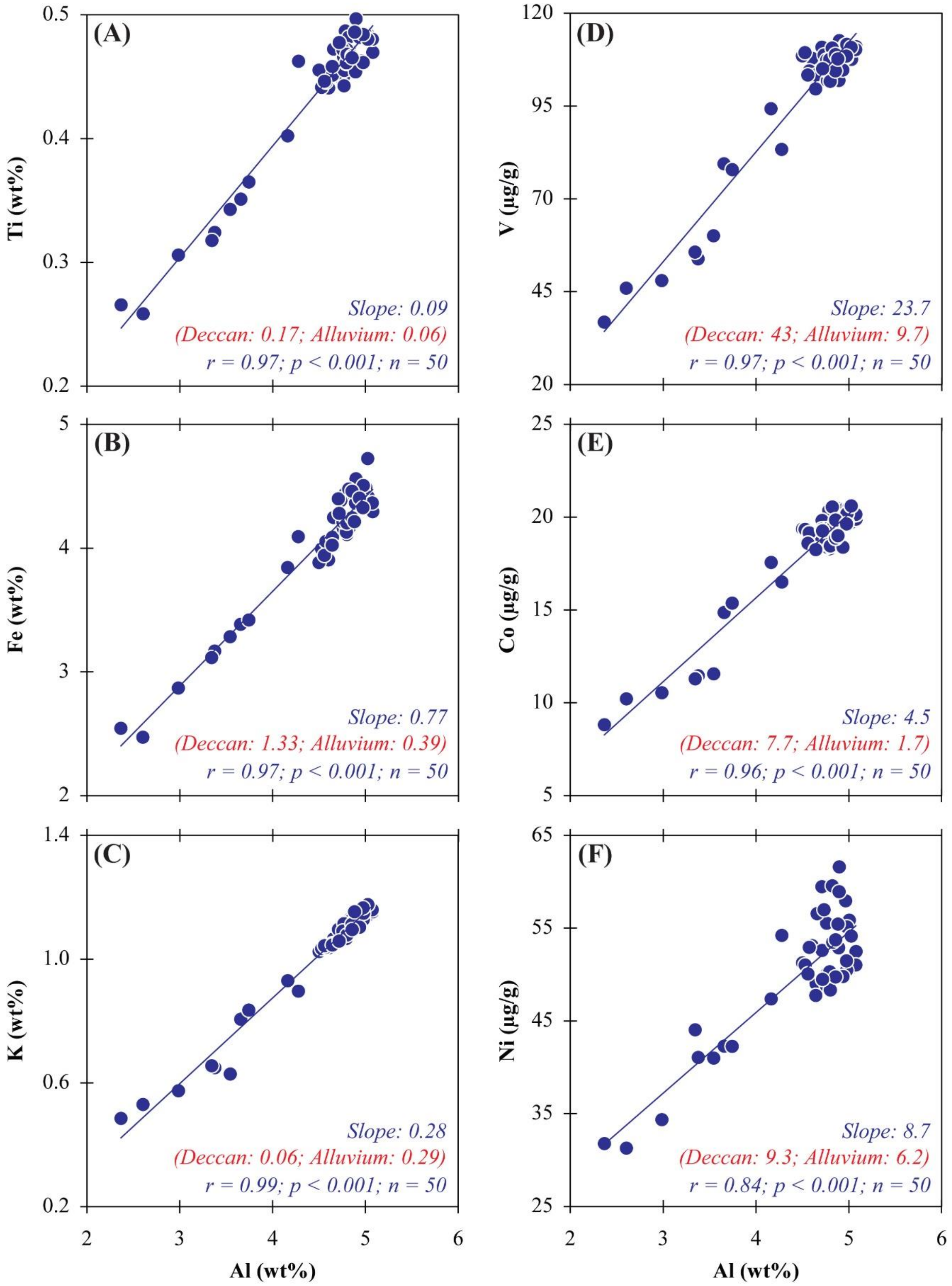

Figure 4.1. *Covariation of Al with selected elements (Ti; Fe; K; V; Co, and Ni) of the SSK40/GC10 bulk sediments. The slopes of these linear trends are intermediated to corresponding Al-normalized elemental ratios of their possible sources (Deccan and Indus River sediments).*

$$EF_U = \frac{\left(\frac{U}{Al}\right)_{sample}}{\left(\frac{U}{Al}\right)_{UCC}} \qquad (4.4)$$

The subscript, UCC, stands for the average composition of the upper continental crust (Rudnick and Gao, 2003).

The CIA* values for the SSK40/GC10 samples range from 67 to 78 with an average value of 76 ± 2, which is consistent with that reported for the possible sediment sources to this core site, which includes Deccan Traps flowing river sediment (~75; Das and Krishnaswami, 2007), Thar Desert (64 ± 3; Roy et al., 2006), and sediments from nearby river basins (Mahi River (71 ± 7; Sharma et al., 2013), Narmada River (73 ± 4; Sharma et al., 2010), Tapi River (79 ± 5; Sharma et al., 2010)). Further, these CIA* values for the SSK40/GC10 core are also comparable but marginally lower than the average CIA* value of the western continental margin of Indian sediments (~83; Kurian et al., 2013).

4.2.1 Discussion

4.2.1.1 Temporal variations in the continental weathering

The sediment core (SSK40/GC10) was raised from the shallow marine settings (water depth ~50m; about 70 km away from the nearest continent) eastern Arabian Sea (cf. Chapter 2; section 2.1.2). Considering the low water depth and its land proximity, the core site is expected to receive sediments mainly from the nearby river basins (Narmada, Tapi, and Mahi) and the Thar Desert and is less likely to receive sediments from the Indus river basin. The possible major detrital sources to the SSK40/GC10 site, therefore, are the rivers flowing through the Deccan Traps and Quaternary alluvium and also aeolian supply from the Thar region (cf. Chapter 2; Fig. 2.3). The major Deccan-flowing rivers (e.g., Tapi and Narmada) deliver ~100 million tons (Alagarsamy and Zhang, 2005; Chandramohan and Balchnad, 2007) of sediment annually and an equal amount of dust (~100 million tons; Ramaswamy and Nair, 1994) is also being supplied from nearby deserts (e.g., Thar, Somalia, and the Arabian Peninsula) to the eastern Arabian Sea. The aeolian dust from the Thar region, however, is mainly reworked-sediments from the Indus and hence, has similar chemical compositions as that of the Indus river sediments (East et al., 2015). Additionally, the core site is also expected to receive significant biogenic supplies, mainly due to high oceanic productivity in this part of the Arabian Sea (Calvert et al., 1995; Kessarkar et al., 2018).

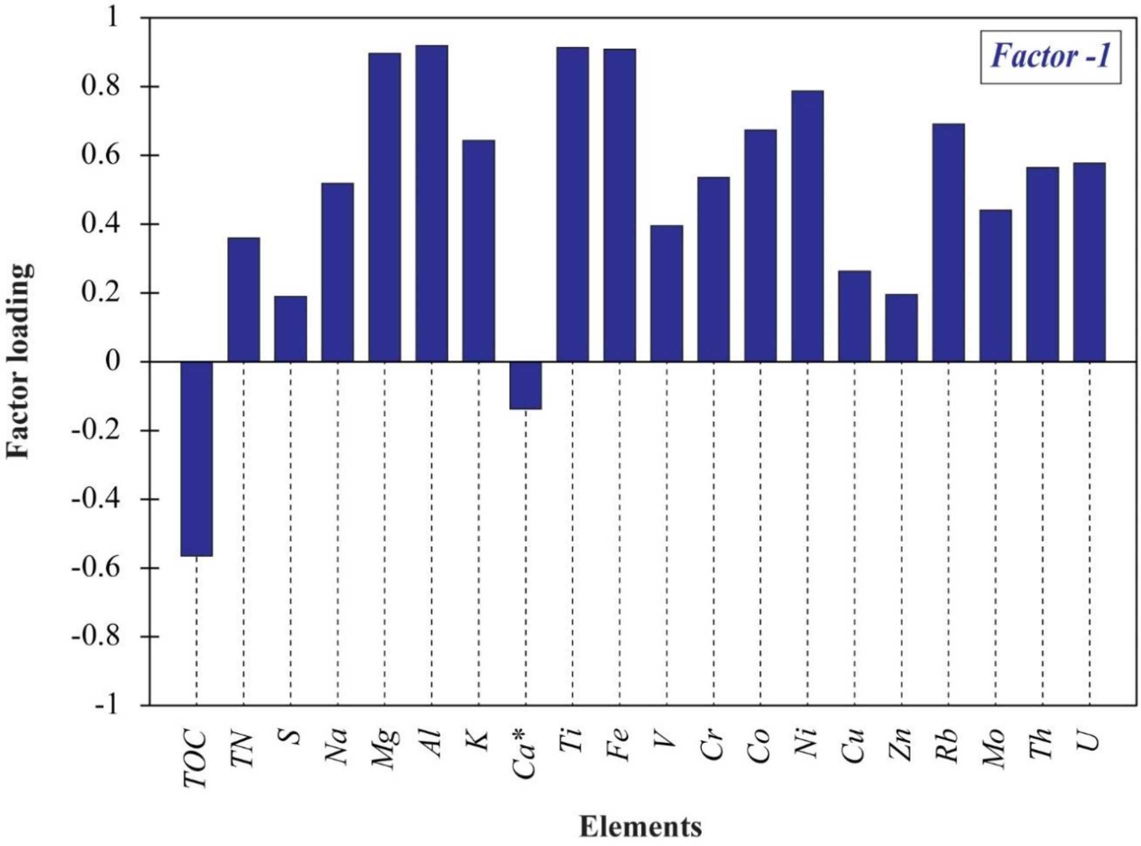

Figure 4.2. *Factor loading of elements for the dominant source explains 38 % of the total variance. This factor, with high loading for immobile elements (Al and Ti) during chemical weathering, possibly indicates detrital sources.*

In order to better constrain these sources, we have carried out a factor analysis of the geochemical compositions of the sediments after correcting for carbonate contribution. Results from this factor analysis are provided in Table 4.1. This analysis identifies four major factors with an Eigen value > 1, which together can explain ~80 % of the total variance of the dataset. Among these factors, the dominant *Factor 1* explains about 38 % of the total variance (Table 4.1). This factor is mainly characterized by high factor loadings of lithogenic elements, e.g., Al, Ti, and K (Fig. 4.2), confirming its association with the detrital source. *Factor 2* explains about 26 % of the variance and is characterized by high loadings for TOC, TN, and several redox-sensitive elements (Mo, U, Cr, Cu, and Ni). This combination of elements associated with *Factor 2* points to authigenic/biogenic scavenging of these elements together with organic matter. It is interesting to note that the sulfur content is not positively linked with this factor. This indicates that *Factor 2* is mainly linked to the anoxic (and non-sulfidic) removal of elements from the seawater. The loading of sulfur is found higher for *Factor 3* (Table 4.1), which accounts for about 10 % of the total variance. Although the exact source could not be identified, *Factor 3* seems to be linked with the scavenging of selected elements (V, Cu, and Co) in sulfidic conditions. *Factor 4* is mainly associated with Mo and a few other trace metals. In addition to detrital sources (*Factor 1*), sedimentary Mo is mainly linked to their authigenic removal from seawater through sulfidic or oxic water conditions (Algeo and Tribovillard, 2009; Helz et al., 1996). Considering that *Factor 3* reflects the sulfidic pathway, *Factor 4* seems to explain the removal of trace metals to the sediments from the oxygenated surface water. The factor analysis of this dataset, therefore, shows that the sedimentary chemistry of the eastern Arabian Sea is mainly regulated by detrital and authigenic input. In the case of authigenic supply, the abundances of trace elements seem to be regulated by the variable redox state of the bottom water column and/or the sediment/water interface.

We have evaluated the Al-normalized ratios of K, Fe, and Ti to infer sediment provenances for the SSK40/GC10 core (Fig. 4.3). Aluminium (Al) is an immobile element during weathering processes; the Al-normalized ratios, hence, may retain source signatures and are less influenced by size sorting and/or sediment dilution (Tripathy et al., 2014). Figure 4.3A depicts the mixing diagram between K/Al and Fe/Al ratios for the sediments with their possible source compositions. This plot shows that the sediment chemistry of the SSK40/GC10 can be explained by sediment supply from nearby river basins (Narmada, Tapi, Mahi, and Indus) and the Thar region. Most of the data are found proximal to the Mahi River composition. The Mahi River mainly drains through the Quaternary alluvium, indicating a dominant sediment supply from this geological unit to this core site (Fig. 4.3A). Earlier studies have documented that the sedimentary K/Al ratios in oceanic basins may also be influenced by the preferential release of K (over Al) during continental (chemical) weathering processes (Limmer et al., 2012). Recognizing this limitation, the covariation between Ti/Al and Fe/Al ratios was also assessed to constrain the sedimentary sources (Fig. 4.3B). The Fe/Al-Ti/Al plot also confirms the dominant supply of sediments from nearby river basins, with an appreciable supply from the Thar region. Most of the data in these mixing plots (Fig. 4.3A and 4.3B) fall together and show a minimal change in the source contribution during the studied period. For closer scrutiny, we have also evaluated the down-core variation of Al-normalized ratios for elements (K, Fe, Ti, V, and Co) with high factor loading in *Factor 1* (Fig. 4.2) to ascertain the temporal changes in the provenances (Fig. 4.4). Figure 4.4 shows near-uniform elemental ratios in the lower part of the core till 2.6 kyr BP and changes significantly in the recent periods. For instance, the Fe/Al ratio of the lower part of the core remains mostly invariant with an average value of 0.89 ±

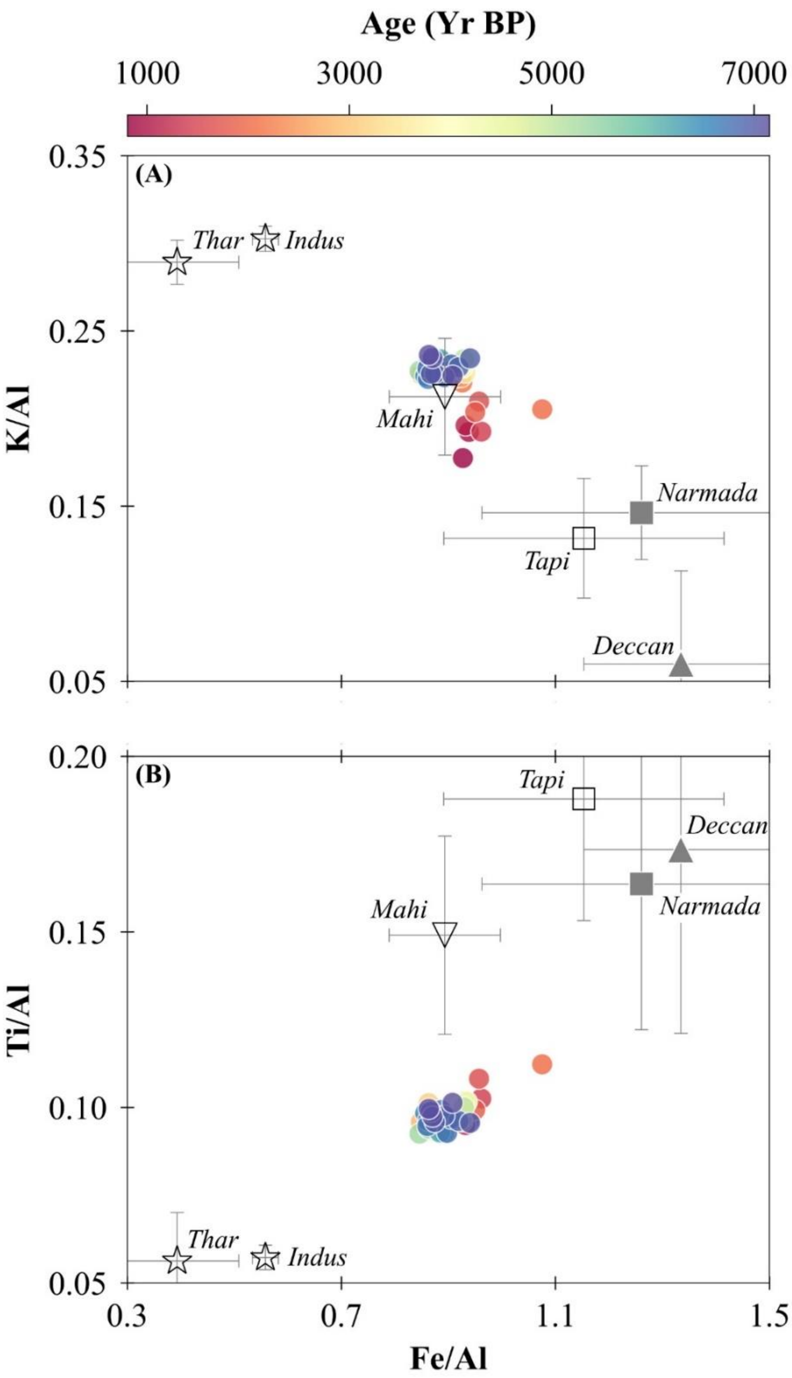

Figure 4.3. *Mixing diagrams between (A) K/Al and Fe/Al and (B) Ti/Al and Fe/Al ratios for bulk sediments. For reference, elemental ratios for possible major sedimentary sources (Deccan basalt (Mahoney et al., 2000), Thar Desert (Roy et al., 2006), and river sediments from Indus (Clift et al., 2010), Mahi (Sharma et al., 2013), Tapi and Narmada (Sharma et al., 2010)) are also shown.*

0.03, which increases to 0.95 ± 0.05 for the samples deposited since 2.6 kyr BP. The characteristics Fe/Al ratios for the sources (e.g., Deccan basalts (1.3 ± 0.2; Mahoney et al., 2000), Thar Desert (0.4 ± 0.1; Roy et al., 2006) and Mahi (0.9 ± 0.1; Sharma et al., 2013); Table 4.1) indicates that the recent increase in Fe/Al ratio can be attributed to increased sediment contribution from the Deccan regions and the Mahi basin and/or decreased sediment supply from the Thar region. This trend is also consistent with the temporal change observed for Ti/Al ratios (Fig. 4.4), pointing to a recent increase in sediment supply from nearby basins (Narmada, Tapi, and Mahi; cf. Chapter 2; Fig. 2.3). Interestingly, the V/Al ($\times 10^{-4}$) ratio shows a declining trend from a value of 18.6 ± 0.6 in the lower part of the core to 16 ± 2 for the samples deposited since 2.6 kyr BP. Comparison of V/Al ($\times 10^{-4}$) ratios for the SSK40/GC10 samples with the source compositions (e.g., Deccan basalts (43 ± 6; Mahoney et al., 2000), Thar Desert (14 ± 1; Kumar et al., 2020), and Mahi (27 ± 4; Sharma et al., 2013)) indicates that the recent decline in V/Al ratio can be attributed to reduced sediment contribution from the Deccan traps and/or increased sediment supply from the Thar region. As V/Al can also be influenced by ocean redox condition, we have evaluated other elemental proxies (Fe/Al, Ti/Al and Co/Al). The trend of V/Al is also supported by the down-core profile of Co/Al ratios. The observed increased sediment influx of trace metals (V and Co) from the Thar regions since 2.6 kyr BP, in contrast to Fe and Ti trends, is less likely due to their lesser or comparable concentrations in other river sediments. The exact cause for this difference in trends is not clear. One possible explanation is the appreciable sediment supply from the Indus basin, which can explain the recent changes in elemental ratios during recent periods to the core site. A more detailed provenance study based on Sr-Nd isotopes can be useful in ascertaining this proposition and the factors influencing these changes.

The down-core variation of the CIA* shows mostly an invariant trend (76 ± 2) in the lower half of the core (Fig. 4.4), which subsequently fluctuates between 2.6 and 1.6 kyr BP (73 ± 4). This CIA* fluctuation in the upper part of the core can be attributed to changes in both sediment provenance and/or chemical erosion patterns. To decipher the exact possibility, we have compared the K/Al and CIA* trends for this time period. An intensification in chemical weathering should lead to a higher CIA* value and lower K/Al ratios. An anti-correlation between K/Al and CIA* value, therefore, can be linked to changes in chemical weathering. Similar to K/Al, trends of Na/Al also show an anti-correlation with CIA*. Figure 4.4 shows an anti-correlation between K/Al and CIA* trends since 1.6 kyr BP, pointing to the recent intensification of chemical weathering.

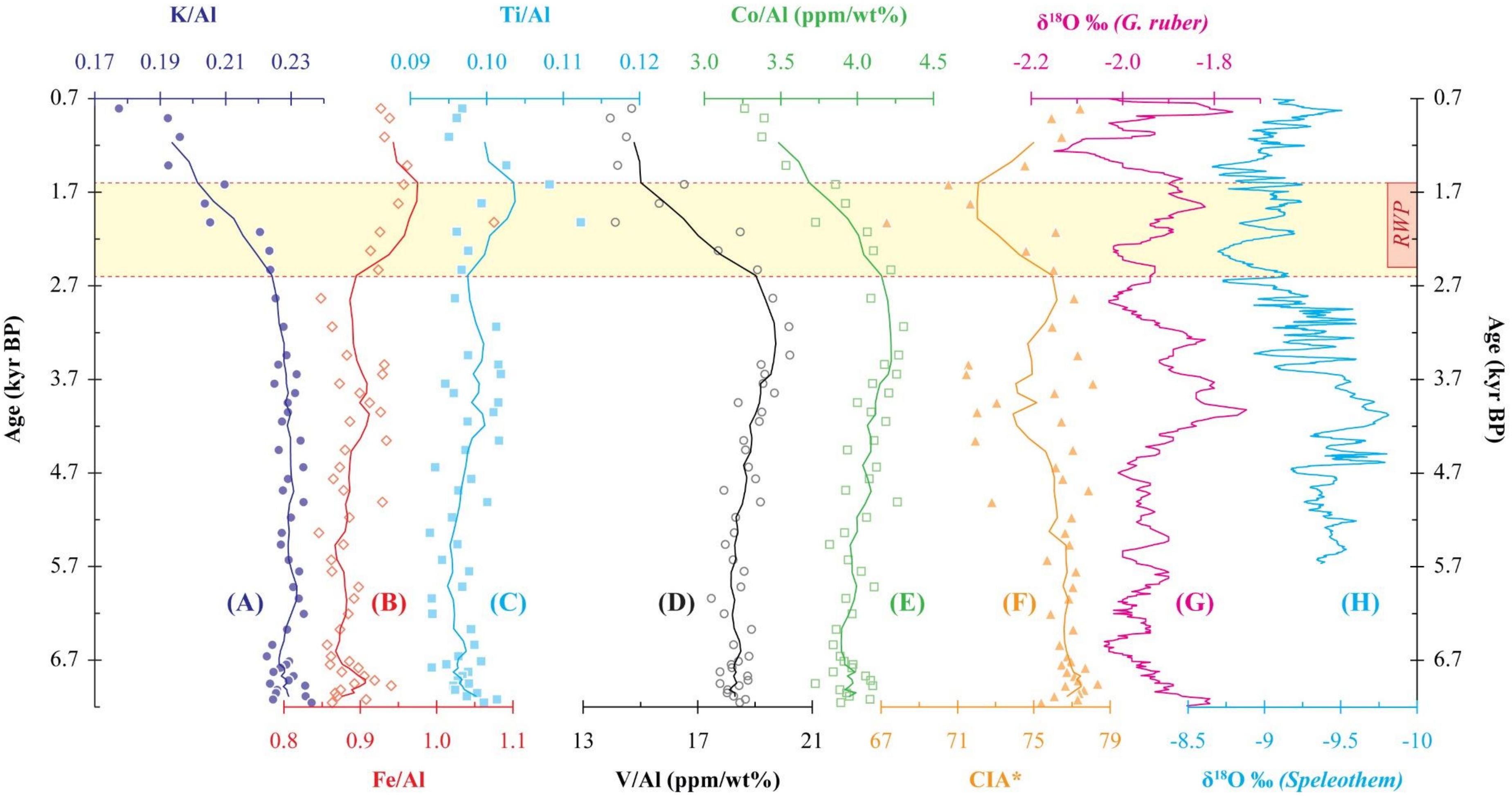

Figure 4.4. *Temporal variations in Al-normalized ratios for elements (K; Fe; Ti; V and Co) and CIA* of the SSK40/GC10 core. For reference, paleoclimatic $\delta^{18}O$ records for the Arabian Sea (foraminifera; Staubwasser et al., 2003) and northern India (speleothem; Kathayat et al., 2017) have also been shown. RWP: Roman Warm Period.*

Our observation on a significant change in land-surface processes since 2.6 kyr BP is consistent with earlier reported weathering changes in sediment records from south-western India (Banerji et al., 2021) and western India (Banerji et al., 2017, 2019; Sinha et al., 2006) and Himalayan (Bali et al., 2017) regions. This time period (2.6-1.6 kyr BP) of weathering changes is synchronous to earlier reported (Roman) Warm Period (2500-1600 Yr BP; Kathayat et al., 2017; Wang et al., 2012), hinting at climatic control on the weathering pattern. A warm climatic period is often found to intensify the Indian summer monsoon, which is likely to enhance the weathering rates of river basins. Available climatic records from India during the Roman Warm Period, however, provide diverging evidence about the monsoon intensity (Misra et al., 2019) and show both strengthening and weakening of the monsoon during this period. These diverging monsoon trends make it complicated to ascertain the exact mechanism controlling the weathering changes. In addition to climate, recent studies have also invoked the impact of man-made activities (land-use patterns and sustained agricultural practices) in regulating the continental weathering processes in tropical regions (Wan et al., 2015). As the present trends of weathering indices continue to change after the warm period also, the recent influence of non-climatic parameters on weathering cannot be ruled out.

4.2.1.2 Variability in the oceanic redox state

The abundance of redox-sensitive elements in marine sediments can provide valuable clues about temporal changes in the ocean redox state. These elements mostly form oxyanions in oxygenated water conditions and get scavenged during reduced conditions to the underlying sediments by forming organo-metallic/sulfidic complexes (Algeo et al., 2011; Tribovillard et al., 2006). Figure 4.5 depicts the depth profiles of selected proxies ($CaCO_3$/Al; TOC/Al, TOC/N, S, S/Al, Ba/Al, EF_{Mo}, and EF_U) for the SSK40/GC10 core to constrain biogenic input and bottom water condition of the eastern Arabian Sea. The $CaCO_3$/Al ratios in marine sediments are likely to reflect the relative change in biogenic to detrital input. For instance, the sedimentary inorganic carbonates are largely supplied by biogenic pathways, whereas the sedimentary Al is regulated by its supply through weathering of detrital aluminosilicates. The $CaCO_3$/Al ratios of the SSK40/GC10 core, although remain constant in the lower part of the core, show an increasing trend after ~2.6 kyr BP. This recent enrichment in the $CaCO_3$/Al is synchronous to the changes in detrital proxies (Fig. 4.4) and hence, may be linked to a change (decrease) in detrital influxes than biogenic changes. In contrast to the $CaCO_3$ trends, the TOC/Al ratios show no major excursion around 2.6 kyr BP (Fig. 4.5).

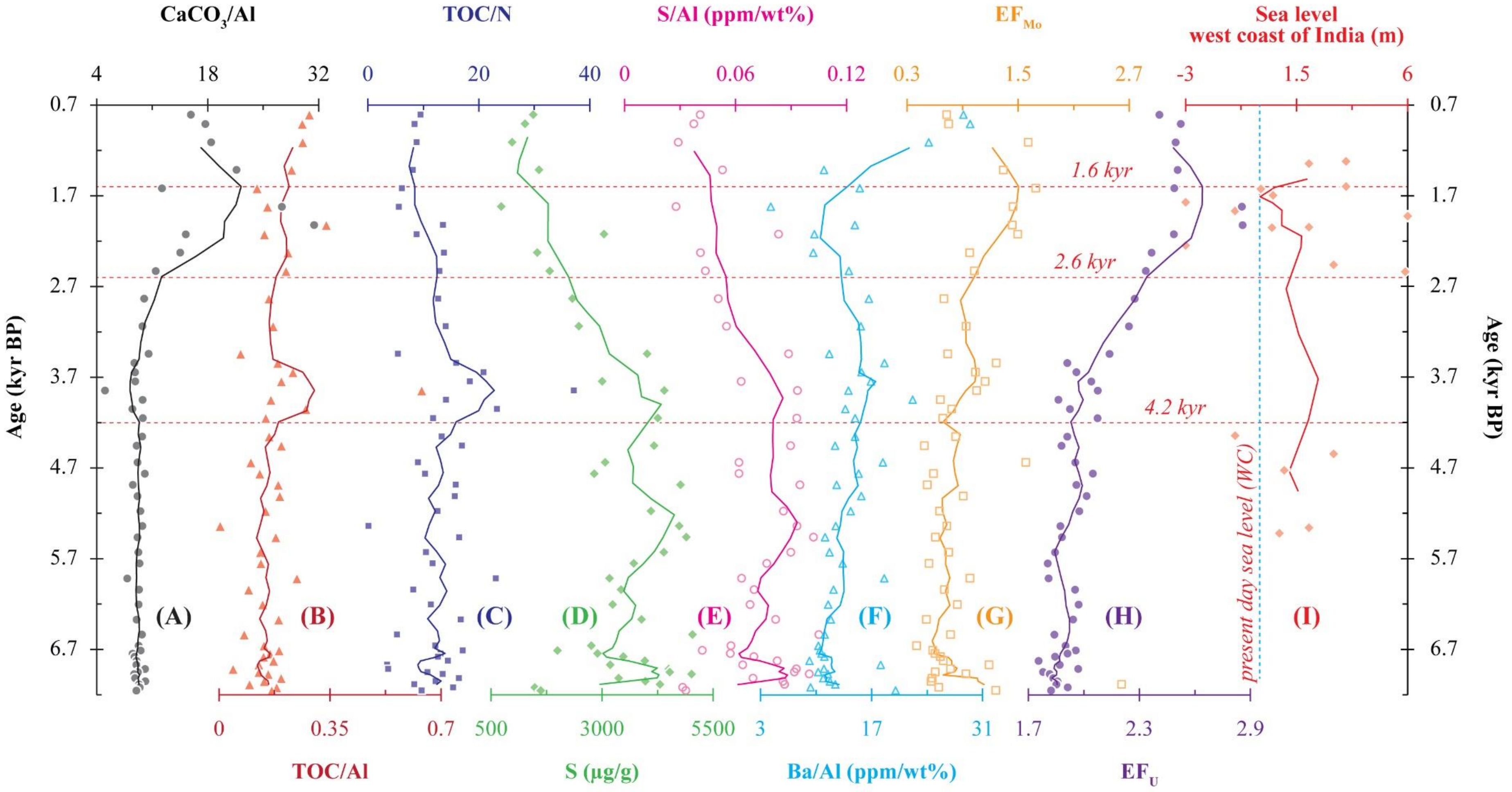

Figure 4.5. *Down-core variation of selected biogenic and redox-sensitive elemental ratios ($CaCO_3/Al$, TOC/Al, TOC/N, S, S/Al, Ba/Al, EF_{Mo}, and EF_U) are shown. Large variations in these proxies point to fluctuation in the bottom water redox state of the eastern Arabian Sea. The sea-level variations in the western coast (WC) of India have also been shown (Data source: Banerji et al., 2021 and references therein).*

The TOC/Al can be regulated by the relative supply of organic matter from terrestrial and oceanic sources. The sedimentary TOC/TN ratios have distinct values for terrestrial (≥ 20) and marine (~6.6) organic matter (Meyers, 1994; Redfield, 1958) and hence, may provide clues for their sources. The TOC/TN ratios, like TOC/Al, show no major change at around 2.6 kyr BP. The TOC/TN trend, however, shows a peak of about 300 years at around 4.2 kyr BP (Fig. 4.5), pointing to an increased terrestrial supply and/or decreased oceanic organic matter to the core site.

The sedimentary S concentrations and S/Al ratios show a sustained declining trend immediately after 4.2 kyr BP, pointing to a significant shift in the ocean redox state (Fig. 4.5). These trends are synchronous to the down-core changes for Ba/Al and enrichment factors of Mo and U. The average EF_{Mo} values increase from 0.8 (± 0.4) for samples before 4.2 kyr BP to 1.1 (± 0.3) since 4.2 kyr BP. A concomitant change is also observed for EF_{U}, which increases from 1.9 (before 4.2 kyr BP) to 2.3 (since 4.2 kyr BP). An increase in EF_{Mo} and EF_{U} since 4.2 kyr can be attributed to an oceanic transition towards a reducing condition of bottom water. Consistent with these trends, the Ba/Al ratio also shows an increasing trend since 4.2 kyr BP. The Ba/Al ratio in oceanic sediments reflects the intensity of primary productivity of the depositional basin (Bishop, 1988; Dehairs et al., 1980). A High Ba/Al ratio since 4.2 kyr BP points to an increase in productivity, which may have influenced the bottom water conditions. An increase in productivity and related organic material deposition can lead to a reducing bottom water condition, using up the oxygen for decomposition. A reduced bottom water condition may further increase the concentrations of redox-sensitive trace elements. However, the Ba/Al ratio in the upper part of the core does not follow similar trends as that of Mo and U EFs. This difference indicates that additional factors may also be contributing to the redox state. The observed shift from oxic to anoxic bottom water at 4.2 kyr BP is also synchronous to a drought phase (Berkelhammer et al., 2012), which is followed by a weakening monsoon phase during the late Holocene period (Dixit et al., 2014a). This climatic change has influenced the river basins from western India severely (Banerji et al., 2017, 2019; Sinha et al., 2006). Although the observed transition to anoxic water condition seems to have climatic linkage, the exact mechanism leading to this climatic-driven redox change during the late Holocene is not clear. We have assessed the impact of sea-level changes during the studied period for the west coast of India (Banerji et al., 2021; Panchang and Sen, 2021) on the bottom water redox state. Compilation of literature data shows that the sea level has varied by a few meters during the late Holocene (Fig. 4.5). The oxygen minimum zones in the eastern Arabian Sea have often been observed in water depths of more than 150 m (Qasim, 1982; Sen Gupta and Naqvi, 1984; Wyrtki, 1971), and hence, water level variations of 2-3 m at a depth of 50 m may not have a significant impact on redox state. Another possible explanation for the observed sediment enrichment can be attributed to reduced water conditions at the sediment-water interface, which in turn can scavenge dissolved redox-sensitive elements to the sediments. Further, reduced freshwater influx and poor ventilation of the coastal water during the dry phases can also trigger an anoxic water condition during the late Holocene period. This proposition, however, can be better constrained through a detailed paleo-oceanographic investigation of the eastern Arabian Sea involving robust proxies of continental weathering and redox proxies.

4.3 Sediment chemistry of the SSK40/GC06 core

The details and chronological information about the SSK40/GC06 sediment core from the eastern Arabian Sea are included in an earlier chapter (cf. Chapter 2, section 2.1.2). The sediments from the SSK40/GC06 core are mainly silty in nature. The geochemical composition of SSK40/GC06 sediments is given in Table 4.3. Major elemental ((Na (0.7-1.1 wt%), K (1.2-1.6 wt%), Ca (4.1-6.9 wt%), Mg (2.0-2.4 wt%), Al (5.8-7.7 wt%), Ti (0.8-1.2 wt%), and Fe (5.4-7.1 wt%)) concentration show significant temporal variation. The Al (7.1 ± 0.4 wt%) and Ti (0.8 ± 0.1 wt%) concentrations show minimal (5-7 %) down-core variations (Table A4.2). The rare earth elements (REEs) concentrations (total REE) of the SSK40/GC06 sediments vary between 110 and 144 µg/g, with an average of 127 ± 6 µg/g (Table 4.3). The average REE value is intermediate to that reported earlier for the Indus river (159 ± 17 µg/g; Clift et al., 2010), Thar desert (131 ± 51 µg/g; Roy and Smykatz-Kloss, 2007), and Deccan Basalts (100 ± 38 µg/g; Mahoney et al., 2000).

The TOC concentrations of these samples vary from 0.6 to 2.8 wt% (mean: 1.3 ± 0.4 wt%). In comparison, the TN concentrations vary from 0.06 to 0.13 wt% with an average value of 0.10 ± 0.02 wt%. The average TOC/TN (atomic) ratio is 13.1 ± 1.5, which falls in between the numbers reported for the marine (~6.6; Redfield, 1958) and terrestrial (≥ 20; Meyers, 1994) organic matter. The inorganic carbon ($CaCO_3$) content of the SSK40/GC06 sediments also shows a large variation (7.2 -15.9 wt%) with a mean value of 11.0 ± 1.9 wt%. However, the organic carbon isotopic ($\delta^{13}C_{org}$) composition of SSK40/GC06 sediments shows a relatively lower variation -20.4 to -19.2 ‰ (Table 4.4). The average $\delta^{13}C_{org}$ of these sediments is -19.6 ‰. The CIA* values for the SSK40/GC06 samples range from 75 to 79 with an average value of 78 ± 1, which is comparable to Indus River sediment(70 ± 1; Clift et al., 2010) and Deccan

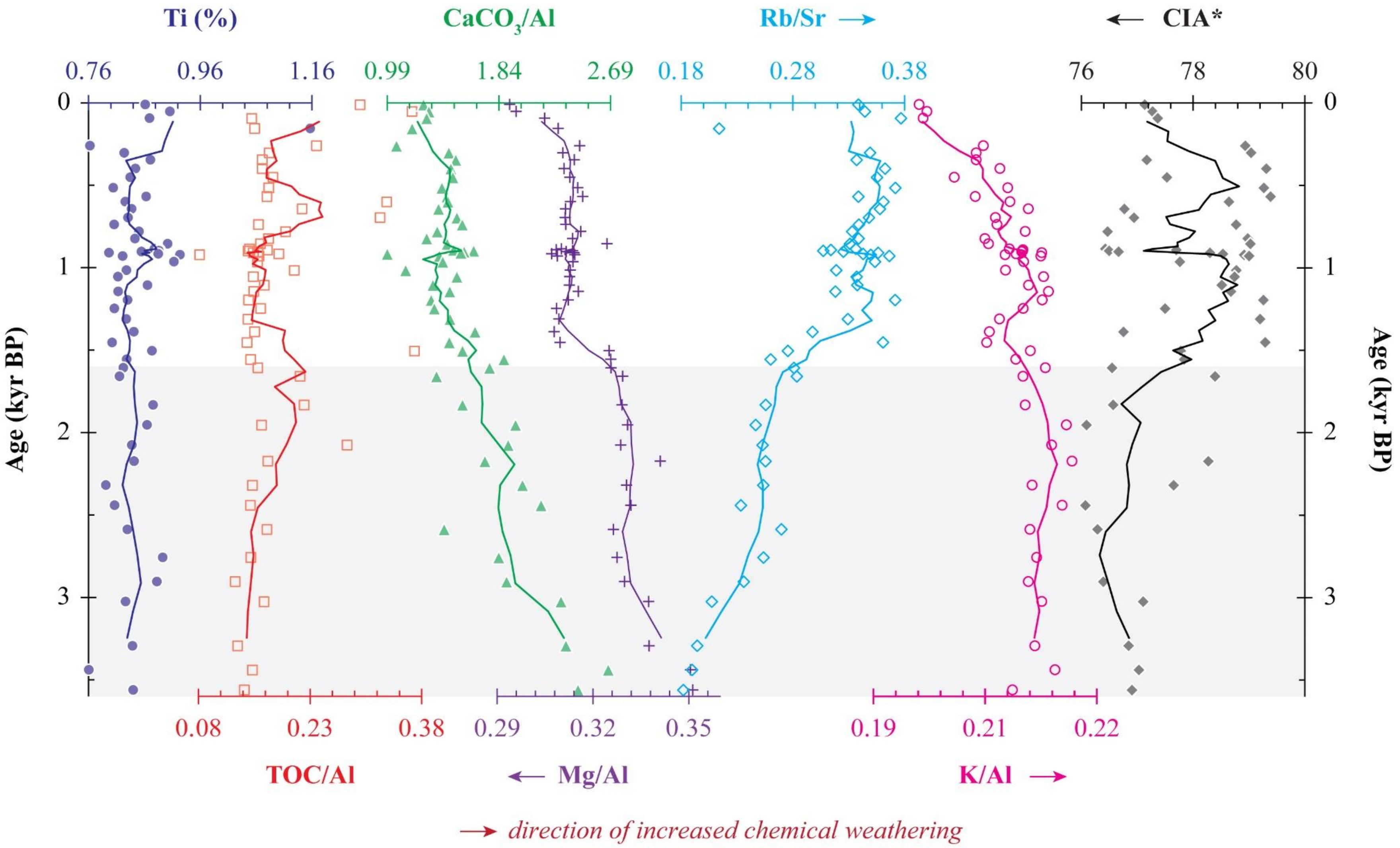

Figure 4.6. *Down-core variations in elemental concentrations and their ratios for the SSK40/GC06 core. These trends indicate intensification in chemical erosion for last 1.6 kyr BP.*

Table 4.3: *Geochemical composition (bulk) of SSK40/GC06 core sediments.*

Depth	Age	Na	K	Ca	Mg	Al	Fe	Ti	V	Cr	Mn	Co	Ni	Cu	Zn	Rb	Sr	Ba	Th	U
cm	Yr BP	wt. %							µg/g											
GC06/1-2	10	1.06	1.52	4.90	2.27	7.73	7.08	0.86	151	144	737	31	74	86	83	82	241	167	8.1	2.6
GC06/5-6	52	1.01	1.48	4.50	2.22	7.52	6.90	0.91	155	143	728	31	74	83	140	80	233	160	8.0	2.7
GC06/9-10	93	0.98	1.44	4.20	2.23	7.31	6.71	0.87	152	147	689	30	73	83	75	82	217	156	8.2	2.9
GC06/15-16	155	1.09	1.20	5.31	1.98	6.39	6.12	1.16	181	151	736	28	58	72	65	59	277	159	9.7	2.3
GC06/25-26	260	0.81	1.55	4.28	2.40	7.59	6.87	0.76	138	147	648	30	78	95	269	89	229	162	8.2	3.2
GC06/29-30	303	0.77	1.47	4.56	2.24	7.22	6.63	0.82	145	144	649	29	73	82	82	84	239	173	8.0	3.2
GC06/33-34	345	0.97	1.50	4.80	2.31	7.35	6.77	0.87	148	144	677	29	73	79	83	84	248	165	8.1	2.8
GC06/38-39	398	0.73	1.50	4.67	2.26	7.26	6.70	0.84	145	138	638	29	69	81	80	82	228	156	7.8	3.0
GC06/43-44	451	0.95	1.48	4.49	2.30	7.36	6.81	0.83	152	145	667	30	77	83	90	83	234	169	8.1	3.2
GC06/49-50	515	0.72	1.49	4.28	2.25	7.15	6.53	0.80	139	141	630	29	71	82	77	82	221	154	7.8	2.7
GC06/54-55	568	0.76	1.52	4.86	2.36	7.45	6.83	0.86	154	150	714	30	76	91	79	86	253	170	8.3	2.9
GC06/57-58	600	0.78	1.49	4.34	2.25	7.17	6.63	0.83	150	171	667	29	74	84	80	85	234	159	8.3	3.2
GC06/61-62	642	0.95	1.49	4.50	2.21	7.09	6.54	0.84	145	141	635	28	68	78	76	82	229	159	7.9	3.0
GC06/66-67	695	0.94	1.45	4.66	2.19	7.05	6.48	0.83	145	146	634	28	69	77	70	82	235	154	8.2	3.2
GC06/70-71	738	0.76	1.46	4.52	2.20	7.05	6.40	0.81	141	144	650	29	69	77	73	82	243	149	8.0	3.0
GC06/74-75	780	1.00	1.51	4.78	2.27	7.19	6.62	0.85	153	140	697	30	71	81	74	84	253	165	7.8	3.1
GC06/78-79	823	0.77	1.49	4.63	2.27	7.25	6.67	0.84	153	146	702	30	74	98	82	83	245	167	8.1	3.1
GC06/81-82	855	0.79	1.53	4.99	2.42	7.46	6.94	0.90	158	151	760	32	74	93	93	89	268	182	8.5	3.0
GC06/90-91	885	0.98	1.45	4.60	2.16	6.96	6.29	0.88	158	143	705	30	70	79	80	85	252	175	8.7	2.8
GC06/95-96	892	0.86	1.50	5.01	2.20	7.14	6.43	0.89	151	136	678	29	68	75	74	82	262	169	8.5	3.1

Table 4.3 *(continued)*

Depth	**Age**	**Na**	**K**	**Ca**	**Mg**	**Al**	**Fe**	**Ti**	**V**	**Cr**	**Mn**	**Co**	**Ni**	**Cu**	**Zn**	**Rb**	**Sr**	**Ba**	**Th**	**U**
cm	Yr BP	wt. %							µg/g											
GC06/99-100	897	0.99	1.51	5.26	2.25	7.19	6.58	0.89	157	143	696	29	70	77	82	85	277	167	8.6	3.2
GC06/103-104	902	0.96	1.49	4.89	2.21	7.08	6.34	0.85	143	138	680	28	69	77	78	83	256	161	7.9	2.8
GC06/108-109	909	0.74	1.42	4.46	2.09	6.67	6.05	0.80	137	131	637	27	65	74	66	80	225	155	7.7	2.6
GC06/113-114	916	0.80	1.53	4.73	2.25	7.32	6.64	0.88	153	136	696	29	68	81	75	84	245	167	8.2	2.8
GC06/117-118	921	0.79	1.56	4.85	2.36	7.52	6.88	0.92	157	144	734	30	72	93	80	88	251	177	8.8	3.2
GC06/123-124	929	0.75	1.56	4.55	2.27	7.36	6.63	0.82	145	136	672	29	71	84	75	85	232	166	8.4	2.8
GC06/132-133	964	0.89	1.55	4.59	2.31	7.38	6.93	0.91	157	141	712	29	70	82	86	87	245	166	8.8	3.0
GC06/136-137	1015	0.74	1.44	4.69	2.16	6.91	6.25	0.83	143	138	684	28	68	78	78	81	255	158	8.1	2.8
GC06/139-140	1054	0.74	1.51	4.68	2.22	7.09	6.48	0.81	140	150	658	29	70	81	83	84	250	170	8.0	3.0
GC06/143-144	1105	0.81	1.56	4.63	2.31	7.40	6.82	0.87	153	141	704	30	73	86	90	84	250	164	7.9	2.9
GC06/146-147	1144	0.78	1.58	4.87	2.34	7.42	6.68	0.81	145	143	671	29	74	88	74	85	267	164	7.8	3.0
GC06/150-151	1195	0.72	1.56	4.30	2.29	7.33	6.59	0.83	147	137	649	28	70	84	79	84	226	160	8.0	3.1
GC06/154-155	1247	0.90	1.52	4.08	2.23	7.24	6.43	0.81	143	136	651	28	69	81	85	86	218	162	8.1	3.0
GC06/159-160	1311	0.75	1.52	4.93	2.27	7.34	6.62	0.83	143	138	668	29	69	84	78	83	253	162	7.9	2.6
GC06/165-166	1388	0.97	1.45	5.06	2.17	7.05	6.20	0.84	141	136	674	27	66	73	69	78	263	164	8.2	2.6
GC06/170-171	1453	0.72	1.45	4.28	2.19	7.07	6.40	0.80	135	137	618	27	66	79	76	78	217	156	7.6	2.3
GC06/174-175	1504	0.86	1.53	5.44	2.35	7.23	6.50	0.87	146	149	663	28	70	85	77	83	302	171	8.1	3.2
GC06/178-179	1556	0.82	1.44	5.65	2.24	6.88	6.17	0.83	137	142	650	28	67	77	76	80	306	164	8.0	2.8
GC06/182-183	1607	0.92	1.45	5.07	2.21	6.80	6.14	0.82	132	140	636	27	66	70	70	79	280	158	7.8	2.7
GC06/186-187	1659	0.78	1.47	5.08	2.30	7.00	6.22	0.82	140	140	655	28	67	77	78	80	281	163	7.9	2.5

Table 4.3 *(continued)*

Depth	Age	Na	K	Ca	Mg	Al	Fe	Ti	V	Cr	Mn	Co	Ni	Cu	Zn	Rb	Sr	Ba	Th	U
cm	Yr BP	wt. %							µg/g											
GC06/195-196	1832	0.95	1.46	5.65	2.28	6.92	6.20	0.88	142	140	644	28	64	70	71	78	306	173	8.2	3.0
GC06/200-201	1953	0.93	1.43	5.90	2.19	6.61	6.03	0.86	142	148	637	26	64	66	69	79	319	170	8.4	3.3
GC06/205-206	2075	0.99	1.48	5.81	2.27	6.91	6.13	0.84	140	138	628	27	66	70	71	79	311	173	7.7	3.2
GC06/209-210	2173	0.77	1.53	5.67	2.41	7.06	6.31	0.84	140	150	636	28	71	83	97	83	323	164	8.2	3.4
GC06/215-216	2319	0.77	1.34	5.26	2.09	6.34	5.74	0.79	135	138	598	27	64	70	76	76	300	155	8.9	3.0
GC06/220-221	2440	0.92	1.39	5.80	2.15	6.48	5.86	0.81	130	128	590	26	61	64	60	73	312	165	7.9	2.9
GC06/226-227	2587	0.99	1.48	5.38	2.29	7.00	6.14	0.83	136	141	595	27	65	69	70	78	291	155	8.0	2.6
GC06/233-234	2757	1.02	1.46	5.84	2.26	6.90	6.29	0.89	138	138	633	27	63	68	69	76	301	165	7.6	2.5
GC06/239-240	2903	0.99	1.50	5.98	2.34	7.10	6.39	0.88	146	142	661	28	66	73	115	77	325	163	7.8	2.9
GC06/244-245	3025	0.81	1.34	6.16	2.13	6.32	5.76	0.83	132	135	623	26	62	76	90	72	347	154	7.6	3.1
GC06/255-256	3293	0.84	1.35	6.43	2.15	6.37	5.81	0.84	136	138	639	26	60	69	102	71	365	152	7.7	3.3
GC06/261-262	3439	0.75	1.25	6.10	2.05	5.84	5.38	0.76	123	125	604	25	57	66	77	67	353	136	6.9	3.1
GC06/266-267	3561	0.86	1.35	6.90	2.28	6.49	5.98	0.84	138	143	656	28	63	71	84	73	401	150	7.6	3.3

Table 4.3 *(continued)*

Sample ID	La	Ce	Pr	Nd	Sm	Eu	Gd	Tb	Dy	Ho	Er	Tm	Yb	Lu
	µg/g													
GC06/1-2	25	54	6.4	25	5.6	1.5	5.5	0.9	5.0	1.0	2.7	0.4	2.4	0.4
GC06/5-6	24	52	6.1	24	5.4	1.4	5.5	0.9	4.8	0.9	2.6	0.4	2.3	0.3
GC06/9-10	24	52	6.2	24	5.6	1.4	5.4	0.8	4.9	0.9	2.7	0.4	2.4	0.4
GC06/15-16	27	58	7.0	26	6.0	1.5	5.6	0.8	4.7	1.0	2.6	0.4	2.4	0.3
GC06/25-26	24	50	6.0	24	5.3	1.4	5.4	0.8	4.7	0.9	2.4	0.4	2.4	0.3
GC06/29-30	24	50	6.0	23	5.3	1.3	5.2	0.8	4.6	0.9	2.3	0.4	2.4	0.3
GC06/33-34	24	51	6.1	24	5.1	1.4	5.5	0.8	4.6	0.9	2.5	0.4	2.4	0.4
GC06/38-39	23	50	5.9	23	5.2	1.4	5.3	0.9	4.7	0.9	2.5	0.4	2.3	0.3
GC06/43-44	24	52	6.2	24	5.4	1.5	5.5	0.9	4.6	1.0	2.6	0.4	2.4	0.3
GC06/49-50	23	49	5.8	22	5.2	1.3	5.3	0.8	4.4	0.9	2.3	0.4	2.2	0.3
GC06/54-55	25	53	6.3	24	5.6	1.5	5.5	0.8	4.7	1.0	2.7	0.4	2.5	0.3
GC06/57-58	24	51	6.0	23	5.3	1.4	5.4	0.8	4.8	0.9	2.6	0.4	2.2	0.3
GC06/61-62	23	50	5.9	23	5.2	1.3	5.2	0.8	4.6	0.9	2.4	0.4	2.2	0.3
GC06/66-67	23	50	5.8	23	4.9	1.3	5.2	0.8	4.5	0.9	2.5	0.4	2.4	0.3
GC06/70-71	23	50	5.8	22	5.2	1.3	5.2	0.8	4.6	0.9	2.5	0.4	2.4	0.3
GC06/74-75	24	52	6.1	24	5.3	1.4	5.4	0.8	4.9	0.9	2.5	0.4	2.4	0.3
GC06/78-79	24	51	5.9	24	5.6	1.4	5.3	0.8	4.8	0.9	2.5	0.4	2.3	0.3
GC06/81-82	26	55	6.5	25	6.1	1.5	5.6	0.9	5.0	1.0	2.8	0.4	2.5	0.3
GC06/90-91	25	53	6.2	25	5.3	1.4	5.1	0.9	4.8	1.0	2.5	0.4	2.4	0.3
GC06/95-96	25	53	6.1	24	5.4	1.4	5.4	0.8	4.7	0.9	2.5	0.4	2.3	0.4
GC06/99-100	24	53	6.0	24	5.4	1.4	5.2	0.8	4.7	0.9	2.6	0.4	2.5	0.4
GC06/103-104	24	51	6.1	23	5.2	1.4	5.1	0.8	4.4	0.9	2.4	0.4	2.3	0.3
GC06/108-109	23	48	5.8	22	4.9	1.3	5.0	0.7	4.4	0.8	2.3	0.3	2.1	0.3
GC06/113-114	24	52	6.0	24	5.3	1.5	5.3	0.8	4.5	0.9	2.4	0.4	2.4	0.3
GC06/117-118	26	56	6.7	26	5.8	1.5	5.6	0.8	5.0	1.0	2.7	0.4	2.6	0.3
GC06/123-124	24	51	6.1	24	5.3	1.4	5.4	0.8	4.5	0.9	2.5	0.4	2.4	0.3
GC06/132-133	25	54	6.4	25	5.6	1.4	5.6	0.8	4.9	1.0	2.7	0.4	2.5	0.3
GC06/136-137	23	51	6.0	23	5.2	1.3	5.2	0.8	4.5	0.9	2.4	0.3	2.3	0.3
GC06/139-140	23	50	5.8	23	5.1	1.3	5.1	0.8	4.4	0.9	2.3	0.3	2.2	0.3
GC06/143-144	24	52	6.1	24	5.4	1.4	5.4	0.8	4.6	1.0	2.6	0.4	2.3	0.3
GC06/146-147	24	51	6.1	24	5.3	1.4	5.4	0.8	4.7	0.9	2.5	0.4	2.4	0.3
GC06/150-151	23	50	5.9	23	5.1	1.3	5.0	0.8	4.6	0.9	2.5	0.4	2.3	0.3
GC06/154-155	24	51	5.9	23	5.1	1.4	5.2	0.8	4.5	0.9	2.4	0.4	2.2	0.3
GC06/159-160	23	50	6.0	23	5.2	1.3	5.1	0.8	4.5	0.9	2.5	0.4	2.3	0.3
GC06/165-166	22	49	5.9	22	5.0	1.2	5.1	0.8	4.4	0.9	2.4	0.4	2.2	0.3

Table 4.3 *(continued)*

Sample ID	La	Ce	Pr	Nd	Sm	Eu	Gd	Tb	Dy	Ho	Er	Tm	Yb	Lu
	µg/g													
GC06/170-171	22	47	5.6	22	4.8	1.3	4.9	0.8	4.3	0.8	2.3	0.4	2.3	0.3
GC06/174-175	24	51	6.1	24	5.4	1.3	5.2	0.8	4.5	0.9	2.5	0.4	2.3	0.3
GC06/178-179	23	48	5.8	22	5.3	1.3	5.0	0.8	4.4	0.9	2.4	0.3	2.2	0.3
GC06/182-183	23	48	5.8	22	5.0	1.3	5.0	0.8	4.4	0.9	2.3	0.3	2.2	0.3
GC06/186-187	23	49	5.9	23	5.5	1.3	5.1	0.8	4.5	0.9	2.5	0.3	2.2	0.4
GC06/195-196	23	50	5.9	23	5.1	1.3	4.9	0.8	4.5	0.9	2.3	0.4	2.3	0.3
GC06/200-201	25	52	6.2	24	5.3	1.4	5.4	0.8	4.5	0.9	2.4	0.4	2.3	0.3
GC06/205-206	23	48	5.7	22	5.0	1.3	4.9	0.8	4.4	0.9	2.3	0.3	2.2	0.3
GC06/209-210	24	50	6.0	23	5.4	1.3	5.1	0.8	4.5	0.9	2.3	0.4	2.3	0.3
GC06/215-216	23	47	5.6	22	5.0	1.3	5.1	0.8	4.2	0.9	2.2	0.4	2.2	0.3
GC06/220-221	23	48	5.5	22	5.1	1.3	5.0	0.8	4.4	0.9	2.4	0.3	2.2	0.3
GC06/226-227	22	47	5.8	22	5.1	1.4	5.1	0.8	4.4	0.9	2.3	0.3	2.3	0.3
GC06/233-234	23	48	5.7	23	4.9	1.3	4.9	0.8	4.4	0.9	2.4	0.3	2.2	0.3
GC06/239-240	23	50	5.7	23	5.2	1.4	5.3	0.8	4.5	0.9	2.4	0.4	2.5	0.3
GC06/244-245	23	49	5.8	23	5.0	1.3	5.2	0.8	4.3	0.9	2.3	0.3	2.2	0.3
GC06/255-256	22	48	5.7	23	4.9	1.3	4.9	0.8	4.5	0.9	2.4	0.4	2.2	0.3
GC06/261-262	21	43	5.1	20	4.6	1.2	4.6	0.7	4.1	0.8	2.2	0.3	2.0	0.3
GC06/266-267	23	48	5.7	22	5.0	1.4	5.0	0.8	4.5	0.9	2.3	0.4	2.2	0.3

Table 4.3 *(continued)*

Sample ID	$CaCO_3$	TOC	TN	TOC/TN
	wt. %			Atomic
GC06/1-2	9.8	1.06	0.11	10.9
GC06/5-6	9.8	1.05	0.11	10.8
GC06/9-10	9.4	1.05	0.11	11.7
GC06/15-16	7.5	0.84	0.06	17.3
GC06/25-26	8.0	1.60	0.13	13.9
GC06/29-30	10.5	1.22	0.13	11.3
GC06/33-34	11.1	1.17	0.12	11.2
GC06/38-39	10.7	1.16	0.12	11.6
GC06/43-44	11.0	1.13	0.11	11.6
GC06/49-50	10.1	1.14	0.11	12.0
GC06/54-55	10.8	1.18	0.11	12.4
GC06/57-58	10.4	1.12	0.11	12.0
GC06/61-62	9.8	1.20	0.11	13.0
GC06/66-67	10.7	1.12	0.11	11.6
GC06/70-71	11.0	1.05	0.11	11.3

Table 4.3 *(continued)*

Sample ID	**$CaCO_3$**	**TOC**	**TN**	**TOC/TN**
	wt. %			Atomic
GC06/74-75	9.9	1.14	0.10	13.4
GC06/78-79	9.4	1.13	0.10	13.7
GC06/81-82	10.8	1.08	0.10	13.1
GC06/90-91	10.4	0.97	0.09	12.4
GC06/95-96	10.7	1.03	0.10	12.4
GC06/99-100	11.8	1.03	0.10	11.8
GC06/103-104	11.2	1.02	0.10	12.2
GC06/108-109	10.3	1.03	0.09	12.7
GC06/113-114	7.2	1.36	0.10	16.3
GC06/117-118	10.5	1.05	0.10	12.8
GC06/123-124	10.2	1.04	0.10	12.0
GC06/132-133	10.4	1.13	0.10	12.6
GC06/136-137	7.8	1.38	0.10	16.3
GC06/139-140	10.8	1.04	0.10	12.2
GC06/143-144	9.9	1.09	0.10	13.3
GC06/146-147	10.9	1.11	0.10	13.2
GC06/150-151	9.7	1.05	0.10	12.6
GC06/154-155	9.8	1.01	0.09	13.2
GC06/159-160	10.8	1.07	0.09	13.5
GC06/165-166	11.7	0.99	0.09	13.3
GC06/170-171	10.3	0.97	0.09	12.4
GC06/174-175	11.3	1.05	0.09	13.2
GC06/178-179	12.9	0.96	0.09	12.6
GC06/182-183	12.0	1.00	0.09	12.8
GC06/186-187	9.6	1.25	0.09	16.4
GC06/195-196	10.8	1.23	0.09	16.4
GC06/200-201	13.0	1.01	0.09	13.1
GC06/205-206	13.2	0.96	0.08	13.3
GC06/209-210	12.2	1.15	0.10	13.9
GC06/215-216	12.8	0.90	0.08	13.0
GC06/220-221	14.0	0.91	0.08	13.3
GC06/226-227	10.0	1.15	0.08	16.6
GC06/233-234	12.7	0.88	0.08	13.5
GC06/239-240	13.5	0.81	0.07	12.6
GC06/244-245	14.6	0.88	0.07	14.2
GC06/255-256	15.0	0.78	0.07	12.7
GC06/261-262	15.6	0.83	0.07	13.5
GC06/266-267	15.9	0.81	0.07	13.1

Table 4.4: *Carbon isotopic ($\delta^{13}C_{org}$) and geochemical composition of the silicate fraction of SSK40/GC10 core sediments.*

Sample ID	$\delta^{13}C_{org}$	Na	Mg	Al	Si	P	K	Ca	Ti	Fe	V	Cr	Mn	Co	Ni	Cu	Zn	As	Rb	Sr	Mo	Ba
	‰	wt. %									µg/g											
GC06/1-2/S	-19.9	0.75	1.03	7.68	25.51	0.04	1.30	0.59	1.16	6.27	141	219	416	14	91	64	50	0.67	90	92	2.32	234
GC06/5-6/S	-19.5	0.73	1.04	7.64	25.23	0.04	1.29	0.55	1.14	6.35	165	177	405	13	72	64	41	1.01	87	89	5.61	198
GC06/9-10/S	-19.4	0.67	0.99	7.48	24.71	0.03	1.26	0.44	1.11	6.13	142	190	378	13	79	58	43	0.80	90	84	3.19	208
GC06/15-16/S	-20.3	1.15	1.08	6.84	27.52	0.03	1.17	1.48	1.46	6.12	202	201	570	15	78	56	53	0.95	66	135	5.49	219
GC06/25-26/S	-19.6	0.66	1.01	7.71	25.48	0.03	1.35	0.37	1.13	6.51	148	166	356	12	68	59	41	1.00	92	77	5.19	205
GC06/29-30/S	-19.5	0.68	0.99	7.55	25.07	0.04	1.34	0.40	1.09	6.21	149	153	358	12	60	57	41	0.98	92	82	4.71	209
GC06/33-34/S	-19.8	0.69	0.97	7.59	25.44	0.03	1.34	0.41	1.12	6.13	147	171	360	12	69	58	36	0.97	94	82	5.21	218
GC06/38-39/S	-19.2	0.65	1.00	7.64	25.17	0.04	1.37	0.37	1.11	6.44	152	181	367	12	76	61	47	1.01	94	80	5.53	228
GC06/43-44/S	-19.3	0.64	0.98	7.51	24.82	0.03	1.33	0.35	1.09	6.30	148	169	354	12	68	60	54	0.96	92	79	5.11	204
GC06/49-50/S	-19.4	0.66	1.02	7.71	25.18	0.03	1.38	0.39	1.10	6.43	151	180	368	13	75	62	48	1.00	92	81	5.41	210
GC06/54-55/S	-19.5	0.67	1.02	7.58	24.66	0.03	1.33	0.44	1.09	6.39	158	191	387	14	76	64	47	0.97	95	85	5.29	219
GC06/57-58/S	-19.2	0.66	1.04	7.71	24.96	0.03	1.37	0.39	1.10	6.48	152	188	365	13	77	61	51	0.92	93	81	5.57	213
GC06/61-62/S	-19.5	0.70	0.98	7.55	25.40	0.03	1.37	0.44	1.12	6.24	151	178	368	12	73	60	43	1.06	92	84	5.31	216
GC06/66-67/S	-19.7	0.71	0.98	7.47	25.01	0.03	1.35	0.45	1.11	6.12	153	189	386	13	79	60	44	0.91	92	91	4.16	214
GC06/70-71/S	-19.2	0.70	0.98	7.49	24.79	0.03	1.34	0.42	1.11	5.98	152	225	372	13	96	60	46	0.97	91	86	6.97	212
GC06/74-75/S	-19.3	0.74	1.02	7.58	25.95	0.03	1.39	0.48	1.15	6.35	148	186	365	12	75	59	44	0.99	88	85	5.13	220
GC06/78-79/S	-19.2	0.69	1.03	7.64	25.31	0.03	1.37	0.45	1.13	6.37	153	198	368	13	80	61	44	0.96	89	83	5.38	236
GC06/81-82/S	-19.4	0.71	1.06	7.71	25.51	0.03	1.36	0.47	1.15	6.54	153	177	371	12	72	57	38	0.95	89	84	4.72	203
GC06/90-91/S	-19.9	0.80	1.03	7.50	25.42	0.03	1.38	0.61	1.16	6.17	162	185	406	13	73	59	50	1.00	92	100	4.97	238

Table 4.4 *(continued)*

Sample ID	$\delta^{13}C_{org}$	Na	Mg	Al	Si	P	K	Ca	Ti	Fe	V	Cr	Mn	Co	Ni	Cu	Zn	As	Rb	Sr	Mo	Ba
	‰	wt. %									µg/g											
GC06/95-96/S	-19.5	0.79	1.00	7.46	25.58	0.03	1.38	0.56	1.15	6.01	159	194	394	13	74	57	51	0.97	91	97	5.18	230
GC06/99-100/S	-19.9	0.78	0.98	7.47	25.85	0.03	1.41	0.53	1.16	6.13	153	223	384	13	95	58	44	0.97	90	94	6.55	267
GC06/103-104/S	-19.7	0.74	0.95	7.37	25.45	0.03	1.34	0.49	1.15	6.09	153	199	379	12	83	56	42	0.98	88	90	5.82	230
GC06/108-109/S	-19.7	0.75	0.96	7.38	25.43	0.03	1.38	0.49	1.14	6.00	150	181	374	12	74	57	39	0.94	90	91	5.03	222
GC06/113-114/S	-19.6	0.76	0.97	7.32	25.70	0.03	1.39	0.48	1.15	6.26	154	187	379	13	79	60	43	0.96	91	88	5.43	236
GC06/117-118/S	-19.7	0.71	0.97	7.43	24.88	0.02	1.34	0.44	1.12	6.25	153	221	376	13	95	62	40	1.00	90	87	6.39	231
GC06/123-124/S	-19.4	0.65	0.99	7.61	25.22	0.03	1.40	0.37	1.09	6.30	143	192	347	12	75	58	39	0.97	94	79	5.41	222
GC06/132-133/S	-19.7	0.67	0.97	7.60	25.25	0.03	1.39	0.34	1.10	6.18	146	190	357	12	80	60	42	1.02	95	83	5.41	236
GC06/136-137/S	-19.7	0.74	0.92	7.46	25.74	0.03	1.37	0.46	1.14	5.95	146	181	357	12	74	57	52	0.97	92	91	5.21	232
GC06/139-140/S	-19.6	0.69	0.95	7.50	25.10	0.02	1.36	0.38	1.11	6.08	143	180	353	12	72	58	45	1.01	92	83	5.07	210
GC06/143-144/S	-19.4	0.66	0.99	7.61	25.23	0.03	1.38	0.37	1.10	6.37	151	180	361	13	73	59	48	0.97	95	83	4.75	232
GC06/146-147/S	-19.6	0.70	0.99	7.50	25.29	0.02	1.37	0.42	1.12	6.35	153	181	368	13	75	60	55	0.99	97	84	4.79	223
GC06/150-151/S	-19.4	0.65	0.95	7.57	25.57	0.03	1.41	0.34	1.12	6.10	133	221	350	13	96	59	46	0.78	97	82	0.95	225
GC06/154-155/S	-19.5	0.62	0.98	7.68	25.12	0.03	1.41	0.28	1.07	6.17	142	180	336	12	74	54	43	0.95	98	78	5.09	212
GC06/159-160/S	-19.9	0.66	0.94	7.47	24.79	0.03	1.35	0.33	1.09	5.98	146	163	348	12	66	58	48	0.99	95	80	4.30	220
GC06/165-166/S	-19.9	0.79	0.96	7.29	25.40	0.03	1.37	0.57	1.12	5.97	156	182	381	13	74	58	44	0.96	91	99	4.80	232
GC06/170-171/S	-19.3	0.65	0.95	7.51	24.78	0.03	1.36	0.33	1.09	6.03	145	174	346	12	69	56	44	0.99	96	81	4.59	225
GC06/174-175/S	-20.0	0.82	0.97	7.35	25.53	0.02	1.37	0.57	1.13	6.01	153	175	390	12	68	54	49	0.98	90	99	4.67	233
GC06/178-179/S	-19.7	0.76	0.93	7.25	25.25	0.03	1.36	0.49	1.12	5.83	128	214	372	12	90	54	39	0.66	93	95	1.20	218
GC06/182-183/S	-19.7	0.75	0.96	7.34	25.09	0.03	1.37	0.46	1.10	5.98	150	200	373	13	81	56	47	1.00	92	91	5.36	231
GC06/186-187/S	-19.6	0.72	0.98	7.45	25.41	0.03	1.38	0.42	1.12	6.06	147	187	364	12	78	56	48	0.96	92	88	4.86	222

Table 4.4 *(continued)*

Sample ID	$\delta^{13}C_{org}$	Na	Mg	Al	Si	P	K	Ca	Ti	Fe	V	Cr	Mn	Co	Ni	Cu	Zn	As	Rb	Sr	Mo	Ba
	‰	wt. %									µg/g											
GC06/195-196/S	-19.5	0.79	1.00	7.48	25.63	0.03	1.38	0.53	1.13	6.06	151	188	379	12	72	54	46	0.96	89	94	4.70	227
GC06/200-201/S	-19.6	0.86	0.96	7.40	26.26	0.03	1.42	0.61	1.15	5.82	146	185	369	11	72	53	43	0.97	88	101	5.20	234
GC06/205-206/S	-19.8	0.81	0.92	7.25	25.72	0.02	1.35	0.56	1.13	5.69	143	168	362	11	63	49	37	0.97	85	98	4.77	220
GC06/209-210/S	-20.0	0.78	0.96	7.37	25.25	0.02	1.40	0.48	1.10	5.91	145	176	359	12	68	52	41	0.93	92	94	4.61	224
GC06/215-216/S	-19.9	0.83	0.92	7.29	25.52	0.02	1.34	0.57	1.13	5.64	136	199	370	12	80	51	47	0.76	89	101	2.64	222
GC06/220-221/S	-19.4	0.83	0.92	7.23	25.57	0.03	1.37	0.57	1.13	5.76	148	190	370	12	75	53	40	0.95	88	101	4.91	228
GC06/226-227/S	-19.9	0.85	0.93	7.28	25.95	0.02	1.37	0.59	1.15	5.78	147	154	364	11	57	50	40	0.93	86	98	3.92	217
GC06/233-234/S	-19.6	0.88	0.94	7.34	26.45	0.02	1.38	0.65	1.17	5.95	149	185	377	12	73	53	40	0.94	85	101	4.73	219
GC06/239-240/S	-19.5	0.86	0.90	7.26	26.19	0.02	1.35	0.57	1.16	5.69	149	202	369	11	83	52	35	0.94	85	101	5.47	218
GC06/244-245/S	-20.4	0.88	0.97	7.26	26.57	0.02	1.36	0.69	1.19	6.36	155	178	401	13	70	54	43	1.00	84	109	4.75	227
GC06/255-256/S	-20.3	0.86	0.88	6.74	24.89	0.02	1.27	0.69	1.11	5.52	151	189	384	12	75	51	35	0.93	82	111	5.28	213
GC06/261-262/S	-19.7	0.89	0.91	7.14	26.26	0.02	1.34	0.64	1.18	5.80	150	203	380	12	83	52	38	1.00	83	103	6.04	215
GC06/266-267/S	-20.1	0.88	0.91	7.07	25.94	0.03	1.32	0.63	1.15	5.75	148	172	378	11	67	50	44	0.94	83	105	4.56	230

Table 4.4 *(continued)*

Sample ID	La	Ce	Pr	Nd	Sm	Eu	Gd	Tb	Dy	Ho	Er	Tm	Yb	Lu	Th	U
	μg/g															
GC06/1-2/S	16	31	3.4	12.0	2.5	0.7	2.0	0.3	2.0	0.4	1.3	0.2	1.4	0.2	10.0	1.5
GC06/5-6/S	16	31	3.4	11.9	2.1	0.6	2.0	0.3	2.0	0.4	1.2	0.2	1.4	0.2	10.4	1.5
GC06/9-10/S	15	28	3.1	10.9	2.1	0.5	1.7	0.3	1.8	0.4	1.2	0.2	1.3	0.2	9.9	1.4
GC06/15-16/S	21	42	4.7	16.7	3.3	0.9	2.7	0.4	2.7	0.6	1.5	0.2	1.7	0.2	11.3	1.6
GC06/25-26/S	14	28	3.0	10.5	1.9	0.5	1.5	0.3	1.7	0.4	1.1	0.2	1.3	0.2	10.0	1.4
GC06/29-30/S	15	28	3.0	10.8	2.0	0.6	1.8	0.3	1.8	0.4	1.2	0.2	1.3	0.2	9.9	1.4
GC06/33-34/S	15	28	3.1	10.4	1.9	0.6	1.8	0.3	1.8	0.4	1.1	0.2	1.3	0.2	10.3	1.4
GC06/38-39/S	15	28	3.2	10.9	1.9	0.5	1.7	0.3	1.8	0.4	1.2	0.2	1.3	0.2	9.8	1.4
GC06/43-44/S	14	28	3.1	10.5	1.9	0.5	1.7	0.3	1.8	0.4	1.1	0.2	1.3	0.2	9.9	1.4
GC06/49-50/S	15	29	3.1	10.9	2.1	0.6	1.7	0.3	1.8	0.4	1.1	0.2	1.3	0.2	9.8	1.4
GC06/54-55/S	15	30	3.2	11.3	2.2	0.6	1.8	0.3	1.9	0.4	1.2	0.2	1.3	0.2	10.2	1.4
GC06/57-58/S	15	28	3.1	10.8	2.1	0.6	1.8	0.3	1.8	0.4	1.1	0.2	1.3	0.2	9.9	1.4
GC06/61-62/S	15	30	3.2	11.1	2.0	0.6	1.8	0.3	1.8	0.4	1.1	0.2	1.4	0.2	10.0	1.4
GC06/66-67/S	16	31	3.4	11.8	2.3	0.6	2.0	0.3	1.9	0.4	1.2	0.2	1.3	0.2	10.1	1.4
GC06/70-71/S	15	30	3.3	11.2	2.0	0.6	1.8	0.3	1.9	0.4	1.2	0.2	1.3	0.2	10.1	1.4
GC06/74-75/S	15	30	3.3	11.4	2.2	0.6	1.8	0.3	1.8	0.4	1.2	0.2	1.3	0.2	10.1	1.5
GC06/78-79/S	15	28	3.1	10.8	2.1	0.6	1.8	0.3	1.8	0.4	1.2	0.2	1.3	0.2	9.9	1.4
GC06/81-82/S	15	29	3.3	11.3	2.2	0.6	1.9	0.3	1.8	0.4	1.2	0.2	1.4	0.2	10.0	1.4
GC06/90-91/S	17	32	3.6	12.4	2.4	0.7	1.9	0.3	2.0	0.4	1.3	0.2	1.4	0.2	10.7	1.5
GC06/95-96/S	17	33	3.7	12.7	2.4	0.7	2.0	0.3	2.1	0.4	1.3	0.2	1.5	0.2	10.4	1.5
GC06/99-100/S	17	32	3.5	12.5	2.3	0.6	1.9	0.3	1.9	0.4	1.2	0.2	1.3	0.2	10.3	1.5
GC06/103-104/S	16	31	3.4	11.7	2.3	0.6	1.9	0.3	2.0	0.4	1.2	0.2	1.3	0.2	10.3	1.5
GC06/108-109/S	16	31	3.4	12.0	2.2	0.6	1.9	0.3	1.9	0.4	1.3	0.2	1.3	0.2	10.2	1.4
GC06/113-114/S	16	30	3.4	11.5	2.1	0.6	1.8	0.3	1.9	0.4	1.3	0.2	1.3	0.2	10.1	1.5
GC06/117-118/S	15	30	3.3	11.3	2.1	0.6	1.9	0.3	1.9	0.4	1.2	0.2	1.3	0.2	9.9	1.4
GC06/123-124/S	15	29	3.2	11.4	2.1	0.6	1.7	0.3	1.8	0.4	1.2	0.2	1.3	0.2	9.9	1.4
GC06/132-133/S	15	29	3.2	11.2	1.9	0.5	1.7	0.3	1.8	0.4	1.2	0.2	1.4	0.2	10.0	1.4
GC06/136-137/S	16	31	3.5	11.4	2.2	0.6	1.9	0.3	1.9	0.4	1.2	0.2	1.4	0.2	10.3	1.5
GC06/139-140/S	15	30	3.4	11.0	2.1	0.5	1.8	0.3	1.7	0.4	1.1	0.2	1.3	0.2	10.0	1.5
GC06/143-144/S	16	30	3.3	11.4	2.1	0.6	1.8	0.3	1.8	0.4	1.2	0.2	1.4	0.2	10.0	1.5
GC06/146-147/S	16	31	3.3	11.8	2.1	0.6	1.8	0.3	1.9	0.4	1.2	0.2	1.4	0.2	10.6	1.5
GC06/150-151/S	16	30	3.4	11.5	2.0	0.6	1.8	0.3	1.9	0.4	1.2	0.2	1.4	0.2	10.2	1.5
GC06/154-155/S	15	29	3.1	10.7	2.0	0.6	1.6	0.3	1.7	0.4	1.2	0.2	1.3	0.2	10.1	1.4
GC06/159-160/S	15	29	3.3	11.3	2.0	0.6	1.8	0.3	1.8	0.4	1.2	0.2	1.3	0.2	10.2	1.5
GC06/165-166/S	16	32	3.5	12.2	2.3	0.6	1.9	0.3	1.9	0.4	1.2	0.2	1.3	0.2	9.9	1.4

Table 4.4 *(continued)*

Sample ID	La	Ce	Pr	Nd	Sm	Eu	Gd	Tb	Dy	Ho	Er	Tm	Yb	Lu	Th	U
	μg/g															
GC06/170-171/S	15	30	3.2	11.5	2.0	0.5	1.6	0.3	1.7	0.4	1.1	0.2	1.3	0.2	9.9	1.4
GC06/174-175/S	16	31	3.4	11.5	2.0	0.6	2.0	0.3	2.0	0.4	1.2	0.2	1.4	0.2	9.9	1.5
GC06/178-179/S	16	31	3.4	12.0	2.3	0.6	1.9	0.3	1.9	0.4	1.2	0.2	1.4	0.2	9.8	1.5
GC06/182-183/S	16	31	3.4	11.8	2.2	0.6	1.9	0.3	1.9	0.4	1.2	0.2	1.4	0.2	10.1	1.5
GC06/186-187/S	15	29	3.2	11.0	2.1	0.6	1.8	0.3	1.8	0.4	1.2	0.2	1.3	0.2	9.8	1.4
GC06/195-196/S	16	31	3.4	12.0	2.3	0.6	1.9	0.3	1.9	0.4	1.2	0.2	1.3	0.2	9.8	1.5
GC06/200-201/S	17	34	3.7	13.2	2.4	0.7	2.0	0.3	1.9	0.4	1.2	0.2	1.4	0.2	10.2	1.6
GC06/205-206/S	16	32	3.5	11.9	2.3	0.6	2.0	0.3	1.9	0.4	1.3	0.2	1.3	0.2	9.9	1.5
GC06/209-210/S	16	30	3.4	11.9	2.2	0.6	1.8	0.3	1.8	0.4	1.2	0.2	1.3	0.2	9.9	1.5
GC06/215-216/S	16	32	3.6	12.3	2.3	0.6	2.0	0.3	2.0	0.4	1.2	0.2	1.4	0.2	9.9	1.5
GC06/220-221/S	16	31	3.6	12.5	2.3	0.7	2.0	0.3	2.1	0.4	1.3	0.2	1.4	0.2	10.2	1.6
GC06/226-227/S	16	32	3.5	12.1	2.2	0.7	2.0	0.3	1.9	0.4	1.2	0.2	1.4	0.2	9.9	1.5
GC06/233-234/S	16	30	3.3	11.6	2.2	0.6	1.9	0.3	1.9	0.4	1.2	0.2	1.4	0.2	9.6	1.5
GC06/239-240/S	16	31	3.4	12.2	2.1	0.6	1.9	0.3	1.9	0.4	1.2	0.2	1.3	0.2	9.6	1.5
GC06/244-245/S	16	31	3.6	12.3	2.4	0.6	1.9	0.3	1.9	0.4	1.2	0.2	1.4	0.2	9.6	1.5
GC06/255-256/S	16	32	3.6	12.5	2.4	0.7	1.9	0.3	2.0	0.4	1.2	0.2	1.4	0.2	9.5	1.5
GC06/261-262/S	17	32	3.6	12.5	2.4	0.7	2.4	0.3	2.0	0.4	1.2	0.2	1.3	0.2	9.8	1.5
GC06/266-267/S	17	33	3.7	12.4	2.5	0.7	1.9	0.3	2.0	0.4	1.3	0.2	1.4	0.2	10.0	1.6

Traps (~75; Das and Krishnaswami, 2007), their possible sediment sources.

4.3.1 Discussion

The sedimentary carbonates are mostly supplied by biogenic sources, whereas aluminium is supplied through detrital inputs. The TOC/Al ratios, excluding two episodes with higher ratios (Fig. 4.6), by and large show no major regime shift (Fig. 4.6). In contrast, the $CaCO_3$/Al ratios show distinctly higher values before 1600 yr BP (2.0 ± 0.4) than that (1.4 ± 0.2) for the last 1600 yr (Fig. 4.6). The $CaCO_3$/Al ratio, therefore, may reflect the relative proportion of detrital to biogenic input to the core site. The lowering of the $CaCO_3$/Al ratio during the last 1.6 kyr BP can be attributed either to a relative increase in detrital sediment flux or a decrease in biogenic carbonate production. Considering no major shift in the TOC/Al ratios (another proxy for oceanic productivity), the recent decline in $CaCO_3$/Al is more likely a result of an increase in sediment flux from the continent to the Arabian Sea.

Figure 4.6 depicts the down-core variation of various weathering indices, such as Mg/Al, Rb/Sr, K/Al, and CIA*. These indices represent abundance ratios of mobile (K, Mg, Sr) to immobile (Al, Rb) elements. An increase in chemical weathering intensity is expected to release the mobile elements from sediments to the dissolved phase, which in turn should lower their concentrations (relative to immobile elements) in sediments. All these proxies indicate a synchronous increase in chemical weathering intensity from 1600 yr BP to the present (Fig. 4.6). The down-core variation in the Rb/Sr ratios shows distinctly different values before (0.24 ± 0.03) and after (0.34 ± 0.03) 1.6 kyr BP. Consistently, the Mg/Al ratios also show a systematically lower value in the upper part of the core (0.31 ± 0.01) than that before 1.6 kyr BP (0.33 ± 0.01). This decline in Mg/Al ratio (Fig. 4.6) is attributable to the release of Mg to the dissolved phase due to increased chemical weathering of Mg-rich silicate and/or dolomitic carbonates. The K/Al ratios is a reliable chemical weathering proxy (Limmer et al., 2012; Miriyala et al., 2017), temporal trends of K/Al shows relatively lower values in samples younger than 1600 yrs BP. The K/Al trend confirm a recent intensification of continental weathering (Fig. 4.6). Similar to all these indices, the CIA* values also shift towards an increased value since 1.6 kyr BP to present with minor fluctuations. The samples deposited after 1.6 kyr BP has a higher CIA* value (78 ± 1) than those deposited before this time (77 ± 1; Fig. 4.6). The increased CIA* value, together with temporal trends of other proxies, establishes a strong shift in continental weathering pattern towards intensification of chemical weathering since 1.6 kyr BP.

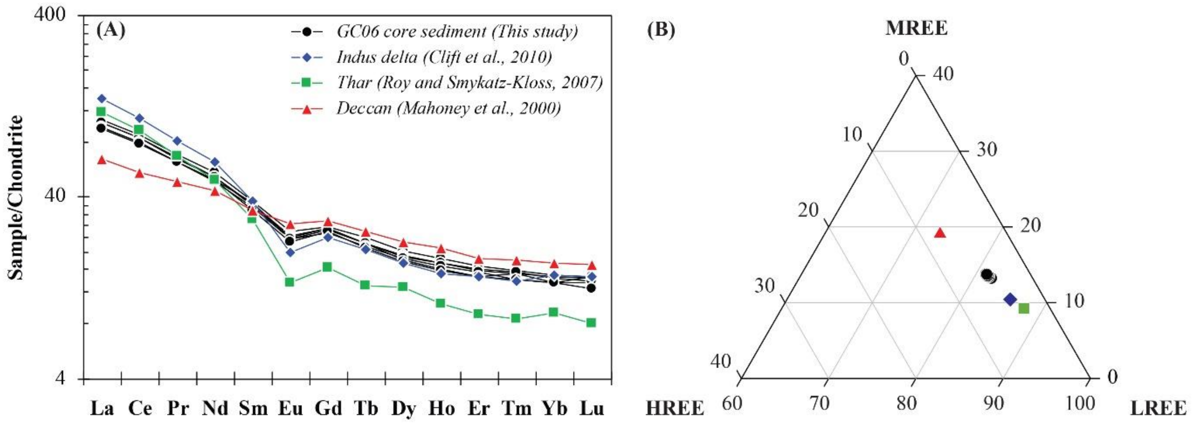

Figure 4.7. *Insignificant change in (A) chondrite-normalized REE pattern for five selected depths and (B) LREE-MREE-HREE ternary plot of all the samples indicates no major change in the sediment provenance during the studied period. For reference, REE compositions for possible major sources (e.g. Indus River, Thar Desert and Deccan basalts) are also shown here.*

Another possible explanation for the observed geochemical variations could be the relative change in sediment contribution from different provenances. The major detrital sources to the SSK40/GC06 core site are Indus River, Deccan Traps, and Thar Desert (cf. Chapter 2; Fig. 2.3). Recent estimations show that the aeolian supply (0.29-1.05 gm/cm^2/kyr) is insignificant compared to the riverine fluxes (~160 gm/cm^2/kyr) to offshore western India (Clift et al., 2020). There are no major Deccan-flowing rivers falling closer to this studied location (cf. Chapter 2; Fig. 2.3). The major river systems from the Traps (e.g., Tapi and Narmada) supply sediments to the south of this location, which may not be efficiently transported to the core site mainly due to non-favourable (clockwise) oceanic circulation during the monsoon period and high (Indus) sediment discharge from the north (cf. Chapter 2; Fig. 2.3). The Indus River, therefore, is likely to be the dominant source for the SSK40/GC06 sediments. This proposition draws support from the similarity of REE patterns between the core samples and the Indus river sediments (Fig. 4.7). The REE patterns do not alter significantly during sediment transport and chemical weathering processes, and hence, can serve as a reliable provenance indicator (Limmer et al., 2012; Nath et al., 2000). The chondrite-normalized REE patterns are similar to that of the Indus River sediments (aeolian input and Deccan Traps; Fig. 4.7). We have also evaluated the distribution of LREE (La-Nd), MREE (Sm-Dy), and HREE (Ho-Lu) of the SSK40/GC06 sediments in a ternary plot and compared these data with representative compositions for major sources (Fig. 4.7B). These data fall closer to the Indus sediment composition, ascertaining the dominancy of Indus in supplying sediments with minor contributions from other sources to the core site. The REE patterns in the ternary plot show no major temporal changes, which confirms the minimal change in sediment provenance during the late Holocene period. Similar to our observation, there exists several sediment chemistry data from the Bay of Bengal (Peketi et al., 2020), Arabian Sea (Limmer et al., 2012), South China Sea (Wan et al., 2015), and Central Africa (Bayon et al., 2012) showing recent intensification of chemical weathering in watersheds. The exact timing of this shift, however, is found to be different for these sites, which can be due to chronological uncertainties and sediment residence time in the flood plains. Our observed trend is synchronous with that reported in the South China Sea, and hence, a similar sediment storage time (~500 years; Wan et al., 2015 is also expected for the basin investigated herein. One possible factor that can influence this weathering intensification is climatic change. To evaluate this proposition, we have assessed several past climatic records available in the literature, such as $\delta^{18}O$ of speleothem (Kathayat et al., 2017) and planktonic foraminifera (Staubwasser et al., 2003), the abundance of *G. Bulloides* (Gupta et al., 2005) and varve thickness (von Rad et al., 1999), from and around the Arabian Sea region (Fig. 4.8). These proxies show no major change in the summer (southwest: SW) monsoon strength for the last 1.6 kyr BP, and hence, a climatic impact in intensifying the chemical erosion pattern seems less likely. On the contrary, the varve thickness data from the Makran coast (Fig. 4.8E) hint at the intensification of the winter (northeast: NE) monsoon during this period. This observed strengthening in NE monsoon at Makran, which receives significant NE monsoonal (~75-90 %) rainfall, may have limited influence on erosion pattern of the Indus basin (the dominant provenance to the SSK40/GC06 core site), which is mostly regulated by SW (85 % at Karachi; Lückge et al., 2001) rainfall. With no major SW monsoon change, the observed intensification in weathering, therefore, may not be linked to climatic forcing (Fig. 4.8).

Earlier studies from the South China Sea (Wan et al., 2015) and Africa (Bayon et al., 2012) have attributed a synchronous shift in weathering intensity to human-induced land-use patterns. A similar process involving increased agricultural practices, crop types, and their sustained production may also explain the observed weathering intensification in this study.

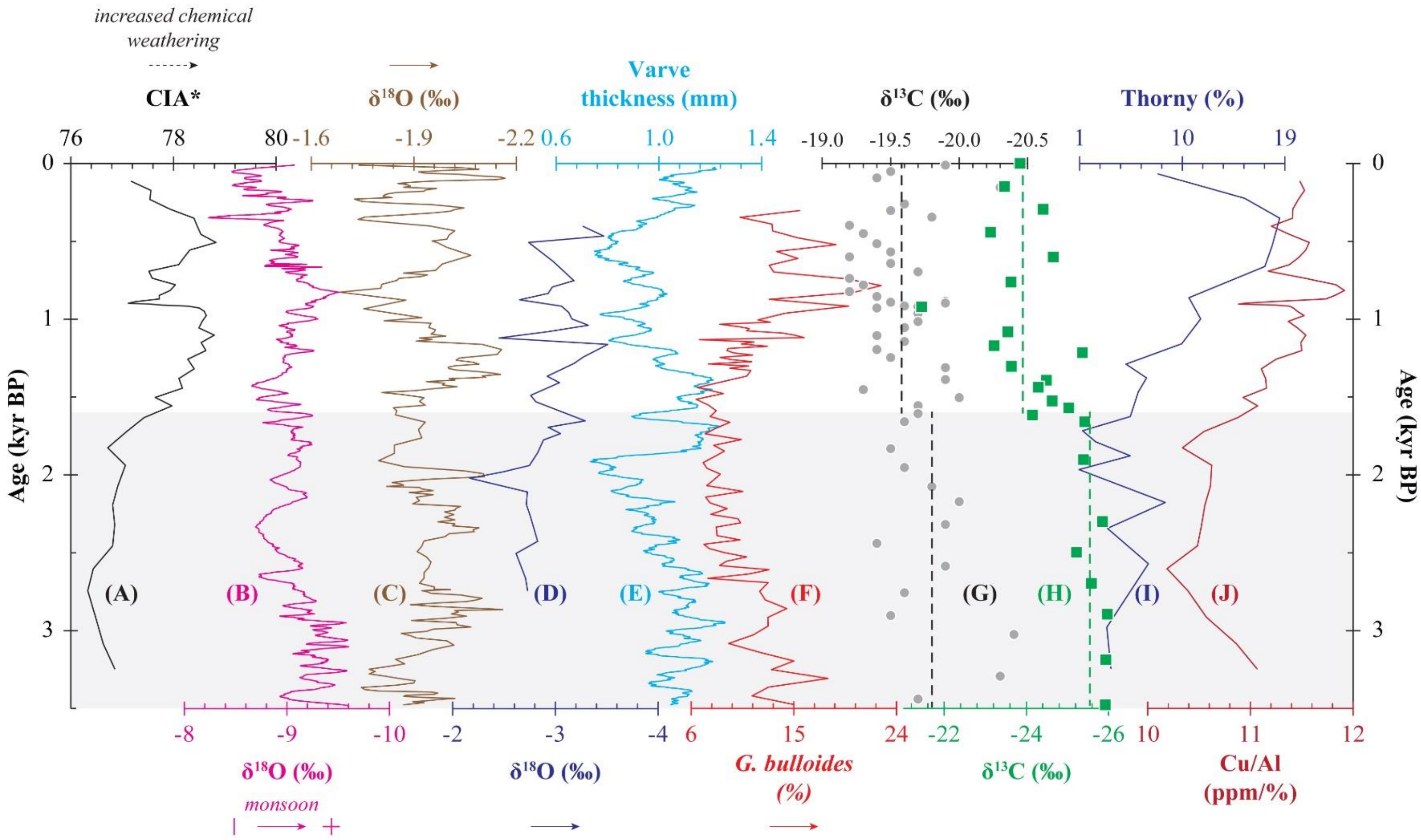

Figure 4.8. *Comparison of temporal variation of (A) Chemical Index of Alteration (modified CIA*) for SSK40/GC06 core sediments with available records for past climate and vegetation ((B) speleothem δ^{18}O (Kathayat et al., 2017)), (C, D) δ^{18}O ratios for G. Ruber (Staubwasser et al., 2003; Tiwari et al., 2006), (E) varve thickness (von Rad et al., 1999) (F) abundance of G. Bulloides (Gupta et al., 2005), (G, H) sedimentary δ^{13}C data for the Godavari basin (This study; Ponton et al., 2012), (I) thorny vegetation pattern (digitally extracted data from Zorzi et al., 2015) and (J) Cu/Al ratios (This study)) pattern. The dotted lines in the panel (G, H) stand for average δ^{13}C values for sediments deposited before and after 1600 yr BP.*

Similar C4 vegetation rise trends have also been documented using isotopic and pollen proxies from different parts of India (Sengupta et al., 2019; Sharma et al., 2020; Zorzi et al., 2015). These vegetation changes, however, are different than the near-constant $\delta^{13}C$ trend reported for the NE-dominated Makran region (Kahkashan et al., 2020). Considering the dominancy of SW monsoon in the source (Indus and western Indian) regions, it seems evident that the recent increase in C4 vegetation is not climatic-driven (Fig. 4.8) and may have linkages to land use patterns and ancient agricultural practices. The impact of human activities on erosional processes is also evident from high Cu/Al ratios (Fig. 4.8I) during the last 1.6 kyr as this heavy metal may reflect alloys production and their usage in agricultural practices. Historically, this period is contemporary to the Gupta dynasty in India, when large-scale development of irrigation, water harvesting systems, and sustained agricultural crop (such as rice, sugarcane, millet, etc.) productions were commenced (Fuller, 2006; Pandey, 2016). The human-induced rise in C4 vegetation, unlike tropical forests with deep roots, is expected to promote efficient sediment transport and intense erosion of young soils, which are characterized by faster weathering kinetics.

4.4 Conclusion

This study, based on the chemistry of two sediment cores (SSK440/GC10 and SSK40/GC06) from the eastern Arabian Sea, establishes the chemical erosion pattern during the late-Holocene period. The outcome shows that these core sites mainly receive sediments from the nearby river basins and aeolian dust from the Thar region. Depth profiles of Al-normalized ratios of multiple lithogenic elements (K, Fe, Ti, V, and Co) and CIA* values show that the relative supply from these provenances and chemical erosion pattern of the western Indian regions remain near-constant during 7.2-2.6 kyr BP. In contrast, a significant change in these weathering proxies was observed during the Roman Warm Period. Further, variations in several redox proxies (TOC/Al, Ba/Al, S/Al, EF_{Mo}, and EF_U) show significant fluctuation in the bottom water redox state during the studied period. The bottom water at the SSK40/GC10 location was mostly oxic, which shifted to a reducing condition since 4.2 kyr BP. This redox change is synchronous to the drought phase that occurred during this period. However, the geochemical signature of SSK40/GC06 core sediments establishes the intensification of chemical erosion since the last 1600 yr BP and its linkage with ancient agricultural practices. This observation also confirms that the contemporary river water chemistry has already been anthropogenically influenced and may not be a true representative for continental input in long-term chemical budgets. Several earlier studies, however, have used modern-day river data as continental input in oceanic budget calculations (e.g., $^{87}Sr/^{86}Sr$, $^{187}Os/^{188}Os$) over million-year timescales, which may not be strictly valid. Results are shown in this study, therefore, underscore a need to revise these calculations with appropriate riverine input and temporal changes in its composition, which may explain some of the existing imbalances in isotopic budgets.

Chapter 5

Himalayan Erosion Pattern during the Last Glacial-Interglacial Period: Evidence from Terrestrial Archives

5.1 Introduction

Chemical and isotopic investigations of terrestrial sedimentary records (such as lake, flood plain, and river section sediments) have been found successful in reconstructing past erosion patterns. As mentioned in the introductory chapter, several studies have interpreted the Himalayan erosion pattern using sediment records from the nearby ocean basins, the Bay of Bengal, and the Arabian Sea (Acharya and Chakrabarti, 2019; Galy et al., 2008; Goswami et al., 2012; Limmer et al., 2012; Peketi et al., 2020; Tripathy et al., 2011). Although the marine sedimentary records are capable of preserving the records of continental erosional patterns, sediment transportation from the continental sources to the ocean basins, sediment storage and the reworking of old sediments in the floodplains could introduce a time lag between the erosional signatures and sedimentary signatures (Armitage et al., 2013; Blöthe and Korup, 2013; Carretier et al., 2020; Clift and Giosan, 2014; Métivier et al., 1999; and the references therein). Earlier studies based on uranium-series disequilibria of river sediments have shown that the sediment residence time in the river floodplain could vary from a few hundred to kilo years depending on the sediment grain size (Chabaux et al., 2006; Garnet et al., 2007, 2010) whereas a few kyr in the Amazon basin (Dosseto et al., 2006). On the contrary, recent studies based on ^{10}Be cosmogenic nuclide of river sediments have shown a much shorter residence time (~1400 years) in the Ganga floodplain (Lupker et al., 2012). The terrestrial records provide a more robust picture of the continental erosion pattern with higher temporal resolution during the kilo-year scale, mainly due to their limited sediment sources and higher sedimentation rates.

This chapter presents the geochemical and Sr-Nd isotopic signatures of a river section sediments from the Zanskar River basin, upper Indus basin, to reconstruct the Himalaya erosion patterns during the last glacial and interglacial cycles.

5.2 Results and Discussion

Geochemical and Sr-Nd isotopic data for the PDM18 sediments are included in Table 5.1 and 5.2. The depth-age relation of this core has been discussed earlier (cf. Chapter 2; section 2.1.3.1). These radiocarbon ages show that the core preserves past erosion records between ~22.4 and 1.4 kyr BP, with no major hiatus. The average sedimentation rate of the PDM18 section is ~11.2 cm/kyr, with relatively enhanced rates in the middle part of the section. The Si concentrations of these sediments vary between 31.7 and 36.2 wt%, whereas the Al concentrations vary from 5.6 to 8.4 wt%. The average Si/Al ratio is 4.9 ± 0.6 (n = 35). This ratio is intermediate or comparable to that reported for rocks from the Higher Himalaya (HH) (4.8 ± 0.2; Galy and France-Lanord, 2001), Lesser Himalaya (LH) (4.1 ± 0.4; Galy and France-Lanord, 2001), and Tethyan Sedimentary Sequence (TSS) (4.3 ± 1.1; Richards et al., 2005). The depth profile of the Si/Al ratio is shown in Figure 5.1, which shows a major excursion at around 12-15 kyr. Consistent with Si/Al, the K/Al and CIA also show significant excursion around this period. The average CIA of these sediments is 60 ± 5, which falls between those reported for the HH (~65) and LH (~58) rocks (Singh et al., 2008). The CIA also increases to a value of ~72 during this excursion at around 13.5 kyr (Fig. 5.1). The PDM18 sediments are comprised of average TOC content of 0.2 ± 0.1 wt%. These sediments are rich in carbonates, with their $CaCO_3$ contents varying between 36 and 68 wt% (53 ± 11 wt%; n = 35). The high carbonate content is consistent with appreciable exposure of the Tethyan carbonates of Triassic-Cretaceous ages (Jonell et al., 2017; Fig. 2.5) in this basin. The depth profile of the carbonates shows significant change with about two-times increase in the carbonates in the upper part of the section (Fig. 5.1B).

The Sr and Nd isotopes of the PDM18 sediments are measured in their silicate fractions. The $^{87}Sr/^{86}Sr$ ratios of these sediments show significant variation (0.726 to 0.779) within the studied period. These Sr isotopic ratios fall between their possible sources, viz. HH (0.76 ± 0.03; Singh et al., 2008) and TSS (0.727 ± 0.012; Singh et al., 2008). Further, the average $^{87}Sr/^{86}Sr$ ratio (0.737 ± 0.010) of the PDM18 matches well with that reported for modern-day river sediments from the Zanskar River basin (0.729 ± 0.015; Jonell et al., 2017). The Zanskar River, as mentioned earlier (cf. Chapter 2, section 2.1.3.1), is composed of two major tributaries (Stod and Tsarap), and the PDM18 is presently part of the Tsarap sub-basin. Available limited Sr isotopic data (Jonell et al., 2017) constrains the $^{87}Sr/^{86}Sr$ ratios of the Stod (0.724 ± 0.0002; n = 2) and Tsarap (0.735 ± 0.020; excluding one outlier), and also, tributaries of the Tsarap

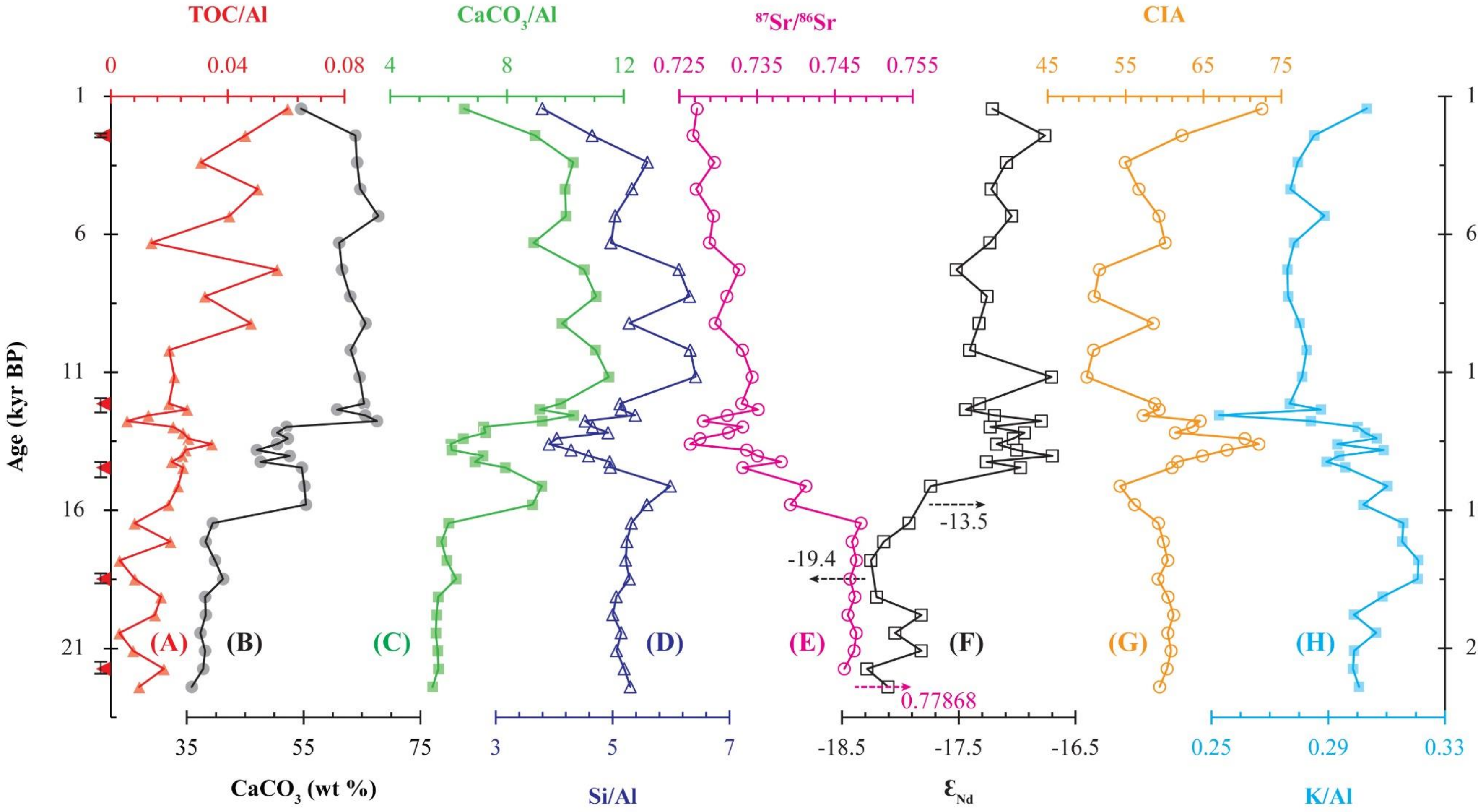

Figure 5.1. *Downcore variation of selected geochemical, Al normalized ratios (of TOC, $CaCO_3$ and K) and CIA and isotopic ($^{87}Sr/^{86}Sr$ and ε_{Nd}) parameters of PDM18 sedimentary records are shown. Red triangles represent the ^{14}C dates where black bars on the triangles are the age uncertainties. Some of the error bars are smaller than the symbol size.*

Table 5.1: *Major elemental and Sr-Nd isotopic composition of the silicate fraction of the PDM18 sediments.*

Sample Name	**Age**	**Na**	**Mg**	**Al**	**Si**	**P**	**K**	**Ca**	**Ti**	**Fe**	**$^{87}Sr/^{86}Sr$**	**ε_{Nd}**
	kyr BP	wt. %										
PDM18/0-2/S	1.4	0.94	0.98	8.36	31.72	0.03	2.53	0.01	0.58	2.87	0.72728	-17.2
PDM18/2-4/S	2.4	0.91	0.82	7.13	33.13	0.03	2.03	0.10	0.61	3.35	0.72680	-16.8
PDM18/4-6/S	3.4	0.96	0.73	6.25	34.97	0.02	1.75	0.00	0.44	2.71	0.72953	-17.1
PDM18/6-8/S	4.4	0.94	0.74	6.48	34.54	0.02	1.79	0.00	0.44	2.80	0.72719	-17.2
PDM18/8-10/S	5.3	0.95	0.79	6.77	34.13	0.02	1.95	0.00	0.44	2.72	0.72940	-17.0
PDM18/10-12/S	6.3	1.01	0.81	6.85	34.08	0.02	1.91	0.00	0.53	2.98	0.72888	-17.2
PDM18/12-14/S	7.3	1.01	0.77	5.79	35.54	0.02	1.60	0.09	0.53	2.96	0.73272	-17.5
PDM18/14-16/S	8.2	1.00	0.68	5.70	36.01	0.01	1.57	0.13	0.56	2.63	0.73111	-17.3
PDM18/16-18/S	9.2	1.06	0.76	6.64	35.07	0.02	1.86	0.00	0.44	2.63	0.72960	-17.3
PDM18/18-20/S	10.2	1.02	0.67	5.71	36.17	0.01	1.61	0.00	0.41	2.34	0.73312	-17.4
PDM18/20-22/S	11.2	0.97	0.70	5.62	36.10	0.01	1.58	0.03	0.41	2.46	0.73439	-16.7
PDM18/22-24/S	12.1	1.05	0.86	6.63	34.04	0.02	1.84	0.12	0.55	3.20	0.73305	-17.3
PDM18/24-26/S	12.3	1.13	0.85	6.65	34.26	0.01	1.91	0.07	0.51	2.77	0.73515	-17.4
PDM18/26-28/S	12.6	1.03	0.90	6.37	34.35	0.01	1.61	0.56	0.50	3.05	0.73119	-17.2
PDM18/28-30/S	12.8	1.03	0.89	7.34	33.26	0.02	2.08	0.13	0.55	2.97	0.72812	-16.8
PDM18/30-32/S	13.0	1.01	0.92	7.23	33.67	0.02	2.17	0.04	0.55	2.97	0.73315	-17.2
PDM18/32-34/S	13.2	1.02	0.84	6.94	34.18	0.02	2.10	0.04	0.60	2.75	0.73133	-16.9
PDM18/34-36/S	13.4	1.01	0.90	8.05	32.56	0.02	2.47	0.00	0.60	2.65	0.72764	-17.0
PDM18/36-38/S	13.6	1.01	0.88	8.30	32.46	0.02	2.43	0.00	0.61	2.71	0.72643	-17.2
PDM18/38-40/S	13.8	1.09	0.89	7.69	33.01	0.02	2.38	0.09	0.53	2.72	0.73366	-17.0
PDM18/40-42/S	14.0	1.09	1.00	7.32	33.62	0.02	2.15	0.15	0.52	3.33	0.73506	-16.7
PDM18/42-44/S	14.2	1.13	0.88	6.90	34.16	0.01	2.00	0.21	0.44	2.88	0.73812	-17.3
PDM18/44-46/S	14.4	1.04	0.89	6.88	34.16	0.02	2.04	0.08	0.51	2.91	0.73317	-17.0
PDM18/46-48/S	15.1	1.10	0.83	5.99	35.88	0.01	1.86	0.14	0.37	2.36	0.74126	-17.7
PDM18/48-50/S	15.8	1.08	0.90	6.25	34.90	0.01	1.89	0.13	0.40	3.20	0.73928	-13.5
PDM18/50-52/S	16.5	1.18	0.90	6.57	34.97	0.01	2.07	0.03	0.38	2.39	0.74833	-17.9
PDM18/52-54/S	17.1	1.16	0.93	6.64	34.83	0.01	2.09	0.09	0.40	2.56	0.74720	-18.1
PDM18/54-56/S	17.8	1.16	0.87	6.71	35.04	0.01	2.15	0.06	0.42	2.32	0.74778	-18.3
PDM18/56-58/S	18.5	1.12	0.87	6.58	34.81	0.01	2.11	0.05	0.41	2.27	0.74694	-19.4
PDM18/58-60/S	19.1	1.13	0.99	6.76	34.20	0.01	2.09	0.05	0.40	2.82	0.74755	-18.2
PDM18/60-62/S	19.8	1.15	1.03	6.85	34.26	0.01	2.05	0.09	0.39	2.90	0.74666	-17.8
PDM18/62-64/S	20.4	1.20	0.94	6.70	34.51	0.01	2.05	0.11	0.38	2.55	0.74775	-18.0
PDM18/64-66/S	21.1	1.18	1.00	6.77	34.33	0.01	2.02	0.13	0.37	2.76	0.74748	-17.8
PDM18/66-68/S	21.7	1.23	0.95	6.69	34.77	0.01	2.00	0.12	0.37	2.70	0.74619	-18.3
PDM18/68-70/S	22.4	1.24	0.91	6.58	34.88	0.01	1.98	0.08	0.35	2.48	0.77868	-18.1

Table 5.2: *Geochemical composition of Zanskar River section (bulk) sediments (PDM18).*

Sample ID	Age	Na	Mg	Al	K	Ca	Ti	Fe
	kyr BP	wt. %						
PDM18/0-2	1.4	0.52	1.61	4.07	1.27	19.8	0.24	2.23
PDM18/2-4	2.4	0.47	1.59	3.01	0.92	24.0	0.23	1.93
PDM18/4-6	3.4	0.51	1.56	2.65	0.82	24.8	0.17	1.53
PDM18/6-8	4.4	0.52	1.50	2.72	0.81	25.9	0.16	1.53
PDM18/8-10	5.3	0.48	1.48	2.61	0.84	26.5	0.16	1.45
PDM18/10-12	6.3	0.56	1.62	3.09	0.92	23.0	0.22	1.84
PDM18/12-14	7.3	0.55	1.70	2.67	0.79	24.0	0.21	1.72
PDM18/14-16	8.2	0.53	1.65	2.49	0.76	24.8	0.23	1.68
PDM18/16-18	9.2	0.54	1.63	2.72	0.83	25.8	0.16	1.55
PDM18/18-20	10.2	0.55	1.61	2.50	0.79	24.6	0.16	1.41
PDM18/20-22	11.2	0.54	1.56	2.37	0.77	25.7	0.16	1.36
PDM18/22-24	12.1	0.54	1.55	2.84	0.84	25.4	0.21	1.79
PDM18/24-26	12.3	0.60	1.66	3.10	0.96	23.4	0.20	1.83
PDM18/26-28	12.6	0.54	1.79	2.64	0.74	25.4	0.20	1.68
PDM18/28-30	12.8	0.52	1.62	2.98	0.91	26.8	0.20	1.81
PDM18/30-32	13.0	0.64	1.79	3.87	1.24	19.7	0.26	2.26
PDM18/32-34	13.2	0.62	1.85	3.97	1.22	18.9	0.30	2.36
PDM18/34-36	13.4	0.64	2.03	4.41	1.41	19.4	0.28	2.50
PDM18/36-38	13.6	0.64	1.88	4.74	1.41	18.8	0.29	2.63
PDM18/38-40	13.8	0.70	1.73	4.55	1.47	17.7	0.27	2.48
PDM18/40-42	14.0	0.66	1.75	4.09	1.29	20.7	0.25	2.31
PDM18/42-44	14.2	0.75	1.76	4.18	1.32	18.6	0.23	2.39
PDM18/44-46	14.4	0.63	1.82	3.67	1.14	21.3	0.24	2.13
PDM18/46-48	15.1	0.66	1.45	3.12	1.04	22.3	0.17	1.65
PDM18/48-50	15.8	0.65	1.52	3.26	1.09	21.9	0.19	1.82
PDM18/50-52	16.5	0.84	1.38	4.35	1.45	15.5	0.22	2.11
PDM18/52-54	17.1	0.86	1.42	4.59	1.53	14.9	0.24	2.41
PDM18/54-56	17.8	0.82	1.42	4.47	1.51	15.7	0.24	2.35
PDM18/56/58	18.5	0.79	1.42	4.43	1.46	15.8	0.24	2.34
PDM18/58-60	19.1	0.87	1.42	4.65	1.52	14.9	0.24	2.35
PDM18/60-62	19.8	0.84	1.43	4.48	1.48	14.8	0.23	2.38
PDM18/62-64	20.4	0.89	1.45	4.65	1.53	14.4	0.22	2.33
PDM18/64-66	21.1	0.90	1.49	4.61	1.51	14.7	0.22	2.27
PDM18/66-68	21.7	0.90	1.47	4.65	1.46	14.7	0.22	2.24
PDM18/68-70	22.4	0.91	1.45	4.59	1.52	13.6	0.22	2.19

Table 5.2 *(continued)*

Sample ID	V	Cr	Mn	Co	Ni	Cu	Zn	As	Rb	Sr	Mo	Ba	Th	U
	μg/g													
PDM18/0-2	49	48	361	7.9	12.9	18	41	0.95	75	470	0.70	269	10.1	2.2
PDM18/2-4	36	39	372	5.6	9.1	14	30	1.02	53	531	0.70	151	12.7	2.6
PDM18/4-6	26	56	287	4.1	19.2	13	35	1.02	46	569	1.14	135	6.8	1.7
PDM18/6-8	26	35	281	3.5	7.5	13	28	1.00	47	604	0.57	120	7.0	1.7
PDM18/8-10	26	32	272	3.4	6.4	15	58	1.02	46	564	0.58	194	6.5	1.6
PDM18/10-12	32	58	323	5.0	19.6	16	39	0.99	52	543	1.05	153	8.9	2.1
PDM18/12-14	29	128	339	5.9	57.7	15	25	1.07	42	524	2.63	122	10.0	3.7
PDM18/14-16	26	57	359	4.7	19.0	16	36	1.07	41	551	1.23	155	11.6	2.5
PDM18/16-18	25	57	303	3.8	19.0	13	26	1.04	46	586	0.92	151	7.6	1.8
PDM18/18-20	23	53	298	3.7	17.5	12	23	0.99	45	558	1.00	116	7.3	1.6
PDM18/20-22	20	30	286	2.9	5.7	11	16	1.00	42	571	0.54	140	6.1	1.6
PDM18/22-24	28	138	402	5.6	64.1	15	28	1.06	47	524	2.83	163	9.0	2.2
PDM18/24-26	32	60	371	5.1	21.2	16	37	1.01	53	500	0.99	169	9.1	2.0
PDM18/26-28	31	61	399	4.3	20.2	17	40	1.04	42	464	1.00	147	8.6	2.8
PDM18/28-30	35	62	347	5.5	20.9	15	24	1.07	52	540	0.98	149	10.3	2.5
PDM18/30-32	45	44	401	7.3	11.9	24	44	1.06	68	453	0.58	226	13.1	2.8
PDM18/32-34	46	141	402	9.3	64.7	19	40	1.10	64	446	2.73	210	14.3	3.0
PDM18/34-36	53	46	321	7.9	12.5	18	71	1.01	76	474	0.64	248	12.9	2.5
PDM18/36-38	56	50	330	8.6	13.4	19	47	1.09	80	483	0.62	247	14.0	2.7
PDM18/38-40	52	47	436	7.7	12.8	19	52	1.08	84	425	0.54	308	11.9	2.4
PDM18/40-42	49	46	457	7.3	11.8	19	33	1.06	73	441	0.56	251	10.5	2.4
PDM18/42-44	46	46	591	6.4	11.9	16	35	1.01	74	393	0.53	275	10.5	2.6
PDM18/44-46	42	141	352	7.4	63.6	16	30	1.09	63	462	2.78	222	9.2	2.1
PDM18/46-48	32	35	313	3.8	6.7	12	41	1.00	59	443	0.44	208	6.5	1.8
PDM18/48-50	36	40	332	3.9	8.6	14	31	1.01	63	451	0.55	238	6.9	2.0
PDM18/50-52	43	43	383	5.2	10.3	16	37	1.03	82	318	0.63	343	8.9	2.5
PDM18/52-54	49	45	420	6.0	28.1	17	47	1.00	88	304	0.53	374	9.8	2.9
PDM18/54-56	47	48	393	6.2	12.6	17	48	1.11	85	320	0.70	369	9.9	3.0
PDM18/56/58	47	125	409	7.6	54.3	18	40	1.11	84	325	2.33	342	9.3	2.8
PDM18/58-60	48	42	452	6.1	9.6	17	42	1.05	91	314	0.50	369	10.4	2.8
PDM18/60-62	47	43	487	6.1	11.2	17	39	1.04	85	306	0.84	370	9.6	2.6
PDM18/62-64	48	42	460	5.7	9.7	16	40	1.08	89	290	0.45	389	9.5	2.7
PDM18/64-66	46	40	454	5.8	9.4	19	43	1.03	86	297	0.47	383	8.5	2.5
PDM18/66-68	45	143	440	7.2	65.9	18	31	1.06	86	292	2.75	349	8.7	2.3
PDM18/68-70	45	39	381	5.3	8.9	15	36	0.99	86	277	0.47	356	9.1	2.5

Table 5.2 *(continued)*

Sample ID	La	Ce	Pr	Nd	Sm	Eu	Gd	Tb	Dy	Ho	Er	Tm	Yb	Lu
	µg/g													
PDM18/0-2	27	51	5.8	21	4.0	0.8	3.6	0.5	3.0	0.6	1.7	0.2	1.6	0.2
PDM18/2-4	33	65	7.3	27	4.9	0.7	4.2	0.6	3.2	0.6	1.6	0.2	1.5	0.2
PDM18/4-6	18	35	4.2	15	3.2	0.6	2.9	0.4	2.3	0.5	1.2	0.2	1.2	0.2
PDM18/6-8	19	37	4.4	16	3.3	0.6	2.9	0.4	2.3	0.5	1.2	0.2	1.2	0.2
PDM18/8-10	18	35	4.1	15	2.9	0.6	2.6	0.4	2.0	0.4	1.1	0.2	1.1	0.1
PDM18/10-12	25	50	5.7	21	4.0	0.7	3.6	0.5	3.0	0.6	1.5	0.2	1.5	0.2
PDM18/12-14	25	49	5.6	21	4.3	0.8	4.0	0.6	3.6	0.8	2.1	0.3	2.0	0.3
PDM18/14-16	29	59	6.7	25	4.9	0.8	4.4	0.6	3.2	0.6	1.7	0.2	1.6	0.2
PDM18/16-18	22	43	4.9	18	3.6	0.7	3.1	0.4	2.2	0.5	1.2	0.2	1.2	0.2
PDM18/18-20	22	42	4.9	18	3.6	0.6	2.9	0.4	2.3	0.5	1.2	0.2	1.2	0.2
PDM18/20-22	18	35	4.1	15	3.1	0.6	2.7	0.4	2.2	0.4	1.2	0.2	1.2	0.2
PDM18/22-24	24	48	5.6	20	4.1	0.7	3.5	0.5	2.9	0.6	1.6	0.2	1.6	0.2
PDM18/24-26	24	48	5.5	20	4.2	0.7	3.7	0.5	2.7	0.6	1.5	0.2	1.5	0.2
PDM18/26-28	23	47	5.3	20	3.8	0.6	3.3	0.5	3.2	0.6	2.0	0.3	1.8	0.3
PDM18/28-30	26	51	5.9	22	4.3	0.7	3.6	0.5	2.9	0.6	1.5	0.2	1.4	0.2
PDM18/30-32	35	69	7.9	29	5.6	0.9	4.8	0.7	3.7	0.7	2.0	0.3	2.0	0.3
PDM18/32-34	36	71	8.3	30	5.8	1.0	4.8	0.7	3.9	0.8	2.0	0.3	2.0	0.3
PDM18/34-36	33	65	7.3	27	5.4	0.9	4.7	0.6	3.7	0.7	2.0	0.3	2.0	0.3
PDM18/36-38	35	70	8.0	29	5.7	1.0	5.1	0.7	4.0	0.8	2.2	0.3	2.1	0.3
PDM18/38-40	30	58	6.8	24	4.7	0.8	4.2	0.6	3.4	0.7	1.9	0.3	1.9	0.3
PDM18/40-42	29	56	6.5	23	4.5	0.9	4.0	0.6	3.5	0.7	2.0	0.3	2.0	0.3
PDM18/42-44	28	54	6.3	22	4.6	0.8	4.1	0.6	3.4	0.7	2.1	0.3	2.1	0.3
PDM18/44-46	25	50	5.8	21	4.3	0.7	3.5	0.5	2.7	0.5	1.5	0.2	1.4	0.2
PDM18/46-48	20	39	4.5	16	3.3	0.7	2.9	0.4	2.3	0.5	1.2	0.2	1.1	0.2
PDM18/48-50	21	41	4.7	17	3.3	0.7	3.0	0.4	2.3	0.5	1.2	0.2	1.2	0.2
PDM18/50-52	25	50	5.7	21	4.1	0.8	3.5	0.5	2.8	0.6	1.4	0.2	1.5	0.2
PDM18/52-54	26	52	6.0	22	4.2	0.8	3.8	0.5	2.9	0.6	1.8	0.2	1.6	0.2
PDM18/54-56	27	53	6.2	22	4.6	0.9	3.7	0.5	3.1	0.6	1.7	0.3	1.7	0.2
PDM18/56/58	26	52	5.9	21	4.3	0.8	3.6	0.5	2.8	0.6	1.5	0.2	1.4	0.2
PDM18/58-60	28	56	6.3	23	4.5	0.9	4.0	0.6	3.3	0.6	1.9	0.3	1.7	0.3
PDM18/60-62	26	51	5.9	21	4.1	0.8	3.7	0.5	3.1	0.6	1.7	0.3	1.7	0.2
PDM18/62-64	26	51	5.8	21	4.2	0.8	3.6	0.6	3.1	0.6	1.8	0.3	1.7	0.3
PDM18/64-66	23	45	5.1	18	3.7	0.7	3.2	0.5	2.7	0.5	1.6	0.2	1.5	0.2
PDM18/66-68	23	46	5.4	19	3.8	0.8	3.3	0.5	2.6	0.5	1.4	0.2	1.3	0.2
PDM18/68-70	24	48	5.4	20	4.1	0.8	3.5	0.5	2.9	0.6	1.5	0.2	1.5	0.2

Table 5.2 *(continued)*

Sample ID	**$CaCO_3$**	**TOC**	**TN**	**C/N**
	wt. %			Atomic
PDM18/0-2	55	0.51	0.068	8.7
PDM18/2-4	64	0.33	0.042	9.0
PDM18/4-6	64	0.19	0.025	8.8
PDM18/6-8	65	0.33	0.033	11.7
PDM18/8-10	68	0.27	0.030	10.9
PDM18/10-12	61	0.09	0.025	4.4
PDM18/12-14	62	0.33	0.018	21.8
PDM18/14-16	63	0.18	0.017	12.7
PDM18/16-18	66	0.32	0.023	15.8
PDM18/18-20	63	0.11	0.018	7.6
PDM18/20-22	65	0.12	0.015	9.3
PDM18/22-24	65	0.13	0.017	8.9
PDM18/24-26	61	0.17	0.016	12.6
PDM18/26-28	66	0.08	0.014	6.8
PDM18/28-30	68	0.04	0.019	2.4
PDM18/30-32	52	0.15	0.021	8.4
PDM18/32-34	50	0.17	0.023	8.9
PDM18/34-36	52	0.21	0.028	8.9
PDM18/36-38	50	0.29	0.031	10.9
PDM18/38-40	47	0.20	0.027	8.6
PDM18/40-42	53	0.18	0.022	9.7
PDM18/42-44	48	0.14	0.018	9.1
PDM18/44-46	55	0.17	0.021	9.3
PDM18/46-48	55	0.14	0.014	11.3
PDM18/48-50	55	0.12	0.015	9.5
PDM18/50-52	39	0.05	0.018	3.5
PDM18/52-54	38	0.14	0.019	8.3
PDM18/54-56	40	0.02	0.019	1.2
PDM18/56/58	41	0.05	0.018	3.4
PDM18/58-60	38	0.12	0.019	7.2
PDM18/60-62	38	0.10	0.019	6.5
PDM18/62-64	37	0.02	0.017	1.3
PDM18/64-66	38	0.05	0.018	3.3
PDM18/66-68	38	0.12	0.016	8.8
PDM18/68-70	36	0.06	0.017	4.2

(Fig. 5.2). The ε_{Nd} ratio of the PDM18 sediments varies from -19.4 to -13.5, with an average value of -17.3 ± 0.9. These Nd isotopic ratios are comparable with those reported for the TSS (-13) and HH (-15 ± 1.4) rocks.

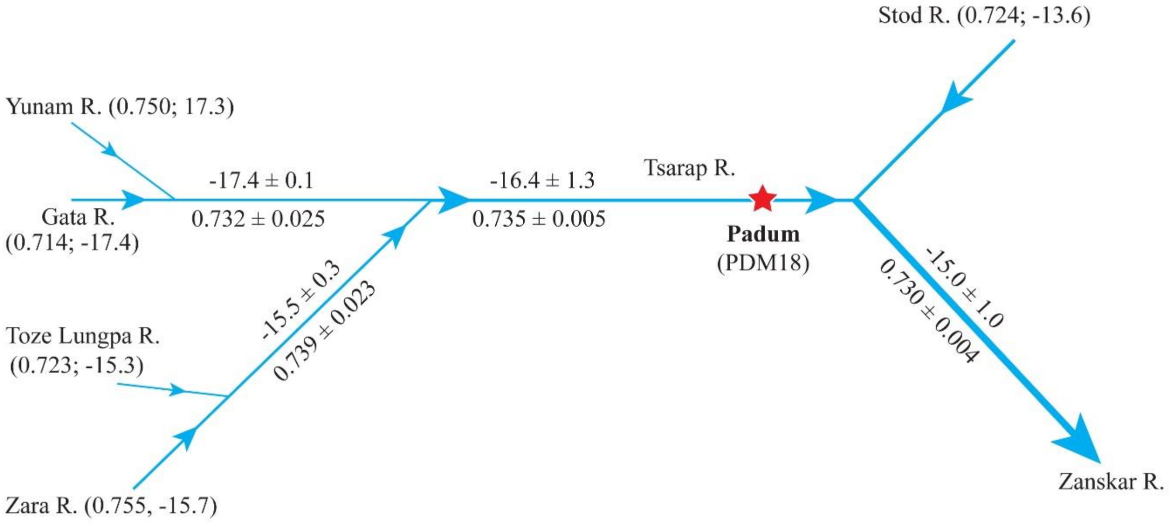

Figure 5.2. *Spatial distribution of modern-day $^{87}Sr/^{86}Sr$ and ε_{Nd} isotopic compositions for the Zanskar River system (Data source: Jonell et al., 2017). The star symbol in the figure show the sampling location of the studied core.*

The mixing plot between $^{87}Sr/^{86}Sr$ and ε_{Nd} ratios of the PDM18 sediments and their possible sources is presented in Fig. 5.3. The Sr-Nd isotopic mixing diagram clearly depicts that ε_{Nd} values of the PDM18 sediments match well with that of the modern-day Tsarap River. Although this plot confirms the dominant sediment supply from the TSS and its possible sediment supply from various streams from the Zanskar basin, an additional sediment source with a high $^{87}Sr/^{86}Sr$ and low ε_{Nd} ratio seem to be missing. This missing source(s) with high $^{87}Sr/^{86}Sr$ (depleted ε_{Nd}) values could be K-rich leucogranites, Nyimaling-Tso Morari gneiss dome, and/or metasediments exposed in the basin (Fig. 2.5; cf. Chapter 2). The lack of isotopic data for these litho units hinders proper assessing relative sediment contribution from these units to the basin. The Sr-Nd isotopic plot shows that the samples fall in two distinct isotopic zones, and interestingly, these isotopic changes (in silicate fractions) are comprised of distinct carbonate contents. In this basin, the carbonate content may serve as a possible source indicator, depending on the exposure of carbonates within the sub-basins. The modern-day carbonate content of the Tsarap River is mainly supplied by the Gata stream. The other major (Stod) tributary of the Zanskar River is comprised of minimal carbonates. The samples with relatively low $^{87}Sr/^{86}Sr$ and high ε_{Nd} values are also comprised of higher $CaCO_3$ content (Fig. 5.3). These isotopic values and high carbonate contents are observed in the upper part of the section. Comparison of these isotopic and carbonate values with their possible sources, the upper part of the sediment section seems to have a higher sediment supply from the tributary, Gata.

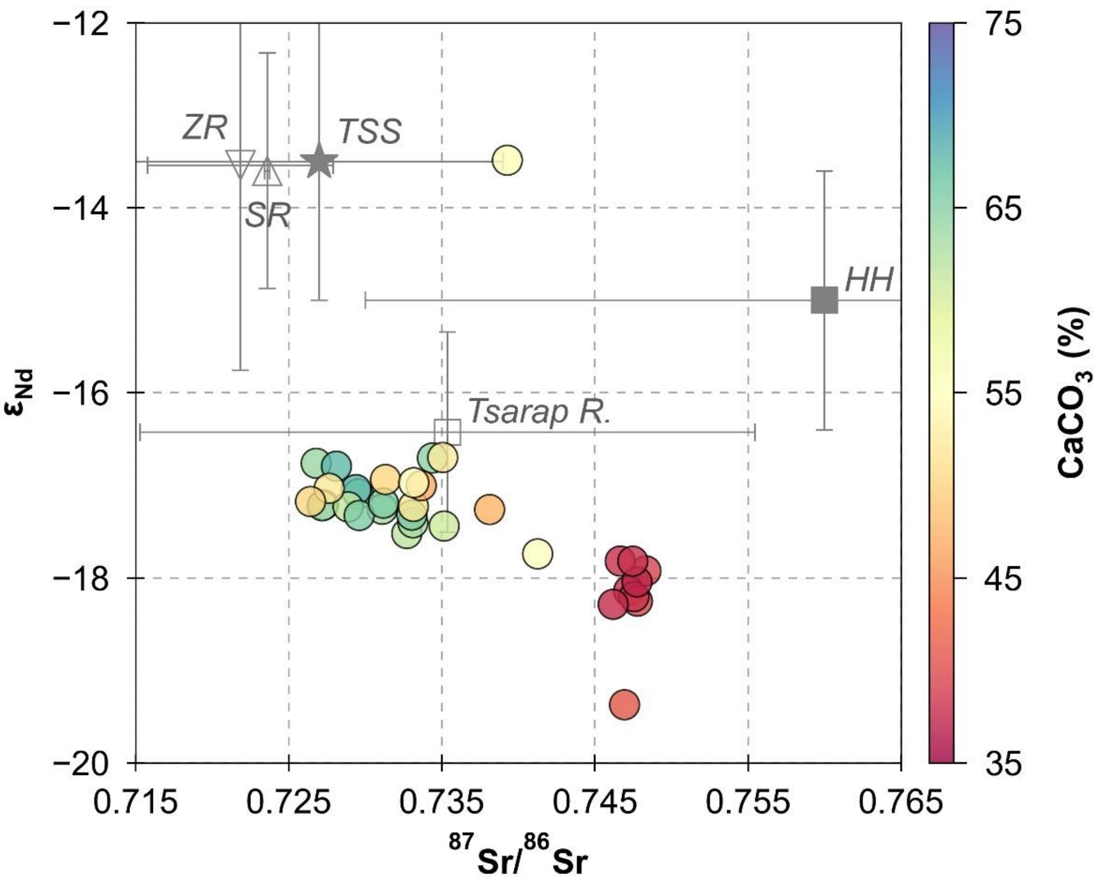

Figure 5.3. *Mixing diagram between $^{87}Sr/^{86}Sr$ and ε_{Nd}. For reference various source composition are plotted. For reference, compositions of the major sediments sources, Higher Himalaya (HH), Tethyan sedimentary sequence (TSS), river sediment compositions of Zanskar (ZR), Stod (SR) and Tsarap, to the sampling site are also plotted. The Sr-Nd isotopic compositions of the PDM18 sediments matches well with modern day sediment compositions of the Tsarap River. Whereas the symbol colors represent their corresponding $CaCO_3$ content. See text for the data source for the provenances. (Data source: TSS and HH from Singh et al., 2008; ZR, SR and Tsarap from Jonell et al., 2017).*

Additional to these provenance changes, the depth profiles of the weathering indices (CIA, K/Al, and K/Si*) point to an increase in chemical erosion during the Bølling-Allerød (B-A) warm period (Fig. 5.4). The CIA values show a sudden rise from 60 to 72 during this event, hinting at an intensification of chemical erosion during this period. A similar observation could be made from a lower K/Al ratio, reflecting the increased release of mobile K from sediments to the dissolved phase. As the changes in sediment provenances precede these elemental ratio changes, the K/Si* trends also ensure that these inferences are linked to chemical weathering changes and not linked to the size-sorting effect. This intensification of chemical erosion is also evident from the sedimentary $CaCO_3$ content in comparison to the provenance proxies. The Nd isotopes show a shift from an enriched to depleted value across the B-A warm event. Although the carbonate contents document this change, the $CaCO_3$ content is also characterized with an intermediate value of ~54 wt% during the B-A event. Following Nd isotopic trends, a provenance change should have led to a carbonate content change from its pre-B-A (41 wt%) to post-B-A (63 wt%) values. The observed intermediate step in carbonate content, therefore, is different than that observed for provenance proxies and may reflect the increased dissolution of carbonates during this event. This intermediate carbonate content (~53 wt%) is about 16% lower than that expected (~63 wt%) based on Nd isotopic trends (Fig. 5.4).

The observed sedimentary provenance changes and chemical erosion intensification are synchronous to the warm and humid Bølling-Allerød period. Earlier studies based on the oxygen isotopic ($\delta^{18}O$) records from the Dongge and Hulu caves, East Asia, show a sharp depletion which indicates an intensification of monsoon strength during this time (Dykoski et al., 2005; Yuan et al., 2004). Also, Yancheva et al. (2007) have documented stronger monsoon phases during this warm climatic phase by investigating the lake record from China. Similarly, the temporal variation of oxygen isotopic record ($\delta^{18}O$) for the Guliya ice core from the Tibetan Plateau glaciers and the Greenland Ice Sheet also confirms a warm climate during B-A (Stuiver and Grootes, 2000; Thompson et al., 1997). Rainfall reconstruction for the core monsoon zone of India, based on speleothem oxygen isotopic records, documents a rapid increase in the rainfall from 14.8 to 12.6 kyr BP (Gautam et al., 2019). This conducive climatic condition, a warm climate with an increase in rainfall amount, is ideal for promoting chemical erosion patterns in the river basin. The warm B-A event with intensified monsoon is expected to enhance the efficiency of sediment transport and exposed fresh mineral surfaces, which in turn intensify the chemical erosion rates of this Himalayan basin. These outcomes establish a strong control of climate on the Himalayan erosion pattern.

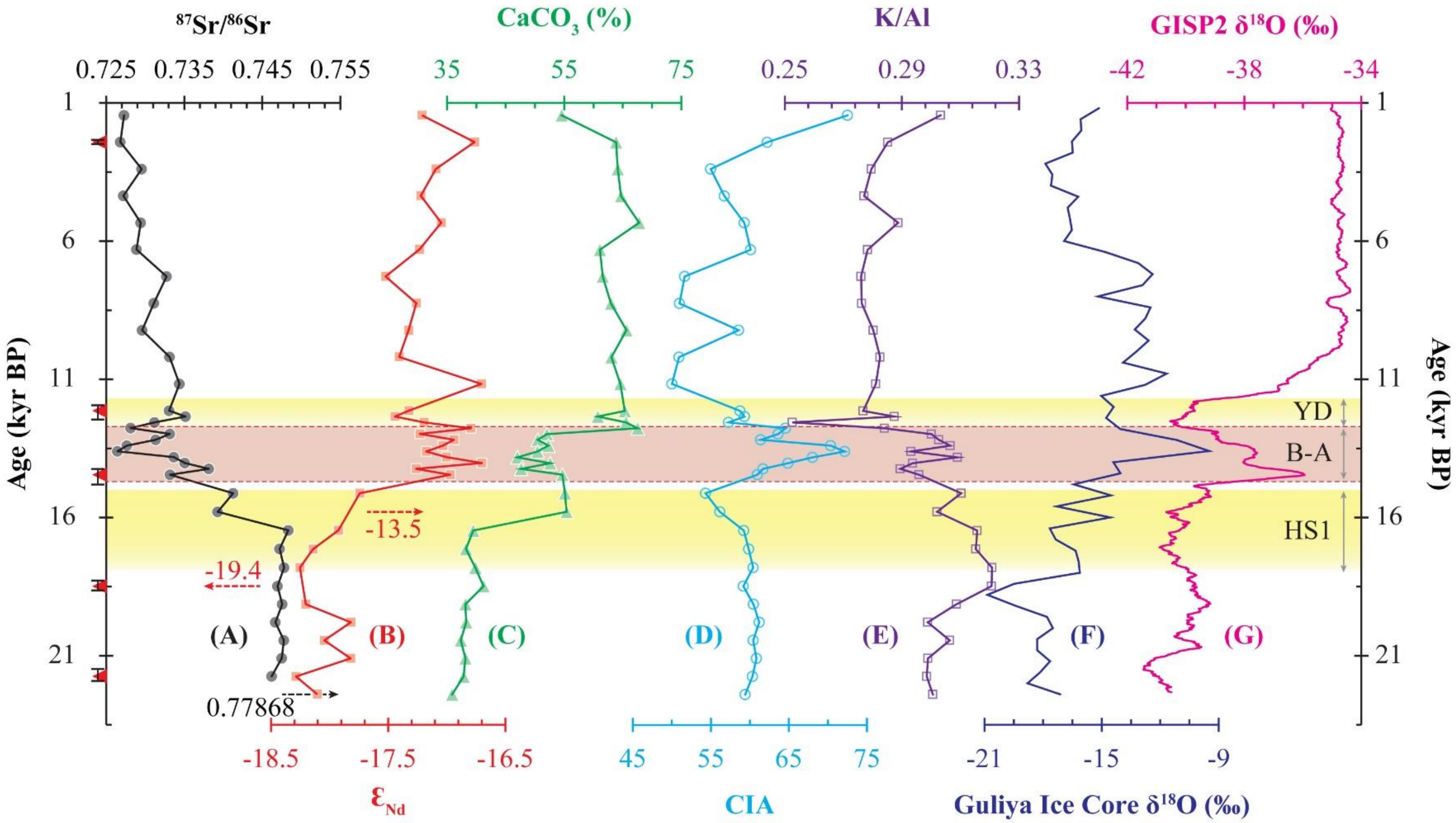

Figure 5.4. *Depth profile of provenance (^{87}Sr/^{86}Sr, ε_{Nd} and CaCO$_3$), weathering intensity (CIA) and size-sorting effect indicating (K/Si*) indices for the PDM18 sedimentary record show a major shift in sediment supply before and after the climatic event Bølling-Allerød (B-A) and an intensification in chemical erosion during this warm and humid period. For reference paleoclimate patterns, oxygen isotopic record from the Guliya ice core (Thompson et al., 1997) and Greenland Ice Sheet (Greenland Ice Sheet Project Two (GISP2); Stuiver and Grootes, 2000), and other major climatic events Younger Dryas (YD) and Heinrich Stadial 1 (HS1) are also presented. Red triangles are the ^{14}C dates with age ranges.*

5.3. Conclusion

Chemical and Sr-Nd isotopes of terrestrial sedimentary records from the upper Indus basin were investigated to understand the Himalayan erosion patterns and sediment provenance during the last glacial-interglacial cycle. Temporal records of erosion patterns show significant change during this time. The temporal records of Sr-Nd isotopes and sedimentary carbonate contents depict a sudden shift in sediment provenance around the Bølling-Allerød warmer event. Also, the chemical erosion indices (CIA and K/Al) point to the intensification of chemical erosion during this warm phase. These changes in the erosion process are possibly linked to glacial retreat and exposure to fresher minerals during this warm period and hence, underscore a strong coupling between climate and Himalayan erosion.

Chapter 6

Natural Variability of Indian Summer Monsoon during Mid-Holocene Period

6.1 Introduction

The Indian summer monsoon (ISM) is a manifestation of seasonal wind reversal due to differential atmospheric heating over land and ocean and related moisture supply from the Indian Ocean to the sub-continent. This ocean-atmosphere coupled process is an important component of the tropical hydrological and energy cycles with large agro-economic significance as this season (June-September) alone contributes ~80% of the annual rainfall in the region. In comparison to instrumental rainfall records, large variations in the ISM intensity have been reported during the Holocene (11,700 yr BP to present) period (Mayewski et al., 2004; Kaushal et al., 2018). Reconstruction of these natural ISM variations in the past is required to better constrain monsoon trends and drivers, which in turn could improve our short-term forecasting capabilities.

Chemical, isotopic, and/or paleontological investigations of marine and lake sediments, peat bogs, cave calcites, and corals have been found successful in reconstructing past monsoon variabilities. These studies focusing on the Holocene period, by and large, show stronger monsoon during the early and middle Holocene, which subsequently shifted towards a relatively drier phase during the late Holocene period (Kaushal et al., 2018). Mega-droughts lasting several decades are well documented during the past millennia (Cook et al., 2010; Sinha et al., 2011) and had a devastating impact on societies of the periods (Kathayat et al., 2017). In addition, multi-century super-droughts like those associated with global dry events around 4.2 kyr BP and 8.2 kyr BP have been known for the demise of civilizations in the region (Gupta et al., 2006; Dixit et al., 2014a). Apart from these two major dry events, continental records from India based on oxygen isotopic composition of speleothems (Berkelhammer et al., 2012; Dutt et al., 2015) and bio-apatites (Sarkar et al., 2016), and carbon isotopic study of a peninsular river (Godavari) sediments (Ponton et al., 2012) also indicate a weakening of ISM around 6.5 kyr BP. A global compilation of climatic records also shows a synchronous (6.5-5.9 kyr BP) cold and dry event (Wanner et al., 2008). Further, isotopic and paleontological studies for marine sediments and foraminifera from the Arabian Sea indicate a major climatic excursion during this time period (Kessarkar et al., 2018; Saraswat et al., 2016; Gupta et al., 2005). These signatures, however, are regulated by several oceanic processes (primary productivity, oceanic SST, and salinity) with significant uncertainty in their linkages to ISM rainfall variability. Even with some uncertainty in the chronology, a high-resolution oxygen isotope from a central Indian cave also indicates a dry event around this period (Band et al., 2018). All these records together confirm the occurrence of a large-scale dry phase at around 6.5 kyr that might have adversely influenced civilizations during the period. Although there are limited archaeological studies focusing on this period, the significant demographic decline in Arabia (Petraglia et al., 2020) and Sahara (Manning and Timpson, 2014) seem to have occurred in response to this drought event. Despite its global and regional significance, reliable quantification of the timing and temporal extent, magnitude, and driving mechanism for this potential Indian monsoon super-drought phase has been lacking. This chapter presents high-resolution oxygen isotopic data for a speleothem from the core monsoon zone (Rajeevan et al., 2010) supported by U-Th chronology to reconstruct natural variations in ISM rainfall intensity for about 5000 years covering the entire Northgrippian (also known as, mid-Holocene) stage. With better resolution and chronology, this thesis work also explores the regional significance and global connection of the super-drought event and provides a plausible driving mechanism.

6.2 Speleothem δ^{18}O record from the Gupteswar cave, India

The mineralogical composition is one of the most crucial factors which determines the usability of any speleothem record as a paleoclimate and/or paleohydrology indicator. The mineralogy of the GPT-1 speleothem was determined based on the x-ray diffraction (XRD) technique. The XRD spectra of powdered samples from four different depths confirm their mineral composition to be calcite (Fig. 6.1). Hendy's test was carried out to determine the speleothem growth in isotopic equilibration conditions. Briefly, carbon and oxygen isotopic compositions were analysed for eight samples from one layer across the growth axis, and minimal δ^{18}O change within a layer (± 0.8 ‰) with poor correlation with δ^{13}C values confirms isotopic equilibration during deposition of the speleothem. This process was repeated for four different growth layers; all four layers showed similar results (Fig. 6.2).

The oxygen isotopic composition of speleothem is regulated primarily by temperature and rainfall. Additionally, a few other factors (moisture source, evaporation during vapour transport and seasonality in precipitation) may influence these isotopic signatures (Cai et al., 2012; Kaushal et al., 2018). The speleothem $\delta^{18}O$ value typically shows a depletion of ~0.23 ‰ per 1 °C increase in cave temperature. Considering a temperature variation of ~1 °C during the mid-Holocene (Mayewski et al., 2004), the expected temperature-induced isotopic change (~0.23 ‰) during this period is significantly lower than the observed $\delta^{18}O$ change (~3 ‰; Fig. 6.3) for the GPT-1.

A few available studies from the core-monsoon region have successfully employed the speleothem $\delta^{18}O$ values for reliable reconstruction of past ISM variability (Band et al., 2018; Yadava and Ramesh, 2005; Sinha et al., 2007). Yadava and Ramesh (2005) have reported a linear correlation between monthly-average $\delta^{18}O$ of rainwater and precipitation amount at a location closer to Gupteswar. This amount effect depicts a $\delta^{18}O$ depletion of 2.2 (± 0.8) ‰ per 100 mm increase in rainfall, which is statistically similar to the global (1.5 ± 0.2 ‰/100 mm) trend (Yadava and Ramesh, 2005). Based on this observation, the long-term variability with ~3 ‰

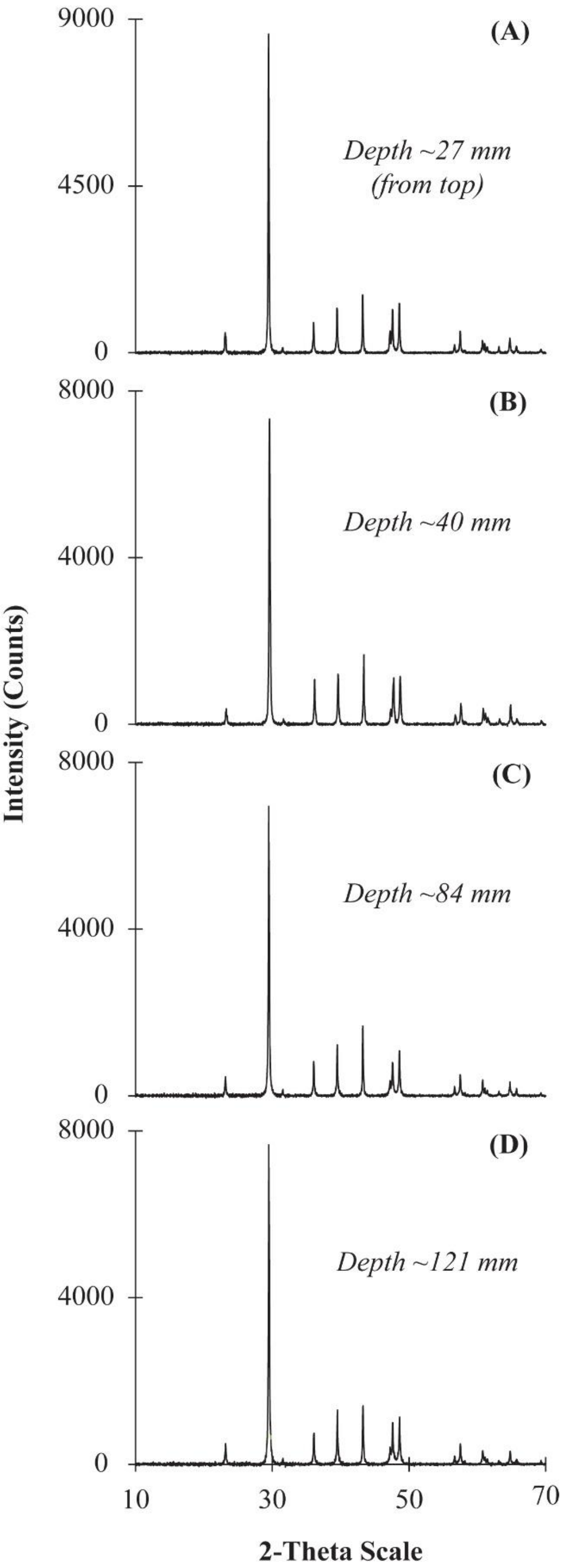

Figure 6.1. *XRD spectra of four powder samples from the GPT-1 speleothem confirm their calcite mineralogy. The depth of these samples from top of the speleothem is also included in the figure.*

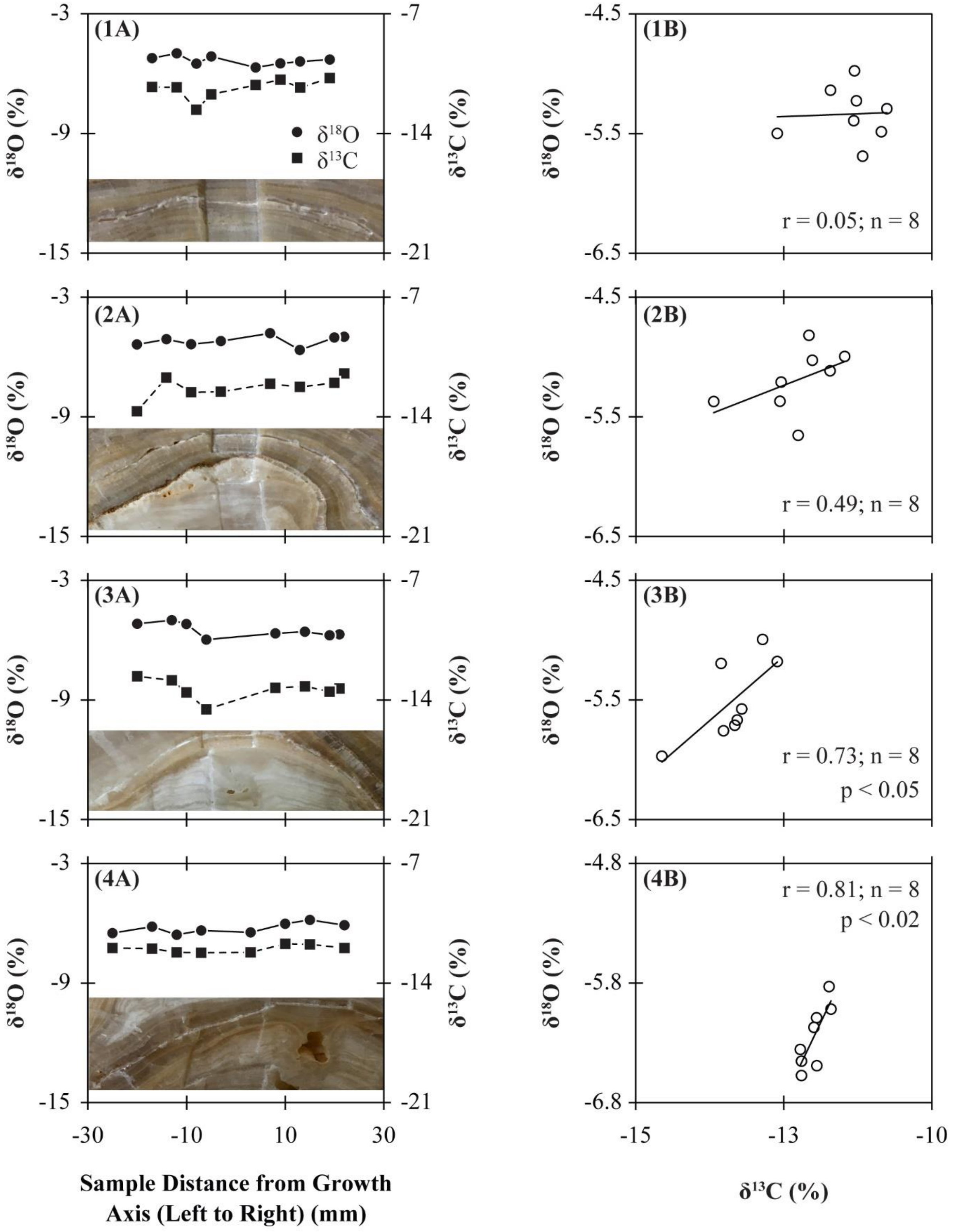

Figure 6.2. *Hendy's test (Hendy, 1971) based on stable carbon and isotopic compositions of GPT-1 samples. Minimal variations of* $\delta^{18}O$ *and* $\delta^{13}C$ *along a laminae from four different depths (shown in figure subpanels-1A, 2A, 3A, 4A) and poor correlation between* $\delta^{18}O$ *and* $\delta^{13}C$ *(shown in figure subpanels-1B, 2B, 3B, 4B) confirming isotopic equilibrium of the speleothem. For reference speleothem photographs with sampling positions are also provided (1A, 2A, 3A, 4A).*

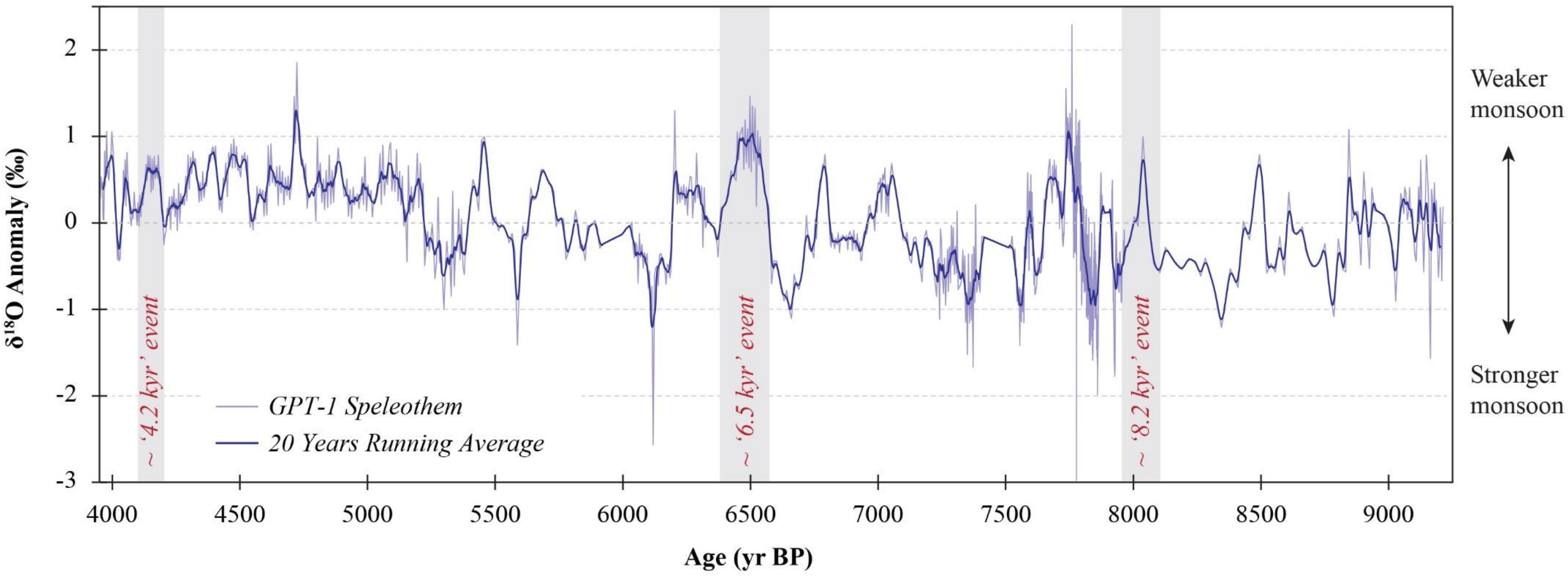

Figure 6.3. *Temporal variation of (20-year moving average) δ^{18}O-anomaly of the speleothem (GPT-1) for the Gupteswar Cave. The anomaly value for individual sample is computed as difference between δ^{18}O sample and average δ^{18}O of the GPT-1. The grey band represents the three major global drought events at around 4.2, 6.5 and 8.2 kyrs BP.*

and multi-centennial variability with ~1.5 ‰ changes in our $\delta^{18}O$ record for the Gupteswar speleothem (Fig. 6.3) seems to be regulated dominantly by rainfall variations. In most periods of multi-decadal variabilities with 0.75-1.0 ‰, changes are controlled mainly by rainfall variations, making the $\delta^{18}O$ of Gupteswar speleothem a reliable proxy for reconstructing natural ISM rainfall variability during the mid-Holocene period. We have also computed the "$\delta^{18}O$ anomaly" for all samples as the deviation of their $\delta^{18}O$ values from the average $\delta^{18}O$ value of GPT-1 (-5.53 ‰). This anomaly value can serve as a reliable proxy for past rainfall intensity, and at a global scale, about -1.5 ‰ of $\delta^{18}O$ anomaly can be attributed to a rainfall increase of about 100 mm (Fig. 6.3). The $\delta^{18}O$ ratios of the GPT-1 sample show wide variations ranging between -3.2 and -8.5 ‰, with an average value of -5.5 ± 0.6 ‰ ($n = 1013$; Fig. 6.3, Table A6.1, Annexure Table). Temporal variation in the $\delta^{18}O$ values show an increasing trend ($y = -0.00015 \times - 4.5$; $r = 0.37$, $p < 0.001$) with relatively enriched values being observed for the younger samples. This broad change in $\delta^{18}O$ (-0.15 ‰/kyr) points to a shift from the wetter to the drier phase during the speleothem growth period (Fig. 6.3). The y-intercept value (-4.5 ‰) of this trend matches well with that reported for the active stalactite layer (~-4.3 ‰) from this cave (Yadava and Ramesh, 2005). Further, the observed $\delta^{18}O$ lapse rate (-0.15 ‰/kyr) for the Gupteswar is consistent with that reported for Dongge (-0.19 ‰/kyr) and Qunf (-0.17 ‰/kyr) cave records (Cai et al., 2012) for the mid-Holocene period. The high growth rate of the speleothem in the lower part than that in the upper part also supports a shift from a stronger to weaker monsoon phase (Fig. 2.4D, cf. Chapter 2, section 2.1.3.2). The $\delta^{18}O$ anomaly values of the speleothem shifted to positive values since 5.2 kyr BP (Fig. 6.3), corroborating a rainfall shift towards a drier monsoon phase.

Spectral analysis of the $\delta^{18}O$ data for the GPT-1 speleothem was carried out using PAST software (REDFIT approach). This analysis reveals few statistically significant (within 95% confidence interval) periodicities of multi-centennial (657 yr and 263 yr) and decadal (22 yr, 11 yr, and 10 yr) scales (Fig. 6.4). Several earlier studies on low latitude rainfall have reported periodicities ranging between 630-780 years throughout the Holocene, which occurs in coherence with the global ^{14}C production rate (Staubwasser et al., 2003; Thamban et al., 2007). Our observed periodicity of 657 years overlaps with these reported periodicities. Further, the observed periodicities of 263 years are similar to the 210-230 year cycle reported for Arabian Sea sediments (Agnihotri et al., 2002). These periodicities, similar to the 210 years Suess cycle, are linked to solar activity and confirm a stronger role of solar activity in regulating the mid-Holocene ISM variability. In addition to these centennial periodicities, the $\delta^{18}O$ spectral also show the occurrence of a multi-decadal periodicity of ~22 and ~11 yrs, hinting at the potential contribution from Pacific Decadal Oscillation (PDO; Krishnan and Sugi, 2003) and ENSO-type natural climate modes on the mid-Holocene ISM rainfall variability.

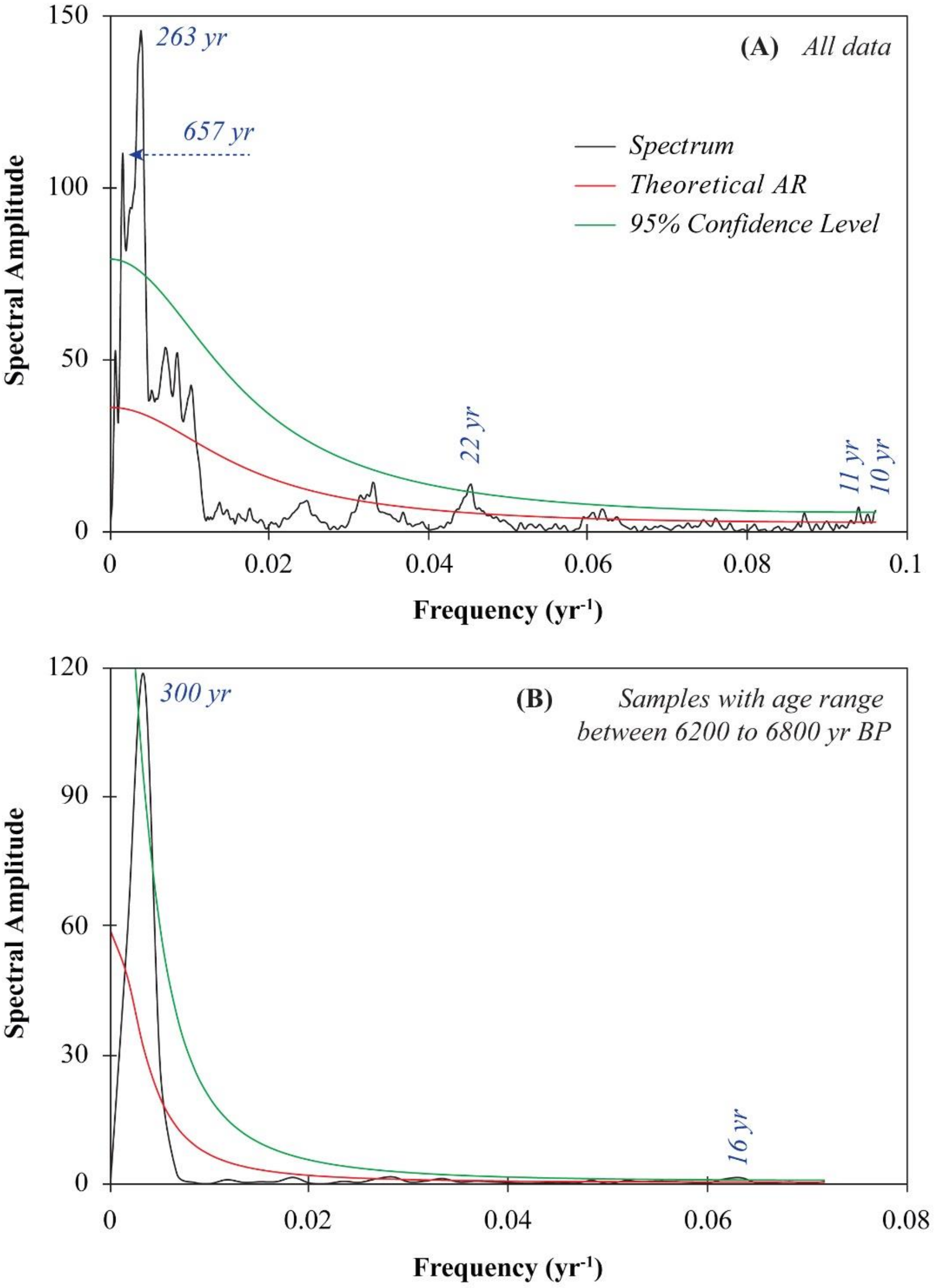

Figure 6.4. *Spectral analyses of (A) the $\delta^{18}O$ dataset for all samples from the GPT-1 and (B) the $\delta^{18}O$ dataset of samples (age range: 6.2-6.8 kyr BP) around the "6.5-kyr" drought event. All samples from the GPT-1 show five significant periodicities (657 yr, 263 yr, 22 yr, 11 yr, 10 yr), whereas the samples around 6.5 kyr BP show two prominent periodicities (300 yr, 16 yr). REDFIT method was done using PAST software (http://palaeo-electronica.org/2001_1/past/issue1_01.htm).*

In our exploration for a driving mechanism, we note that the temporal changes of ISM rainfall have been linked to the Intertropical convergence zone (ITCZ) movement in response to external (orbital and solar) and/or internal (sea surface temperature (SST) changes in the various ocean, e.g. Indian, Pacific and Atlantic, basins) forcing, where northward (southwards) shift of ITCZ results in more (less) rainfall over the south Asian region. Several studies have invoked that the teleconnection between the ISM pattern and remote external forcing is through non-uniform zonal heating processes that could influence the Walker circulation and the monsoon strength. Although the mechanistic possibility for direct forcing of total solar insolation (TSI) on the ISM has been challenged due to small inter-decadal TSI changes, Zhang et al. (2014) have invoked the impact of higher UV components in the solar radiation on stratigraphic heating and subsequent intensification of the Hardley cell to explain synchronous relation between rainfall changes in the Galápagos island and solar activity during the Holocene. Additional to these external forcing, several paleoclimate records have shown a strong influence of the El Niño-southern oscillation (ENSO) like activity driven by SST gradient between tropical east Pacific and Indian Ocean on the ISM intensity in kilo-year timescales. A weak ENSO period modulated by cooler Pacific SST can strengthen the Walker circulation and, therefore, the ISM intensity over the Indian region. While the ENSO-like events were reported to be mostly absent during the early Holocene (Moy et al., 2002) period, their influence on the ISM may also be overridden by the Indian Ocean Dipole (IOD) effect (Ashok et al., 2001) and Atlantic multi-decadal oscillation (AMO; Goswami et al., 2006). A colder SST over the western Indian Ocean (negative IOD) and the northern Atlantic Ocean can lead to a weakening in ISM strength (Ashok et al., 2001).

6.2.1 The 6.5-kyr super-drought event

Our high-resolution data has unravelled a major super-drought event at about 6.5 kyr BP (6381-6575 kyr BP) that persisted for nearly 200 years (Fig. 6.3) with high sampling during the period providing confidence in the amplitude and duration of the event. The $\delta^{18}O$ anomaly values show an enrichment up to 1.4 ‰ during this event, corresponding to a rainfall decline of ~100 mm. A synchronous (6.5-5.9 kyr BP) cold and dry event have been reported at several locations globally (Wanner et al., 2008). Further, similar drought phases were also documented in various speleothem records (e.g., central India (Band et al., 2018), north-eastern India (Berkelhammer et al., 2012; Dutt et al., 2015), China (Dykoski et al., 2005), Oman (Fleitmann et al., 2007), Australia (Denniston et al., 2013) and Japan (Sone et al., 2013)) around this time,

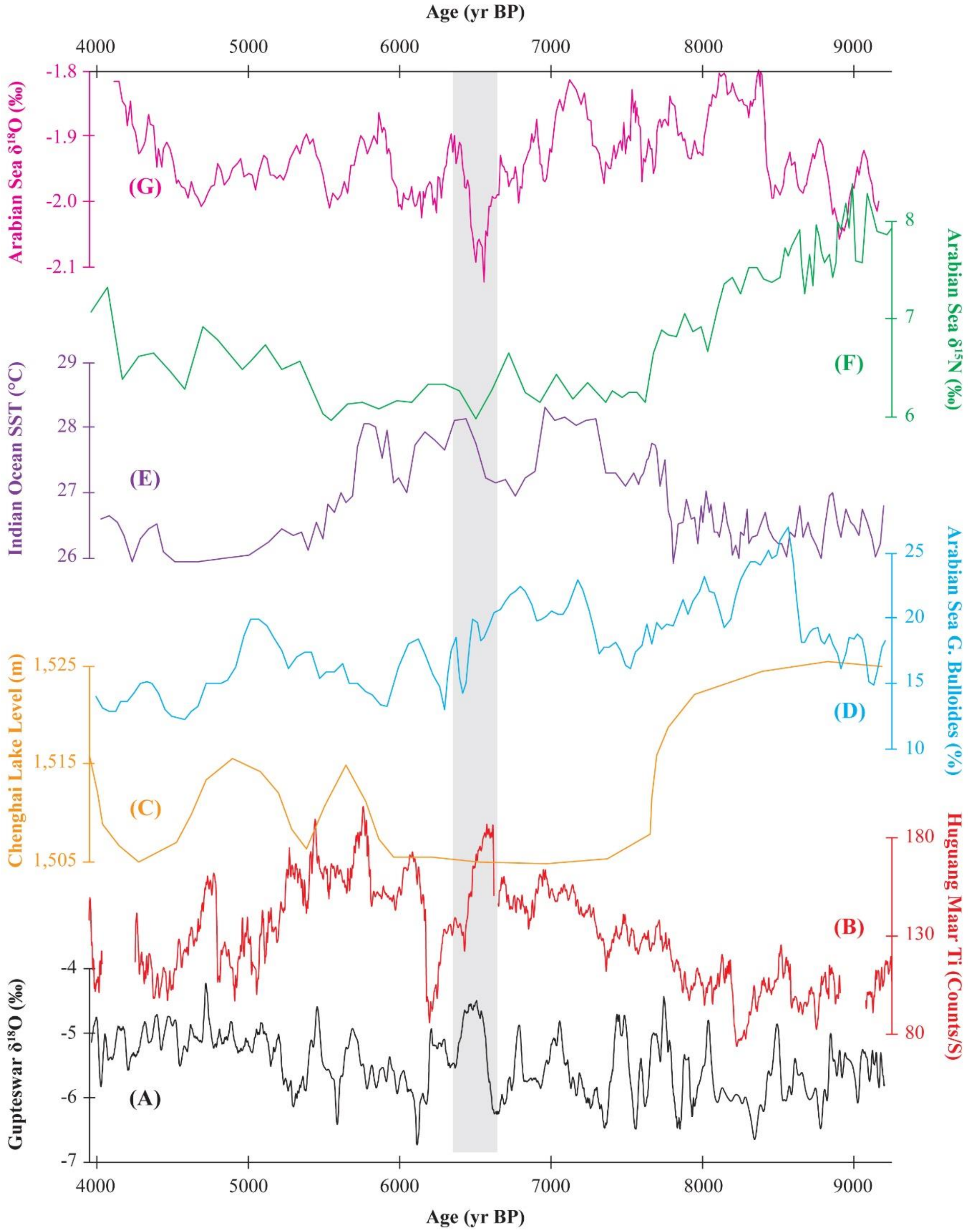

Figure 6.5. *Comparison of the time-series data which shows climatic changes near around 6.5 kyr BP. These time-averaged records include (A) δ^{18}O of the GPT-1 Speleothem (This study); (B) Ti data from Lake Huguang Maar, China (Yancheva et al., 2007); (C) Chenghai Lake level, China (Xu et al., 2020); (D) Western Indian Ocean SST (Kuhnert et al., 2014); (E) G. Bulloides (%) from the Arabian Sea (Gupta et al., 2005); (F) δ^{15}N record of Arabian Sea sediment (Kessarkar et al., 2018); (G) δ^{18}O record from the Indus delta sediment (Staubwasser et al., 2003).*

confirming the event to be a non-local climatic episode (Fig. 6.5). These observed trends, however, show different magnitude and duration of this event which may be attributed to uncertainties associated with chronological interpolation, time-resolution of the dataset, and $\delta^{18}O$ values at the source and their regulating mechanisms. In addition to the southwest monsoon, lake sediment chemistry from China also confirms the northeast monsoon decline around this period (Fig. 6.5).

An abrupt drier phase in Oman synchronous to the super-drought at 6.5 kyr BP has been linked with a reduction in ISM intensity due to the southward retreat of the ITCZ (Fleitmann et al., 2007). To evaluate this proposition, we compare the GPT-1 $\delta^{18}O$ record (Fig. 6.6) with available time-series of sedimentary titanium concentration data from the Cariaco Basin (Haug et al., 2001). The Cariaco-Ti data serve as a reliable proxy for ITCZ movement, where higher Ti concentrations reflect enhanced riverine input during the northward shift of the ITCZ. The Cariaco-Ti data during this period (6.3-6.7 kyr BP) were mostly characterized with high values with no major declining trend (Fig. 6.6E), ruling out the dominant role of ITCZ retreat in driving this dry event. Comparison of other global climatic records with Gupteswar $\delta^{18}O$ data reveals the occurrence of a weaker ENSO-like phase with lower eastern Pacific SST during this event (Fig. 6.6F) and, therefore, may not explain the dry phase at ~6.5 kyr BP through an ENSO-related process. A recent study based on the Nd isotopic composition of coral has documented an enhanced Pacific water supply to the Southern Ocean water column and reduced westerly winds in the Southern Hemisphere during the mid-Holocene period (Struve et al., 2020; Fig. 6.6B).

These circulation pattern changes are contemporary to the super-drought event and may derive this abrupt dry event through the Southern Annular Mode (SAM) by influencing the subtropical Indian Ocean SST (Dou et al., 2017). However, this proposition seems less likely as the SAM has a stronger role in regulating the Australian rainfall than the ISM, and the mid-Holocene records show relatively lesser rainfall change in Australia than in India. This conclusion on the impact of SAM on the super-drought can be better constrained with high-resolution mid-Holocene data for both Australian rainfall and SAM. Figure 6.6 shows that the super-drought event is synchronous to a colder NA SST period that may cause a rainfall deficit in India by weakening the tropospheric temperature gradient and increasing the frequency of breaks during the season (Goswami et al., 2006). Although capable, the NA SST alone seems less likely to be responsible for this super-drought event as (i) the period of SST decline is

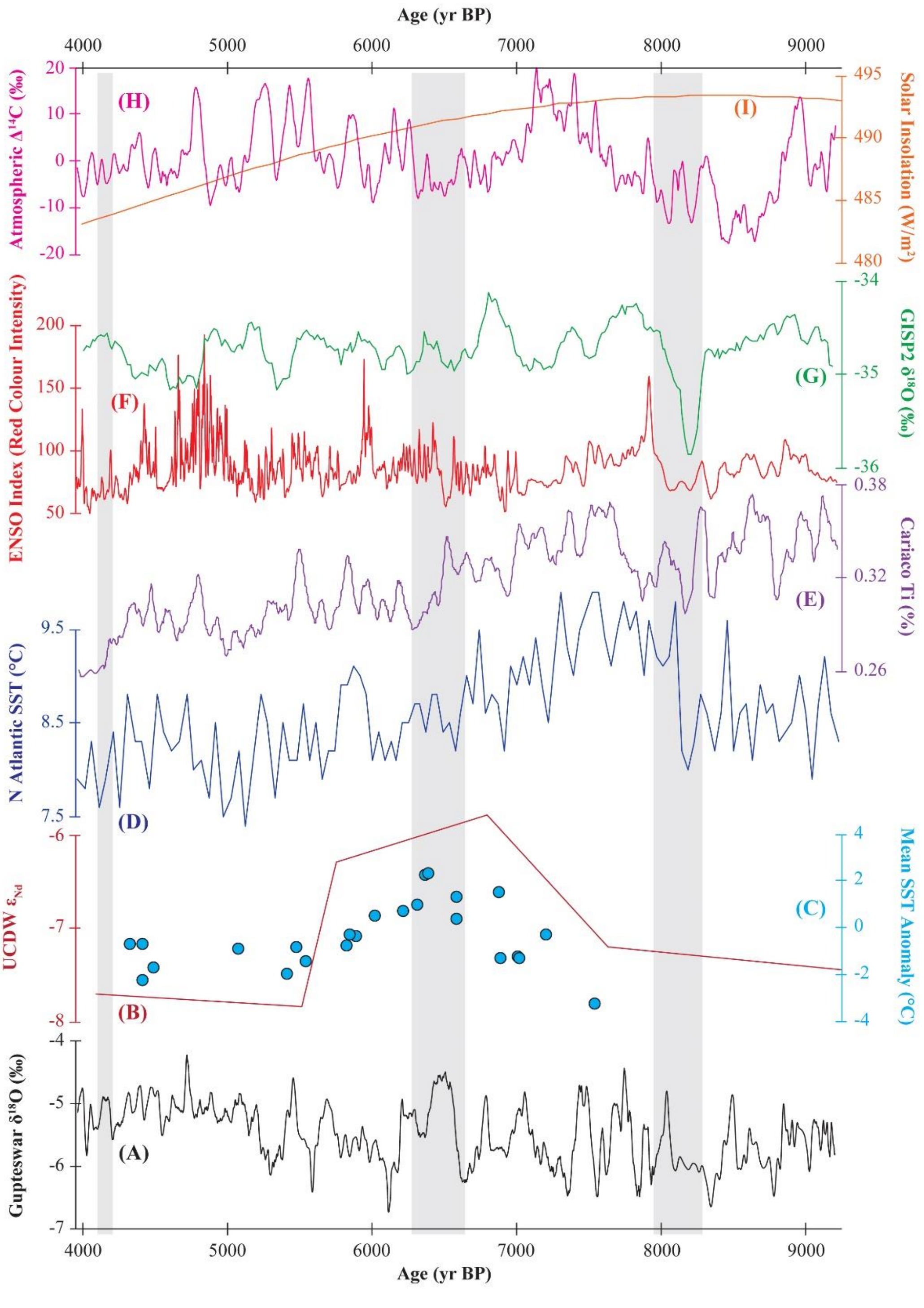

Figure 6.6. *Comparison of time-averaged mid-Holocene (A) δ^{18}O record of the GPT-speleothem (This study) with other climatic proxies, such as (B) ε_{Nd} isotopic value from the Southern Ocean representing the Upper Circumpolar Deep Water (UCDW) (Struve et al., 2020); (C) mean SST anomalies from eastern Indian Ocean (Abram et al., 2009); (D) North Icelandic shelf summer SST (Jiang et al., 2015); (E) sedimentary Ti concentrations for Cariaco Basin (Haug et al., 2001); (F) ENSO Index variability (Moy et al., 2002); (G) GISP2 δ^{18}O (Stuiver and Grootes, 2000); (H) atmospheric Δ^{14}C (Stuiver et al., 1998); (I) solar insolation (Laskar et al., 2004). The gray bands represent the major mid-Holocene dry events around 4.2, 6.5 and 8.2 kyr BP.*

smaller compared to the drought episode and also, (ii) a similar (or even higher amount of) decline in NA SST throughout the GPT-1 record does not lead to such large-scale drought phase. Abram et al. (2009), based on Sr/Ca data of corals from Sumatra and Papua New Guinea, documents a warmer SST of the Indo-Pacific Warm Pool (IPWP) by 1.3 ± 0.3 °C between 6600 and 6300 yrs BP (Fig. 6.6C). This warm phase in the eastern Indian Ocean is expected to lead to a negative-IOD (Indian Ocean dipole) phase, which in turn can explain the observed drought phase. Spectral analyses of Gupteswar $\delta^{18}O$ data (n = 88) for this episode indicate a decadal variability with a period of ~16 yr (Fig. 6.4), similar to decadal modulation (with period ~15 yrs) of correlation between IOD and ISMR in recent years (Goswami et al., 2006) supporting the proposed IOD connection. The intensification of the IPWP and a strong negative IOD also means a westward expansion of the warm pool over the Indian Ocean and an overall increase in the equatorial Indian Ocean (IO) SST. Such warming of IO SST and associated weakening of Indian monsoon (winds) leads to the positive feedback of increasing IO SST further and weakening the Indian monsoon even more (Swapna et al., 2014), contributing to the extent of the super-drought. Therefore, a combination of a weaker tropospheric temperature caused by the cooler NA SST coupled with a persistent negative IOD condition caused by warmer IPWP exacerbated this mega-drought of the Indian monsoon. Consistent with this observation, an earlier study from Central India has also shown a linkage between IPWP and prolonged drought phases (Prasad et al., 2014). These outcomes, therefore, underscore the dominant role of Indian Ocean SST changes in regulating sustained extreme ISM conditions.

The Indian monsoon super-drought event of around 6.5 kyr BP is distinct from mega-droughts associated with the global "8.2-kyr" and "4.2-kyr" dry events (Fig. 6.3) not only in its amplitude and temporal extent but also in its driving mechanisms. The 8.2-kyr event is a cold (1-3 °C decline) and dry event which sustained for about 160 years and was observed at various global sites (Dixit et al., 2014b; Kaushal et al., 2018; Mayewski et al., 2004). This cold event resulted from the cooling of the Northern Hemisphere due to the natural breaking of an ice-dammed lake (Dixit et al., 2014b). Our dataset records a dry event between 7955 and 8106 kyr BP, with the $\delta^{18}O$ anomaly value reaching up to 1 ‰ (Fig. 6.3). The timing and magnitude of this ISM weakening event are consistent with previous reports from India (Dixit et al., 2014b; Gupta et al., 2003). Comparison of this $\delta^{18}O$ enrichment with global climatic records shows concurrent cooling in the Northern Atlantic Ocean, reconfirming earlier suggestions on the role of NA cooling in driving the 8.2 kyr event. The other mid-Holocene dry event at 4.2 kyr BP has received significant attention mainly due to its linkage with the demise of several ancient civilizations in India, Egypt, and Greece. This ISM decline phase, which is sustained for 200-300 yrs, has been previously suggested to be regulated either by solar insolation (Staubwasser et al., 2003) or by combined effects of negative IOD phases and increased ENSO activities (Dixit et al., 2014a). Figure 6.3 records a steady increase in $\delta^{18}O$ value by ~0.8 ‰ during 4106-4199 kyr BP, which is synchronous to the global dry event. This event is concurrent with a decline in Ti concentration of the Carico basin, indicating a southward ITCZ retreat, which is expected to decline the ISM strength. Further, the paleo-climatic records show an increased ENSO activity during this period. Based on these observations, the 4.2-kyr event seems to be regulated in an El Niño-type scenario which has resulted in a southward ITCZ shift and hence, a decline in ISM. Although the impact of IOD on the 4.2 kyr event could not be evaluated due to a lack of proper proxy data for past IOD changes, a negative IOD phase has been suggested as a possible driver for the 4.2-kyr dry event (Dixit et al., 2014a) and other prolonged drought phases in India (Prasad et al., 2014). The differences in the timing of the event in GPT-1 data and that over Kutumsar (Band et al., 2018) are likely to be due to larger chronological uncertainty in the Kutumsar data. At the same time, the evidence presented here indicates that, like the other two super-droughts of ISM, the one around 6.5 kyr BP is also part of a global scale cold and dry event (Wanner et al., 2008). However, the event being synchronous in GPT-1 and Dongge caves but out of phase encourages us to speculate that the spatial scale of this event may be smaller than the other two events, with the core monsoon region being the epicentre of the super-drought. Based on our and earlier observations, this study underscores the importance of the IOD phases in regulating the sustained climatic extreme events around the Indian region.

6.3. Conclusion

High resolution (5-yr) oxygen isotopic ($\delta^{18}O$) records of a speleothem sample collected from the Gupteswar Cave, located in the core monsoon zone, were investigated to reconstruct the mid-Holocene variability of ISM. This reconstruction shows a declining trend of ISM from the mid to late-Holocene period, along with some extreme cold and arid phases, e.g., during 8.2 kyr, 6.5 kyr, and 4.2 kyr BP. The ~6.5 kyr event is a super-drought event spanned around 200 years. Warming of Indian Ocean surface temperature (SST) linked with IPWP and the subsequent negative Indian Ocean Dipole phase possibly reduced moisture supply deep inside the ISM domain and created drought phases around 6.5 kyr BP. This study reveals that the broad trends of ISM are primarily synchronous to the NA climatic condition, cooling, controlled mainly by the solar insolation. In contrast, the Indian Ocean surface temperate (SST) is more responsible for short-term extreme climatic events.

Chapter 7

Summary and Future Perspectives

This thesis work was mainly focused to understand the changes in erosion pattern and its climatic sensitivity at different time scales, ranging between seasonal and kilo-years. Towards this, geochemical and isotopic studies of a variety of samples, which includes river water, speleothems, and marine and terrestrial sedimentary records, have been carried out. Time-series analysis of river water chemistry for the Brahmaputra River, one of the largest Himalayan river systems, was carried out at a weekly to biweekly interval to understand the climatic sensitivity of chemical erosion at a seasonal time scale. Two sediment cores from the eastern Arabian Sea were investigated to reconstruct the tropical erosion pattern during the Holocene period. Whereas, the terrestrial sedimentary records from the upper Indus River basin were used to infer the Himalayan erosion pattern during the last glacial-interglacial period. Additionally, oxygen isotopic records were also used to reconstruct the past variability of the Indian summer monsoon during the mid-Holocene period. The significant outcomes of this thesis are summarized below.

7.1 Seasonality in chemical erosion pattern: Evidence from River water chemistry

Dissolved major ions and Sr concentrations of the Brahmaputra River at Guwahati, India, have been investigated at weekly intervals for one year to understand the seasonality in erosion patterns and the relative contribution of solute from the possible sources. Comparison of major ions datasets from present and earlier studies shows no appreciable change during the last ~50 years. Elemental concentrations and Ca/Na* (Na* = Na - Cl) ratio of the Brahmaputra co-vary (inversely) with the water discharge; the degree of seasonality, however, is less pronounced compared to other Himalayan (e.g., Ganga and Salween) rivers. The monthly-averaged Ca/Si ratios of the Brahmaputra (3.7 ± 0.2), which is lower by ~2 times than those reported earlier for the Ganga outflow (6 ± 1), show minimal (~6 %) seasonal changes. The silicate-derived cations (Cat_S) and Sr (Sr_S) have been estimated using an inversion method. Although these estimated values broadly show seasonal changes, the average Cat_S and Sr_S values for the monsoon (26 ± 4 % (Cat_S); 26 ± 6 % (Sr_S)) and non-monsoon (27 ± 3 % (Cat_S);

24 ± 4 % (Sr_s)) seasons are statistically same. These estimates indicate a weak runoff-erosion linkage for the Brahmaputra River. Outcomes from this study, therefore, suggest that the chemical erosion intensity of this basin is more dominated by rapid regional (physical) erosion around the eastern syntaxis than the climatic (runoff) parameters.

7.2 Holocene variability of the erosion pattern: Evidence from marine records

Major and trace elemental geochemistry of two sediment cores (SSK40/GC06 and SSK40/GC10) from the eastern Arabian Sea have been investigated to reconstruct the continental erosion pattern and ocean redox state during the Holocene period.

The SSK40/GC10 core preserves the sedimentation record between 7.2 and 0.8 kyr BP. The covariations of Fe/Al with K/Al and Ti/Al ratios of the SSK40/GC10 sediment core indicate that the western-flowing Indian rivers (e.g., Narmada, Tapi, and Mahi) and aeolian supply from the Thar regions are the major sediment suppliers to this location. Factor analysis of the geochemical dataset identifies four major factors explaining about 80 % of the total variance. Down-core profiles of several detrital proxies (Fe/Al, Ti/Al, V/Al, and Co/Al) show that the sediment sources were nearly uniform until 2.6 kyr BP. However, the chemical erosion indices, K/Al ratios, and CIA* (modified Chemical Index of Alteration), show significant changes in the upper part of the core. The period of these erosion changes (2.6-1.6 kyr BP) mostly overlaps with the Roman Warm Period, indicating an erosion-climate linkage. Variations in the Ba/Al ratios and enrichment factors of U (EF_U) and Mo (EF_{Mo}), along with TOC/Al, and S/Al trends, indicate a fluctuating oceanic (bottom water) redox state during the studied period. These trends point to a shift from oxic to anoxic bottom water condition since ~ 4.2 kyr BP. The timing of this change is synchronous to the earlier reported drought phase at the beginning of the Meghalayan stage, underscoring climatic control on the bottom water redox state.

The geochemical study of the SSK40/GC06 core has also allowed us to reconstruct the erosion intensity changes for the last ~3560 years. The SSK40/GC06 sediments are mostly silty (70 ± 15 %) with an appreciable amount of organic carbon (1.3 ± 0.4 %) and $CaCO_3$ (11 ± 2 %) in them. Insignificant temporal changes in immobile elemental (Al, Ti, and rare earth elements (REE)) concentrations and REE patterns in this core indicate no significant provenance change during this period. However, the depth profiles of multiple erosion indices (Mg/Al, Rb/Sr, K/Al, and Chemical Index of Alteration (CIA)) show a major shift towards intensifying chemical erosion since 1600 yr BP to present. Available climatic and sedimentary records confirm no significant change in the southwest (SW) monsoon during this period. These records, however, point to a synchronous rise in C4 vegetation, possibly due to sustained agricultural practices in the tropical regions. The human-induced increase in C4 vegetation with shallow root systems may promote efficient sediment transport and hence, intense erosion of young soils with faster dissolution kinetics.

7.3 Himalayan erosion pattern during the Last Glacial-Interglacial cycle

Temporal variation in sediment provenance and erosion pattern of the Himalayan river basin have been reconstructed using geochemical and Sr-Nd isotopic compositions of a riverine sedimentary section from the upper Zanskar River basin. These samples preserve the sedimentation record between ~23 and ~1 kyr BP. The isotopic and geochemical compositions of this sediment section show significant temporal variations. The $CaCO_3$ content varies from 36 to 68 % with two major step-like patterns; the $CaCO_3$ concentrations were relatively lower (mean: 38 ± 1 %) before 16 kyr BP than that (mean: 64 ± 3 %) after 12.5 kyr BP, with an intermediate concentration (53 ± 3 %) level during ~16 to 12.5 kyr BP. The major shift in the geochemical composition is also synchronous with $^{87}Sr/^{86}Sr$ and ε_{Nd}. The $^{87}Sr/^{86}Sr$ ratio systematically changes from 0.74732 to 0.73187 at around 16 kyr, whereas the ε_{Nd} increases from -18.1 to -17.1 ‰ during the same period. These Sr-Nd isotopic shifts point to a significant change in the sediment provenance to the study site, and this change is synchronous with the Bølling-Allerød warm period. This change in sedimentary sources supports strong control of climatic changes on the land-surface processes. Additional to provenances, temporal trends of several erosion indices such as CIA and K/Si also show significant changes in the chemical erosion intensity. The observed higher intensity of chemical erosion in the basin during the Bølling-Allerød period is attributable to enhance rock dissolution during this warm period and also exposure of fresh minerals during glacial retreat. The observed changes in sediment provenances and chemical erosion intensity underscore the strong coupling between Himalayan erosion and climate during the last glacial-interglacial period.

7.4 Natural variability of Indian summer monsoon during Mid-Holocene period

In addition to past erosion reconstruction, this study has also attempted to reconstruct the natural variability of the Indian summer monsoon during the mid-Holocene stage. The rainfall pattern was reconstructed using the high-resolution oxygen isotopic ($\delta^{18}O$) data of a speleothem (age ~ 9200-3950 yr BP) from the core monsoon region (Gupteswar cave, India). Oxygen isotopic composition of tropical speleothem serves as a reliable measure of rainfall intensity. The present dataset fills a gap in chronologically well-constrained past Indian Summer Monsoon (ISM) variations during the mid-Holocene. The $\delta^{18}O$ trend of the Gupteswar speleothem unravels space-time characteristics of a super-drought event sustaining for ~200 yrs around ~6.5 kyr BP. Asynchronous warm phase in the eastern Indian Ocean and a persistent negative Indian Ocean Dipole (IOD) with the event confirm the critical role of unstable regional ocean-atmosphere feedbacks in driving the super-drought. Further, the $\delta^{18}O$ dataset shows a broad decline in ISM strength during the mid-Holocene period in response to North Atlantic (NA) climate change and/or southward retreat of the intertropical convergence zone (ITCZ). These observations suggest the dominancy of the IOD effect in controlling large-magnitude ISM changes, whereas the NA climate is responsible for the lower-frequency ISM variability.

7.5 Future directions

This detailed and comprehensive study was useful in constraining the climatic sensitivity of erosion patterns of the Indian sub-continent at different time scales. This thesis work have shown a strong coupling between erosion and climate in kilo-year timescales, whereas the erosion pattern during the last few kilo-years seems to have the influence of the human-induced land use pattern. Further, the chemical erosion pattern also shows significant seasonality, which is less driven by climate and more linked to regional physical erosion patterns in the Brahmaputra basin. Additional to these key conclusions, this thesis work also identifies a few future research scopes which can enhance our understanding on land-surface processes in the tropical regions. Some of these future research aspects are listed below.

1) The concentration-discharge relationship in large and small river systems can be useful in assessing the exact role of the critical zone processes and hydrological pathways in regulating the mobility and fluxes of chemical constituents from the land to the nearby oceanic ecosystems. These types of studies in the Indian regions are limited due to lack of simultaneous measurement of water discharge and water chemistry. Thorough and rigorous time-series monitoring of river water chemistry together with key hydrological parameters, therefore, can be useful in better constraining the short-term climatic impact on the chemical erosion rates.

2) The chemical and isotopic study of terrestrial sedimentary records seems to provide better clues about erosion pattern in the high-altitude regions. Composition of these records,

unlike the oceanic cores, is regulated by limited sources and hence, can provide more accurate information about erosion changes in the mountainous regions. More isotopic investigation of terrestrial records of the river and/or lake sediments in the Himalayas will be a beneficial approach to establish past Himalaya erosion and its regulating factors. Considering the global importance of the Himalaya, these studies can provide a thorough assessment on the impact of the Himalayan erosion on global biogeochemical cycles in kilo-year timescales.

3) This study was successful in reconstructing the Holocene variability of the chemical erosion patterns using chemical and isotopic signatures of the Arabian Sea sediments. However, these efforts demanded better understanding of sediment storage time within the river basin and the related time lag between oceanic records and the continental processes. It is also important to understand the sediment residence time for assessing the continental erosional flux to the oceans. Isotopic study of uranium and beryllium in river and nearby oceanic sediments should be attempted to infer about these sediment transport processes and the possible time lag between continental processes and oceanic signatures (Dosseto et al., 2006).

4) This thesis, based on chemical signatures of the Arabian Sea, has invoked the possible impact of man-made activities on the chemical flux during the last millennia. To better constrain the land use patterns on the erosion process, high-resolution chemical and isotopic study of lake sediments is essential to reconstruct both paleo-vegetational changes and their relation with the land-surface processes. These researches will also be crucial to evaluate the reliability of using modern river composition in long-term global chemical budgets.

References

Abram, N.J., McGregor, H.V., Gagan, M.K., Hantoro, W.S. and Suwargadi, B.W., 2009. Oscillations in the southern extent of the Indo-Pacific Warm Pool during the mid-Holocene. Quaternary Science Reviews, 28, 2794-2803.

Acharya, S.S. and Chakrabarti, R., 2019. Variations in trace metal concentrations and Sr, Nd isotopic compositions in sediments from two contrasting settings in the Eastern Arabian Shelf: Implications for provenance and paleoclimate reconstruction. Chemical Geology, 509, 134-151.

Acharya, S.S., Panigrahi, M.K., Gupta, A.K. and Tripathy, S., 2015. Response of trace metal redox proxies in continental shelf environment: The Eastern Arabian Sea scenario. Continental Shelf Research, 106, 70-84.

Agnihotri, R., Dutta, K., Bhushan, R. and Somayajulu, B.L.K., 2002. Evidence for solar forcing on the Indian monsoon during the last millennium. Earth and Planetary Science Letters, 198, 521-527.

Alagarsamy, R. and Zhang, J., 2005. Comparative studies on trace metal geochemistry in Indian and Chinese rivers. Current Science, 299-309.

Algeo, T.J. and Tribovillard, N., 2009. Environmental analysis of paleoceanographic systems based on molybdenum-uranium covariation. Chemical Geology, 268, 211-225.

Algeo, T.J., Kuwahara, K., Sano, H., Bates, S., Lyons, T., Elswick, E., Hinnov, L., Ellwood, B., Moser, J. and Maynard, J.B., 2011. Spatial variation in sediment fluxes, redox conditions, and productivity in the Permian-Triassic Panthalassic Ocean. Palaeogeography, Palaeoclimatology, Palaeoecology, 308, 65-83.

Anandh, P.C. and Vissa, N.K., 2020. On the linkage between extreme rainfall and the Madden-Julian Oscillation over the Indian region. Meteorological Applications, 27, e1901.

Armitage, J.J., Jones, T.D., Duller, R.A., Whittaker, A.C. and Allen, P.A., 2013. Temporal buffering of climate-driven sediment flux cycles by transient catchment response. Earth and Planetary Science Letters, 369, 200-210.

Arz, H.W., Lamy, F. and Pätzold, J., 2006. A pronounced dry event recorded around 4.2 ka in brine sediments from the northern Red Sea. Quaternary Research, 66, 432-441.

Ashok, K., Guan, Z. and Yamagata, T., 2001. Impact of the Indian Ocean dipole on the relationship between the Indian monsoon rainfall and ENSO. Geophysical Research Letters, 28, 4499-4502.

Ayalon, A., Bar-Matthews, M. and Sass, E., 1998. Rainfall-recharge relationships within a karstic terrain in the Eastern Mediterranean semi-arid region, Israel: $\delta^{18}O$ and δD characteristics. Journal of Hydrology, 207, 18-31.

Bali, R., Chauhan, M.S., Mishra, A.K., Ali, S.N., Tomar, A., Khan, I., Singh, D.S. and Srivastava, P., 2017. Vegetation and climate change in the temperate-subalpine belt of Himachal Pradesh since 6300 cal. yrs. BP, inferred from pollen evidence of Triloknath palaeolake. Quaternary International, 444, 11-23.

Band, S., Yadava, M.G., Lone, M.A., Shen, C.C., Sree, K. and Ramesh, R., 2018. High-resolution mid-Holocene Indian summer monsoon recorded in a stalagmite from the Kotumsar Cave, Central India. Quaternary International, 479, 19-24.

Banerji, U.S., Bhushan, R. and Jull, A.J.T., 2017. Mid-late Holocene monsoonal records from the partially active mudflat of Diu Island, southern Saurashtra, Gujarat, western India. Quaternary International, 443, 200-210.

Banerji, U.S., Bhushan, R. and Jull, A.J.T., 2019. Signatures of global climatic events and forcing factors for the last two millennia from the active mudflats of Rohisa, southern Saurashtra, Gujarat, western India. Quaternary International, 507, 172-187.

Banerji, U.S., Shaji, J., Arulbalaji, P., Maya, K., Mohan, S.V., Dabhi, A.J., Shivam, A., Bhushan, R. and Padmalal, D., 2021. Mid-late Holocene evolutionary history and climate reconstruction of Vellayani lake, south India. Quaternary International, 599, 72-94.

Bar-Matthews, M., Ayalon, A. and Kaufman, A., 1997. Late Quaternary paleoclimate in the eastern Mediterranean region from stable isotope analysis of speleothems at Soreq Cave, Israel. Quaternary Research, 47, 155-168.

Bar-Matthews, M., Ayalon, A., Gilmour, M., Matthews, A. and Hawkesworth, C.J., 2003. Sea-land oxygen isotopic relationships from planktonic foraminifera and speleothems in the Eastern Mediterranean region and their implication for paleorainfall during interglacial intervals. Geochimica et Cosmochimica Acta, 67, 3181-3199.

Bar-Matthews, M., Ayalon, A., Matthews, A., Sass, E. and Halicz, L., 1996. Carbon and oxygen isotope study of the active water-carbonate system in a karstic Mediterranean cave: Implications for paleoclimate research in semiarid regions. Geochimica et Cosmochimica Acta, 60, 337-347.

Battisti, D.S., Ding, Q. and Roe, G.H., 2014. Coherent pan-Asian climatic and isotopic response to orbital forcing of tropical insolation. Journal of Geophysical Research: Atmospheres, 119, 11-997.

Bayon, G., Dennielou, B., Etoubleau, J., Ponzevera, E., Toucanne, S. and Bermell, S., 2012. Intensifying weathering and land use in Iron Age Central Africa. Science, 335, 1219-1222.

Berkelhammer, M., Sinha, A., Mudelsee, M., Cheng, H., Edwards, R.L. and Cannariato, K., 2010. Persistent multidecadal power of the Indian Summer Monsoon. Earth and Planetary Science Letters, 290, 166-172.

Berkelhammer, M., Sinha, A., Stott, L., Cheng, H., Pausata, F.S. and Yoshimura, K., 2012. An abrupt shift in the Indian monsoon 4000 years ago. In: AGU Geophysical Monograph on Climate and Civilization, 198, 75-87.

Berner, E.K. and Berner, R.A., 2012. Global Environment: Water, Air, and Geochemical Cycles. (Second Ed.) Princeton University Press, Princeton, NJ.

Berner, R.A., 1995. Chemical weathering and its effect on atmospheric CO_2 and climate. In White, A. F., Brantley, S. L. (Eds.). Chemical weathering rates of silicate minerals. Reviews of Mineralogy, 31, Mineralogical Society of America, Washington, D.C., 565-583.

Bhushan, R., Dutta, K. and Somayajulu, B.L.K., 2001. Concentrations and burial fluxes of organic and inorganic carbon on the eastern margins of the Arabian Sea. Marine Geology, 178, 95-113.

Bickle, M.J., Chapman, H.J., Bunbury, J., Harris, N.B., Fairchild, I.J., Ahmad, T. and Pomiès, C., 2005. Relative contributions of silicate and carbonate rocks to riverine Sr fluxes in the headwaters of the Ganges. Geochimica et Cosmochimica Acta, 69, 2221-2240.

Bickle, M.J., Chapman, H.J., Tipper, E., Galy, A., Christina, L. and Ahmad, T., 2018. Chemical weathering outputs from the flood plain of the Ganga. Geochimica et Cosmochimica Acta, 225, 146-175.

Bishop, J.K., 1988. The barite-opal-organic carbon association in oceanic particulate matter. Nature, 332, 341-343.

Blöthe, J.H. and Korup, O., 2013. Millennial lag times in the Himalayan sediment routing system. Earth and Planetary Science Letters, 382, 38-46.

Blum, J.D. and Erel, Y., 1995. A silicate weathering mechanism linking increases in marine ^{87}Sr/^{86}Sr with global glaciation. Nature, 373, 415-418.

Bluth, G.J. and Kump, L.R., 1994. Lithologic and climatologic controls of river chemistry. Geochimica et Cosmochimica Acta, 58, 2341-2359.

Bond, G., Kromer, B., Beer, J., Muscheler, R., Evans, M.N., Showers, W., Hoffmann, S., Lotti-Bond, R., Hajdas, I. and Bonani, G., 2001. Persistent solar influence on North Atlantic climate during the Holocene. Science, 294, 2130-2136.

Bookhagen, B. and Burbank, D.W., 2010. Toward a complete Himalayan hydrological budget: Spatiotemporal distribution of snowmelt and rainfall and their impact on river discharge. Journal of Geophysical Research: Earth Surface, 115, F03019.

Bookhagen, B., Barbara, U.C.S., Barbara, S., 2009. High resolution spatiotemporal distribution of rainfall seasonality and extreme events based on a 12-year TRMM timeseries. https://www.geog.ucsb.edu/~bodo/TRMM/.

Bookhagen, B., Thiede, R.C. and Strecker, M.R., 2005. Abnormal monsoon years and their control on erosion and sediment flux in the high, arid northwest Himalaya. Earth and Planetary Science Letters, 231, 131-146.

Boral, S., Peucker-Ehrenbrink, B., Hemingway, J.D., Sen, I.S., Galy, V. and Fiske, G.J., 2021. Controls on short-term dissolved $^{87}Sr/^{86}Sr$ variations in large rivers: Evidence from the Ganga-Brahmaputra. Earth and Planetary Science Letters, 566, 116958.

Bouchez, J., Moquet, J.S., Espinoza, J.C., Martinez, J.M., Guyot, J.L., Lagane, C., Filizola, N., Noriega, L., Hidalgo Sanchez, L. and Pombosa, R., 2017. River mixing in the Amazon as a driver of concentration-discharge relationships. Water Resources Research, 53, 8660-8685.

Breitenbach, S.F.M., Rehfeld, K., Goswami, B., Baldini, J.U., Ridley, H.E., Kennett, D.J., Prufer, K.M., Aquino, V.V., Asmerom, Y., Polyak, V.J. and Cheng, H., 2012. Constructing proxy records from age models (COPRA). Climate of the Past, 8, 1765-1779.

Burbank, D.W., Blythe, A.E., Putkonen, J., Pratt-Sitaula, B.G.A.B.E.T., Gabet, E., Oskin, M., Barros, A. and Ojha, T.P., 2003. Decoupling of erosion and precipitation in the Himalayas. Nature, 426, 652-655.

Burbank, D.W., Bookhagen, B., Gabet, E.J. and Putkonen, J., 2012. Modern climate and erosion in the Himalaya. Comptes Rendus Geoscience, 344, 610-626.

Burchfiel, B.C. and Royden, L.H., 1985. North-south extension within the convergent Himalayan region. Geology, 13, 679-682.

Burchfiel, B.C., 1992. The South Tibetan detachment system, Himalayan orogen: Extension contemporaneous with and parallel to shortening in a collision mountain belt. Geological Society of America Special Paper, 267, 41.

Cai, M., Xu, Z., Clift, P.D., Lim, D., Khim, B.K., Yu, Z., Kulhanek, D.K., Li, T., Chen, H. and Sun, R., 2019. Depositional history and Indian summer monsoon controls on the silicate weathering of sediment transported to the eastern Arabian Sea: Geochemical records from IODP Site U1456 since 3.8 Ma. Geochemistry, Geophysics, Geosystems, 20, 4336-4353.

Cai, Y., Zhang, H., Cheng, H., An, Z., Edwards, R.L., Wang, X., Tan, L., Liang, F., Wang, J. and Kelly, M., 2012. The Holocene Indian monsoon variability over the southern Tibetan Plateau and its teleconnections. Earth and Planetary Science Letters, 335, 135-144.

Calvert, S.E., Pedersen, T.F., Naidu, P.D. and Von Stackelberg, U., 1995. On the organic carbon maximum on the continental slope of the eastern Arabian Sea. Journal of Marine Research, 53, 269-296.

Carretier, S., Guerit, L., Harries, R., Regard, V., Maffre, P. and Bonnet, S., 2020. The distribution of sediment residence times at the foot of mountains and its implications for proxies recorded in sedimentary basins. Earth and Planetary Science Letters, 546, 116448.

Caves Rugenstein, J.K., Ibarra, D.E. and von Blanckenburg, F., 2019. Neogene cooling driven by land surface reactivity rather than increased weathering fluxes. Nature, 571, 99-102.

Cerling, T.E., Pederson, B.L. and Von Damm, K.L., 1989. Sodium-calcium ion exchange in the weathering of shales: Implications for global weathering budgets. Geology, 17, 552-554.

Chabaux, F., Granet, M., Pelt, E., France-Lanord, C. and Galy, V., 2006. ^{238}U-^{234}U-^{230}Th disequilibria and timescale of sedimentary transfers in rivers: clues from the Gangetic plain rivers. Journal of Geochemical Exploration, 88, 373-375.

Chahal, P., Kumar, A., Sharma, C.P., Singhal, S., Sundriyal, Y.P. and Srivastava, P., 2019. Late Pleistocene history of aggradation and incision, provenance and channel connectivity of the Zanskar River, NW Himalaya. Global and Planetary Change, 178, 110-128.

Chakrapani, G.J. and Saini, R.K., 2009. Temporal and spatial variations in water discharge and sediment load in the Alaknanda and Bhagirathi Rivers in Himalaya, India. Journal of Asian Earth Sciences, 35, 545-553.

Chamberlin, T.C., 1899. An attempt to frame a working hypothesis of the cause of glacial periods on an atmospheric basis. The Journal of Geology, 7, 545-584.

Chandramohan, T. and Balchand, A.N., 2007. Regional sediment yield pattern for the west flowing rivers of Kerala State, India. Materials and Geoenvironment, 54, 501.

Chapman, H., Bickle, M., Thaw, S.H. and Thiam, H.N., 2015. Chemical fluxes from time series sampling of the Irrawaddy and Salween Rivers, Myanmar. Chemical Geology, 401, 15-27.

Chatterjee, A. and Ray, J.S., 2017. Sources and depositional pathways of mid-Holocene sediments in the Great Rann of Kachchh, India: Implications for fluvial scenario during the Harappan Culture. Quaternary International, 443, 177-187.

Chen, J., Wang, F., Xia, X. and Zhang, L., 2002. Major element chemistry of the Changjiang (Yangtze River). Chemical Geology, 187, 231-255.

Chiang, J.C., Cheng, W. and Bitz, C.M., 2008. Fast teleconnections to the tropical Atlantic sector from Atlantic thermohaline adjustment. Geophysical Research Letters, 35, L07704.

Clift, P.D. and Giosan, L., 2014. Sediment fluxes and buffering in the post-glacial Indus Basin. Basin Research, 26, 369-386.

Clift, P.D., Carter, A., Krol, M. and Kirby, E., 2002. Constraints on India-Eurasia collision in the Arabian Sea region taken from the Indus Group, Ladakh Himalaya, India. Geological Society, London, Special Publications, 195, 97-116.

Clift, P.D., Giosan, L., Blusztajn, J., Campbell, I.H., Allen, C., Pringle, M., Tabrez, A.R., Danish, M., Rabbani, M.M., Alizai, A. and Carter, A., 2008, Holocene erosion of the Lesser Himalaya triggered by intensified summer monsoon: Geology, 36, 79-82.

Clift, P.D., Giosan, L., Carter, A., Garzanti, E., Galy, V., Tabrez, A.R., Pringle, M., Campbell, I.H., France-Lanord, C., Blusztajn, J. and Allen, C., 2010. Monsoon control over erosion patterns in the western Himalaya: possible feed-back into the tectonic evolution. Geological Society, London, Special Publications, 342, 185-218.

Clift, P.D., Shimizu, N., Layne, G.D., Blusztajn, J.S., Gaedicke, C., Schluter, H.U., Clark, M.K. and Amjad, S., 2001. Development of the Indus Fan and its significance for the erosional history of the Western Himalaya and Karakoram. Geological Society of America Bulletin, 113, 1039-1051.

Clow, D.W. and Mast, M.A., 2010. Mechanisms for chemostatic behavior in catchments: Implications for CO_2 consumption by mineral weathering. Chemical Geology, 269, 40-51.

Cook, E.R., Anchukaitis, K.J., Buckley, B.M., D'Arrigo, R.D., Jacoby, G.C. and Wright, W.E., 2010. Asian monsoon failure and megadrought during the last millennium. Science, 328, 486-489.

Craw, D., Koons, P.O., Zeitler, P.K. and Kidd, W.S.F., 2005. Fluid evolution and thermal structure in the rapidly exhuming gneiss complex of Namche Barwa-Gyala Peri, eastern Himalayan syntaxis. Journal of Metamorphic Geology, 23, 829-845.

Crocket, J.H. and Paul, D.K., 2004. Platinum-group elements in Deccan mafic rocks: a comparison of suites differentiated by Ir content. Chemical Geology, 208, 273-291.

Cruz Jr, F.W., Karmann, I., Viana Jr, O., Burns, S.J., Ferrari, J.A., Vuille, M., Sial, A.N. and Moreira, M.Z., 2005. Stable isotope study of cave percolation waters in subtropical Brazil: Implications for paleoclimate inferences from speleothems. Chemical Geology, 220, 245-262.

Cullen, H.M., Demenocal, P.B., Hemming, S., Hemming, G., Brown, F.H., Guilderson, T. and Sirocko, F., 2000. Climate change and the collapse of the Akkadian empire: Evidence from the deep sea. Geology, 28, 379-382.

Dalai, T.K., Krishnaswami, S. and Sarin, M.M., 2002. Major ion chemistry in the headwaters of the Yamuna river system: Chemical weathering, its temperature dependence and CO_2 consumption in the Himalaya. Geochimica et Cosmochimica Acta, 66, 3397-3416.

Dansgaard, W., 1964. Stable isotopes in precipitation. Tellus, 16, 436-468.

Das, A. and Krishnaswami, S., 2007. Elemental geochemistry of river sediments from the Deccan Traps, India: implications to sources of elements and their mobility during basalt-water interaction. Chemical Geology, 242, 232-254.

Das, A., Krishnaswami, S., Sarin, M.M. and Pande, K., 2005. Chemical weathering in the Krishna Basin and Western Ghats of the Deccan Traps, India: Rates of basalt weathering and their controls. Geochimica et Cosmochimica Acta, 69, 2067-2084.

Das, P., Sarma, K.P., Jha, P.K., Ranjan, R., Herbert, R. and Kumar, M., 2016. Understanding the cyclicity of chemical weathering and associated CO_2 consumption in the Brahmaputra River Basin (India): the role of major rivers in climate change mitigation perspective. Aquatic Geochemistry, 22, 225-251.

DeCelles, P.G., Gehrels, G.E., Najman, Y., Martin, A.J., Carter, A. and Garzanti, E., 2004. Detrital geochronology and geochemistry of Cretaceous-Early Miocene strata of Nepal: implications for timing and diachroneity of initial Himalayan orogenesis. Earth and Planetary Science Letters, 227, 313-330.

Dehairs, F., Chesselet, R. and Jedwab, J., 1980. Discrete suspended particles of barite and the barium cycle in the open ocean. Earth and Planetary Science Letters, 49, 528-550.

Dehairs, F., Fagel, N., Antia, A.N., Peinert, R., Elskens, M. and Goeyens, L., 2000. Export production in the Bay of Biscay as estimated from barium-barite in settling material: a comparison with new production. Deep Sea Research Part I: Oceanographic Research Papers, 47, 583-601.

Denniston, R.F., Wyrwoll, K.H., Polyak, V.J., Brown, J.R., Asmerom, Y., Wanamaker Jr, A.D., LaPointe, Z., Ellerbroek, R., Barthelmes, M., Cleary, D. and Cugley, J., 2013. A Stalagmite record of Holocene Indonesian-Australian summer monsoon variability from the Australian tropics. Quaternary Science Reviews, 78, 155-168.

Dèzes, P.J., Vannay, J.C., Steck, A., Bussy, F. and Cosca, M., 1999. Synorogenic extension: Quantitative constraints on the age and displacement of the Zanskar shear zone (northwest Himalaya). Geological Society of America Bulletin, 111, 364-374.

Dixit, Y., Hodell, D.A. and Petrie, C.A., 2014a. Abrupt weakening of the summer monsoon in northwest India ~4100 yr ago. Geology, 42, 339-342.

Dixit, Y., Hodell, D.A., Sinha, R. and Petrie, C.A., 2014b. Abrupt weakening of the Indian summer monsoon at 8.2 kyr BP. Earth and Planetary Science Letters, 391, 16-23.

Dixon, J.L. and von Blanckenburg, F., 2012. Soils as pacemakers and limiters of global silicate weathering. Comptes Rendus Geoscience, 344, 597-609.

Dong, B.W. and Sutton, R.T., 2002. Adjustment of the coupled ocean-atmosphere system to a sudden change in the thermohaline circulation. Geophysical Research Letters, 29, 1728.

Dorale, J.A., González, L.A., Reagan, M.K., Pickett, D.A., Murrell, M.T. and Baker, R.G., 1992. A high-resolution record of Holocene climate change in speleothem calcite from Cold Water Cave, northeast Iowa. Science, 258, 1626-1630.

Dosseto, A., Bourdon, B., Gaillardet, J., Maurice-Bourgoin, L. and Allegre, C.J., 2006. Weathering and transport of sediments in the Bolivian Andes: Time constraints from uranium-series isotopes. Earth and Planetary Science Letters, 248, 759-771.

Dou, J., Wu, Z. and Zhou, Y., 2017. Potential impact of the May Southern Hemisphere annular mode on the Indian summer monsoon rainfall. Climate Dynamics, 49, 1257-1269.

Dupré, B., Dessert, C., Oliva, P., Goddéris, Y., Viers, J., François, L., Millot, R. and Gaillardet, J., 2003. Rivers, chemical weathering and Earth's climate. Comptes Rendus Geoscience, 335, 1141-1160.

Dutt, S., Gupta, A.K., Clemens, S.C., Cheng, H., Singh, R.K., Kathayat, G. and Edwards, R.L., 2015. Abrupt changes in Indian summer monsoon strength during 33,800 to 5500 years BP. Geophysical Research Letters, 42, 5526-5532.

Dykoski, C.A., Edwards, R.L., Cheng, H., Yuan, D., Cai, Y., Zhang, M., Lin, Y., Qing, J., An, Z. and Revenaugh, J., 2005. A high-resolution, absolute-dated Holocene and deglacial Asian monsoon record from Dongge Cave, China. Earth and Planetary Science Letters, 233, 71-86.

East, A.E., Clift, P.D., Carter, A., Alizai, A. and VanLaningham, S., 2015. Fluvial-eolian interactions in sediment routing and sedimentary signal buffering: an example from the Indus Basin and Thar Desert. Journal of Sedimentary Research, 85, 715-728.

Evans, M.J. and Derry, L.A., 2002. Quartz control of high germanium/silicon ratios in geothermal waters. Geology, 30, 1019-1022.

Evans, M.J., Derry, L.A. and France-Lanord, C., 2004. Geothermal fluxes of alkalinity in the Narayani river system of central Nepal. Geochemistry, Geophysics, Geosystems, 5, Q08011.

Evans, M.J., Derry, L.A., Anderson, S.P. and France-Lanord, C., 2001. Hydrothermal source of radiogenic Sr to Himalayan rivers. Geology, 29, 803-806.

Fleitmann, D., Burns, S.J., Mangini, A., Mudelsee, M., Kramers, J., Villa, I., Neff, U., Al-Subbary, A.A., Buettner, A., Hippler, D. and Matter, A., 2007. Holocene ITCZ and Indian monsoon dynamics recorded in stalagmites from Oman and Yemen (Socotra). Quaternary Science Reviews, 26, 170-188.

Fleitmann, D., Burns, S.J., Mudelsee, M., Neff, U., Kramers, J., Mangini, A. and Matter, A., 2003. Holocene forcing of the Indian monsoon recorded in a stalagmite from southern Oman. Science, 300, 1737-1739.

Fontorbe, G., Christina, L., Chapman, H.J. and Bickle, M.J., 2013. The silicon isotopic composition of the Ganges and its tributaries. Earth and Planetary Science Letters, 381, 21-30.

Foster, G.L. and Vance, D., 2006. Negligible glacial-interglacial variation in continental chemical weathering rates. Nature, 444, 918-921.

Fricke, H.C. and O'Neil, J.R., 1999. The correlation between $^{18}O/^{16}O$ ratios of meteoric water and surface temperature: its use in investigating terrestrial climate change over geologic time. Earth and Planetary Science Letters, 170, 181-196.

Fuchs, G., 1987. The geology of southern Zanskar (Ladakh); evidence for the autochthony of the Tethys zone of the Himalaya. Jahrbuch der Geologischen Bundesanstalt Wien, 130, 465-491.

Fuller, D.Q., 2006. Agricultural origins and frontiers in South Asia: a working synthesis. Journal of World Prehistory, 20, 1-86.

Gaetani, M., Casnedi, P., Fois, E., Garzanti, E., Jadoul, F., Nicora, A., and Tintori, A., 1986, Stratigraphy of the Tethys Himalaya in Zanskar, Ladakh: Rivista Italiana di Paleontologia e Stratigrafia, 91, 443-478.

Gaetani, M., Nicora, A., Silva, I.P., Fois, E., Garzanti, E. and Tintori, A., 1983. Upper Cretaceous and Paleocene in Zanskar Range (NW Himalaya). Rivista Italiana di Paleontologia e Stratigrafia, 89, 81-118.

Gaillardet, J., Dupré, B., Louvat, P. and Allegre, C.J., 1999. Global silicate weathering and CO_2 consumption rates deduced from the chemistry of large rivers. Chemical Geology, 159, 3-30.

Galy, A. and France-Lanord, C., 1999. Weathering processes in the Ganges-Brahmaputra basin and the riverine alkalinity budget. Chemical Geology, 159, 31-60.

Galy, A. and France-Lanord, C., 2001. Higher erosion rates in the Himalaya: Geochemical constraints on riverine fluxes. Geology, 29, 23-26.

Galy, V., François, L., France-Lanord, C., Faure, P., Kudrass, H., Palhol, F. and Singh, S.K., 2008. C4 plants decline in the Himalayan basin since the Last Glacial Maximum. Quaternary Science Reviews, 27, 1396-1409.

Garzanti, E., Andó, S., France-Lanord, C., Censi, P., Vignola, P., Galy, V. and Lupker, M., 2011. Mineralogical and chemical variability of fluvial sediments 2. Suspended-load silt (Ganga-Brahmaputra, Bangladesh). Earth and Planetary Science Letters, 302, 107-120.

Garzanti, E., Casnedi, R. and Jadoul, F., 1986. Sedimentary evidence of a Cambro-Ordovician orogenic event in the northwestern Himalaya. Sedimentary Geology, 48, 237-265.

Gascoyne, M., 1992. Palaeoclimate determination from cave calcite deposits. Quaternary Science Reviews, 11, 609-632.

Gautam, P.K., Narayana, A.C., Band, S.T., Yadava, M.G., Ramesh, R., Wu, C.C. and Shen, C.C., 2019. High-resolution reconstruction of Indian summer monsoon during the Bølling-Allerød from a central Indian stalagmite. Palaeogeography, Palaeoclimatology, Palaeoecology, 514, 567-576.

Gehrels, G.E., Yin, A. and Wang, X.F., 2003. Detrital-zircon geochronology of the northeastern Tibetan plateau. Geological Society of America Bulletin, 115, 881-896.

Genty, D., Labuhn, I., Hoffmann, G., Danis, P.A., Mestre, O., Bourges, F., Wainer, K., Massault, M., Van Exter, S., Régnier, E. and Orengo, P., 2014. Rainfall and cave water isotopic relationships in two South-France sites. Geochimica et Cosmochimica Acta, 131, 323-343.

Godsey, S.E., Kirchner, J.W. and Clow, D.W., 2009. Concentration–discharge relationships reflect chemostatic characteristics of US catchments. Hydrological Processes: An International Journal, 23, 1844-1864.

Goswami, B.N. and Xavier, P.K., 2005. ENSO control on the south Asian monsoon through the length of the rainy season. Geophysical Research Letters, 32, L18717.

Goswami, B.N., Kripalani, R.H., Borgaonkar, H.P. and Preethi, B., 2015. Multi-decadal variability in Indian summer monsoon rainfall using proxy data. In Climate Change: Multidecadal and Beyond, 327-345.

Goswami, B.N., Madhusoodanan, M.S., Neema, C.P. and Sengupta, D., 2006. A physical mechanism for North Atlantic SST influence on the Indian summer monsoon. Geophysical Research Letters, 33, L02706.

Goswami, D.C., 1985. Brahmaputra River, Assam, India: Physiography, basin denudation, and channel aggradation. Water Resources Research, 21, 959-978.

Goswami, V., Singh, S.K., Bhushan, R. and Rai, V.K., 2012. Temporal variations in ^{87}Sr/^{86}Sr and ε_{Nd} in sediments of the southeastern Arabian Sea: Impact of monsoon and surface water circulation. Geochemistry, Geophysics, Geosystems, 13, Q01001.

Granet, M., Chabaux, F., Stille, P., Dosseto, A., France-Lanord, C. and Blaes, E., 2010. U-series disequilibria in suspended river sediments and implication for sediment transfer time in alluvial plains: the case of the Himalayan rivers. Geochimica et Cosmochimica Acta, 74, 2851-2865.

Granet, M., Chabaux, F., Stille, P., France-Lanord, C. and Pelt, E., 2007. Time-scales of sedimentary transfer and weathering processes from U-series nuclides: clues from the Himalayan rivers. Earth and Planetary Science Letters, 261, 389-406.

Green, O.R., Searle, M.P., Corfield, R.I. and Corfield, R.M., 2008. Cretaceous-Tertiary carbonate platform evolution and the age of the India-Asia collision along the Ladakh Himalaya (northwest India). The Journal of Geology, 116, 331-353.

Gupta, A.K., Anderson, D.M. and Overpeck, J.T., 2003. Abrupt changes in the Asian southwest monsoon during the Holocene and their links to the North Atlantic Ocean. Nature, 421, 354-357.

Gupta, A.K., Anderson, D.M., Pandey, D.N. and Singhvi, A.K., 2006. Adaptation and human migration, and evidence of agriculture coincident with changes in the Indian summer monsoon during the Holocene. Current Science, 90, 1082-1090.

Gupta, A.K., Das, M. and Anderson, D.M., 2005. Solar influence on the Indian summer monsoon during the Holocene. Geophysical Research Letters, 32, L17703.

Handa, B.K., 1972. Technical report No. 7 on the hydrogeochemistry of the Brahmaputra River. Hydrological Review, 4, 99-105.

Haug, G.H., Hughen, K.A., Sigman, D.M., Peterson, L.C. and Rohl, U., 2001. Southward migration of the intertropical convergence zone through the Holocene. Science, 293, 1304-1308.

Hein, C.J., Galy, V., Galy, A., France-Lanord, C., Kudrass, H. and Schwenk, T., 2017. Post-glacial climate forcing of surface processes in the Ganges-Brahmaputra river basin and implications for carbon sequestration. Earth and Planetary Science Letters, 478, 89-101.

Hellstrom, J., 2006. U-Th dating of speleothems with high initial ^{230}Th using stratigraphical constraint. Quaternary Geochronology, 1, 289-295.

Helz, G.R., Miller, C.V., Charnock, J.M., Mosselmans, J.F.W., Pattrick, R.A.D., Garner, C.D. and Vaughan, D.J., 1996. Mechanism of molybdenum removal from the sea and its concentration in black shales: EXAFS evidence. Geochimica et Cosmochimica Acta, 60, 3631-3642.

Henderson, A.L., Najman, Y., Parrish, R., BouDagher-Fadel, M., Barford, D., Garzanti, E. and Andò, S., 2010. Geology of the Cenozoic Indus Basin sedimentary rocks:

Paleoenvironmental interpretation of sedimentation from the western Himalaya during the early phases of India-Eurasia collision. Tectonics, 29, TC6015.

Hendy, C.H., 1971. The isotopic geochemistry of speleothems-I. The calculation of the effects of different modes of formation on the isotopic composition of speleothems and their applicability as palaeoclimatic indicators. Geochimica et cosmochimica Acta, 35, 801-824.

Herren, E., 1987. Zanskar shear zone: Northeast-southwest extension within the Higher Himalayas (Ladakh, India). Geology, 15, 409-413.

Herzschuh, U., 2006. Palaeo-moisture evolution in monsoonal Central Asia during the last 50,000 years. Quaternary Science Reviews, 25, 163-178.

Hilley, G.E., Chamberlain, C.P., Moon, S., Porder, S. and Willett, S.D., 2010. Competition between erosion and reaction kinetics in controlling silicate-weathering rates. Earth and Planetary Science Letters 293, 191-199.

Honegger, K., Dietrich, V., Frank, W., Gansser, A., Thöni, M. and Trommsdorff, V., 1982. Magmatism and metamorphism in the Ladakh Himalayas (the Indus-Tsangpo suture zone). Earth and Planetary Science Letters, 60, 253-292.

Horton, F. and Leech, M.L., 2013. Age and origin of granites in the Karakoram shear zone and Greater Himalaya Sequence, NW India. Lithosphere, 5, 300-320.

Hren, M.T., Bookhagen, B., Blisniuk, P.M., Booth, A.L. and Chamberlain, C.P., 2009. $\delta^{18}O$ and δD of streamwaters across the Himalaya and Tibetan Plateau: Implications for moisture sources and paleoelevation reconstructions. Earth and Planetary Science Letters, 288, 20-32.

Hren, M.T., Chamberlain, C.P., Hilley, G.E., Blisniuk, P.M. and Bookhagen, B., 2007. Major ion chemistry of the Yarlung Tsangpo-Brahmaputra river: chemical weathering, erosion, and CO_2 consumption in the southern Tibetan plateau and eastern syntaxis of the Himalaya. Geochimica et Cosmochimica Acta, 71, 2907-2935.

Hu M., Stallard, R. F., and Edmond, J.M., 1982. Major ion chemistry of some large Chinese rivers. Nature, 298, 550-553.

Huang, C., Zeng, T., Ye, F., Xie, L., Wang, Z., Wei, G., Lo, L., Deng, W. and Rao, Z., 2018. Natural and anthropogenic impacts on environmental changes over the past 7500 years based on the multi-proxy study of shelf sediments in the northern South China Sea. Quaternary Science Reviews, 197, 35-48.

Ibarra, D.E., Caves, J.K., Moon, S., Thomas, D.L., Hartmann, J., Chamberlain, C.P. and Maher, K., 2016. Differential weathering of basaltic and granitic catchments from concentration-discharge relationships. Geochimica et Cosmochimica Acta, 190, 265-293.

Immerzeel, W.W., Van Beek, L.P. and Bierkens, M.F., 2010. Climate change will affect the Asian water towers. Science, 328, 1382-1385.

Islam, M.R., Begum, S.F., Yamaguchi, Y. and Ogawa, K., 1999. The Ganges and Brahmaputra rivers in Bangladesh: basin denudation and sedimentation. Hydrological Processes, 13, 2907-2923.

Jacobsen, S.B. and Wasserburg, G.J., 1980. Sm-Nd isotopic systematics of chondrites and achondrites. Meteoritics, 15, 307.

Jacobson, A.D., Blum, J.D. and Walter, L.M., 2002. Reconciling the elemental and Sr isotope composition of Himalayan weathering fluxes: insights from the carbonate geochemistry of stream waters. Geochimica et Cosmochimica Acta, 66, 3417-3429.

Jain, S.K., Agarwal, P.K. and Singh, V.P., 2007. Hydrology and Water Resources of India. Springer, Netherlands, 1260.

Jenckes, J., Ibarra, D.E. and Munk, L.A., 2022. Concentration-Discharge Patterns Across the Gulf of Alaska Reveal Geomorphological and Glacierization Controls on Stream Water Solute Generation and Export. Geophysical Research Letters, 49, e2021GL095152.

Jha, P.K., Tiwari, J., Singh, U.K., Kumar, M. and Subramanian, V., 2009. Chemical weathering and associated CO_2 consumption in the Godavari river basin, India. Chemical Geology, 264, 364-374.

Jiang, H., Muscheler, R., Björck, S., Seidenkrantz, M.S., Olsen, J., Sha, L., Sjolte, J., Eiríksson, J., Ran, L., Knudsen, K.L. and Knudsen, M.F., 2015. Solar forcing of Holocene summer sea-surface temperatures in the northern North Atlantic. Geology, 43, 203-206.

Jonell, T.N., Carter, A., Böning, P., Pahnke, K. and Clift, P.D., 2017. Climatic and glacial impact on erosion patterns and sediment provenance in the Himalayan rain shadow, Zanskar River, NW India. Bulletin, 129, 820-836.

Kahkashan, S., Chen, J., Wang, X., Clift, P.D., Jalali, B., Inam, A., Saleem, M., Aftab, J., Ji, Z., Bai, Y. and Li, Z., 2020. Holocene organic geochemical record from the Western Indus continental shelf (northern Arabian Sea). The Holocene, 30, 810-819.

Kaser, G., Großhauser, M. and Marzeion, B., 2010. Contribution potential of glaciers to water availability in different climate regimes. Proceedings of the National Academy of Sciences, 107, 20223-20227.

Kathayat, G., Cheng, H., Sinha, A., Yi, L., Li, X., Zhang, H., Li, H., Ning, Y. and Edwards, R.L., 2017. The Indian monsoon variability and civilization changes in the Indian subcontinent. Science Advances, 3, e1701296.

Kaushal, N., Breitenbach, S.F., Lechleitner, F.A., Sinha, A., Tewari, V.C., Ahmad, S.M., Berkelhammer, M., Band, S., Yadava, M., Ramesh, R. and Henderson, G.M., 2018. The Indian summer monsoon from a speleothem $\delta^{18}O$ perspective-A review. Quaternary, 1, 29.

Kessarkar, P.M., Naqvi, S.W.A., Thamban, M., Fernandes, L.L., Siebert, C., Rao, V.P., Kawahata, H., Ittekkot, V. and Frank, M., 2018. Variations in denitrification and ventilation within the Arabian Sea oxygen minimum zone during the Holocene. Geochemistry, Geophysics, Geosystems 19, 2179-2193.

Kessarkar, P.M., Rao, V.P., Ahmad, S.M. and Babu, G.A., 2003. Clay minerals and Sr-Nd isotopes of the sediments along the western margin of India and their implication for sediment provenance. Marine Geology, 202, 55-69.

Kleiven, H.K.F., Kissel, C., Laj, C., Ninnemann, U.S., Richter, T.O. and Cortijo, E., 2008. Reduced North Atlantic deep water coeval with the glacial Lake Agassiz freshwater outburst. Science, 319, 60-64.

Knight, J. and Harrison, S., 2013. The impacts of climate change on terrestrial Earth surface systems. Nature Climate Change, 3, 24-29.

Krishnan, R. and Sugi, M., 2003. Pacific decadal oscillation and variability of the Indian summer monsoon rainfall. Climate Dynamics, 21, 233-242.

Krishnaswami, S. and Singh, S.K., 1998. Silicate and carbonate weathering in the drainage basins of the Ganga-Ghaghara-Indus head waters: Contributions to major ion and Sr isotope geochemistry. Proceedings of the Indian Academy of Sciences-Earth and Planetary Sciences, 107, 283-291.

Krishnaswami, S., Singh, S. K. and Dalai, T., 1999. Silicate weathering in the Himalaya: Role in contributing to major ions and radiogenic Sr to the Bay of Bengal. In Ocean Science, Trends and Future Directions. (Ed.), Somalyajulu, B. L. K., Indian National Science Academy and Akad. Int., New Delhi, 23-51.

Krishnaswami, S., Trivedi, J.R., Sarin, M.M., Ramesh, R. and Sharma, K.K., 1992. Strontium isotopes and rubidium in the Ganga-Brahmaputra river system: Weathering in the Himalaya, fluxes to the Bay of Bengal and contributions to the evolution of oceanic ^{87}Sr/^{86}Sr. Earth and Planetary Science Letters, 109, 243-253.

Kuhnert, H., Kuhlmann, H., Mohtadi, M., Meggers, H., Baumann, K.H. and Pätzold, J., 2014. Holocene tropical western Indian Ocean sea surface temperatures in covariation with climatic changes in the Indonesian region. Paleoceanography, 29, 423-437.

Kumar, A., Suresh, K. and Rahaman, W., 2020. Geochemical characterization of modern aeolian dust over the Northeastern Arabian Sea: Implication for dust transport in the Arabian Sea. Science of the Total Environment, 729, 138576.

Kumar, G., 1997. Geology of the Arunachal Pradesh. Geological Society of India.

Kurian, S., Nath, B.N., Kumar, N.C. and Nair, K.K.C., 2013. Geochemical and isotopic signatures of surficial sediments from the western continental shelf of India: inferring provenance, weathering, and the nature of organic matter. Journal of Sedimentary Research, 83, 427-442.

Larsen, I.J. and Montgomery, D.R., 2012. Landslide erosion coupled to tectonics and river incision. Nature Geoscience, 5, 468-473.

Larsen, I.J., Almond, P.C., Eger, A., Stone, J.O., Montgomery, D.R. and Malcolm, B., 2014. Rapid soil production and weathering in the Southern Alps, New Zealand. Science, 343, 637-640.

Larsen, I.J., Montgomery, D.R. and Korup, O., 2010. Landslide erosion controlled by hillslope material. Nature Geoscience, 3, 247-251.

Lasaga, A.C., 1984. Chemical kinetics of water-rock interactions. Journal of Geophysical Research: Solid Earth, 89, 4009-4025.

Lasaga, A.C., Soler, J.M., Ganor, J., Burch, T.E. and Nagy, K.L., 1994. Chemical weathering rate laws and global geochemical cycles. Geochimica et Cosmochimica Acta, 58, 2361-2386.

Laskar, J., Robutel, P., Joutel, F., Gastineau, M., Correia, A.C.M. and Levrard, B., 2004. A long-term numerical solution for the insolation quantities of the Earth. Astronomy & Astrophysics, 428, 261-285.

Lauritzen, S.E. and Lundberg, J., 1999. Calibration of the speleothem delta function: an absolute temperature record for the Holocene in northern Norway. The Holocene, 9, 659-669.

Lechleitner, F.A., Breitenbach, S.F., Cheng, H., Plessen, B., Rehfeld, K., Goswami, B., Marwan, N., Eroglu, D., Adkins, J. and Haug, G., 2017. Climatic and in-cave influences on δ^{18}O and δ^{13}C in a stalagmite from northeastern India through the last deglaciation. Quaternary Research, 88, 458-471.

Lee, S.Y., Seong, Y.B., Owen, L.A., Murari, M.K., Lim, H.S., Yoon, H.I. and Yoo, K.C., 2014. Late Quaternary glaciation in the Nun-Kun massif, northwestern India. Boreas, 43, 67-89.

LeGrande, A.N. and Schmidt, G.A., 2009. Sources of Holocene variability of oxygen isotopes in paleoclimate archives. Climate of the Past, 5, 441-455.

Leloup, P.H., Mahéo, G., Arnaud, N., Kali, E., Boutonnet, E., Liu, D., Xiaohan, L. and Haibing, L., 2010. The South Tibet detachment shear zone in the Dinggye area: Time constraints on extrusion models of the Himalayas. Earth and Planetary Science Letters, 292, 1-16.

Li, X., Gollan, G., Greatbatch, R.J. and Lu, R., 2018. Intraseasonal variation of the East Asian summer monsoon associated with the Madden-Julian oscillation. Atmospheric Science Letters, 19, e794.

Limmer, D.R., Böning, P., Giosan, L., Ponton, C., Köhler, C.M., Cooper, M.J., Tabrez, A.R. and Clift, P.D., 2012. Geochemical record of Holocene to Recent sedimentation on the Western Indus continental shelf, Arabian Sea. Geochemistry, Geophysics, Geosystems, 13, Q01008.

Liu, Y.H., Henderson, G.M., Hu, C.Y., Mason, A.J., Charnley, N., Johnson, K.R. and Xie, S.C., 2013. Links between the East Asian monsoon and North Atlantic climate during the 8,200 year event. Nature Geoscience, 6, 117-120.

Lone, M.A., Ahmad, S.M., Dung, N.C., Shen, C.C., Raza, W. and Kumar, A., 2014. Speleothem based 1000-year high resolution record of Indian monsoon variability during the last deglaciation. Palaeogeography, Palaeoclimatology, Palaeoecology, 395, 1-8.

Lückge, A., Doose-Rolinski, H., Khan, A.A., Schulz, H. and Von Rad, U., 2001. Monsoonal variability in the northeastern Arabian Sea during the past 5000 years: geochemical evidence from laminated sediments. Palaeogeography, Palaeoclimatology, Palaeoecology, 167, 273-286.

Lupker, M., Blard, P.H., Lavé, J., France-Lanord, C., Leanni, L., Puchol, N., Charreau, J. and Bourlès, D., 2012. ^{10}Be-derived Himalayan denudation rates and sediment budgets in the Ganga basin. Earth and Planetary Science Letters, 333, 146-156.

Lupker, M., France-Lanord, C., Galy, V., Lavé, J. and Kudrass, H., 2013. Increasing chemical weathering in the Himalayan system since the Last Glacial Maximum. Earth and Planetary Science Letters, 365, 243-252.

Maher, K., 2011. The role of fluid residence time and topographic scales in determining chemical fluxes from landscapes. Earth and Planetary Science Letters, 312, 48-58.

Mahoney, J.J., Sheth, H.C., Chandrasekharam, D. and Peng, Z.X., 2000. Geochemistry of flood basalts of the Toranmal section, northern Deccan Traps, India: implications for regional Deccan stratigraphy. Journal of Petrology, 41, 1099-1120.

Mandal, S.K., Lupker, M., Burg, J.P., Valla, P.G., Haghipour, N. and Christl, M., 2015. Spatial variability of ^{10}Be-derived erosion rates across the southern Peninsular Indian escarpment: A key to landscape evolution across passive margins. Earth and Planetary Science Letters, 425, 154-167.

Manning, K. and Timpson, A., 2014. The demographic response to Holocene climate change in the Sahara. Quaternary Science Reviews, 101, 28-35.

Marshall, M.H., Lamb, H.F., Huws, D., Davies, S.J., Bates, R., Bloemendal, J., Boyle, J., Leng, M.J., Umer, M. and Bryant, C., 2011. Late Pleistocene and Holocene drought events at Lake Tana, the source of the Blue Nile. Global and Planetary Change, 78, 147-161.

Mayewski, P.A., Rohling, E.E., Stager, J.C., Karlén, W., Maasch, K.A., Meeker, L.D., Meyerson, E.A., Gasse, F., van Kreveld, S., Holmgren, K. and Lee-Thorp, J., 2004. Holocene climate variability. Quaternary Research, 62, 243-255.

Métivier, F. and Gaudemer, Y., 1999. Stability of output fluxes of large rivers in South and East Asia during the last 2 million years: implications on floodplain processes. Basin Research, 11, 293-303.

Meybeck, M., 2003. Global Occurrence of Major Elements in Rivers. (Ed.), Drever, J. I., Treatise on Geochemistry, Vol. 5, Elsevier Science, 207-223.

Meyers, P.A., 1994. Preservation of elemental and isotopic source identification of sedimentary organic matter. Chemical Geology, 114, 289-302.

Milliman, J.D. and Farnsworth, K.L., 2013. River Discharge to the Coastal Ocean: A Global Synthesis. Cambridge University Press.

Milliman, J.D. and Meade, R.H., 1983. World-wide delivery of river sediment to the oceans. The Journal of Geology, 91, 1-21.

Milliman, J.D., Quraishee, G.S. and Beg, M.A.A., 1984. Sediment discharge from the Indus River to the ocean: past, present and future. Marine Geology and Oceanography of Arabian Sea and Coastal Pakistan, 65-70.

Millot, R., Gaillardet, J., Dupré, B. and Allègre, C.J., 2002. The global control of silicate weathering rates and the coupling with physical erosion: new insights from rivers of the Canadian Shield. Earth and Planetary Science Letters, 196, 83-98.

Millot, R., Gaillardet, J., Dupré, B. and Allègre, C.J., 2003. Northern latitude chemical weathering rates: clues from the Mackenzie River Basin, Canada. Geochimica et Cosmochimica Acta, 67, 1305-1329.

Miriyala, P., Sukumaran, N.P., Nath, B.N., Ramamurty, P.B., Sijinkumar, A.V., Vijayagopal, B., Ramaswamy, V. and Sebastian, T., 2017. Increased chemical weathering during the deglacial to mid-Holocene summer monsoon intensification. Scientific Reports, 7, 1-11.

Misra, P., Tandon, S.K. and Sinha, R., 2019. Holocene climate records from lake sediments in India: Assessment of coherence across climate zones. Earth-Science Reviews, 190, 370-397.

Moon, S., Chamberlain, C.P. and Hilley, G.E., 2014. New estimates of silicate weathering rates and their uncertainties in global rivers. Geochimica et Cosmochimica Acta, 134, 257-274.

Moon, S., Huh, Y., Qin, J. and van Pho, N., 2007. Chemical weathering in the Hong (Red) River basin: rates of silicate weathering and their controlling factors. Geochimica et Cosmochimica Acta, 71, 1411-1430.

Morse, J.W. and Mackenzie, F.T., 1990. Geochemistry of sedimentary carbonates. Elsevier.

Moy, C.M., Seltzer, G.O., Rodbell, D.T. and Anderson, D.M., 2002. Variability of El Niño/Southern Oscillation activity at millennial timescales during the Holocene epoch. Nature, 420, 162-165.

Myers, C.G., Oster, J.L., Sharp, W.D., Bennartz, R., Kelley, N.P., Covey, A.K. and Breitenbach, S.F., 2015. Northeast Indian stalagmite records Pacific decadal climate change: Implications for moisture transport and drought in India. Geophysical Research Letters, 42, 4124-4132.

Naidu, P.D. and Malmgren, B.A., 1995. A 2,200 years periodicity in the Asian monsoon system. Geophysical Research Letters, 22, 2361-2364.

Nath, B.N., Kunzendorf, H. and Pluger, W.L., 2000. Influence of provenance, weathering, and sedimentary processes on the elemental ratios of the fine-grained fraction of the bedload sediments from the Vembanad Lake and the adjoining continental shelf, southwest coast of India. Journal of Sedimentary Research, 70, 1081-1094.

Négrel, P., Allègre, C.J., Dupré, B. and Lewin, E., 1993. Erosion sources determined by inversion of major and trace element ratios and strontium isotopic ratios in river water: the Congo Basin case. Earth and Planetary Science Letters, 120, 59-76.

Nesbitt, H. and Young, G.M., 1982. Early Proterozoic climates and plate motions inferred from major element chemistry of lutites. Nature, 299, 715-717.

Noble, S.R. and Searle, M.P., 1995. Age of crustal melting and leucogranite formation from U-Pb zircon and monazite dating in the western Himalaya, Zanskar, India. Geology, 23, 1135-1138.

Noh, H., Huh, Y., Qin, J. and Ellis, A., 2009. Chemical weathering in the Three Rivers region of Eastern Tibet. Geochimica et Cosmochimica Acta, 73, 1857-1877.

Owen, L.A. and Benn, D.I., 2005. Equilibrium-line altitudes of the Last Glacial Maximum for the Himalaya and Tibet: an assessment and evaluation of results. Quaternary International, 138, 55-78.

Panchang, R. and Sen, A., 2021. Revisiting late Quaternary sea levels along the Indian sub-continent with a novel approach in the face of climate change. In N., Khare (Ed.), Quaternary climate change over the Indian subcontinent. CRC Press.

Pandey, A., 2016. Society and environment in ancient India (Study of Hydrology): International Journal of Humanities and Social Science Invention, 5, 26-31.

Pedersen, R.B., Searle, M.T. and Corfield, R.I., 2001. U-Pb zircon ages from the Spontang ophiolite, Ladakh Himalaya. Journal of the Geological Society, 158, 513-520.

Peketi, A., Mazumdar, A., Pillutla, S.P.K., Rai, V.K., Sawant, B. and Chaitanya, A.V.S., 2020. Monsoon rainfall and contrasting source rocks influenced sediment composition of peninsular basins along the east coast of India (western Bay of Bengal). Marine and Petroleum Geology, 118, 104433.

Petraglia, M.D., Groucutt, H.S., Guagnin, M., Breeze, P.S. and Boivin, N., 2020. Human responses to climate and ecosystem change in ancient Arabia. Proceedings of the National Academy of Sciences, 117, 8263-8270.

Peucker-Ehrenbrink, B., Miller, M.W., Arsouze, T. and Jeandel, C., 2010. Continental bedrock and riverine fluxes of strontium and neodymium isotopes to the oceans. Geochemistry, Geophysics, Geosystems, 11, Q03016.

Pognante, U., Castelli, D., Benna, P., Genovese, G., Oberli, F., Meier, M. and Tonarini, S., 1990. The crystalline units of the High Himalayas in the Lahul-Zanskar region (northwest India): Metamorphic–tectonic history and geochronology of the collided and imbricated Indian plate. Geological Magazine, 127, 101-116.

Pognante, U.T. and Lombardo, B., 1989. Metamorphic evolution of the High Himalayan crystallines in SE Zanskar, India. Journal of Metamorphic Geology, 7, 9-17.

Ponton, C., Giosan, L., Eglinton, T.I., Fuller, D.Q., Johnson, J.E., Kumar, P. and Collett, T.S., 2012. Holocene aridification of India. Geophysical Research Letters, 39, L03704.

Prasad, S., Anoop, A., Riedel, N., Sarkar, S., Menzel, P., Basavaiah, N., Krishnan, R., Fuller, D., Plessen, B., Gaye, B. and Röhl, U., 2014. Prolonged monsoon droughts and links to Indo-Pacific warm pool: A Holocene record from Lonar Lake, central India. Earth and Planetary Science Letters, 391, 171-182.

Qasim, S.Z., 1977. Biological productivity of the Indian Ocean 6. Indian Journal of Marine Sciences, 122-137.

Qasim, S.Z., 1982. Oceanography of the northern Arabian Sea. Deep Sea Research Part A. Oceanographic Research Papers, 29, 1041-1068.

Rahaman, W., Singh, S.K., Sinha, R. and Tandon, S.K., 2009. Climate control on erosion distribution over the Himalaya during the past ~100 ka. Geology, 37, 559-562.

Rai, S.K. and Singh, S.K., 2007. Temporal variation in Sr and $^{87}Sr/^{86}Sr$ of the Brahmaputra: Implications for annual fluxes and tracking flash floods through chemical and isotope composition. Geochemistry, Geophysics, Geosystems, 8, Q08008.

Rai, S.K., Singh, S.K. and Krishnaswami, S., 2010. Chemical weathering in the plain and peninsular sub-basins of the Ganga: impact on major ion chemistry and elemental fluxes. Geochimica et Cosmochimica Acta, 74, 2340-2355.

Rajeevan, M., Gadgil, S. and Bhate, J., 2010. Active and break spells of the Indian summer monsoon. Journal of Earth System Science, 119, 229-247.

Ramaswamy, V. and Nair, R.R., 1994. Fluxes of material in the Arabian Sea and Bay of Bengal-Sediment trap studies. Proceedings of the Indian Academy of Sciences-Earth and Planetary Sciences, 103, 189-210.

Rawat, V., Rawat, S., Srivastava, P., Negi, P.S., Prakasam, M. and Kotlia, B.S., 2021. Middle Holocene Indian summer monsoon variability and its impact on cultural changes in the Indian subcontinent. Quaternary Science Reviews, 255, 106825.

Raymo, M.E. and Ruddiman, W.F., 1992. Tectonic forcing of late Cenozoic climate. Nature, 359, 117-122.

Raza, W., Ahmad, S.M., Lone, M.A., Shen, C.C., Sarma, D.S. and Kumar, A., 2017. Indian summer monsoon variability in southern India during the last deglaciation: Evidence from a high resolution stalagmite $\delta^{18}O$ record. Palaeogeography, Palaeoclimatology, Palaeoecology, 485, 476-485.

Reddy, P., Gandhi, N. and Krishnan, R., 2021. Review of speleothem records of the late Holocene: Indian summer monsoon variability & interplay between the solar and oceanic forcing. Quaternary International. https://doi.org/10.1016/j.quaint.2021.06.018.

Redfield, A.C., 1958. The biological control of chemical factors in the environment. American Scientist, 46, 230A-221.

Reimer, P.J., Bard, E., Bayliss, A., Beck, J.W., Blackwell, P.G., Ramsey, C.B., Buck, C.E., Cheng, H., Edwards, R.L., Friedrich, M. and Grootes, P.M., 2013. IntCal13 and

Marine13 radiocarbon age calibration curves 0-50,000 years cal BP. Radiocarbon, 55, 1869-1887.

Rengarajan, R., Singh, S.K., Sarin, M.M. and Krishnaswami, S., 2009. Strontium isotopes and major ion chemistry in the Chambal River system, India: implications to silicate erosion rates of the Ganga. Chemical Geology, 260, 87-101.

Richards, A., Argles, T., Harris, N., Parrish, R., Ahmad, T., Darbyshire, F. and Draganits, E., 2005. Himalayan architecture constrained by isotopic tracers from clastic sediments. Earth and Planetary Science Letters, 236, 773-796.

Riebe, C.S., Kirchner, J.W. and Finkel, R.C., 2004. Erosional and climatic effects on long-term chemical weathering rates in granitic landscapes spanning diverse climate regimes. Earth and Planetary Science Letters, 224, 547-562.

Robyr, M., Hacker, B.R. and Mattinson, J.M., 2006. Doming in compressional orogenic settings: New geochronological constraints from the NW Himalaya. Tectonics, 25, TC2007.

Roy, P.D. and Smykatz-Kloss, W., 2007. REE geochemistry of the recent playa sediments from the Thar Desert, India: an implication to playa sediment provenance. Geochemistry, 67, 55-68.

Roy, P.D., Smykatz-Kloss, W. and Sinha, R., 2006. Late Holocene geochemical history inferred from Sambhar and Didwana playa sediments, Thar Desert, India: comparison and synthesis. Quaternary International, 144, 84-98.

Rudnick, R.L. and Gao, S., 2003. Composition of the continental crust. In R. L. Rudnick (Ed.). The Crust. Elsevier Science: Amsterdam, 1-70.

Saraswat, R., Naik, D.K., Nigam, R. and Gaur, A.S., 2016. Timing, cause and consequences of mid-Holocene climate transition in the Arabian Sea. Quaternary Research, 86, 162-169.

Sarin, M.M., Krishnaswami, S., Dilli, K., Somayajulu, B.L.K. and Moore, W.S., 1989. Major ion chemistry of the Ganga-Brahmaputra river system: weathering processes and fluxes to the Bay of Bengal. Geochimica et Cosmochimica Acta, 53, 997-1009.

Sarkar, A., Mukherjee, A.D., Bera, M.K., Das, B., Juyal, N., Morthekai, P., Deshpande, R.D., Shinde, V.S. and Rao, L.S., 2016. Oxygen isotope in archaeological bioapatites from India: Implications to climate change and decline of Bronze Age Harappan civilization. Scientific Reports, 6, 1-9.

Sarkar, A., Ramesh, R., Bhattacharya, S.K. and Rajagopalan, G., 1990. Oxygen isotope evidence for a stronger winter monsoon current during the last glaciation. Nature, 343, 549-551.

Sarma, J. N., 2005. Fluvial process and morphology of the Brahmaputra River in Assam, India. Geomorphology, 70, 226-256.

Schlup, M., Carter, A., Cosca, M. and Steck, A., 2003. Exhumation history of eastern Ladakh revealed by ^{40}Ar/^{39}Ar and fission-track ages: the Indus River-Tso Morari transect, NW Himalaya. Journal of the Geological Society, 160, 385-399.

Schlup, M., Steck, A., Carter, A., Cosca, M., Epard, J.L. and Hunziker, J., 2011. Exhumation history of the NW Indian Himalaya revealed by fission track and ^{40}Ar/^{39}Ar ages. Journal of Asian Earth Sciences, 40, 334-350.

Searle, M.P., 1986. Structural evolution and sequence of thrusting in the High Himalayan, Tibetan-Tethys and Indus suture zones of Zanskar and Ladakh, Western Himalaya. Journal of Structural Geology, 8, 923-936.

Searle, M.P., Pickering, K.T. and Cooper, D.J.W., 1990. Restoration and evolution of the intermontane Indus molasse basin, Ladakh Himalaya, India. Tectonophysics, 174, 301-314.

Searle, M.P., Waters, D.J., Rex, D.C. and Wilson, R.N., 1992. Pressure, temperature and time constraints on Himalayan metamorphism from eastern Kashmir and western Zanskar. Journal of the Geological Society, 149, 753-773.

Sebastian, T., Nath, B.N., Venkateshwarlu, M., Miriyala, P., Prakash, A., Linsy, P., Kocherla, M., Kazip, A. and Sijinkumar, A.V., 2019. Impact of the Indian Summer Monsoon variability on the source area weathering in the Indo-Burman ranges during the last 21 kyr-A sediment record from the Andaman Sea. Palaeogeography, Palaeoclimatology, Palaeoecology, 516, 22-34.

Sen Gupta, R. and Naqvi, S.W.A., 1984. Chemical oceanography of the Indian Ocean, north of the equator. Deep Sea Research Part A. Oceanographic Research Papers, 31, 671-706.

Sengupta, T., Deshpande Mukherjee, A., Bhushan, R., Ram, F., Bera, M.K., Raj, H., Dabhi, A.J., Bisht, R.S., Rawat, Y.S., Bhattacharya, S.K. and Juyal, N., 2020. Did the Harappan settlement of Dholavira (India) collapse during the onset of Meghalayan stage drought? Journal of Quaternary Science, 35, 382-395.

Sharma, A., Sensarma, S., Kumar, K., Khanna, P.P. and Saini, N.K., 2013. Mineralogy and geochemistry of the Mahi River sediments in tectonically active western India: Implications for Deccan large igneous province source, weathering and mobility of elements in a semi-arid climate. Geochimica et Cosmochimica Acta, 104, 63-83.

Sharma, C.P., Rawat, S.L., Srivastava, P., Meena, N.K., Agnihotri, R., Kumar, A., Chahal, P., Gahlaud, S.K.S. and Shukla, U.K., 2020. High-resolution climatic (monsoonal) variability reconstructed from a continuous ~2700-year sediment record from Northwest Himalaya (Ladakh). The Holocene, 30, 441-457.

Sharma, S.K. and Subramanian, V., 2010. Source and distribution of trace metals and nutrients in Narmada and Tapti river basins, India. Environmental Earth Sciences, 61, 1337-1352.

Sinclair, H.D. and Jaffey, N., 2001. Sedimentology of the Indus Group, Ladakh, northern India: implications for the timing of initiation of the palaeo-Indus River. Journal of the Geological Society, 158, 151-162.

Singh, S. K., 2007. Erosion and weathering in the Brahmaputra River system. (Ed.), Gupta, A., Large Rivers: Geomorphology and Management. Wiley, Chichester, 373-393.

Singh, S.K. and France-Lanord, C., 2002. Tracing the distribution of erosion in the Brahmaputra watershed from isotopic compositions of stream sediments. Earth and Planetary Science Letters, 202, 645-662.

Singh, S.K., Kumar, A. and France-Lanord, C., 2006. Sr and $^{87}Sr/^{86}Sr$ in waters and sediments of the Brahmaputra river system: Silicate weathering, CO_2 consumption and Sr flux. Chemical Geology, 234, 308-320.

Singh, S.K., Rai, S.K. and Krishnaswami, S., 2008. Sr and Nd isotopes in river sediments from the Ganga Basin: sediment provenance and spatial variability in physical erosion. Journal of Geophysical Research: Earth Surface, 113, F03006.

Singh, S.K., Sarin, M.M. and France-Lanord, C., 2005. Chemical erosion in the eastern Himalaya: major ion composition of the Brahmaputra and $\delta^{13}C$ of dissolved inorganic carbon. Geochimica et Cosmochimica Acta, 69, 3573-3588.

Singh, S.K., Trivedi, J.R., Pande, K., Ramesh, R. and Krishnaswami, S., 1998. Chemical and strontium, oxygen, and carbon isotopic compositions of carbonates from the Lesser Himalaya: Implications to the strontium isotope composition of the source waters of the Ganga, Ghaghara, and the Indus rivers. Geochimica et Cosmochimica Acta, 62, 743-755.

Sinha, A., Cannariato, K.G., Stott, L.D., Cheng, H., Edwards, R.L., Yadava, M.G., Ramesh, R. and Singh, I.B., 2007. A 900-year (600 to 1500 AD) record of the Indian summer monsoon precipitation from the core monsoon zone of India. Geophysical Research Letters, 34, L16707.

Sinha, A., Cannariato, K.G., Stott, L.D., Li, H.C., You, C.F., Cheng, H., Edwards, R.L. and Singh, I.B., 2005. Variability of Southwest Indian summer monsoon precipitation during the Bølling-Allerød. Geology, 33, 813-816.

Sinha, A., Stott, L., Berkelhammer, M., Cheng, H., Edwards, R.L., Buckley, B., Aldenderfer, M. and Mudelsee, M., 2011. A global context for megadroughts in monsoon Asia during the past millennium. Quaternary Science Reviews, 30, 47-62.

Sinha, N., Gandhi, N., Chakraborty, S., Krishnan, R., Yadava, M.G. and Ramesh, R., 2018. Abrupt climate change at ~2800 yr BP evidenced by a stalagmite record from peninsular India. The Holocene, 28, 1720-1730.

Sinha, R., Smykatz-Kloss, W., Stüben, D., Harrison, S.P., Berner, Z. and Kramar, U., 2006. Late Quaternary palaeoclimatic reconstruction from the lacustrine sediments of the Sambhar playa core, Thar Desert margin, India. Palaeogeography, Palaeoclimatology, Palaeoecology, 233, 252-270.

Sone, T., Kano, A., Okumura, T., Kashiwagi, K., Hori, M., Jiang, X. and Shen, C.C., 2013. Holocene stalagmite oxygen isotopic record from the Japan Sea side of the Japanese Islands, as a new proxy of the East Asian winter monsoon. Quaternary Science Reviews, 75, 150-160.

Southon, J., Kashgarian, M., Fontugne, M., Metivier, B. and Yim, W.W., 2002. Marine reservoir corrections for the Indian Ocean and Southeast Asia. Radiocarbon, 44, 167-180.

Staubwasser, M., Sirocko, F., Grootes, P.M. and Segl, M., 2003. Climate change at the 4.2 ka BP termination of the Indus valley civilization and Holocene south Asian monsoon variability. Geophysical Research Letters, 30, 1425.

Steck, A., Spring, L., Vannay, J.C., Masson, H., Stutz, E., Bucher, H., Marchant, R. and Tieche, J.C., 1993. Geological Transsect Across the Northwestern Himalaya in Eastern Ladakh and Lahul-A Model for the Continental Collision of India and Asia. Eclogae Geologicae Helvetiae, 86, 219-263.

Struve, T., Wilson, D.J., van de Flierdt, T., Pratt, N. and Crocket, K.C., 2020. Middle Holocene expansion of pacific deep water into the Southern Ocean. Proceedings of the National Academy of Sciences, 117, 889-894.

Stuiver, M. and Braziunas, T.F., 1993. Sun, ocean, climate and atmospheric $^{14}CO_2$: an evaluation of causal and spectral relationships. The Holocene, 3, 289-305.

Stuiver, M. and Grootes, P. M., 2000. GISP2 oxygen isotope rations. Quaternary Research, 53, 277-284.

Stuiver, M., Reimer, P. J., Bard, E., Beck, J. W., Burr, G. S., Hughen, K. A., Kromer, B., McCormac, F. G., Plicht, J. V. D., and Spurk, M., 1998. INTCAL98 Radiocarbon Age Calibration, 24,000-0 cal BP. Radiocarbon, 40, 1041-1083.

Stuiver, M., Reimer, P.J., and Reimer, R.W., 2021, CALIB 8.2 [WWW program] at http://calib.org.

Swapna, P., Krishnan, R. and Wallace, J.M., 2014. Indian Ocean and monsoon coupled interactions in a warming environment. Climate Dynamics, 42, 2439-2454.

Syvitski, J.P., Cohen, S., Kettner, A.J. and Brakenridge, G.R., 2014. How important and different are tropical rivers?-An overview. Geomorphology, 227, 5-17.

Szramek, K. and Walter, L.M., 2004. Impact of carbonate precipitation on riverine inorganic carbon mass transport from a mid-continent, forested watershed. Aquatic Geochemistry, 10, 99-137.

Tarantola, A., 2005. The least square criterion, in Inverse Problem Theory and Methods for Model Parameter Estimation. Society for Industrial and Applied Mathematics, Philadelphia, PA 68-72.

Taylor, P.J. and Mitchell, W.A., 2000. The Quaternary glacial history of the Zanskar Range, north-west Indian Himalaya. Quaternary International, 65, 81-99.

Thakur, V.C., 1981. Regional framework and geodynamic evolution of the Indus-Tsangpo suture zone in the Ladakh Himalayas. Earth and Environmental Science Transactions of the Royal Society of Edinburgh, 72, 89-97.

Thamban, M., Kawahata, H. and Rao, V.P., 2007. Indian summer monsoon variability during the Holocene as recorded in sediments of the Arabian Sea: timing and implications. Journal of oceanography, 63, 1009-1020.

Thompson, L.O., Yao, T., Davis, M.E., Henderson, K.A., Mosley-Thompson, E., Lin, P.N., Beer, J., Synal, H.A., Cole-Dai, J. and Bolzan, J.F., 1997. Tropical climate instability: The last glacial cycle from a Qinghai-Tibetan ice core. Science, 276, 1821-1825.

Tipper, E.T., Bickle, M.J., Galy, A., West, A.J., Pomiès, C. and Chapman, H.J., 2006. The short term climatic sensitivity of carbonate and silicate weathering fluxes: insight from seasonal variations in river chemistry. Geochimica et Cosmochimica Acta, 70, 2737-2754.

Tiwari, M., Ramesh, R., Somayajulu, B.L.K., Jull, A.J.T. and Burr, G.S., 2005. Early deglacial (~19-17 ka) strengthening of the northeast monsoon. Geophysical Research Letters, 32, L19712.

Tiwari, M., Ramesh, R., Yadava, M.G., Somayajulu, B.L.K., Jull, A.J.T. and Burr, G.S., 2006. Is there a persistent control of monsoon winds by precipitation during the late Holocene? Geochemistry, Geophysics, Geosystems, 7, Q03001.

Torres, M.A., West, A.J. and Clark, K.E., 2015. Geomorphic regime modulates hydrologic control of chemical weathering in the Andes-Amazon. Geochimica et Cosmochimica Acta, 166, 105-128.

Tribovillard, N., Algeo, T.J., Lyons, T. and Riboulleau, A., 2006. Trace metals as paleoredox and paleoproductivity proxies: an update. Chemical Geology, 232, 12-32.

Tripathy, G.R. and Das, A., 2014. Modeling geochemical datasets for source apportionment: Comparison of least square regression and inversion approaches. Journal of Geochemical Exploration, 144, 144-153.

Tripathy, G.R. and Singh, S.K., 2010. Chemical erosion rates of river basins of the Ganga system in the Himalaya: Reanalysis based on inversion of dissolved major ions, Sr, and $^{87}Sr/^{86}Sr$. Geochemistry, Geophysics, Geosystems, 11, Q03013.

Tripathy, G.R., Goswami, V., Singh, S.K. and Chakrapani, G.J., 2010. Temporal variations in Sr and $^{87}Sr/^{86}Sr$ of the Ganga headwaters: estimates of dissolved Sr flux to the mainstream. Hydrological Processes: An International Journal, 24, 1159-1171.

Tripathy, G.R., Singh, S.K. and Ramaswamy, V., 2014. Major and trace element geochemistry of Bay of Bengal sediments: Implications to provenances and their controlling factors. Palaeogeography, Palaeoclimatology, Palaeoecology, 397, 20-30.

Tripathy, G.R., Singh, S.K., Bhushan, R. and Ramaswamy, V., 2011. Sr-Nd isotope composition of the Bay of Bengal sediments: impact of climate on erosion in the Himalaya. Geochemical Journal, 45, 175-186.

Von Blanckenburg, F., 2005. The control mechanisms of erosion and weathering at basin scale from cosmogenic nuclides in river sediment. Earth and Planetary Science Letters, 237, 462-479.

Von Blanckenburg, F., Bouchez, J., Ibarra, D.E. and Maher, K., 2015. Stable runoff and weathering fluxes into the oceans over Quaternary climate cycles. Nature Geoscience, 8, 538-542.

Von Rad, U., Schaaf, M., Michels, K.H., Schulz, H., Berger, W.H. and Sirocko, F., 1999. A 5000-yr record of climate change in varved sediments from the oxygen minimum zone off Pakistan, Northeastern Arabian Sea. Quaternary Research, 51, 39-53.

Walker, C.B., Searle, M.P. and Waters, D.J., 2001. An integrated tectonothermal model for the evolution of the High Himalaya in western Zanskar with constraints from thermobarometry and metamorphic modeling. Tectonics, 20, 810-833.

Walker, J.C., Hays, P.B. and Kasting, J.F., 1981. A negative feedback mechanism for the long-term stabilization of Earth's surface temperature. Journal of Geophysical Research: Oceans, 86, 9776-9782.

Walling, D. E., and Webb, B.W., 1986. Solutes in river systems, in Solute Processes. (Ed.) Trudgill, S. T. 251-327, John Wiley, Hoboken, NJ.

Wan, S., Clift, P.D., Zhao, D., Hovius, N., Munhoven, G., France-Lanord, C., Wang, Y., Xiong, Z., Huang, J., Yu, Z. and Zhang, J., 2017. Enhanced silicate weathering of tropical shelf sediments exposed during glacial lowstands: a sink for atmospheric CO_2. Geochimica et Cosmochimica Acta, 200, 123-144.

Wan, S., Toucanne, S., Clift, P.D., Zhao, D., Bayon, G., Yu, Z., Cai, G., Yin, X., Révillon, S., Wang, D. and Li, A., 2015. Human impact overwhelms long-term climate control of weathering and erosion in southwest China. Geology, 43, 439-442.

Wang, T., Surge, D. and Mithen, S., 2012. Seasonal temperature variability of the Neoglacial (3300-2500 BP) and Roman Warm Period (2500-1600 BP) reconstructed from oxygen isotope ratios of limpet shells (Patella vulgata), Northwest Scotland. Palaeogeography, Palaeoclimatology, Palaeoecology, 317, 104-113.

Wanner, H., Beer, J., Bütikofer, J., Crowley, T.J., Cubasch, U., Flückiger, J., Goosse, H., Grosjean, M., Joos, F., Kaplan, J.O. and Küttel, M., 2008. Mid-to Late Holocene climate change: an overview. Quaternary Science Reviews, 27, 1791-1828.

West, A.J., 2012. Thickness of the chemical weathering zone and implications for erosional and climatic drivers of weathering and for carbon-cycle feedbacks. Geology, 40, 811-814.

West, A.J., Galy, A. and Bickle, M., 2005. Tectonic and climatic controls on silicate weathering. Earth and Planetary Science Letters, 235, 211-228.

White, A.F. and Blum, A.E., 1995. Effects of climate on chemical weathering in watersheds. Geochimica et Cosmochimica Acta, 59, 1729-1747.

White, A.F., Blum, A.E., Bullen, T.D., Vivit, D.V., Schulz, M. and Fitzpatrick, J., 1999. The effect of temperature on experimental and natural chemical weathering rates of granitoid rocks. Geochimica et Cosmochimica Acta, 63, 3277-3291.

Willenbring, J.K. and von Blanckenburg, F., 2010. Meteoric cosmogenic Beryllium-10 adsorbed to river sediment and soil: Applications for Earth-surface dynamics. Earth-Science Reviews, 98, 105-122.

Wu, L., Huh, Y., Qin, J., Du, G. and van Der Lee, S., 2005. Chemical weathering in the upper Huang He (Yellow River) draining the eastern Qinghai-Tibet plateau. Geochimica et Cosmochimica Acta, 69, 5279-5294.

Wyrtki, K., Bennett, E.B. and Rochford, D.J., 1971. Oceanographic atlas of the international Indian Ocean expedition, 531. Washington, DC: National Science Foundation.

Xu, H., Goldsmith, Y., Lan, J., Tan, L., Wang, X., Zhou, X., Cheng, J., Lang, Y. and Liu, C., 2020. Juxtaposition of western Pacific subtropical high on Asian Summer Monsoon shapes subtropical East Asian precipitation. Geophysical Research Letters, 47, e2019GL084705.

Yadava, M.G. and Ramesh, R., 2005. Monsoon reconstruction from radiocarbon dated tropical Indian speleothems. The Holocene, 15, 48-59.

Yadava, M.G. and Ramesh, R., 2006. Stable oxygen and carbon isotope variations as monsoon proxies: a comparative study of speleothems from four different locations in India. Journal Geological Society of India, 68, 461.

Yancheva, G., Nowaczyk, N.R., Mingram, J., Dulski, P., Schettler, G., Negendank, J.F., Liu, J., Sigman, D.M., Peterson, L.C. and Haug, G.H., 2007. Influence of the intertropical convergence zone on the East Asian monsoon. Nature, 445, 74-77.

Yin, A. and Harrison, T.M., 2000. Geologic evolution of the Himalayan-Tibetan orogen. Annual Review of Earth and Planetary Sciences, 28, 211-280.

Yuan, D., Cheng, H., Edwards, R.L., Dykoski, C.A., Kelly, M.J., Zhang, M., Qing, J., Lin, Y., Wang, Y., Wu, J. and Dorale, J.A., 2004. Timing, duration, and transitions of the last interglacial

Yurtsever, Y. and Gat, J.R., 1981. Stable isotope hydrology: deuterium and oxygen-18 in the water cycle. Atmospheric Waters, 103-142.

Zhang, S.R., Lu, X.X., Higgitt, D.L., Chen, C.T.A., Sun, H.G. and Han, J.T., 2007. Water chemistry of the Zhujiang (Pearl River): natural processes and anthropogenic influences. Journal of Geophysical Research: Earth Surface, 112, F01011.

Zorzi, C., Goni, M.F.S., Anupama, K., Prasad, S., Hanquiez, V., Johnson, J. and Giosan, L., 2015. Indian monsoon variations during three contrasting climatic periods: The Holocene, Heinrich Stadial 2 and the last interglacial-glacial transition. Quaternary Science Reviews, 125, 50-60.

Annexure

Table A2.1: *Details of the loss of ignition (LOI) during ashing of decarbonated sediment samples at 650 °C for 4 hours.*

Sample ID	Sample Weight		Weight Loss	LOI
	Before Heating	After Heating		
		g		%
GC06/1-2/S	0.68	0.59	0.0831	12.3
GC06/5-6/S	0.77	0.67	0.0972	12.7
GC06/9-10/S	0.50	0.44	0.0640	12.8
GC06/15-16/S	1.25	1.15	0.1006	8.0
GC06/25-26/S	0.51	0.44	0.0702	13.7
GC06/29-30/S	0.79	0.68	0.1042	13.3
GC06/33-34/S	0.71	0.61	0.0966	13.6
GC06/38-39/S	0.77	0.67	0.1031	13.3
GC06/43-44/S	0.78	0.67	0.1085	13.9
GC06/49-50/S	0.79	0.69	0.1066	13.4
GC06/54-55/S	0.63	0.55	0.0804	12.8
GC06/57-58/S	0.91	0.79	0.1212	13.3
GC06/61-62/S	0.72	0.63	0.0945	13.1
GC06/66-67/S	0.64	0.56	0.0808	12.6
GC06/70-71/S	0.64	0.56	0.0832	13.0
GC06/74-75/S	0.75	0.66	0.0937	12.5
GC06/78-79/S	0.89	0.77	0.1161	13.0
GC06/81-82/S	0.65	0.57	0.0849	13.0
GC06/90-91/S	0.76	0.67	0.0876	11.5
GC06/95-96/S	0.79	0.70	0.0956	12.1
GC06/99-100/S	0.76	0.67	0.0901	11.9
GC06/103-104/S	0.46	0.41	0.0561	12.1
GC06/108-109/S	0.71	0.62	0.0869	12.2
GC06/113-114/S	0.83	0.72	0.1048	12.7
GC06/117-118/S	0.69	0.60	0.0847	12.3
GC06/123-124/S	0.78	0.68	0.1033	13.2
GC06/132-133/S	0.78	0.67	0.1049	13.5
GC06/136-137/S	0.61	0.53	0.0794	12.9
GC06/139-140/S	0.64	0.56	0.0851	13.2
GC06/143-144/S	0.83	0.72	0.1086	13.1
GC06/146-147/S	0.61	0.53	0.0786	12.9
GC06/150-151/S	0.66	0.57	0.0901	13.6
GC06/154-155/S	0.71	0.61	0.0962	13.6

Table A2.1 *(continued)*

Sample ID	Sample Weight		Weight Loss	LOI
	Before Heating	After Heating		
		g		%
GC06/159-160/S	0.65	0.56	0.0841	13.0
GC06/165-166/S	0.61	0.54	0.0724	11.9
GC06/170-171/S	0.70	0.61	0.0901	12.9
GC06/174-175/S	0.65	0.57	0.0752	11.6
GC06/178-179/S	0.72	0.63	0.0877	12.2
GC06/182-183/S	0.73	0.64	0.0891	12.2
GC06/186-187/S	0.73	0.64	0.0958	13.0
GC06/195-196/S	0.90	0.79	0.1088	12.1
GC06/200-201/S	0.81	0.71	0.0958	11.9
GC06/205-206/S	0.60	0.53	0.0717	11.9
GC06/209-210/S	0.61	0.54	0.0745	12.2
GC06/215-216/S	0.68	0.60	0.0786	11.5
GC06/220-221/S	0.53	0.47	0.0622	11.7
GC06/226-227/S	0.80	0.71	0.0953	11.9
GC06/233-234/S	0.78	0.69	0.0907	11.6
GC06/239-240/S	0.70	0.62	0.0849	12.1
GC06/244-245/S	0.42	0.37	0.0486	11.6
GC06/255-256/S	0.69	0.61	0.0769	11.2
GC06/261-262/S	0.71	0.63	0.0840	11.8
GC06/266-267/S	0.73	0.65	0.0851	11.6
PDM18/0-2/S	0.70	0.67	0.0293	4.2
PDM18/2-4/S	0.76	0.73	0.0255	3.4
PSM18/4-6/S	0.87	0.85	0.0210	2.4
PDM18/6-8/S	0.68	0.66	0.0196	2.9
PDM18/8-10/S	0.78	0.76	0.0223	2.8
PDM18/10-12/S	0.79	0.77	0.0206	2.6
PDM18/12-14/S	0.76	0.74	0.0152	2.0
PDM18/14-16/S	0.80	0.78	0.0158	2.0
PDM18/16-18/S	0.83	0.81	0.0217	2.6
PDM18/18-20/S	0.76	0.75	0.0146	1.9
PDM18/20-22/S	0.76	0.75	0.0144	1.9
PDM18/22-24/S	0.65	0.63	0.0146	2.3
PDM18/24-26/S	0.84	0.82	0.0181	2.1

Table A2.1 *(continued)*

Sample ID	Sample Weight		Weight Loss	LOI
	Before Heating	After Heating		
		g		%
PDM18/26-28/S	0.81	0.80	0.0157	1.9
PDM18/28-30/S	0.80	0.78	0.0225	2.8
PDM18/30-32/S	1.08	1.05	0.0267	2.5
PDM18/32-34/S	1.07	1.05	0.0241	2.3
PDM18/34-36/S	0.80	0.77	0.0234	2.9
PDM18/36-38/S	0.85	0.82	0.0245	2.9
PDM18/38-40/S	0.84	0.82	0.0227	2.7
PDM18/40-42/S	0.84	0.82	0.0204	2.4
PDM18/42-44/S	0.73	0.71	0.0141	1.9
PDM18/44-46/S	0.91	0.89	0.0204	2.2
PDM18/46-48/S	0.94	0.92	0.0162	1.7
PDM18/48-50/S	0.84	0.83	0.0152	1.8
PDM18/50-52/S	0.94	0.92	0.0170	1.8
PDM18/52-54/S	0.93	0.91	0.0165	1.8
PDM18/54-56/S	0.98	0.97	0.0174	1.8
PDM18/56-58/S	1.01	0.99	0.0181	1.8
PDM18/58-60/S	1.10	1.08	0.0199	1.8
PDM18/60-62/S	1.02	1.00	0.0191	1.9
PDM18/62-64/S	1.03	1.02	0.0182	1.8
PDM18/64-66/S	0.81	0.80	0.0146	1.8
PDM18/66-68/S	1.06	1.05	0.0180	1.7
PDM18/68-70/S	0.90	0.89	0.0154	1.7

Table A6.1: *Oxygen isotopic ($\delta^{18}O$) data for the GPT-1 speleothem from the Gupteswar Cave, India.*

Age	**Age: 2.5%-Quantile**	**Age: 97.5%-Quantile**	**$\delta^{18}O$**
	Yr BP		‰ VPDB
3954	3407	4648	-5.2
3956	3410	4650	-5.0
3959	3411	4652	-5.1
3962	3413	4655	-5.1
3964	3414	4658	-5.5
3967	3417	4662	-5.5
3970	3419	4665	-4.7
3973	3421	4668	-5.1
3975	3425	4671	-4.9
3978	3429	4675	-4.5
3981	3431	4678	-4.9
3984	3435	4680	-5.0
3987	3439	4682	-5.0
3990	3442	4684	-4.9
3993	3445	4685	-4.8
3996	3448	4688	-4.7
3999	3451	4690	-4.5
4002	3453	4693	-4.6
4005	3455	4696	-4.7
4008	3458	4699	-5.2
4011	3461	4701	-5.2
4014	3465	4703	-5.3
4017	3467	4705	-5.7
4020	3471	4708	-6.0
4024	3474	4712	-5.7
4027	3477	4715	-6.0
4030	3480	4718	-5.9
4033	3483	4721	-5.8
4037	3486	4724	-5.6
4040	3488	4727	-5.5
4043	3491	4731	-4.9
4047	3495	4734	-5.2
4050	3499	4737	-4.8
4054	3503	4740	-5.3
4057	3507	4742	-4.7

Table A6.1 *(continued)*

Age	Age: 2.5%-Quantile	Age: 97.5%-Quantile	$\delta^{18}O$
	Yr BP		‰ VPDB
4061	3511	4744	-4.9
4064	3515	4747	-5.2
4068	3518	4750	-5.4
4071	3521	4753	-5.5
4075	3525	4756	-5.6
4079	3529	4759	-5.4
4082	3533	4762	-5.5
4086	3537	4765	-5.2
4090	3541	4767	-5.4
4093	3545	4770	-5.4
4097	3549	4773	-5.6
4101	3553	4776	-5.3
4105	3557	4778	-5.6
4108	3562	4782	-5.2
4112	3566	4785	-5.5
4116	3570	4788	-5.2
4120	3574	4791	-5.3
4124	3578	4794	-5.1
4128	3582	4796	-5.1
4132	3585	4799	-4.9
4136	3589	4802	-5.0
4140	3593	4804	-4.7
4144	3598	4806	-4.9
4148	3602	4809	-4.8
4152	3606	4811	-5.2
4156	3610	4813	-4.8
4160	3615	4816	-5.1
4164	3619	4819	-4.8
4168	3624	4822	-5.0
4172	3628	4825	-4.9
4177	3633	4828	-5.0
4181	3637	4831	-4.7
4185	3642	4834	-5.1
4189	3648	4837	-5.0
4193	3653	4841	-5.4

Table A6.1 *(continued)*

Age	Age: 2.5%-Quantile	Age: 97.5%-Quantile	δ^{18}O
	Yr BP		‰ VPDB
4198	3658	4843	-5.4
4202	3663	4846	-5.8
4206	3668	4848	-5.7
4211	3673	4850	-5.6
4215	3678	4853	-5.4
4219	3683	4854	-5.4
4224	3688	4856	-5.2
4228	3693	4858	-5.6
4233	3698	4861	-5.2
4237	3703	4864	-5.4
4242	3708	4866	-5.1
4246	3713	4869	-5.5
4251	3719	4872	-5.2
4255	3724	4875	-5.6
4260	3729	4878	-5.1
4264	3735	4881	-5.5
4269	3740	4884	-5.2
4274	3745	4887	-5.3
4278	3751	4890	-5.2
4283	3757	4893	-5.3
4287	3762	4895	-5.0
4292	3768	4898	-5.3
4297	3774	4900	-4.7
4302	3780	4901	-5.1
4306	3786	4904	-4.8
4311	3791	4907	-5.0
4316	3797	4911	-4.7
4321	3803	4914	-4.9
4325	3809	4916	-4.8
4330	3815	4918	-5.0
4335	3821	4920	-5.1
4340	3827	4923	-5.3
4345	3833	4927	-5.1
4350	3839	4931	-5.3
4354	3845	4934	-4.9

Table A6.1 *(continued)*

Age	**Age: 2.5%-Quantile**	**Age: 97.5%-Quantile**	**δ^{18}O**
Yr BP			‰ VPDB
4359	3851	4937	-5.2
4364	3858	4940	-5.1
4369	3864	4944	-5.1
4374	3870	4946	-4.9
4379	3876	4950	-4.7
4384	3882	4952	-4.8
4389	3888	4954	-4.7
4394	3894	4956	-4.6
4399	3900	4959	-4.8
4404	3906	4962	-4.6
4409	3913	4966	-4.9
4414	3919	4969	-5.1
4419	3926	4973	-5.4
4425	3932	4977	-5.3
4430	3938	4980	-5.4
4435	3945	4984	-5.0
4440	3951	4987	-5.1
4445	3958	4991	-4.8
4450	3964	4994	-5.2
4455	3970	4998	-4.7
4461	3977	5002	-4.9
4466	3983	5004	-4.6
4471	3990	5007	-4.9
4476	3996	5010	-4.6
4482	4003	5014	-4.9
4487	4009	5017	-4.6
4492	4016	5020	-4.9
4497	4022	5023	-4.9
4503	4029	5025	-5.0
4508	4036	5026	-4.7
4513	4043	5027	-4.8
4519	4050	5029	-4.7
4524	4057	5031	-4.9
4529	4063	5033	-4.8
4535	4070	5037	-5.3

Table A6.1 *(continued)*

Age	Age: 2.5%-Quantile	Age: 97.5%-Quantile	$\delta^{18}O$
	Yr BP		‰ VPDB
4540	4077	5042	-5.6
4546	4084	5045	-5.4
4551	4091	5049	-5.6
4556	4098	5053	-5.4
4562	4104	5057	-5.5
4567	4111	5061	-5.1
4573	4118	5064	-5.3
4578	4125	5067	-5.1
4584	4132	5069	-5.2
4589	4139	5072	-5.1
4595	4145	5075	-5.4
4600	4152	5080	-5.2
4606	4159	5083	-5.4
4611	4166	5085	-4.6
4617	4173	5089	-5.1
4622	4180	5092	-4.6
4628	4187	5096	-5.1
4633	4194	5100	-4.9
4639	4201	5102	-5.1
4644	4209	5105	-4.9
4650	4217	5108	-5.3
4656	4223	5112	-4.9
4661	4231	5116	-5.2
4667	4239	5120	-4.9
4672	4246	5123	-5.3
4678	4253	5126	-5.0
4684	4259	5130	-5.2
4689	4266	5134	-5.0
4695	4273	5137	-5.3
4701	4280	5142	-5.1
4706	4286	5146	-5.0
4712	4293	5150	-4.1
4718	4301	5154	-4.6
4723	4308	5158	-3.7
4729	4315	5161	-4.5

Table A6.1 *(continued)*

Age	Age: 2.5%-Quantile	Age: 97.5%-Quantile	$\delta^{18}O$
	Yr BP		‰ VPDB
4735	4322	5164	-4.7
4740	4330	5167	-4.9
4746	4338	5172	-4.8
4752	4346	5177	-5.0
4757	4353	5180	-4.8
4763	4360	5183	-5.4
4769	4367	5187	-5.2
4775	4374	5191	-5.2
4780	4381	5195	-5.2
4786	4388	5199	-5.1
4792	4395	5202	-5.2
4798	4403	5206	-5.5
4803	4410	5211	-4.5
4809	4418	5216	-5.1
4815	4426	5219	-4.8
4821	4433	5222	-5.3
4827	4440	5226	-5.0
4832	4447	5229	-5.4
4838	4453	5232	-4.9
4844	4461	5236	-5.3
4850	4468	5239	-4.7
4856	4476	5243	-5.3
4861	4483	5246	-4.9
4867	4491	5249	-5.3
4873	4499	5252	-4.9
4879	4506	5256	-4.9
4885	4514	5259	-4.7
4891	4523	5263	-4.8
4896	4530	5266	-4.9
4902	4537	5272	-5.0
4908	4545	5276	-5.2
4914	4552	5279	-5.2
4920	4560	5283	-5.0
4926	4568	5287	-5.5
4931	4575	5292	-5.1

Table A6.1 *(continued)*

Age	Age: 2.5%-Quantile	Age: 97.5%-Quantile	$\delta^{18}O$
	Yr BP		‰ VPDB
4937	4582	5296	-5.5
4943	4590	5301	-5.1
4949	4597	5306	-5.3
4955	4603	5310	-5.2
4961	4611	5314	-5.2
4967	4619	5319	-5.4
4972	4627	5322	-5.2
4978	4635	5327	-5.0
4984	4642	5331	-5.3
4990	4649	5336	-4.8
4996	4657	5340	-5.4
5002	4665	5345	-5.1
5008	4673	5348	-5.2
5014	4681	5352	-5.2
5019	4689	5355	-5.5
5025	4696	5360	-5.3
5031	4703	5365	-5.3
5037	4710	5370	-5.2
5043	4718	5374	-5.1
5049	4726	5378	-4.7
5055	4732	5382	-5.3
5060	4739	5387	-4.6
5066	4746	5392	-5.2
5072	4752	5398	-5.0
5078	4758	5402	-5.1
5084	4765	5406	-4.7
5090	4773	5411	-4.6
5096	4781	5415	-5.2
5102	4789	5421	-4.9
5107	4796	5425	-5.2
5113	4804	5429	-4.7
5119	4810	5433	-5.3
5125	4815	5439	-4.9
5131	4822	5445	-5.3
5137	4829	5449	-5.0

Table A6.1 *(continued)*

Age	Age: 2.5%-Quantile	Age: 97.5%-Quantile	$\delta^{18}O$
	Yr BP		‰ VPDB
5143	4836	5453	-5.6
5148	4842	5458	-5.4
5154	4849	5463	-6.0
5160	4855	5468	-4.9
5166	4863	5473	-5.4
5172	4870	5478	-5.1
5178	4877	5483	-5.4
5183	4884	5488	-5.3
5189	4891	5492	-5.1
5195	4897	5497	-4.7
5201	4903	5503	-5.4
5207	4910	5509	-4.8
5213	4917	5514	-5.3
5218	4923	5518	-5.1
5224	4928	5523	-6.0
5230	4934	5528	-5.8
5236	4940	5534	-5.6
5242	4946	5540	-5.9
5247	4952	5545	-5.7
5253	4959	5550	-5.5
5259	4965	5556	-5.8
5265	4970	5562	-6.2
5271	4977	5565	-6.0
5276	4983	5569	-5.2
5282	4989	5574	-6.0
5288	4996	5579	-5.8
5294	5002	5586	-6.2
5299	5010	5591	-6.5
5305	5016	5596	-6.0
5311	5020	5602	-5.7
5317	5026	5608	-6.0
5322	5031	5614	-6.0
5328	5038	5619	-6.4
5334	5044	5623	-5.2
5339	5050	5628	-6.3

Table A6.1 *(continued)*

Age	**Age: 2.5%-Quantile**	**Age: 97.5%-Quantile**	**$\delta^{18}O$**
	Yr BP		‰ VPDB
5345	5058	5633	-5.8
5351	5062	5639	-5.9
5356	5068	5645	-5.4
5362	5074	5651	-6.0
5368	5079	5657	-5.5
5373	5085	5662	-6.0
5379	5090	5667	-6.1
5385	5095	5671	-5.8
5390	5100	5676	-5.7
5402	5111	5686	-5.3
5413	5120	5697	-5.0
5424	5131	5708	-5.1
5435	5142	5718	-5.4
5446	5153	5729	-4.6
5457	5164	5740	-4.5
5468	5173	5752	-4.8
5479	5183	5764	-5.2
5490	5194	5774	-5.6
5501	5206	5784	-5.5
5512	5215	5795	-5.6
5523	5225	5806	-5.5
5534	5234	5817	-5.6
5545	5243	5827	-5.6
5555	5253	5838	-5.8
5566	5262	5849	-5.7
5577	5271	5860	-5.9
5587	5282	5870	-6.9
5598	5291	5880	-5.9
5608	5298	5890	-5.6
5619	5307	5901	-5.7
5629	5314	5912	-5.7
5639	5322	5922	-5.1
5649	5329	5933	-5.3
5660	5337	5943	-5.2
5670	5346	5953	-5.1

Table A6.1 *(continued)*

Age	Age: 2.5%-Quantile	Age: 97.5%-Quantile	$\delta^{18}O$
	Yr BP		‰ VPDB
5680	5353	5964	-4.9
5690	5363	5973	-4.9
5700	5372	5982	-5.0
5710	5380	5992	-5.1
5720	5388	6002	-5.1
5729	5396	6012	-5.2
5739	5405	6022	-5.6
5749	5414	6032	-5.5
5758	5423	6042	-5.5
5768	5431	6052	-5.5
5777	5439	6062	-5.9
5787	5447	6071	-5.9
5796	5454	6080	-5.7
5805	5462	6089	-5.6
5815	5469	6099	-5.4
5824	5478	6108	-5.5
5833	5487	6117	-5.8
5843	5496	6126	-5.8
5852	5505	6135	-6.0
5862	5515	6145	-5.6
5871	5523	6154	-5.6
5881	5531	6163	-5.5
5890	5539	6172	-5.5
5900	5548	6182	-5.6
5909	5557	6191	-5.8
5919	5566	6200	-5.8
6001	5646	6281	-5.7
6011	5656	6290	-5.6
6021	5666	6299	-5.6
6031	5675	6309	-5.6
6036	5679	6314	-5.5
6040	5684	6318	-5.8
6045	5688	6323	-5.9
6050	5693	6328	-5.8
6055	5698	6332	-5.8

Table A6.1 *(continued)*

Age	Age: 2.5%-Quantile	Age: 97.5%-Quantile	$\delta^{18}O$
	Yr BP		‰ VPDB
6060	5703	6337	-6.2
6065	5708	6342	-5.7
6070	5714	6347	-5.9
6075	5719	6352	-5.8
6080	5723	6357	-6.1
6085	5728	6362	-5.9
6090	5732	6367	-6.0
6095	5736	6371	-5.9
6100	5741	6376	-6.3
6104	5745	6381	-6.1
6109	5750	6386	-6.6
6114	5754	6390	-6.3
6119	5759	6395	-8.1
6124	5764	6400	-6.1
6129	5769	6405	-6.1
6134	5774	6410	-6.0
6139	5778	6414	-6.3
6144	5782	6419	-5.9
6149	5786	6424	-5.9
6154	5791	6429	-5.9
6159	5796	6434	-5.9
6164	5801	6439	-6.1
6169	5806	6444	-6.2
6174	5811	6449	-6.0
6179	5815	6454	-6.0
6184	5820	6459	-6.2
6189	5825	6463	-6.1
6194	5830	6468	-5.6
6199	5835	6473	-5.1
6204	5841	6478	-4.2
6209	5846	6483	-5.1
6214	5851	6488	-5.3
6219	5855	6493	-5.1
6224	5860	6498	-5.3
6229	5865	6503	-5.1

Table A6.1 *(continued)*

Age	Age: 2.5%-Quantile	Age: 97.5%-Quantile	$\delta^{18}O$
	Yr BP		‰ VPDB
6234	5870	6508	-5.3
6239	5875	6512	-5.1
6244	5881	6517	-5.3
6249	5886	6522	-5.1
6254	5891	6527	-5.4
6259	5896	6532	-5.1
6264	5901	6537	-5.0
6269	5906	6542	-5.0
6274	5910	6548	-5.5
6279	5916	6552	-5.2
6284	5921	6557	-5.3
6289	5927	6562	-4.7
6294	5931	6567	-5.2
6299	5935	6572	-5.1
6304	5941	6577	-5.3
6309	5945	6581	-5.1
6314	5950	6586	-5.8
6319	5955	6591	-5.1
6324	5960	6596	-5.6
6334	5970	6606	-5.5
6344	5981	6616	-5.6
6354	5991	6626	-5.6
6364	6002	6635	-5.6
6374	6013	6645	-5.9
6384	6023	6656	-5.4
6394	6034	6666	-5.3
6404	6045	6676	-5.3
6414	6054	6686	-5.2
6424	6063	6695	-4.9
6434	6075	6705	-5.0
6444	6085	6715	-5.0
6449	6090	6719	-4.5
6454	6095	6724	-4.8
6459	6100	6729	-4.5
6464	6105	6735	-4.5

Table A6.1 *(continued)*

Age	Age: 2.5%-Quantile	Age: 97.5%-Quantile	$\delta^{18}O$
	Yr BP		‰ VPDB
6469	6110	6740	-4.4
6474	6114	6745	-4.9
6479	6118	6750	-4.3
6484	6123	6755	-4.8
6489	6128	6760	-4.4
6494	6134	6764	-4.9
6499	6139	6769	-4.1
6503	6144	6775	-4.9
6508	6149	6779	-4.2
6513	6154	6784	-4.8
6518	6160	6788	-4.2
6523	6165	6793	-5.3
6528	6171	6799	-4.5
6533	6176	6803	-4.9
6538	6181	6808	-4.5
6543	6186	6813	-4.9
6553	6197	6823	-5.2
6563	6208	6833	-5.2
6573	6218	6843	-5.4
6583	6228	6852	-6.2
6593	6237	6862	-6.0
6602	6249	6872	-6.0
6612	6259	6882	-6.1
6622	6270	6892	-6.3
6632	6279	6901	-6.4
6642	6290	6911	-6.3
6652	6300	6921	-6.5
6661	6309	6930	-6.6
6671	6320	6940	-6.1
6681	6332	6949	-6.3
6691	6343	6959	-6.3
6700	6353	6968	-6.1
6710	6361	6978	-6.0
6720	6369	6987	-5.4
6729	6380	6997	-5.8

Table A6.1 *(continued)*

Age	Age: 2.5%-Quantile	Age: 97.5%-Quantile	$\delta^{18}O$
	Yr BP		‰ VPDB
6739	6389	7007	-5.8
6749	6398	7018	-5.9
6753	6403	7022	-5.5
6758	6407	7027	-5.7
6763	6412	7032	-5.3
6768	6417	7037	-5.1
6773	6422	7042	-5.1
6777	6427	7047	-5.0
6782	6433	7052	-4.9
6787	6437	7056	-4.9
6792	6442	7061	-4.7
6796	6447	7066	-4.9
6801	6453	7071	-5.0
6806	6458	7076	-5.4
6811	6463	7081	-5.7
6815	6467	7085	-5.8
6820	6472	7091	-5.6
6825	6476	7096	-5.7
6830	6481	7100	-5.8
6834	6485	7105	-5.7
6839	6490	7110	-5.8
6844	6495	7115	-5.6
6848	6500	7119	-5.9
6853	6504	7124	-5.7
6858	6509	7129	-5.7
6863	6514	7134	-5.7
6867	6519	7138	-5.7
6872	6524	7143	-5.7
6877	6529	7148	-5.7
6881	6533	7152	-5.8
6886	6537	7157	-5.7
6891	6542	7161	-5.6
6895	6547	7165	-5.7
6900	6552	7170	-5.8
6904	6556	7174	-5.6

Table A6.1 *(continued)*

Age	Age: 2.5%-Quantile	Age: 97.5%-Quantile	$\delta^{18}O$
	Yr BP		‰ VPDB
6909	6560	7179	-5.8
6914	6565	7184	-5.8
6918	6569	7189	-5.7
6923	6574	7193	-5.9
6927	6578	7198	-5.8
6932	6583	7202	-6.0
6937	6587	7207	-6.0
6941	6592	7212	-5.7
6946	6596	7217	-5.6
6950	6600	7221	-5.6
6955	6605	7226	-5.7
6959	6609	7231	-5.6
6964	6613	7236	-5.3
6968	6618	7241	-5.3
6973	6624	7246	-5.5
6978	6628	7251	-5.5
6982	6632	7256	-5.5
6987	6636	7260	-5.6
6991	6641	7265	-5.3
6996	6646	7269	-5.4
7000	6650	7274	-5.1
7004	6654	7278	-5.1
7009	6658	7283	-5.0
7013	6662	7287	-5.4
7018	6666	7292	-5.0
7022	6670	7297	-5.0
7027	6675	7301	-4.9
7031	6679	7305	-5.4
7036	6683	7310	-5.1
7040	6688	7314	-5.5
7044	6692	7319	-5.1
7053	6700	7328	-4.8
7062	6708	7337	-5.1
7071	6717	7346	-5.2
7079	6725	7355	-5.4

Table A6.1 *(continued)*

Age	**Age: 2.5%-Quantile**	**Age: 97.5%-Quantile**	**$\delta^{18}O$**
	Yr BP		‰ VPDB
7088	6735	7364	-5.5
7096	6743	7372	-5.7
7105	6750	7381	-5.7
7114	6757	7390	-5.6
7122	6764	7398	-5.9
7130	6772	7407	-6.0
7139	6779	7415	-5.7
7147	6785	7423	-5.7
7156	6793	7432	-5.9
7164	6801	7440	-6.0
7172	6808	7449	-6.2
7180	6815	7457	-5.7
7189	6822	7466	-5.6
7197	6829	7474	-5.8
7205	6836	7482	-5.7
7213	6843	7490	-5.8
7221	6851	7498	-6.2
7229	6859	7507	-6.4
7233	6862	7511	-6.0
7237	6865	7515	-5.9
7241	6868	7519	-6.6
7245	6872	7523	-5.6
7249	6875	7527	-5.8
7252	6879	7531	-6.2
7256	6882	7535	-6.3
7260	6886	7539	-5.9
7264	6890	7543	-6.5
7268	6893	7547	-6.1
7272	6897	7551	-5.8
7276	6901	7555	-6.3
7280	6905	7559	-5.8
7283	6908	7563	-6.2
7287	6912	7566	-5.6
7291	6915	7570	-6.0
7295	6919	7573	-5.6

Table A6.1 *(continued)*

Age	**Age: 2.5%-Quantile**	**Age: 97.5%-Quantile**	**$\delta^{18}O$**
	Yr BP		‰ VPDB
7299	6923	7577	-6.1
7302	6926	7581	-5.8
7306	6930	7585	-6.1
7310	6933	7588	-5.4
7314	6936	7592	-6.3
7317	6939	7596	-6.3
7321	6944	7599	-6.3
7325	6948	7603	-6.2
7328	6951	7607	-6.1
7332	6954	7610	-5.8
7336	6958	7614	-6.2
7339	6962	7617	-5.9
7343	6965	7621	-6.7
7347	6968	7624	-6.3
7350	6971	7628	-7.0
7354	6975	7632	-5.9
7357	6978	7635	-6.7
7361	6981	7639	-6.2
7365	6984	7642	-6.7
7368	6988	7646	-5.9
7372	6991	7649	-7.2
7375	6995	7653	-5.8
7379	6999	7656	-6.5
7382	7002	7660	-5.3
7386	7005	7663	-6.3
7392	7012	7670	-6.2
7399	7018	7677	-6.3
7406	7025	7684	-5.7
7519	7135	7797	-5.8
7525	7141	7802	-5.7
7531	7147	7807	-5.9
7536	7152	7812	-5.8
7539	7155	7815	-6.1
7542	7158	7818	-6.1
7544	7161	7821	-6.4

Table A6.1 *(continued)*

Age	**Age: 2.5%-Quantile**	**Age: 97.5%-Quantile**	**$\delta^{18}O$**
Yr BP			‰ VPDB
7547	7163	7823	-6.3
7550	7166	7826	-6.5
7552	7168	7828	-6.3
7555	7171	7831	-6.9
7558	7174	7834	-6.3
7560	7177	7837	-6.7
7563	7180	7840	-6.4
7566	7182	7842	-6.6
7568	7185	7845	-6.1
7571	7188	7847	-6.7
7573	7190	7849	-5.8
7576	7193	7852	-5.9
7578	7196	7854	-5.6
7581	7198	7856	-5.9
7583	7201	7858	-5.4
7586	7204	7860	-4.9
7588	7206	7863	-5.3
7591	7209	7865	-6.1
7593	7211	7867	-5.2
7596	7214	7869	-5.6
7598	7217	7871	-5.0
7600	7219	7873	-5.7
7603	7222	7876	-5.2
7605	7224	7878	-5.9
7607	7227	7880	-5.5
7610	7230	7882	-6.2
7612	7232	7885	-5.9
7614	7235	7887	-6.4
7617	7237	7889	-6.3
7621	7242	7893	-6.2
7625	7248	7896	-6.0
7630	7254	7900	-5.9
7634	7258	7903	-6.1
7638	7264	7907	-6.1
7642	7269	7911	-5.8

Table A6.1 *(continued)*

Age	**Age: 2.5%-Quantile**	**Age: 97.5%-Quantile**	**$\delta^{18}O$**
Yr BP			‰ VPDB
7646	7274	7914	-5.9
7650	7279	7918	-5.3
7654	7284	7921	-5.3
7658	7289	7924	-5.3
7662	7295	7927	-5.2
7665	7301	7931	-5.0
7669	7306	7934	-4.9
7672	7311	7938	-4.8
7676	7315	7940	-5.0
7679	7320	7943	-5.1
7681	7322	7944	-5.2
7682	7324	7945	-5.3
7684	7326	7946	-4.9
7685	7329	7947	-5.0
7687	7331	7947	-5.0
7688	7333	7948	-5.1
7690	7336	7949	-4.8
7692	7338	7950	-4.9
7693	7340	7950	-5.0
7694	7343	7951	-4.9
7696	7345	7952	-5.1
7697	7348	7953	-4.9
7699	7350	7953	-5.1
7700	7352	7954	-5.1
7701	7354	7955	-5.2
7703	7357	7956	-5.1
7704	7360	7957	-5.1
7705	7362	7958	-5.1
7707	7365	7959	-5.1
7708	7367	7960	-5.1
7709	7369	7960	-5.3
7710	7372	7961	-5.6
7712	7374	7961	-5.2
7713	7376	7961	-5.2
7714	7379	7962	-5.2

Table A6.1 *(continued)*

Age	**Age: 2.5%-Quantile**	**Age: 97.5%-Quantile**	**δ^{18}O**
Yr BP			‰ VPDB
7715	7381	7963	-5.2
7716	7383	7963	-5.2
7717	7385	7964	-5.3
7718	7388	7964	-5.2
7719	7390	7964	-5.5
7720	7392	7965	-5.5
7722	7396	7965	-5.7
7724	7400	7965	-5.8
7726	7404	7966	-5.6
7728	7408	7966	-5.7
7730	7412	7967	-5.5
7732	7416	7967	-5.1
7734	7420	7968	-5.0
7736	7424	7969	-4.0
7738	7428	7969	-4.3
7739	7433	7970	-4.4
7741	7438	7971	-4.8
7743	7443	7971	-4.3
7745	7447	7972	-4.4
7747	7451	7972	-4.6
7748	7456	7973	-4.8
7749	7459	7973	-4.5
7750	7461	7973	-4.8
7751	7464	7973	-4.3
7752	7465	7974	-4.5
7753	7467	7974	-4.3
7754	7469	7974	-4.9
7754.6	7471	7975	-4.5
7755.4	7473	7976	-4.8
7756	7476	7976	-4.8
7757	7478	7977	-4.8
7758	7479	7977	-4.6
7759	7481	7977	-3.2
7760	7483	7977	-4.4
7760.5	7485	7978	-5.2

Table A6.1 *(continued)*

Age	**Age: 2.5%-Quantile**	**Age: 97.5%-Quantile**	**$\delta^{18}O$**
	Yr BP		‰ VPDB
7761.4	7488	7978	-5.0
7762	7490	7978	-4.8
7763	7491	7978	-4.7
7764	7493	7979	-5.0
7765	7495	7979	-5.6
7765.5	7497	7979	-4.9
7766.3	7499	7979	-5.9
7767	7501	7980	-5.2
7768	7503	7980	-5.4
7769	7505	7980	-4.9
7769.6	7507	7980	-5.9
7770.4	7509	7980	-4.6
7771	7511	7981	-5.7
7772	7513	7981	-4.8
7773	7515	7981	-5.9
7773.6	7517	7981	-4.8
7774.4	7520	7981	-5.7
7775	7522	7982	-4.2
7776	7524	7982	-5.9
7777	7525	7982	-4.8
7777.5	7527	7983	-8.5
7778.3	7529	7983	-4.5
7779	7531	7983	-5.4
7780	7532	7983	-5.2
7780.6	7534	7983	-5.3
7781.4	7536	7984	-5.1
7782	7538	7984	-5.0
7783	7540	7984	-4.5
7783.7	7542	7984	-5.1
7784.5	7543	7984	-4.4
7785	7545	7984	-5.0
7786	7547	7985	-4.6
7786.7	7550	7985	-5.0
7787.5	7551	7985	-4.8
7788	7552	7986	-5.2

Table A6.1 *(continued)*

Age	Age: 2.5%-Quantile	Age: 97.5%-Quantile	$\delta^{18}O$
	Yr BP		‰ VPDB
7789	7554	7986	-4.3
7789.7	7556	7987	-5.2
7790.4	7558	7988	-4.5
7791	7560	7988	-5.4
7792	7563	7989	-5.0
7792.6	7564	7989	-6.1
7793.4	7566	7990	-4.8
7794	7568	7990	-5.9
7795	7570	7990	-5.1
7795.5	7571	7990	-6.0
7796.2	7573	7991	-5.5
7797	7574	7991	-6.5
7797.7	7576	7991	-5.7
7798.4	7577	7991	-6.5
7799	7579	7991	-5.7
7800	7581	7992	-6.1
7800.5	7583	7992	-5.2
7801.2	7585	7992	-6.2
7802	7587	7992	-5.8
7802.6	7588	7993	-5.8
7803.3	7589	7993	-5.4
7804	7590	7993	-6.0
7804.7	7591	7993	-5.3
7805.4	7592	7993	-6.0
7806	7593	7994	-5.4
7806.7	7594	7994	-6.2
7807.4	7595	7994	-5.6
7808	7596	7995	-6.3
7808.8	7597	7995	-5.7
7809.4	7599	7996	-6.3
7810	7601	7997	-5.7
7810.8	7603	7997	-6.2
7811.5	7605	7997	-5.9
7812	7607	7998	-6.3
7812.8	7609	7998	-5.4

Table A6.1 *(continued)*

Age	Age: 2.5%-Quantile	Age: 97.5%-Quantile	$\delta^{18}O$
	Yr BP		‰ VPDB
7813.5	7610	7998	-6.1
7814	7612	7998	-6.3
7814.8	7614	7998	-6.1
7815.4	7614	7998	-5.4
7816	7615	7999	-6.3
7816.7	7616	7999	-6.6
7817.4	7617	7999	-6.5
7818	7619	8000	-5.9
7818.7	7620	8000	-6.5
7819.3	7621	8001	-5.9
7820	7622	8001	-6.4
7820.6	7624	8001	-5.7
7821.2	7625	8001	-6.6
7822	7626	8002	-5.8
7822.5	7627	8002	-6.5
7823.1	7629	8002	-5.9
7823.8	7630	8003	-6.6
7824.4	7631	8003	-6.1
7825	7632	8003	-6.6
7825.7	7633	8003	-5.5
7826.3	7634	8003	-5.9
7827	7635	8004	-6.1
7827.5	7636	8004	-6.9
7828.1	7637	8004	-6.3
7828.8	7637	8004	-6.7
7829.4	7638	8004	-6.0
7830	7639	8005	-6.8
7830.6	7640	8005	-5.9
7831.2	7641	8006	-6.9
7831.8	7642	8006	-6.5
7832.4	7643	8007	-6.9
7833	7644	8007	-6.6
7833.6	7646	8008	-6.9
7834.2	7647	8008	-6.3
7834.8	7648	8009	-6.2

Table A6.1 *(continued)*

Age	Age: 2.5%-Quantile	Age: 97.5%-Quantile	$\delta^{18}O$
	Yr BP		‰ VPDB
7835.4	7649	8009	-5.9
7836	7650	8009	-6.3
7836.6	7651	8009	-5.6
7837.2	7652	8009	-6.4
7837.8	7652	8009	-6.2
7838.4	7654	8010	-6.8
7839	7655	8010	-6.7
7839.6	7656	8011	-7.0
7840.1	7656	8011	-6.7
7840.7	7657	8011	-7.1
7841.3	7658	8012	-6.3
7841.9	7660	8012	-7.1
7842.5	7661	8013	-6.2
7843	7662	8013	-6.7
7843.6	7663	8013	-6.1
7844.2	7664	8014	-6.8
7844.8	7665	8014	-5.9
7845.3	7667	8014	-6.3
7845.9	7668	8014	-5.8
7846.5	7668	8015	-6.2
7847	7669	8015	-5.5
7847.6	7670	8015	-6.2
7848.2	7671	8016	-5.7
7848.7	7671	8016	-6.4
7849.3	7672	8016	-5.8
7849.9	7673	8017	-6.5
7850.4	7674	8018	-6.0
7851	7675	8018	-6.6
7851.5	7676	8019	-5.9
7852.1	7676	8019	-6.6
7852.6	7677	8019	-5.9
7853.2	7678	8019	-6.5
7853.7	7679	8020	-6.1
7854.3	7680	8020	-6.6
7854.8	7681	8020	-6.0

Table A6.1 *(continued)*

Age	Age: 2.5%-Quantile	Age: 97.5%-Quantile	$\delta^{18}O$
	Yr BP		‰ VPDB
7855.4	7681	8020	-6.7
7855.9	7682	8021	-6.6
7856.5	7683	8021	-7.0
7857	7684	8022	-6.7
7857.6	7685	8022	-7.1
7858.1	7685	8023	-6.7
7858.7	7686	8023	-7.2
7859.2	7686	8023	-7.0
7859.7	7687	8023	-7.5
7860.3	7688	8023	-6.6
7860.8	7688	8023	-7.2
7861.3	7689	8024	-6.7
7861.9	7690	8025	-7.0
7862.4	7690	8025	-6.3
7863	7692	8026	-6.0
7865	7694	8027	-5.8
7866	7695	8028	-5.8
7867	7696	8028	-5.6
7868	7698	8030	-5.7
7869	7699	8031	-5.8
7870	7700	8032	-5.9
7871	7702	8033	-5.3
7872	7703	8034	-5.1
7873	7704	8035	-4.9
7874	7705	8036	-5.0
7875	7706	8038	-5.5
7876	7707	8039	-5.3
7877	7708	8040	-5.2
7878	7709	8042	-5.2
7879	7710	8042	-5.4
7914	7746	8077	-5.4
7915	7748	8078	-5.6
7916	7750	8079	-5.1
7917	7751	8081	-5.2
7918	7751	8083	-5.0

Table A6.1 *(continued)*

Age	**Age: 2.5%-Quantile**	**Age: 97.5%-Quantile**	**$\delta^{18}O$**
	Yr BP		‰ VPDB
7919	7752	8084	-5.8
7921	7754	8086	-6.4
7922	7754	8088	-6.1
7923	7754	8088	-6.6
7924	7756	8091	-6.7
7925	7757	8091	-7.1
7927	7757	8093	-7.3
7928	7759	8094	-7.2
7929	7760	8095	-6.3
7930	7761	8097	-6.1
7932	7762	8099	-5.6
7933	7762	8100	-5.6
7934	7763	8101	-5.7
7936	7765	8103	-6.1
7937	7765	8104	-5.9
7938	7766	8105	-6.0
7940	7768	8107	-6.2
7941	7769	8109	-6.0
7942	7770	8110	-6.3
7944	7771	8112	-6.3
7945	7772	8115	-6.1
7946	7773	8117	-5.9
7948	7774	8120	-5.9
7949	7775	8122	-6.1
7951	7776	8125	-6.2
7952	7777	8127	-6.4
7954	7777	8129	-6.4
7955	7778	8133	-6.1
7957	7778	8136	-6.0
7958	7779	8138	-6.0
7960	7780	8142	-6.0
7961	7780	8144	-5.7
7963	7782	8148	-5.9
7964	7783	8151	-5.6
7966	7783	8153	-5.9

Table A6.1 *(continued)*

Age	Age: 2.5%-Quantile	Age: 97.5%-Quantile	$\delta^{18}O$
Yr BP			‰ VPDB
7972	7786	8167	-5.8
7987	7792	8206	-5.7
8003	7798	8253	-5.5
8019	7805	8296	-5.6
8038	7814	8340	-4.5
8056	7823	8373	-5.4
8079	7842	8400	-6.0
8104	7866	8429	-6.1
8125	7885	8450	-5.8
8165	7920	8488	-6.0
8191	7934	8511	-6.1
8218	7947	8541	-5.9
8245	7959	8578	-6.0
8264	7967	8599	-6.1
8282	7975	8625	-5.9
8319	7989	8689	-6.3
8345	7997	8741	-6.7
8379	8006	8805	-6.1
8410	8014	8859	-6.3
8431	8022	8895	-5.5
8455	8028	8929	-5.7
8470	8035	8946	-5.3
8482	8042	8952	-5.0
8494	8049	8956	-4.7
8510	8062	8965	-5.2
8523	8071	8973	-6.1
8539	8086	8981	-6.0
8556	8103	8991	-6.1
8574	8123	9000	-5.7
8591	8144	9009	-6.1
8609	8166	9018	-5.2
8622	8185	9022	-5.6
8640	8210	9029	-5.7
8662	8246	9041	-5.6
8675	8266	9046	-5.8

Table A6.1 *(continued)*

Age	Age: 2.5%-Quantile	Age: 97.5%-Quantile	$\delta^{18}O$
	Yr BP		‰ VPDB
8698	8301	9056	-6.0
8716	8331	9062	-6.0
8733	8360	9070	-5.9
8751	8391	9078	-5.8
8768	8423	9086	-6.3
8786	8454	9095	-6.6
8803	8481	9105	-5.7
8819	8505	9114	-6.1
8832	8526	9120	-6.1
8844	8546	9128	-4.5
8856	8561	9133	-5.5
8868	8578	9142	-5.4
8880	8597	9150	-5.4
8891	8613	9157	-6.0
8903	8626	9165	-4.9
8914	8639	9173	-5.4
8924	8651	9183	-6.1
8935	8663	9189	-5.1
8945	8674	9196	-5.4
8958	8687	9205	-5.4
8971	8701	9217	-5.4
8982	8711	9230	-5.4
8994	8723	9241	-5.5
9002	8731	9251	-5.6
9009	8739	9258	-5.8
9019	8753	9269	-5.9
9028	8760	9281	-6.4
9040	8773	9295	-5.5
9048	8782	9305	-5.2
9054	8788	9309	-5.3
9059	8798	9313	-5.4
9063	8804	9316	-5.1
9068	8810	9320	-5.2
9073	8817	9326	-5.5
9078	8824	9329	-5.4

Table A6.1 *(continued)*

Age	Age: 2.5%-Quantile	Age: 97.5%-Quantile	$\delta^{18}O$
	Yr BP		‰ VPDB
9082	8828	9332	-5.1
9086	8834	9334	-5.5
9092	8844	9341	-5.4
9096	8847	9345	-5.6
9102	8854	9349	-5.9
9107	8857	9352	-6.0
9112	8862	9356	-5.6
9117	8868	9359	-5.1
9121	8874	9362	-5.5
9125	8878	9365	-4.8
9130	8883	9369	-5.3
9133	8886	9372	-5.7
9138	8892	9377	-6.1
9144	8898	9381	-5.3
9148	8902	9384	-4.7
9151	8904	9388	-4.9
9155	8909	9392	-5.2
9160	8914	9398	-6.4
9164	8918	9403	-7.1
9168	8922	9407	-5.1
9172	8927	9415	-5.3
9175	8930	9422	-5.5
9179	8933	9427	-5.1
9183	8936	9434	-5.4
9187	8939	9438	-5.3
9191	8943	9444	-5.7
9194	8946	9449	-6.2
9199	8949	9456	-5.9
9202	8951	9461	-5.3
9205	8954	9466	-5.6
9208	8956	9471	-6.2
9210	8958	9477	-5.6
9213	8958	9481	-5.3

List of Publications

Peer-Reviewed Journal Articles

1. A.M. Lone, S.P. Singh, R.A. Shah, H. Achyuthan, N. Ahmad, A. Qasim, G.R. Tripathy, **A. Samanta**, and P. Kumar, 2022. The late Holocene hydroclimate variability in the Northwest Himalaya: Sedimentary clues from the Wular Lake, Kashmir Valley. *Journal of Asian Earth Sciences, 229, 105184*. https://doi.org/10.1016/j.jseaes.2022.105184.

2. **A. Samanta**, G.R. Tripathy, B.N. Nath, R. Bhushan, R. Panchang, N. Bharti, and A. Shrivastava, 2022. Holocene variability in chemical weathering and ocean redox state: A reconstruction using sediment geochemistry of the Arabian Sea. *Journal of Asian Earth Sciences, 224, 105029*. https://doi.org/10.1016/j.jseaes.2021.105029.

3. **A. Samanta**, G.R. Tripathy, A.T. Pradeep, and A. Mandal, 2021. Major ion chemistry of two cratonic rivers in the Tropics: Weathering rates and their controlling factors. *Hydrological Processes, 35, 2, e14035*. https://doi.org/10.1002/hyp.14035.

4. **A. Samanta**, G.R. Tripathy, and R. Das, 2019. Temporal variations in water chemistry of the (lower) Brahmaputra River: Implications to seasonality in mineral weathering. *Geochemistry, Geophysics, Geosystems, 20, 2769-2785*. https://doi.org/10.1029/2018GC008047.

5. M. Joshi, **A. Samanta**, G.R. Tripathy, and S. Rajamani, 2017. Formation and stability of prebiotically relevant vesicular systems in terrestrial geothermal environments. *Life, 7, 51, 1-14*. https://doi.org/10.3390/life7040051.

Manuscripts in Preparation

* **A. Samanta**, G.R. Tripathy, R. Panchang, B.N. Nath, R. Bhushan, and N. Bharti. Late Holocene intensification of chemical weathering due to human-induced rise in C4 vegetation.

** **A Samanta**, G.R. Tripathy, N Gandhi, B.N. Goswami and A.P. Reddy. Indian Ocean aided Super-drought event in the core monsoon region around 6.5 kyr BP.

Conference Abstracts

1. **A. Samanta**, G.R. Tripathy, R. Panchang, B.N. Nath, R. Bhushan, and N. Bharti, 2022. Linkage between chemical erosion and human-induced vegetation pattern during the late Holocene period. *EGU22-515, EGU General Assembly*.

2. **A. Samanta** and R. Das, 2021. Evaluation of the concentration-discharge relationship for the Brahmaputra River. *Goldschmidt, Lyon, France*.

3. **A. Samanta** and G.R. Tripathy, 2020. Runoff-independent chemical weathering in the Brahmaputra River basin. *36th International Geological Congress, Delhi*.

4. A. Mandal, G.R. Tripathy, **A. Samanta**, A. Pradeep, 2020. Evidence of sulfide oxidation in the Damodar and Subarnarekha river basins. *36th International Geological Congress, Delhi*.

5. G.R. Tripathy, **A. Samanta**, A.T. Pradeep, and A. Mandal, 2018. Sulfide oxidation in mining-dominated river basins and its impact on long-term carbon cycle. *Humboldt (AvH) Kolleg, Aurangabad, India*.

6. **A. Samanta** and G.R. Tripathy, 2017. Evidence of pyrophosphate bearing dolomitic veins in Paleoproterozoic rocks: Link between life evolution and hydrothermal activity. *Virtual Poster (May 2017) Showcase, American Geophysical Union, Washington, DC*.